Soil Liquefaction during Recent Large-Scale Earthquakes

Editors: Rolando P. Orense,
Ikuo Towhata & Nawawi Chouw

CRC Press
Taylor & Francis Group
A BALKEMA BOOK

SOIL LIQUEFACTION DURING RECENT LARGE-SCALE EARTHQUAKES

This page intentionally left blank

SELECTED PAPERS FROM THE NEW ZEALAND – JAPAN WORKSHOP ON SOIL LIQUEFACTION DURING RECENT LARGE-SCALE EARTHQUAKES, AUCKLAND, NEW ZEALAND, 2–3 DECEMBER 2013

Soil Liquefaction during Recent Large-Scale Earthquakes

Editors

Rolando P. Orense
University of Auckland, New Zealand

Ikuo Towhata
University of Tokyo, Japan

Nawawi Chouw
University of Auckland, New Zealand

CRC Press
Taylor & Francis Group
Boca Raton London New York Leiden

CRC Press is an imprint of the
Taylor & Francis Group, an **informa** business

A BALKEMA BOOK

Cover photos: R.P. Orense (Christchurch earthquake); I. Towhata (Great East Japan earthquake)

CRC Press/Balkema is an imprint of the Taylor & Francis Group, an informa business

Typeset by V Publishing Solutions Pvt Ltd., Chennai, India
Printed and bound in Great Britain by CPI Group (UK) Ltd, Croydon, CR0 4YY

Published by: CRC Press/Balkema
P.O. Box 11320, 2301 EH Leiden, The Netherlands
e-mail: Pub.NL@taylorandfrancis.com
www.crcpress.com – www.taylorandfrancis.com

ISBN: 978-1-138-02643-8 (Hbk)
ISBN: 978-1-315-75941-8 (eBook PDF)

Soil Liquefaction during Recent Large-Scale Earthquakes – Orense, Towhata & Chouw (Eds)
© 2014 Taylor & Francis Group, London, ISBN 978-1-138-02643-8

Table of contents

Soil Liquefaction during Recent Large-Scale Earthquakes – Orense, Towhata & Chouw (Eds)
 ISBN 978-1-138-02643-8

Preface

The 2010–2011 Canterbury earthquakes in New Zealand and the 2011 off the Pacific Coast of Tohoku Earthquake in Japan have caused significant damage to many residential houses due to varying degrees of soil liquefaction over a very wide extent of urban areas unseen in past destructive earthquakes. While soil liquefaction occurred in naturally-sedimented soil formations in Christchurch, most of the areas which liquefied in Tokyo Bay area were reclaimed soil and artificial fill deposits, thus providing researchers with wide range of soil deposits to characterize soil and site response to large-scale earthquake shaking.

Although these earthquakes in New Zealand and Japan both caused extensive damage to life and property, they also serve as an opportunity to understand better the response of soil and building foundations to such large-scale earthquake shaking. With the wealth of information obtained in the aftermath of both earthquakes, information-sharing and knowledge-exchange are vital in achieving liquefaction-proof urban areas in both countries. Data regarding the observed damage to residential houses as well and the lessons learnt are essential for the rebuilding efforts in the coming years and in mitigating buildings located in regions with high liquefaction potential.

As part of collaborative research programme sponsored by the New Zealand's Ministry of Business, Innovation and Development (MBIE) and the Japan Society for the Promotion of Science, the Geomechanics Group of the University of Auckland and the Geotechnical Engineering Laboratory of the University of Tokyo co-hosted the *New Zealand – Japan Workshop on Soil Liquefaction during Recent Large Scale Earthquakes* held at the University of Auckland, New Zealand from 2–3 December 2013. The workshop brought together researchers from both countries, as well as from the United States and Chile, to review the findings and observations from both earthquakes and discuss possible measures to mitigate future damage. The specific research question that was addressed by the workshop was: "Considering the large-scale shaking during the Christchurch and Tohoku earthquakes, what new lessons were learned in terms of soil liquefaction and the associated response of infrastructure?"

Although the workshop was open to the public, the participation of presenters was by invitation only. This is to ensure that the quality of papers would be high and that the presentations will address the needs of the earthquake rebuild programmes. All presenters were submitted a paper describing their work, followed by peer-review process after which preprints were be circulated weeks before the workshop to encourage thinking about the topics to be addressed in the discussion sessions. In addition to paper presentations, two discussion sessions aimed at eliciting important comments about the current state of our understanding on soil liquefaction and to indicate which issues need to be further investigated in the future. After the event, the authors were then requested to revise their papers to include some of the comments made during the workshop presentation.

The proceedings consist of 21 high quality papers from liquefaction experts which have been individually refereed to examine for relevance to the theme of the workshop as well as for quality of technical content and presentation. In addition, full accounts of the two discussion sessions are also included in this volume. The editors hope that the papers presented in this workshop will further advance our understanding of soil liquefaction and associated phenomena.

This page intentionally left blank

Soil Liquefaction during Recent Large-Scale Earthquakes – Orense, Towhata & Chouw (Eds)
© 2014 Taylor & Francis Group, London, ISBN 978-1-138-02643-8

Acknowledgements

The New Zealand–Japan Workshop Organising Committee would like to acknowledge the financial support provided by the Ministry of Business, Innovation and Employment (MBIE). The committee would also like to thank the staff and students of the Department of Civil and Environmental Engineering, University of Auckland, for making the workshop a success. Finally, a sincere thanks to all colleagues and friends who supported this endeavour, especially to those who contributed papers to the workshop and actively participated in the discussion sessions and to the panel of reviewers who donated their precious time, for making this volume possible.

This page intentionally left blank

Soil Liquefaction during Recent Large-Scale Earthquakes – Orense, Towhata & Chouw (Eds)
© 2014 Taylor & Francis Group, London, ISBN 978-1-138-02643-8

Organising committee

Assoc Prof Rolando Orense, *University of Auckland, New Zealand*
Prof Ikuo Towhata, *University of Tokyo, Japan*
Assoc Prof Nawawi Chouw, *University of Auckland, New Zealand*

This page intentionally left blank

Soil Liquefaction during Recent Large-Scale Earthquakes – Orense, Towhata & Chouw (Eds)
© 2014 Taylor & Francis Group, London, ISBN 978-1-138-02643-8

Panel of reviewers

Each paper included in this volume, including the summaries of the discussion sessions, has been carefully reviewed for relevance to the workshop theme as well as for quality of technical content and presentation by the members of a panel consisting of the following experts:

Brendon Bradley
CY Chin
Philip Clayton
Nawawi Chouw
Misko Cubrinovski
Russsell Green
Susumu Iai
Takashi Kiyota
M Muntohar
Rolando Orense
Andy O'Sullivan
Esteban Sáez
Ikuo Towhata
Yochi Tsukamoto
Taro Uchimura
Liam Wotherspoon

Participants of the NZ – Japan Workshop on Soil Liquefaction.

Soil Liquefaction during Recent Large-Scale Earthquakes – Orense, Towhata & Chouw (Eds)
© 2014 Taylor & Francis Group, London, ISBN 978-1-138-02643-8

List of participants

Aboel-Naga, Hossam	University of Auckland	h.naga@auckland.ac.nz
Anderson, Victoria	Geoscience Consulting	Victoria@nzgeoscience.co.nz
Anwar, Sajjad	AECOM	sajjad.anwar@aecom.com
Bainbridge, Sophie	Golder Associates	sbainbridge@golder.co.nz
Bauld, Chris	Tonkin & Taylor Ltd	CBauld@tonkin.co.nz
Belczyk, Emilia	Tonkin & Taylor Ltd	EBelczyk@tonkin.co.nz
Bond, Daniel	Geoscience Consulting	dbond@nzgeoscience.co.nz
Boulanger, Ross	UC Davis	rwboulanger@ucdavis.edu;
Brabharan, Pathmanathan	Opus Consultants	brabha@opus.co.nz
Bradley, Brendon	University of Canterbury	brendon.bradley@canterbury.ac.nz
Bray, Jonathan	UC Berkeley	bray@ce.berkeley.edu
Chan, Yan	KGA Geotechnical Ltd	yan@kga.co.nz
Chituta, Sulanji	KGA Geotechnical Ltd	sulanji@kga.co.nz
Chouw, Nawawi	University of Auckland	n.chouw@auckland.ac.nz
Clayton, Philip	Beca Ltd	philip.clayton@beca.com
Cook, Phil	Cook Costello	phil@coco.co.nz
Cubrinovski, Misko	University of Canterbury	misko.cubrinovski@canterbury.ac.nz
Edwards, Clifton	Tonkin & Taylor Ltd	CEdwards@tonkin.co.nz
Elgamal, Ahmed	UC San Diego	elgamal@ucsd.edu
El-Nahas, Ala'a	Coffey	Ala'a.El-Nahas@coffey.com
Fox, Aaron	WSP Middle East	Aaron.Fox@wspgroup.ae
Gibson, Marcus	BECA Ltd	janice.bundey@beca.com
Giles, Evan	Parsons Brinckerhoff	gilese@pbworld.com
Green, Russell	Virginia Tech	rugreen@vt.edu
Grimes, Chris	BECA Ltd	janice.bundey@beca.com
Gunji, Keigo	University of Tokyo	gunji@geot.t.u-tokyo.ac.jp
Harada, Kenji	Fudo Tetra Corporation	kenji.harada@fudotetra.co.jp
Hargraves, Sally	Coffey	sally.hargraves@coffey.com
Holland, Andrew	AECOM	Andrew.Holland@aecom.com
Hutchison, Rodney	KGA Geotechnical Investigations	rodney@kga.co.nz
Hyodo, Masayuki	Yamaguchi University	hyodo@yamaguchi-u.ac.jp
Iai, Susumu	Kyoto University	iai.susumu.6x@kyoto-u.ac.jp
Idriss, I.M.	UC Davis	imidriss@aol.com
Kiryakos, Mark	Aargus Pty Ltd	mark.kiryakos@aargus.net
Kiyota, Takashi	University of Tokyo	kiyota@iis.u-tokyo.ac.jp
Knott, David	Coffey	David_Knott@coffey.com
Konrad, Ralf	Peters & Cheung Ltd	konradr@peters-cheung.co.nz
Kruyshaar, Jana	Geoscience Consulting	jana@nzgeoscience.co.nz
Ladley, Edwyn	Riley Consultants Ltd	eladley@riley.co.nz
Larkin, Tam	University of Auckland	t.larkin@auckland.ac.nz
Lees, Julian	Tonkin & Taylor Ltd	JLees@tonkin.co.nz
Ma, Kun	Aurecon NZ Ltd	kun.ma@aurecongroup.com
Ma, Martin	Peters & Cheung Ltd	mam@peters-cheung.co.nz

Mahoney, Dominic	Aurecon NZ Ltd	dominic.mahoney@aurecongroup.com
McGann, Christopher	University of Canterbury	christopher.mcgann@canterbury.ac.nz
McManus, Kevin	McManus Geotech Ltd	k.mcmanus@xtra.co.nz
McPherson, Ian	Aurecon NZ Ltd	ian.mcpherson@aurecongroup.com
Murashev, Alexei	Opus Consultants	alexei.murashev@opus.co.nz
Nelson, Aidan	Earthtech Consulting Ltd	aidan.nelson@xtr.co.nz
Nikolaison, Hayden	GHD Limited	hayden.nikolaison@ghd.com
Nogueira, Abilio	KGA Geotechnical Investigations	abilio@kga.co.nz
O'Sullivan, Andy	Highway Geotechnical Ltd	Andy@hiways.co.nz
O'Brien, Michael	O'Brien Geotech Ltd	michael.obrien@paradise.net.nz
Okada, Wataru	Parsons Brinckerhoff	okada@pbworld.com
Orense, Rolando	University of Auckland	r.orense@auckland.ac.nz
Ozutsumi, Osamu	Meisosha Corporation	ozutsumi@meisosha.co.jp
Parrett, Al	Coffey	al.parrett@coffey.com
Pender, Michael	University of Auckland	m.pender@auckland.ac.nz
Plunket, Tim	Aurecon NZ Ltd	tim.plunket@aurecongroup.com
Pranjoto, Satyawan	Riley Consultants Ltd	satyawan.pranjoto@gmail.com
Qin, Xiaoyang	University of Auckland	xqin009@aucklanduni.ac.nz
Reed, Mason	Fraser Thomas Ltd	mreed@ftl.co.nz
Richardson, Michael	DBCON Chartered Engineers	michael@dbcon.co.nz
Sáez, Esteban	Pontificia Universidad Catolica de Chile	esaez@ing.puc.cl
Sandquist, Rob	Babbage Consultants Limited	rob.sandquist@babbage.co.nz
Simmonds, Dan	SKM	DSimmonds@globalskm.com
Stapleton, Malcolm	Babbage Consultants Limited	mjds@babbage.co.nz
Stokoe, Ken	University of Texas Austin	k.stokoe@mail.utexas.edu
Tamari, Yukio	Tokyo Electric Power Services	etamari@tepsco.co.jp
Tate, Don	Riley Consultants Ltd	dtate@riley.co.nz
Toh, Jeremy	PSM	jeremy.toh@psm.com.au
Tokimatsu, Kohji	Tokyo Institute of Technology	kohji@o.cc.titech.ac.jp
Towhata, Ikuo	University of Tokyo	towhata@geot.t.u-tokyo.ac.jp
Van Ballegooy, Sjoerd	Tonkin & Taylor Ltd	svanballegooy@tonkin.co.nz
Wedgwood, Jeff	Wedgwood Engineering Consultants	jeff@wecl.co.nz
Wharmby, Nick	Brian Perry Civil	NickW@fcc.co.nz
Wiley, Matt	Geoscience Consulting	Matt@nzgeoscience.co.nz
Williams, Gareth	Engineering Design Consultants Ltd	garethw@edc.co.nz
Wotherspoon, Liam	University of Auckland	l.wotherspoon@auckland.ac.nz
Wu, Calvin	Engineering Geology Ltd	calvin.wu@enggeo.co.nz
Yan, Maggie	Peters & Cheung Ltd	YanM@peters-cheung.co.nz
Yasuda, Susumu	Tokyo Denki University	yasuda@g.dendai.ac.jp
Zhang, Jessica	KGA Geotechnical Ltd	jessica@kga.co.nz

Soil & site characterisation

This page intentionally left blank

Soil Liquefaction during Recent Large-Scale Earthquakes – Orense, Towhata & Chouw (Eds)
© 2014 Taylor & Francis Group, London, ISBN 978-1-138-02643-8

A summary of strong ground motions observed in the Canterbury earthquake sequence

B. Bradley
Department of Civil and Natural Resources Engineering, University of Canterbury, Christchurch, New Zealand

ABSTRACT: This paper provides a summary of the ground motions observed in the recent Canterbury, New Zealand earthquake sequence. The sequence occurred in a region of relatively moderate seismicity, 130 km to the east of the Alpine Fault, the major plate-boundary in the region. From an engineering perspective, the sequence has been primarily comprised of the initial 04/09/2010 Darfield earthquake (M_w7.1) followed by the 22/02/2011 Christchurch earthquake (M_w6.3), and two aftershocks on 13/06/2011 (M_w5.3 and 6.0, respectively). The dense spacing of strong motions in the region, and their close proximity to the respective causative faults, has resulted in strong ground motions far exceeding the previous catalogue of strong motion observed in New Zealand. The observed ground motions have exhibited clear evidence of: (i) near-source directivity; (ii) sedimentary basin focusing, amplification and basin effect refraction; (iii) non-linear site response; (iv) cyclic mobility post-liquefaction; and (v) extreme vertical ground motions exceeding 2 g, among others.

1 INTRODUCTION

The Canterbury earthquake sequence was initiated following the 04/09/2010 Darfield earthquake. As at the end of 2011, this sequence has been particularly active, producing over 100 events of $M_W > 4$. Figure 1 illustrates the spatial distribution and cumulative event magnitude distribution of this sequence. The sequence has been dominated by four specific events in particular, which are annotated in Figure 1: (i) the 04/09/2010 M_W7.1 Darfield earthquake, which initiated the sequence; (ii) the 22/02/2011 M_w6.2 earthquake, which produced the strongest ground motions in densely populated regions of Christchurch city during the sequence, leading to devastating damage and 185 deaths; (iii) the 13/06/2011 M_W6.0 earthquake, which produced significant ground motions and liquefaction; and (iv) the most recent major event of 23/12/2011, which produced liquefaction in particularly susceptible areas of Christchurch city's eastern suburbs.

As a result of the close proximity of these earthquake events, severe ground motions were observed in central Christchurch and the Canterbury region, causing significant liquefaction of surficial soils and damage to commercial, industrial, and residential structures and severely impacted critical infrastructure and lifelines (NZSEE 2010, NZSEE 2011). Because the most notable ground motions were observed as a result of the 04/09/2010 and 22/02/2011 events, then this paper focuses on the characteristics of observed ground motions for these events alone. Such observations include the significance and extreme nature of the ground motions; source effects such as forward directivity; basin-generated surface waves; nonlinear response of surficial soil layers; liquefaction observation; and intense vertical ground motion amplitudes.

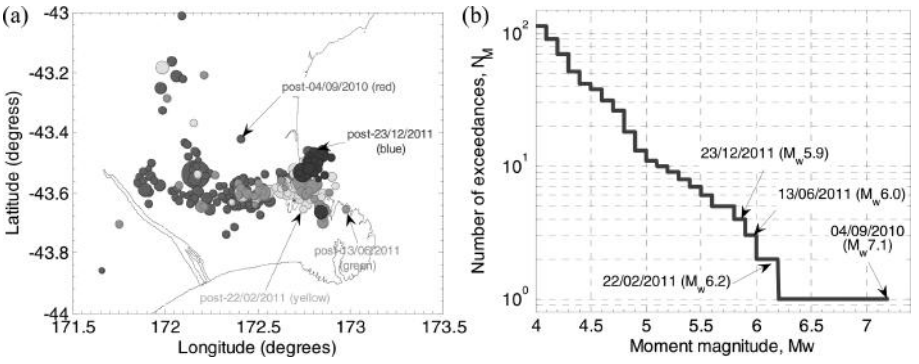

Figure 1. (a) Spatial distribution of events in the Canterbury earthquake sequence (marker size proportional to event magnitude); and (b) Distribution of event magnitudes observed from 04/09/2010–31/12/2011.

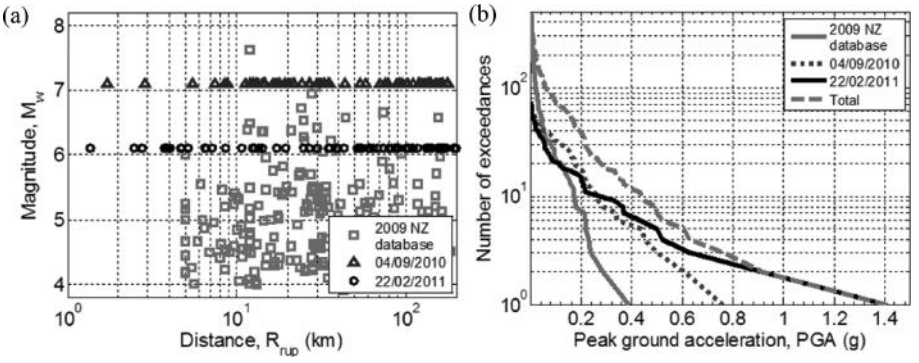

Figure 2. Significance of the 22/02/2011 Christchurch and 04/09/2010 Darfield earthquakes in relation to previously recorded ground motions in New Zealand: (a) magnitude-distance distribution; (b) exceeded values of peak ground acceleration.

2 SUMMARY OF OBSERVED STRONG MOTIONS

Numerous high quality ground motion time series were recorded in the 04/09/2010 Darfield and 22/02/2011 Christchurch earthquakes. Specific (tabulated) details of the ground motion amplitudes are not given here for brevity, and can be found elsewhere (e.g. Bradley 2012, Bradley and Cubrinovski 2011a). Figure 2 provides an illustration of the significance of the recorded ground motions relative to those previously recorded in NZ. Figure 2a illustrates the magnitude-distance distribution of recorded ground motions from active shallow crustal earthquakes up to 2009. Also illustrated in Figure 2a are the ground motions recorded in both the Darfield and Christchurch earthquakes. The significance of the recorded ground motions in these two earthquakes is even more apparent if the ground motions in Figure 2a are plotted in terms of their geometric mean horizontal peak ground acceleration (*PGA*). Figure 2b illustrates the number of ground motions exceeding specific values of *PGA*. It can be seen that up to 2009, the maximum *PGA* recorded in New Zealand was 0.39 g, with only 7 observed ground motions exceeding 0.2 g *PGA*. Figure 2b also illustrates the *PGA* exceedance values observed in the Darfield and Christchurch earthquakes. With the addition of these two events (not to mention records obtained from numerous significant aftershocks which are not discussed herein) it can be seen that horizontal ground motions of up to 1.41 g have now been recorded, with 12 observed ground motions exceeding 0.4 g and 39 exceeding 0.2 g.

3 EXTREME GROUND MOTIONS

Severe ground motion amplitudes were recorded in both the horizontal and vertical components at several strong motion station locations. Figure 3 illustrates details of the ground motions observed at Pages Road (PRPC) and Heathcote Valley (HVSC) in these two events. In particular, maximum PGA's in the vertical component of 2.21 g and 1.88 g were observed at HVSC and PRPC, respectively, in the 22 February 2011 Christchurch earthquake. The ground motion at PRPC also experienced significant forward directivity effects which are

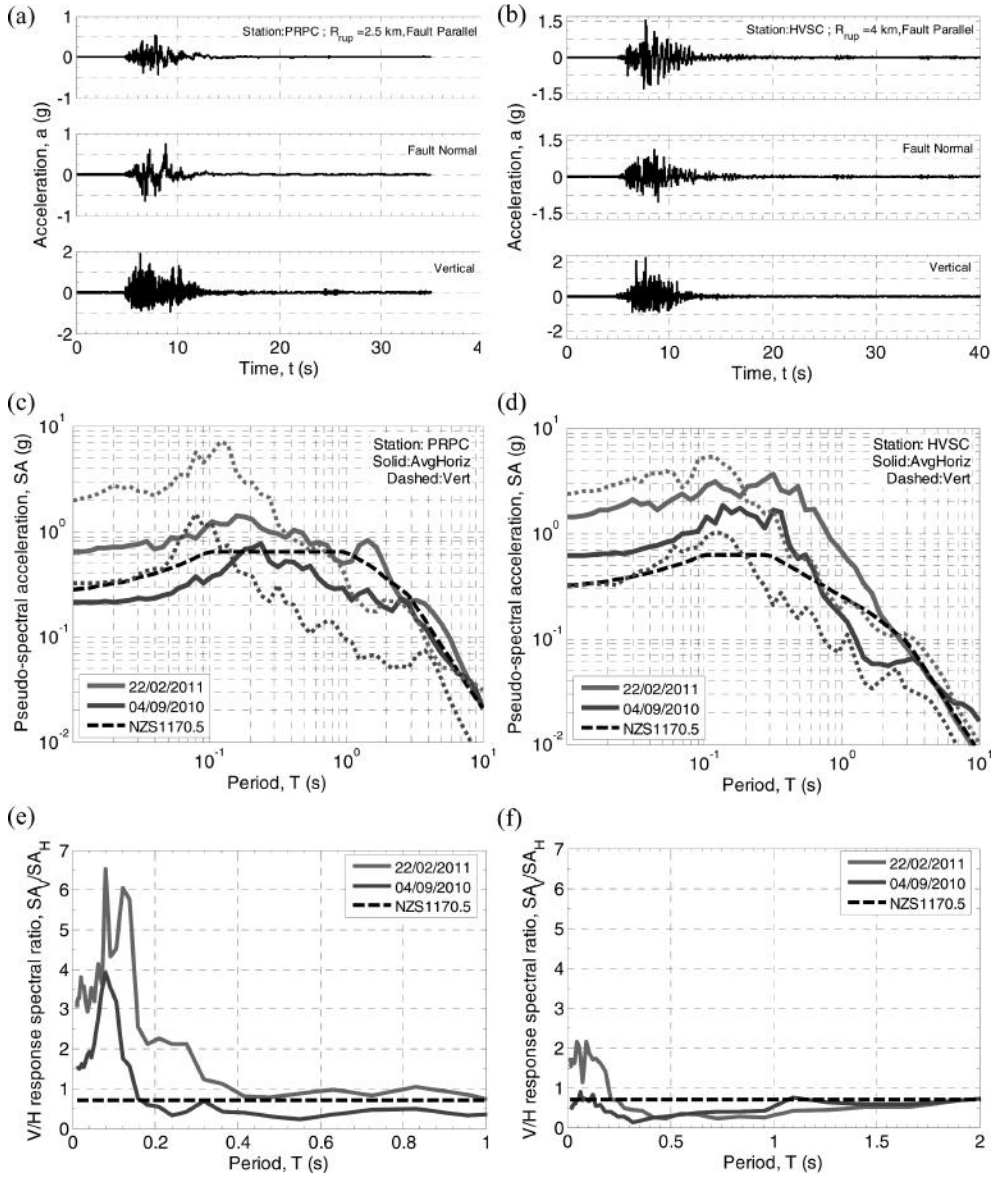

Figure 3. Extreme ground motions observed at Pages Road (PRPC) and Heathcote Valley (HVSC) in the 22 February 2011 Christchurch earthquake in terms of acceleration time history, pseudo-acceleration response spectra, and vertical to horizontal spectral ratios. Note the different scale used for vertical acceleration time histories in Figure 3a and Figure 3b.

evident in the long-period content of the fault normal component in Figure 3a. Figure 3c and Figure 3d illustrate the geometric mean horizontal and vertical pseudo-acceleration response spectra at PRPC and HVSC during both the Christchurch and Darfield earthquakes, and Figure 3e and Figure 3f illustrate the vertical-to-horizontal spectral ratios at these two sites in these two events. It can be clearly seen that the nature of the surface ground motion at each of these sites is similar in each of the two events, but fundamentally different between the two sites. For example, the response at PRPC is dominated by a relatively 'flat' response spectrum for high frequencies, indicative of nonlinear response in soil soft deposits. Furthermore, the vertical ground motion amplitude at high frequencies is particularly large (i.e. Figure 3e), indicating a soil deposit with high compressibility, that is, low P-wave velocity (e.g. clay, silt, peat). In contrast, the response at HVSC is characterised by large short period (i.e. $T < 0.4$ s) ground motion with a rapid fall-off in spectral ordinates at longer periods (the exception being the increase for the Darfield earthquake at long periods due to the forward directivity pulse (Bradley 2012)). The vertical-to-horizontal spectral ratio is also notably lower than that at PRPC and only larger than 1.0 for very high frequencies. In-depth analysis of the strong ground motion at HVSC indicates a strong basin edge effect at this site due to its location near the Port Hills, resulting in constructive interference between direct S-waves propagating through the underlying basin, and diffracted Rayleigh waves induced at the basin edge (Bradley 2012).

4 FORWARD DIRECTIVITY SOURCE EFFECTS

The dense strong motion instrumentation allows for a detailed assessment of the complexity of source rupture during the Darfield and Christchurch earthquakes (Beavan et al. 2011, Holden et al. 2011), in which fault slip in both events is inferred to have occurred on more than a single plane, in particular the Darfield earthquake.

From an engineering-perspective the near-source effect of greatest interest is forward directivity. Forward directivity is a phenomenon which occurs in the near-source region resulting from the alignment of the rupture front, direction of slip, and source-to-site direction. The manifestation of forward directivity is the arrival of a large portion of the radiated seismic energy in a single pulse at the beginning of the ground motion record oriented in the direction normal to the fault strike, and has a particularly large damage potential due to its large amplitude and short duration. Forward-directivity effects occur in the near source region in earthquakes of all magnitudes (Boatwright 2007), and their significance, from an engineering perspective, increases with increasing earthquake magnitude (due to a larger rupture duration). Forward directivity effects do not occur in all directions from a fault in the near-source region. If the direction of rupture propagation is 'away' from the site of interest then backward directivity effects occur, which will result in longer duration ground motion, but of a lower amplitude (Somerville 2003). Forward directivity effects were particularly significant for the 4 September 2010 Darfield earthquake as a result of its size (M_W7.1), strike-slip faulting mechanism and rupture propagation of the central and eastern section of the Greendale fault toward Christchurch (Bradley 2012, Holden et al. 2011). In contrast, forward directivity effects from the 22 February 2011 Christchurch earthquake are less significant, relative to the Darfield earthquake as a result of its size (M_W6.3), and also are prevalent only in a smaller area in the eastern suburbs of Christchurch as a result of the mis-alignment between the direction of slip on the fault and the inferred direction of rupture propagation on the fault (Aagaard et al. 2004, Bradley and Cubrinovski 2011a, Bradley and Cubrinovski 2011b, Holden 2011).

As previously noted, forward directivity effects from the 4 September 2010 Darfield earthquake are most evident in ground motions observed in the near-source region to the east of the causative faults. Figure 4 illustrates the observed velocity time histories at Templeton (TPLC) and Rolleston (ROLC), in which forward directivity effects are clearly evident with peak ground velocities (PGV's) of 80 and 100 cm/s in the fault normal direction, as compared to approximately 30 and 60 cm/s in the fault parallel direction, respectively.

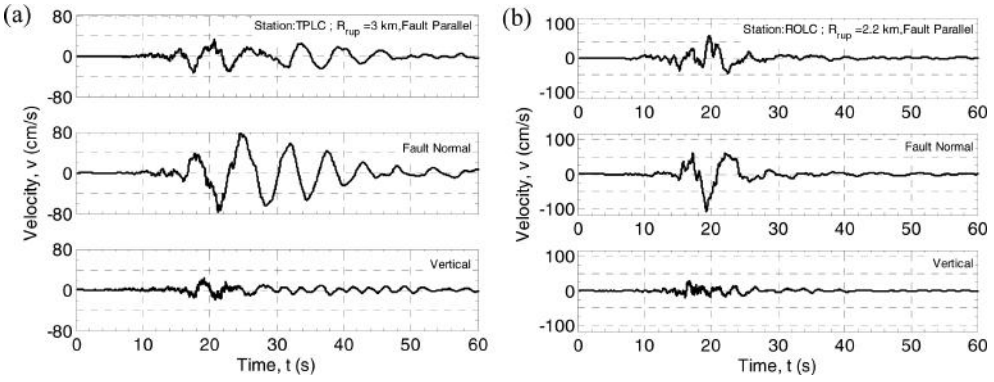

Figure 4. Evidence of strong forward directivity effects at locations to the east of the Greendale fault: (a) Templeton (TPLC); and (b) Rolleston (ROLC) resulting from the 4 September 2010 earthquake.

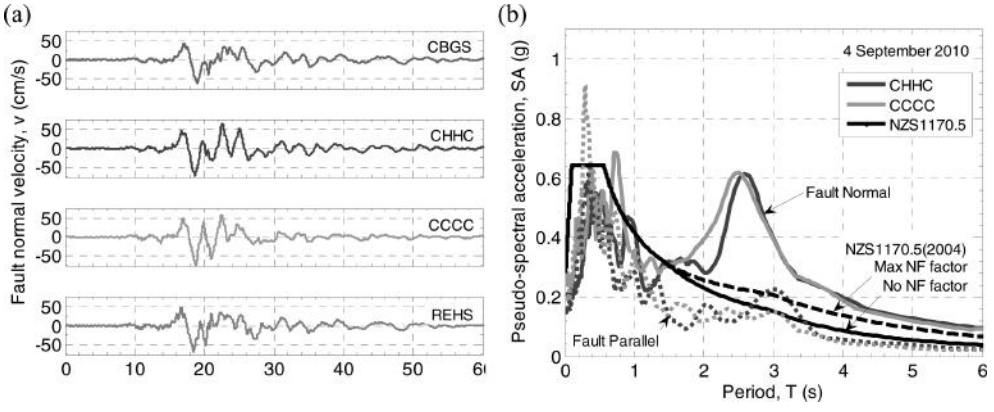

Figure 5. Forward directivity effects observed in the Christchurch central business district (CBD) resulting from the 4 September 2010 earthquake: (a) fault normal velocity time series; and (b) fault normal (plain) and fault parallel (dashed) response spectra in comparison with those prescribed by NZS1170.5:2004.

Figure 5 illustrates the fault normal component velocity time histories observed at the four strong motion stations located in the Christchurch central business district (CBD). It can be seen that the characteristics of the forward directivity velocity pulse are remarkably similar at all stations with PGV's ranging between 62 cm/s (CBGS) and 74 cm/s (CCCC). In contrast, the time history subsequent to the arrival of the velocity pulse varies significantly between the various sites illustrating the importance of both wave scattering and also shallow and deep geologic structure on site-specific site response. Figure 5b illustrates the difference between the fault normal and fault parallel pseudo-spectral acceleration (SA) amplitudes at CHHC and CCCC. There is a ratio of SA amplitudes of the fault normal and parallel components of approximately 5 at the spectral peak of $T = 2.5$ s. For comparison, Figure 5b also illustrates the conventional 500-year return period response spectra prescribed for site class D soil conditions in Christchurch (NZS 1170.5 2004), as well as the maximum prescribed increase in the design spectra due to near-fault forward directivity effects. It can be seen that the maximum permissible increase in the design code response spectra (based on assuming a distance of less than 2 km from the fault to the site), significantly under predicts the amplification of fault normal SA amplitudes relative to those in the fault parallel orientation, despite the fact that the Christchurch CBD is approximately 15 km from the inferred eastern

extent of the Greendale fault. Furthermore, it can be seen that the NZS1170.5 near fault factor produces an amplification over a broad period range, relative to the more narrow range over which significant amplifications are observed in Figure 5b.

It is noted that the near-fault amplitude specified by NZS1170.5:2004, as shown in Figure 5b is based on Somerville et al. (1997) geometric mean forward-directivity amplification. This geometric mean amplification model should be used only for application to the geometric mean response spectral predictions. For NZS1170.5:2004, where the 'larger component' definition (i.e. maximum of the two recorded components) is used, the use of the Somerville et al. geometric mean forward directivity amplification is inappropriate. Somerville et al. also provide a model for the ratio of the fault normal to geometric mean components, and it is the product of these two models which should be used for consistency with NZS1170.5:2004. While changes to the near-fault factor in NZS1170.5:2004 are certainly warranted, it is noted that the Somerville et al. 'broadband' model is now outdated by several newer 'narrow-band' models (e.g. Shahi and Baker 2011).

5 BASIN GENERATED SURFACE WAVES

Christchurch is located on a sedimentary fan deposit with the volcanic rock of Banks peninsula located to the south east. Significant long period ground motion was observed at numerous sites in the 4 September 2010 and 22 February 2011 earthquakes resulting from surface wave generation, in addition to the large amplitude long period ground motion resulting from forward directivity associated with source rupture effects. Figure 4a, for example, illustrates that the velocity pulse associated with forward directivity at TPLC was subsequently followed by several cycles of basin-generated surface waves, which are strongest in the fault normal component, consistent with the strongest SH waves in this component, but also evident in the fault parallel and vertical component velocity time histories. Basin-generated surface waves were also significant in the 22 February 2011 Christchurch earthquake (Bradley and Cubrinovski 2011a), but are not elaborated upon here.

6 NONLINEAR RESPONSE OF NEAR-SURFACE SOIL DEPOSITS

A self-evident illustration of the significance of nonlinear soil response is possible from a comparison of two ground motions recorded at Lyttelton Port during the 22 February 2011 earthquake (Bradley and Cubrinovski 2011b). One of the obtained motions is located on engineering bedrock (LPCC), while the other is located on a relatively thin (~30 m) colluvium layer (LPOC). Figure 6 illustrates the geometric mean pseudo-acceleration response spectra of the horizontal ground motion at the two sites. It can be seen that the observed horizontal ground motion at the LPOC site has significantly lower short period ground motion amplitude, but notably larger response spectral amplitudes at longer periods. In contrast, such site effects are not as pronounced for the vertical component with similar amplitudes and frequency content, as discussed elsewhere (Bradley and Cubrinovski 2011b).

7 SEVERE LIQUEFACTION OBSERVATIONS IN STRONG MOTION RECORDS

The principal cause of damage to residential property in the Canterbury earthquakes has resulted from the extreme severity and spatial extent of liquefaction (Cubrinovski et al. 2011, Cubrinovski et al. 2010). Liquefaction can be clearly observed in strong motion time series from these events (Bradley 2012, Bradley and Cubrinovski 2011b). Figure 7 illustrates the acceleration time history at Hulverstone Drive (HPSC), which is located approximately 200 m from the Avon River, in a region that experienced significant liquefaction. Clear evidence of cyclic mobility, in which large shear strain amplitudes in the soil deposit during strong shaking result in a drastic increase in soil shear stiffness and consequently propagation of high

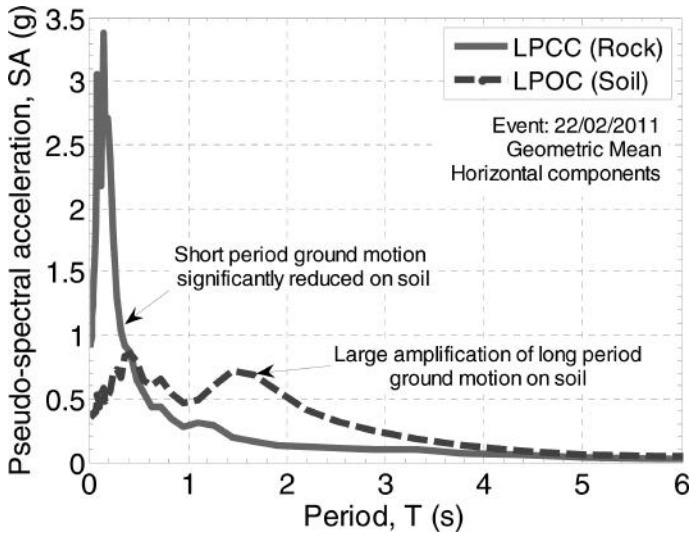

Figure 6. Comparison of the (geometric mean) horizontal ground motion response spectra at Lyttelton Port during the 22 February 2011 earthquake illustrating the importance of surficial soil response.

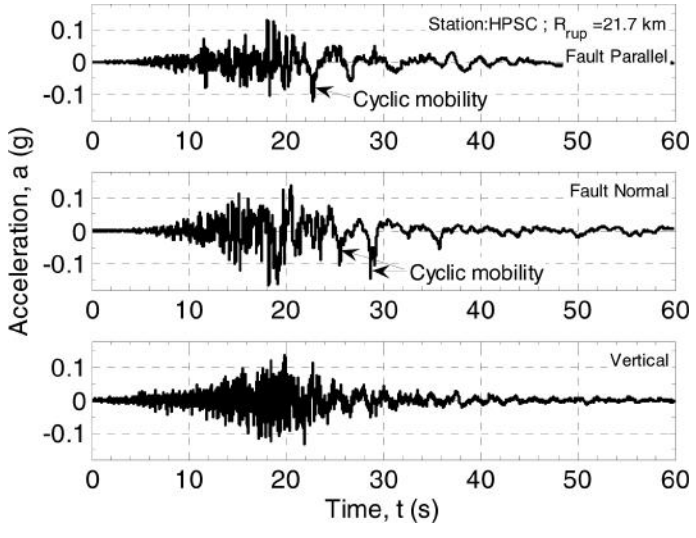

Figure 7. Evidence of liquefaction in the form of cyclic mobility in the acceleration time history recorded at Hulverstone Drive (HPSC) during the 22/02/2011 Christchurch earthquake.

frequency ground motion, can be seen in the horizontal components of ground motion from $T = 2.5$ s onwards, and several 'spikes' manifested as a result of this phenomena are annotated in Figure 7.

8 STRONG VERTICAL GROUND MOTIONS

Large ground motion amplitudes were observed in the vertical component at various locations in both the 4 September 2010 and 22 February 2011 earthquakes (particularly the latter). Such large vertical accelerations can be understood physically, because the majority of

strong motion stations are located on soil sites, and for soil sites in sedimentary basins large vertical accelerations at near-source locations can result from the conversion of inclined SV-waves to P-waves at the sedimentary basin interface which are subsequently amplified and refracted towards vertical incidence due to the basin P-wave gradient (Silva 1997). That is, large vertical accelerations observed at near-source locations are expected, and are not an indication on their own of any peculiarities associated with the earthquake source.

Figure 8a illustrates the geometric mean horizontal pseudo-acceleration response spectra at Pages Road (PRPC), Christchurch Hospital (CHHC), and Riccarton High School (RHSC), and Figure 8b the corresponding vertical-to-horizontal ratios. As has been commonly observed in numerous other studies, it can be seen that the vertical-to-horizontal (V-to-H) spectral ratio is largest at high frequencies with values that can be significantly greater than 1.0, and tends to reduce rapidly for vibration periods greater than $T = 0.1$ s; and also as a function of source to site distance (i.e. $R_{rup} = 2.5$ km, 3.8 km, and 6.5 km for PRPC, CHHC, and RHSC, respectively (Bradley and Cubrinovski 2011b)). Figure 8c and Figure 8d illustrate the V-to-H spectral ratios for vibration periods, $T = 0.0$ and 0.2 s as a function of source-to-site distance for both the 22 February 2011 Christchurch and 4 September 2010 Darfield earthquakes. Also shown for comparison is the empirical model of Bozorgnia and Campbell (2004), and the prescribed ratio of 0.7 for the development of vertical design spectra in NZS1170.5 (2004). Firstly, it can be clearly seen that V-to-H ratios above 1.0 are frequently observed for distances up to $R_{rup} = 40$ km in both these events (as well as other historical

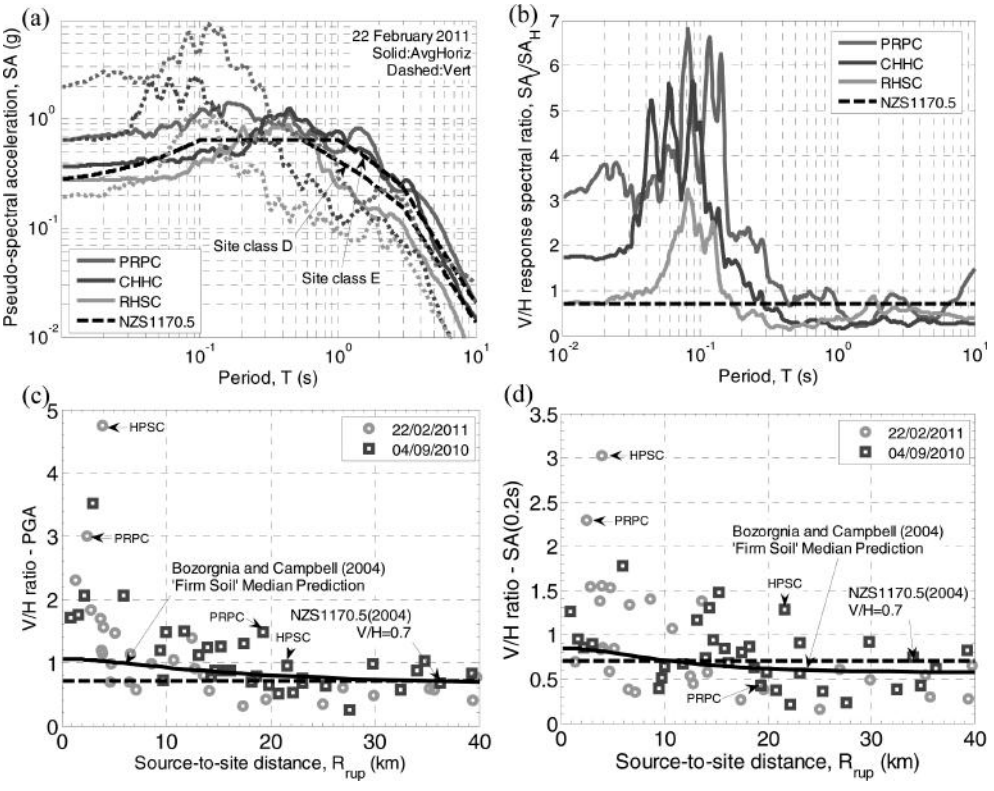

Figure 8. Vertical ground motion response spectral amplitudes observed: (a)-(b) Example geometric mean horizontal and vertical response spectra and their vertical-to-horizontal ratio; (c)-(d) vertical-to-horizontal response spectral ratios for $T = 0.0$ and 0.2 s as a function of distance observed in the 4 September 2010 Darfield and 22 February 2011 Christchurch earthquakes and comparison with the empirical prediction of Bozorgnia and Campbell (2004).

earthquakes worldwide (Bozorgnia and Campbell 2004)), and hence the code prescription of 0.7 is significantly un-conservative. Secondly, it can be seen that while there is significant scatter in the observed ratios, the Bozorgnia and Campbell empirical model is able to capture the overall trends in the observations, except for $R_{rup} < 10$ km for which it underestimates the observed ratios. Comparison of the observations from the Darfield and Christchurch earthquakes also illustrates that the ratios, on average, are principally a function of source-to-site distance and there is no evidence for a systematic differences between the two events due to their different magnitude and style of faulting. This lack of average dependence the seismic source features is consistent with that of Bozorgnia and Campbell (2004). Comparison of the ratios observed at the same station in the two different events (annotated in the figures for PRPC and HPSC) illustrates that there is some systematic site effect, for example, HPSC is always above the average prediction, but this is not always the case for PRPC with the ratio for $T = 0.2$ s well above the prediction in the Christchurch earthquake, but below the prediction in the Darfield earthquake. Given that vertical ground motion is only significant at very high frequencies, then it is expected to be strongly correlated with near-surface P-wave velocity structure, and some of the fluctuations observed in Figure 8 are likely the result of variability in the amplitude of the horizontal ground motion on the V-to-H ratio (due to nonlinearities for example).

9 CONCLUSIONS

The Canterbury earthquake sequence has produced severe ground motions in densely populated regions of Christchurch city from 04/09/2010–31/12/2011. As a result of a dense instrumentation network near the causative faults, numerous strong ground motions have been recorded. For the 4 September 2010 Darfield and 22 February 2011 Christchurch earthquakes, in particular, the dense array of ground motions records enable significant insight into features of the earthquake source, forward directivity during rupture, basin-generated surface waves, and local site effects; some of which were briefly discussed in this paper.

ACKNOWLEDGEMENTS

Financial support from the New Zealand Earthquake Commission (EQC) and Natural Hazards Research Platform (NHRP) is gratefully appreciated.

REFERENCES

Aagaard, B.T., J.F. Hall, T.H. Heaton. 2004. Effects of Fault Dip and Slip Rake Angles on Near-Source Ground Motions: Why Rupture Directivity Was Minimal in the 1999 Chi-Chi, Taiwan, Earthquake, *Bulletin of the Seismological Society of America*, 94, 155–170. 10.1785/0120030053

Beavan, J., E. Fielding, M. Motagh, S. Samsonov, N. Donnelly. 2011. Fault Location and Slip Distribution of the 22 February 2011 Mw 6.2 Christchurch, New Zealand, Earthquake from Geodetic Data, *Seismological Research Letters*, 82, 789–799. 10.1785/gssrl.82.6.789

Boatwright, J. 2007. The Persistence of Directivity in Small Earthquakes, *Bulletin of the Seismological Society of America*, 97, 1850–1861. 10.1785/0120050228

Bozorgnia, Y., K.W. Campbell. 2004. The vertical-to-horizontal response spectral ratio and tentative procedures for developing simplified V/H and vertical design spectra, *Journal of Earthquake Engineering*, 8, 175–207.

Bradley, B.A. 2012. Strong ground motion characteristics observed in the 4 September 2010 Darfield, New Zealand earthquake, *Soil Dynamics and Earthquake Engineering*, 42, 32–46. 10.1016/j.soildyn.2012.06.004

Bradley, B.A., M. Cubrinovski. 2011a. Near-source strong ground motions observed in the 22 February 2011 Christchurch earthquake, *Bulletin of the New Zealand Society for Earthquake Engineering*, 44, 181–194.

Bradley, B.A., M. Cubrinovski. 2011b. Near-source Strong Ground Motions Observed in the 22 February 2011 Christchurch Earthquake, *Seismological Research Letters*, 82, 853–865. 10.1785/gssrl.82.6.853

Cubrinovski, M., B.A. Bradley, L. Wotherspoon, A.G. Green, J. Bray, C. Wood, M. Pender, C.R. Allen, A. Bradshaw, G. Rix, M. Taylor, K. Robinson, D. Henderson, S. Giorgini, K. Ma, A. Winkley, J. Zupan, T.D. O'Rourke, G. DePascale, D.L. Wells. 2011. Geotechnical Aspects of the 22 February 2011 Christchurch Earthquake, *Bulletin of the New Zealand Society for Earthquake Engineering*, 44, 205–226.

Cubrinovski, M., R.A. Green, J. Allen, S.A. Ashford, E. Bowman, B.A. Bradley, B. Cox, T.C. Hutchinson, E. Kavazanjian, R.P. Orense, M. Pender, M. Quigley, L. Wotherspoon. 2010. Geotechnical reconnaissance of the 2010 Darfield (Canterbury) earthquake, *Bulletin of the New Zealand Society for Earthquake Engineering*, 43, 243–320.

Holden, C. 2011. Kinematic Source Model of the 22 February 2011 Mw 6.2 Christchurch Earthquake Using Strong Motion Data, *Seismological Research Letters*, 82, 783–788. 10.1785/gssrl.82.6.783

Holden, C., J. Beavan, B. Fry, M. Reyners, J. Ristau, R. Van Dissen, P. Villamor, M. Quigley. 2011. Preliminary source model of the Mw7.1 Darfield earthquake from geological, geodetic, and seismic data, in *9th Pacific Conference on Earthquake Engineering*: Auckland, New Zealand. 8.

NZS 1170.5. 2004. Structural design actions, Part 5: Earthquake actions—New Zealand. Standards New Zealand: Wellington, New Zealand. 82.

NZSEE 2010. Special Issue: Preliminary observations of the 2010 Darfield (Canterbury) Earthquakes, *Bulletin of the New Zealand Society for Earthquake Engineering*, 43, 215–439.

NZSEE 2011. Special Issue: Preliminary observations of the 2011 Christchurch Earthquake, *Bulletin of the New Zealand Society for Earthquake Engineering*, 44, 181–430.

Shahi, S.K., J.W. Baker. 2011. An Empirically Calibrated Framework for Including the Effects of Near-Fault Directivity in Probabilistic Seismic Hazard Analysis, *Bulletin of the Seismological Society of America*, 101, 742–755. 10.1785/0120100090

Silva, W.J. 1997. Characteristics of vertical strong ground motions for applications to engineering design, FHWA/NCEER Workshop on the National Representation of Seismic Ground Motion for New and Existing Highway Facilities, Burlingame, CA, Proceedings, National Center for Earthquake Engineering Research*, Technical Report NCEER-97-0010*, Buffalo, New York.

Somerville, P.G. 2003. Magnitude scaling of the near fault rupture directivity pulse, *Physics of The Earth and Planetary Interiors*, 137, 201–212. Doi: 10.1016/s0031–9201(03)00015–3

Somerville, P.G., N.F. Smith, R.W. Graves, N.A. Abrahamson 1997. Modification of empirical strong ground motion attenuation relations to include the amplitude and duration effects of rupture directivity, *Seismological Research Letters*, 68, 199–222.

Soil Liquefaction during Recent Large-Scale Earthquakes – Orense, Towhata & Chouw (Eds)

Geotechnical site characterisation using Screw Driving Sounding method

R.P. Orense & Y. Mirjafari
Department of Civil and Environmental Engineering, University of Auckland, New Zealand

N. Suemasa
Department of Urban and Civil Engineering, Tokyo City University, Tokyo, Japan

ABSTRACT: The Screw Driving Sounding (SDS) method developed in Japan is a relatively new in-situ testing technique to characterize soft shallow sites, typically those required for residential house construction. The method consists of driving a rod, equipped with a screw point at the tip, into the ground at different steps of loading while being rotated. The machine used to penetrate the rod can measure continuously the required torque, load, speed of penetration and rod friction; thus, compared to the more popular Standard Penetration Testing (SPT) and Swedish Weight Sounding (SWS) techniques, the method can provide a better insight of the soil profile. In this paper, the SDS method is introduced and the results of its application to characterize Christchurch sites are discussed. Since most of the tests were conducted at sites where Cone Penetration Tests (CPT) and borehole logs are available, the comparison of SDS results with this information shows that the SDS method has great potential as an in-situ testing method for geotechnical site characterization.

1 INTRODUCTION

The conventional method to determine the soil stratigraphy in-situ is by laboratory classification of samples retrieved from boreholes. If a continuous, or nearly continuous, subsurface profile is desired, various field investigation techniques are commonly employed to provide economical alternatives over the traditional methods of sampling and testing. A number of field testing techniques are available to characterize sites, and these include Standard Penetration Tests (SPT), Cone Penetration Tests (CPT) and Swedish Weight Sounding (SWS) method, among others. Although SPT is still popular worldwide, it suffers from many disadvantages such as poor repeatability, no continuous soil profile and the SPT blowcount is dependent on soil type, particle size, and the age and stress history of the deposit, among others. CPT has been the preferred choice recently because it gives a continuous profile and is generally not operator-dependent; although sampling is not possible, soil type (or soil behavior type) can be inferred from the information collected during the test. On the other hand, SWS method is a highly portable and economical technique which provides a continuous profile of the soil. It is used very often in Japan to evaluate the allowable shear strength of soils for residential house construction, and it is officially recommended as an investigation tool by the Ministry of Land, Infrastructure and Transport (Japan).

The Screw Driving Sounding (SDS) method, which has been recently developed in Japan, is an improved version of the SWS technique. While the latter only measures two parameters during the test (weight during static penetration, W_{sw} and number of rotations during rotational penetration, N_{sw}), SDS measures four parameters: required torque, load, speed of penetration and rod friction; these provide more robust way of characterizing soil stratigraphy. The principle behind the SDS method and the test procedure are discussed in this paper, together with its comparison to the SWS method.

Moreover, the authors conducted several SDS tests in Christchurch, which was affected by the 2010–2011 Canterbury earthquake sequence, with the aim of characterizing various sites

in the area for the on-going rebuild programme and estimating liquefaction potential considering future earthquakes. Overall, SDS was performed at 68 sites in Christchurch—both in liquefied zones and no-liquefaction zones. At the tested sites, either CPT data or borehole logs were available and these were compared to the SDS results.

2 PRINCIPLE AND TEST PROCEDURE

2.1 *Swedish Weight Sounding (SWS) method*

Before discussing the principle behind the SDS method, it is worthwhile to provide a background of the SWS technique. The testing procedure and the interpretation of test results are described by Tsukamoto et al. (2004). The SWS apparatus consists of a screw point, sounding rods, a rotating handle and six pieces of weights making a total of 100 kgf (980 N), as shown in Figure 1. The field test, which can be done either automatically (using a machine) or manually, is comprised of two phases: (1) static penetration; and (2) rotational penetration. In the static penetration phase, the screw-shaped point attached to the tip of the rod (weighing 49 N or 5 kgf) is statically penetrated by loading several weights (10, 10, 25, 25, 25 kgf) on top of the rod in stepwise increments until the total load is equal to 980 N (100 kgf). At each load increment, the depth of static penetration is measured and the total weight is denoted as W_{sw} (kN). If the screw point cannot penetrate under the maximum load, static penetration is ceased and rotational penetration is conducted. The horizontal handle attached to the top of the rod is rotated, and the number of half turns necessary to penetrate the rod through 25 cm is denoted as N_a. The values of N_a are then multiplied by 4 and are converted to the number of half turns per metre, N_{sw}.

According to Tsukamoto (2013), Swedish weight sounding tests are relatively good at detecting thin weak soil layers. Although it is sometimes argued that it is not directly feasible to determine depths of groundwater levels and types of soils and soil strata encountered during penetration, it is possible to tell whether the rod surface is dry or wet and also to classify soil particles which adhered to the surface of the penetrated rod during its extraction. In addition, whenever it is possible to acquire any borehole data from standard penetration tests nearby, it is possible to extrapolate the type of soils and soil strata encountered during SWS testing from this data.

Although the SWS test is highly portable and simpler than other sounding tests, this test has some disadvantages, such as the results being fairly influenced by rod friction. In cases where the soil contains gravel, the required load to penetrate, the number of half-turns and, consequently, the soil resistance from the SWS tends to be over-estimated as the rod friction becomes large.

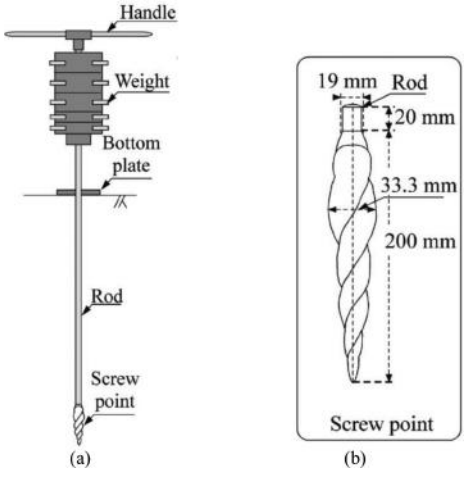

Figure 1. Swedish Weight Sounding (SWS) equipment; and (b) screw point (after Tsukamoto 2013).

Suemasa et al. (2005) investigated the interaction between the torque and the vertical load during SWS implementation and proposed an analogy model based on plasticity theory and the results of SWS miniature test results. Based on these, they noted that the coefficient of yield locus, c_y (which relates the normalized torque and normalized weight applied) and the coefficient of the plastic potential, c_p (which relates the normalized half-turns and the torque on the rod), vary depending on the soil type; i.e. clay, loam, medium sand or dense sand; hence, they proposed that soil can be classified based on the data obtained from SWS tests if the torque can be measured. This resulted in further refinement of the SWS method in terms of operating system, which led to the development of the SDS method.

2.2 *Screw Driving Sounding (SDS) method*

A new system for conducting the SWS method has been recently developed in Japan to minimize the disadvantages of the SWS method and to incorporate a procedure to measure the rod friction. Such method has been referred to as the Screw driving sounding (SDS) test. For this purpose, a small portable machine is used to apply the load monotonically in 7 steps (250 N, 375 N, 500 N, 625 N, 750 N, 875 N, and 1000 N), i.e. the load is increased at every complete rotation of the rod until a 25 cm penetration is reached. During this time, the rod is always rotated at a constant rate (25 rpm). The process is repeated at every 25 cm of penetration. The parameters measured during the test are: the maximum torque (T_{max}), the average torque (T_{avg}), and the minimum torque (T_{min}) on the rod for each applied load; the penetration length (L), the penetration velocity (V) and the number of rotations (N) of the rod. These parameters are measured at every complete rotation of the rod. Note that after each 25 cm of penetration in the SDS method, the rod is lifted up by 1 cm and then rotated to measure the rod friction. Then it is moved down 1 cm back to its original position and the process is repeated. The procedure in performing the SDS test is outlined in Figure 2.

While the SWS method is usually performed manually (i.e. application of weights and rotation of rods are done with human effort), the need for measurement of torque and velocity requires the use of a machine. A machine originally used for the SWS test has been improved to be suitable for the SDS application. Figure 3 illustrates the small-scale machine used in the SDS test, which can be disassembled for ease in transport and handling. With the test capable of measuring more parameters, a better insight of the soil profile and penetration resistance of the layers can be obtained. Furthermore, as mentioned above, classification of the soil type can be performed with the measured torque using the plasticity-based analogy model. Tanaka et al. (2012) made use of this concept to classify soils based on SDS test results.

A comparison between the SDS method and conventional in-situ testing techniques are summarized in Table 1. As observed from the table, the SDS method has many advantages,

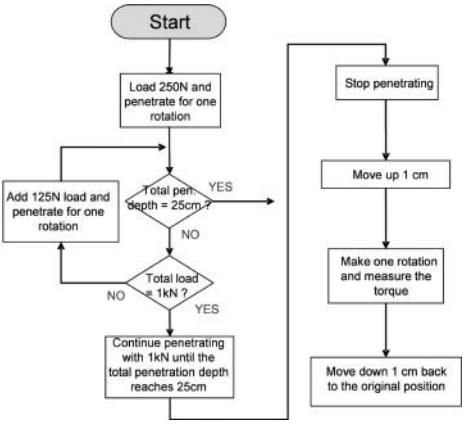

Figure 2. Test procedure for SDS method.

Figure 3. Screw Driving Sounding (SDS) equipment.

Table 1. Comparison between SDS method and conventional sounding methods.

		SDS	SWS (automatic)	SPT	CPT
Basic data	Penetration type	Static **and** rotational penetration	Static **or** rotational penetration	Dynamic penetration	Static penetration
	Penetration ability	SPT N value of around 10	SPT N value of around 10	High	Based on load ability
	Obtained Information	Three components: load, torque, and penetration depth	One component: load or half turns	One component: number of blows (soil type)	Three components: penetration resistance, friction, and pore pressure
	Estimated Information	Soil type, firmness, etc.	N value, q_u	Firmness	Soil type, strength, liquefaction, and consolidation
Workability	Efficiency	Good	Good	Bad	Acceptable
	Working space	Applicable to constricted space	Applicable to constricted space	Equivalent to two vehicles	A little wide
	Installation effort	Easy	Easy	Scaffolding and water supply are required	Anchor casting
	Required skill	Not very high	Not high	High	High
	Environmental impact	Quiet	Quiet	With noise and vibration	Quiet
Cost		Low	Low	High	Slightly high
Remarks		Currently, only JHS	Lacks reliability. Widely used for residential buildings in Japan	Physical testing is available. Widely used in Japan	Difference in apparatus is observed. Widely used in Europe and America

such as simpler system, faster procedure, lighter reaction weight and better cost efficiency than other sounding tests. It has a lot of potential in terms of application especially to residential houses.

3 APPLICATION OF SDS TESTS IN CHRISTCHURCH

The recent earthquakes that have rocked Christchurch and its environs resulted in extensive liquefaction which caused extensive damage to many residential houses, lifeline facilities and other civil engineering infrastructure (e.g., Orense et al. 2011a; 2011b; 2012). Following the major earthquake on 4 September 2010, the Earthquake Commission (EQC) engaged engineering specialists Tonkin & Taylor Ltd (T&T) to coordinate a subsurface investigation of the ground conditions in the Canterbury region. To date, more than 10,000 Cone Penetration tests (CPTs) have been carried out in addition to an accompaniment of boreholes, scala penetrometer tests and shear-wave velocity profiles. This information is currently stored in the Canterbury Geotechnical Database (CGD 2012).

The authors have taken the opportunity to use the SDS method at various sites in Christchurch for three purposes: (1) by comparing the SDS results with available data from adjacent CPT/SPT sites or borehole logs, provide further data to characterize sites in Christchurch and determine their geotechnical properties; (2) add data to the existing database of Japanese soils in order to improve the applicability of SDS method; and (3) explore the possibility of using SDS results to evaluate the liquefaction potential of Christchurch sites.

For this purpose, SDS tests were performed at 68 sites in Christchurch during the period June–August 2013. The locations of these sites are presented in Figure 4. These sites are located at both liquefied and non-liquefied areas following the recent earthquakes. SDS tests were conducted within 2–5 m from CPT/SPT sites, as described in the CGD.

A typical SDS result (SDS-01) is shown in Figure 5. The test was performed along Avonside Drive (see Figure 4 for location). The SDS test was conducted within 2 m of a CPT site and borehole. The SDS results reflect the corrected torque and load (including rod friction) and the penetration velocity at every 25 cm, up to a depth of 8 m. Also shown in the figure

Figure 4. Location of SDS test sites in Christchurch.

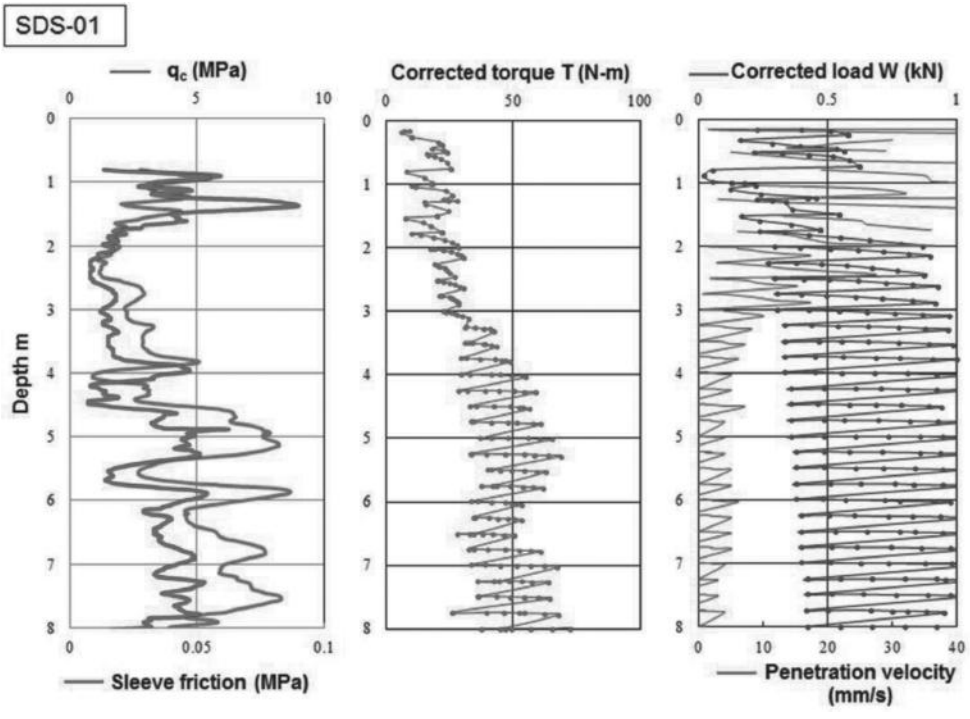

Figure 5. CPT profile and SDS results (torque, load and velocity) at site SDS-01.

is the CPT profile available from the CGD. It can be inferred from the CPT profile that the site consists of loose deposits up to a depth of 4 m overlying a relatively harder layer. Comparison of the CPT tip resistance and measured torque indicates a good correlation between the two, i.e. the torque required to penetrate the screw point increases with increase in cone resistance. Within a given 25 cm interval, the change in torque with the applied load appears to increase when the penetration resistance is high; on the other hand, the change in torque in softer layer is small. Moreover, the penetration velocity significantly decreased when a hard layer is encountered. The corrected load, W, represents the strength of the layer.

More information can be obtained by processing the initial information obtained from SDS tests. Some of the additional plots from the SDS test at site SDS-01 are illustrated in Figure 6. For example, $N_{SD}D$ is the normalized half-turns and is obtained by multiplying the number of half-turns for every 25 cm of penetration ($N_{SD}D$) by the outer diameter of the screw point (D). This number gives an indication of the level of torque required to twist the rod. For the profile shown in the figure, $N_{SD}D$ is low in the upper 3 m and increases below it, reflecting the trend in the penetration resistance from the CPT. Another parameter, $\pi T/WD$, represents the normalized torque and is defined using the torque (T), the weight applied (W) and the outer diameter of the screw point (D). Based on plasticity theory, the coefficient of plastic potential, c_p, is defined as (Suemesa et al. 2005):

$$c_p = \frac{\pi T/WD}{N_{SD}D} \tag{1}$$

Thus, c_p is an indication of the difficulty of penetration. From the Japanese database, the appropriate range of c_p values for different types of soils is as follows (Tanaka et al. 2012): sand layer: >1; silt and clay: 0.3–1; and peat and organic soil: <0.3. The distribution of c_p in Figure 6 appears to indicate generally sandy soil profile in the top 8 m.

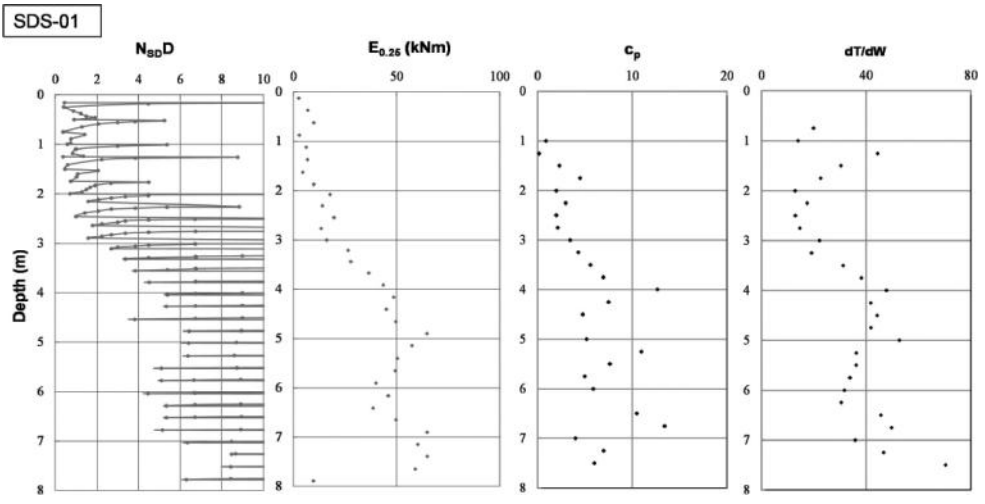

Figure 6. Additional information from test site SDS-01.

Moreover, a plot of the number of normalized half turns ($N_{SD}D$) and normalized torque ($\pi T/WD$) is also an indication of the soil type. The slope tends to have a positive value for frictional soil like sand, and a negative value or zero for clay and silt. $E_{0.25}$, on the other hand, is the total penetration energy for every 25 cm of penetration depth (considering the different increments of weight and torque applied and respective depths of penetration). This parameter is an indication of the layer stiffness. Finally, dT/dW represents the change in torque with the applied weight, analogous to the slope of the shear stress vs confining pressure plot in conventional laboratory testing.

To illustrate the way SDS test classifies soil, consider again the results for test SDS-01. Based on the developed classification system using Japanese database, soils can be classified by using the change in torque with respect to the load, dT/dW, the average required torque, T, and the coefficient of yield potential, c_p. As shown in Figure 6, dT/dW is positive along the soil profile which suggests the soil is coarse-grained. From a depth of 1.0–2.75 m, the average values of corrected torque and c_p are around 20 and 3, respectively; because of these low values, the soil in this region can be classified as sandy silt. Below 2.75 m, the value of dT/dW gradually increased and this trend continues until 4 m. Similarly, the average required torque for penetration increased from 35 kNm to 45 kNm, indicating an increase in soil friction or density. In this region, the value of c_p also gradually increased from 3 to 13. It can be estimated that between 2.75 m and 4 m, the percentage of fines in sand dropped or the soil became more frictional. From 4 m to 5 m, dT/dW increased gradually. The required torque to penetrate this part of the deposit was approximately 50 kNm and average value for c_p was around 8. An increase in dT/dW in this section of the soil profile indicates a medium sand soil type. There was a drop in dT/dW between 5 and 6 m indicating an increase in percentage of fines which reduced the frictional resistance of the soil. Below 6 m depth, an increasing trend for dT/dW and c_p again continued, indicating a reduction in fines content. Soil in this layer can be classified as fine to medium sand.

The obtained soil classification from SDS test is compared with that derived from CPT using the soil behavior type classification proposed by Robertson (1990). Note that similar to the SDS method, the classification scheme developed for CPT is for soil behavior type (SBT) because the cone responds to the in-situ mechanical behavior of the soil and is not directly applicable for soil type classification, which is usually based on grain-size distribution and plasticity index.

Table 2 shows the comparison of the soil classification using SDS, CPT and borehole log. As seen from the table, the results obtained from SDS are very close to those indicated in the

Table 2. Results of soil classification using SDS, CPT and borehole data.

CPT soil description	SDS soil description	Borehole Strength/ Density	Soil description	Depth (m)
–	–	Loose	FILL: Fine sand, dry, poorly graded	0.00–0.80
Silty sand—Sandy silt	Sandy silt	Soft	Sandy silt, moist, low plasticity, sand is fine	0.80–2.75
Sand and Silty sand	Silty sand	Loose	Fine sand with trace silt, wet, poorly graded	2.75–3.00
Silty sand—Sandy silt	Silty sand	Soft	Sandy silt, moist, low plasticity, sand is fine	3.00–3.50
Silty sand—Sandy silt	Sand	Loose	Fine sand with trace silt, wet, poorly graded	3.50–3.75
Sand and Silty sand	Sand			3.75–4.70
Sand and Silty sand	Sand	Loose	Fine to medium sand with trace silt, wet,	4.70–5.25
Silty sand	Silty sand		well graded	5.25–6.00
Silty sand—Sand	Sand			6.00–7.50

borehole description. Thus, even without sampling, SDS can classify soils with acceptable degree of accuracy.

It should be again noted that the SDS-based classification was formulated from a database of Japanese soils. Thus, it is envisioned that these tests in Christchurch, as well as those planned in other parts of New Zealand, will increase the range of soil types in the database and will further refine/improve the proposed classification scheme. Moreover, from the tests conducted in Christchurch, further application of SDS results to identify regions of high liquefaction potential is currently underway and will be reported in the next opportunity.

4 CONCLUSIONS

A new field testing method, referred to as the Screw Driving Sounding (SDS) method, has been recently developed. As an improved version of the conventional Swedish weight sounding (SWS) method, more parameters can be measured during the SDS tests, such as the torque, load and penetration velocity. Using a plasticity-based analogy model and miniature tests in Japan, soil classification can be performed, an added advantage compared to SWS tests.

Based on a large number of tests conducted in Japan, it was shown that soils can be classified using SDS parameters, such as c_p, average corrected torque and dT/dW. To increase the database and further refine/validate the correlations with various soil types, SDS tests were performed at 68 sites in Christchurch. The results of soil classification using SDS parameters were compared with those obtained from adjacent borehole and the CPT-based soil behavior type classification scheme. The results showed that SDS parameters give comparable results as those from CPT, indicating that SDS provides accurate soil classification.

More tests are currently planned in New Zealand to refine the current method of soil classification and to explore the possibility of estimating geotechnical properties from the SDS-measured data. As SDS is a simpler, faster and more economical test than the SPT, it can be a good alternative as an in-situ test for soil characterization.

ACKNOWLEDGEMENTS

The authors would like to acknowledge Nitto Seiko Company for providing the SDS machine and the Japan Home Shield (JHS) Company for providing assistance for this research. We also would like to acknowledge the Canterbury Geotechnical Database (CGD) for providing the borehole data and CPT records in Christchurch and the Christchurch City Council for providing access to the test sites. Finally, the advice and assistance of Prof Misko Cubrinovski of University of Canterbury are gratefully acknowledged.

REFERENCES

Canterbury Geotechnical Database 2012. https://canterburygeotechnicaldatabase. projectorbit.com

Orense, R., Pender, M. & Wotherspoon, L. 2012. Analysis of soil liquefaction during the recent Canterbury (New Zealand) earthquakes. *Geotechnical Engineering Journal of the SEAGS & AGSSEA*, Vol. 43 No. 2, 8–17.

Orense, R., Pender, M., Wotherspoon, L. & Cubrinovski, M. 2011a. Geotechnical aspects of the 2010 Darfield (New Zealand) Earthquake. *Invited Lecture, 8th International Conference on Urban Earthquake Engineering*, Tokyo (Japan), 407–416.

Orense, R.P., Kiyota, T., Yamada, S., Cubrinovski, M., Hosono, Y., Okamura, M. & Yasuda, S. 2011b. Comparative study of liquefaction features observed during the 2010 and 2011 Canterbury earthquakes. *Seismological Research Letters*, Vol. 82, No. 6, 905–918.

Robertson, P.K. 1990. Soil classification using the cone penetration test. *Canadian Geotechnical Journal*, 27(1): 151–158.

Suemasa, N., Shinkai, K., Suzawa, T. & Tamura, M. 2005. A plasticity model for Swedish weight sounding test. *4th Japan—Philippines Workshop on Safety and Stability of Infrastructure against Environmental Impacts*, Univ. of Philippines, pp. 169–177.

Tanaka,T., Suemasa, N. & Ikegame, A. 2012. Classification of strata using screwdriver sounding test. *Proceedings of the 22nd International Offshore and Polar Engineering Conference*, Rhodes, Greece, 851–856.

Tsukamoto,Y. 2013. Integrating the use of Swedish weight sounding tests for earthquake reconnaissance investigations. *International Conference on Earthquake Geotechnical Engineering: From Case History to Practice*, Istanbul, Turkey, 21pp.

Tsukamoto,Y., Ishihara,K. & Sawada, S. 2004. Correlation between penetration resistance of Swedish weight sounding tests and SPT blow counts in sandy soils. *Soils and Foundations*, 44(3):13–24.

This page intentionally left blank

Soil Liquefaction during Recent Large-Scale Earthquakes – Orense, Towhata & Chouw (Eds)

Repeatability of SPT testing in Christchurch soils with reference to the liquefaction potential

P. Clayton
Geotechnical Engineering, Beca Ltd., New Zealand

ABSTRACT: The majority of liquefaction assessments carried out in New Zealand utilise penetrometer testing as the basis for estimation of sandy soil susceptibility. While Cone Penetrometer Testing (CPT) is becoming more common, the Standard Penetrometer Test (SPT) is still considered by many NZ geotechnical engineering practitioners to be the primary tool for assessing the relative density of sandy soils. The potential for poor repeatability of SPT tests has been recognized for many decades. This study considers the apparent variability of SPT tests by comparison against adjacent paired SPT-SPT and SPT—CPT tests compiled from records within the Canterbury Geotechnical Database (CGD). The study also examines variation between SPT N_{60} and a correlated N_{60}' from CPT with respect to $N_{60,}$ depth, drilling method, and observed in hole heave. While the average correlation between tests is found to be in general agreement, the scatter is large and not readily normalized by the factors considered. The implications for SPT based assessment of liquefaction and post-liquefaction consolidation settlement are briefly discussed.

1 INTRODUCTION

The Canterbury Earthquake Sequence resulted in widespread liquefaction related damage to the city of Christchurch. As part of the rebuilding process an extensive program of site investigation is underway to provide information for liquefaction assessments and foundation design. Investigation to date has included a number of penetrometer based methods including Borehole (BH)/Standard Penetrometer (SPT), Cone Penetrometer (CPT), Swedish Weight Sounding and Dynamic Penetrometer methods.

A review of the investigation records uploaded to Canterbury Geotechnical Database (CERA 2013) indicates that vast majority of tests undertaken comprise BH/SPT and CPT. At the time of writing the ratio of Borehole/SPT tests to CPT tests within the database is 1:4, however viewed in dollar terms this suggests an approximately equivalent spend and a substantial ongoing investment in BH/SPT testing.

Numerous researchers have discussed the shortcomings of the SPT test citing poor test repeatability associated with variations in:

- The proportion of the theoretical energy delivered to the drill string by the hammer
- Internal dimensions of the sampler spoon
- Borehole diameter
- Effective stress at test depth
- Hammer strike rate
- Drilling method/borehole stability.

The CPT test on the other hand is often cited as having a high level of repeatability, Robertson (2012) suggests ±1% can be readily achieved, while Jefferies and Davies (1993) suggested that CPT correlations can provide a better estimate of the SPT N-values than the actual SPT test due to the poor repeatability of the SPT.

Notwithstanding concerns about the repeatability, SPT tests remain widely used in Christchurch as the basis for liquefaction assessment for a number of reasons including:

- Shallow gravel interbeds generally preventing adequate penetration of CPT tests;
- CPT tests are unable to penetrate to 'prove' deeper gravel founding layers, refusing close to their surface;
- Preference for soil descriptions based on physical samples rather than CPT derived soil behavior indices and limited availability/familiarity/use of CPT based sampling equipment;
- Familiarity with SPT based empirical correlations and design 'rules of thumb'.

Given the ongoing widespread use of SPT tests it was considered worthwhile to undertake an assessment of repeatability of SPT tests in the Canterbury area by comparison with available paired bores and by comparison against correlated CPT based N_{60}.

2 METHODS OF ASSESSING REPEATABILITY

2.1 *Direct comparison using paired bores*

A measure of SPT test repeatability can be carried out by conducting side by side tests using identical drilling and testing equipment. Such tests have been reported in the literature (Rogers, 2006). However, the variability that might typically be experienced in geotechnical engineering practice can be represented by the use of a range of different contractors, drilling methods and SPT hammer/spoon combinations as can be found within the CGD.

2.1.1 *SPT correction*

Prior to comparison, the tests have been normalised following the process described by Idriss and Boulanger (2008). Correction factors applied in this analysis are summarised in Table 1.

2.1.2 *Results of paired BH/SPT comparison*

Subject to the limitations of suitably paired BH/SPT (10 suitable pairs were identified from an available 2655 bores at the time of writing) we have undertaken a paired borehole/SPT comparison. To reduce the impact of potential adjacent bore disturbance and soil profile variability only bores within 1 and 3 m have been selected.

Figure 1 shows an example plot of two adjacent bores drilled by the same company, using the same equipment at a separation of 1.7 m. Figure 2 shows the ratio between N_{60} recorded

Table 1. Summary of SPT correction factors.

Correction	Factor	Comments
Rod Length Correction Assume: 1.5 m AGL	$C_R = 0.75$ to 1.0	0 to 3 m: 0.75; 3 to 4 m: 0.80; 4 to 6 m: 0.85 6 to 10 m: 0.95; 10 to 30 m: 1.00
Borehole Diameter Correction	$C_B = 1.0$	Diameters between 65 and 115 mm
Hammer Energy (C_E)		
SPT hammer type varies, and have a range of efficiency factors, falling in two categories: 1. Conventional automatic trip hammers with reported efficiencies of 50 to 80% and; 2. Automated hammers with reported efficiencies of between 90 and 100%		
SPT Spoon Correction (C_S)		
Two SPT spoon types are in use in Christchurch. 1. NZ standard spoons with a constant internal diameter of 34.9 mm (13/8") and, 2. ASTM (2011) style spoons with a rebate to accommodate a 3.2 mm (1/8") thick liner, but used without a liner, consequently having an internal diameter of 38.1 mm (11/2"). It is assumed that all tests were carried out using the more common ASTM style. Unfortunately the NZ AGS4 standard does not currently record this information.		

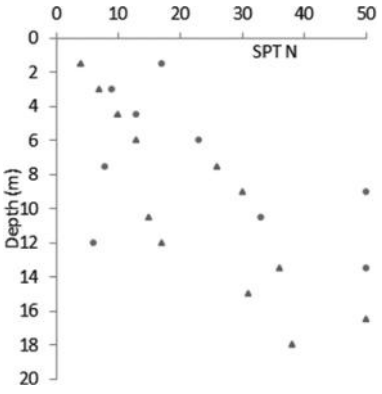

Figure 1. SPTN vs depth example.

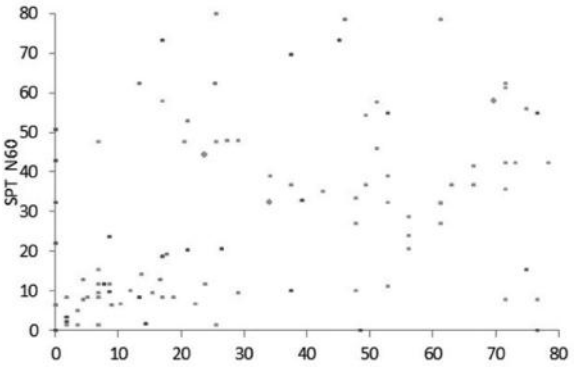

Figure 2. N_{60} against N_{60} pair by pair.

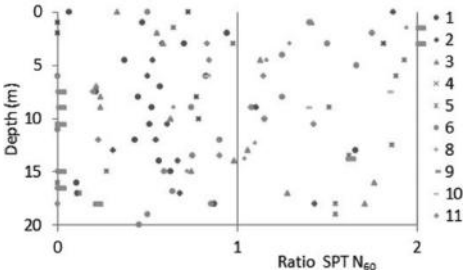

Figure 3. Ratio N_{60} against depth.

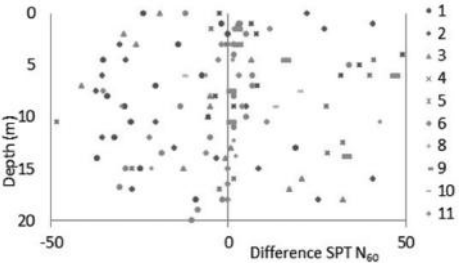

Figure 4. Difference in N_{60} against depth.

Table 2. Summary of BH/SPT analysis from CGD.

		Ratio ($N_{60\,1}/N_{60\,2}$)		Difference ($N_{60\,1}$-$N_{60\,2}$)	
n	Range N_{60} (bl/300 mm)	Mean	Standard Dev.	Mean	Standard Dev.
139	1.7 to 85	1.1	1.1	–2.8	28

for adjacent bores for ten pairs of BH/SPT drilled using a range of equipment by two different contractors.

Figure 3 displays the content of Figure 2 as ratio, where 1.0 would indicate two tests had identical results; Figure 4 displays the numerical difference between adjacent bores for the same dataset, where 0 would indicate identical results.

Results of analysis of available BH/SPT pairs are summarised in Table 2:

The level of repeatability of SPT appears to be poor, with a standard deviation of nearly 30.

Direct investigation of factors affecting the repeatability is problematic due to the small number of suitably paired boreholes in the database and inherent limitations of this process:

- Adjacent boreholes may be subject to the same anomaly e.g. drilling disturbance effects, so while repeatability may be established, bias may be present.
- Variations arising from the use of different drilling methods or equipment are not adequately represented.

2.2 *Indirect comparison using CPT test as a reference*

An alternative to direct comparison is to utilise another test as a reference. In this case an obvious choice is the CPT utilising existing correlations between CPT and SPT *N*.

The use of the CPT test as a reference has a number of potential advantages, including:

- Twinned BH/CPT tests are significantly more numerous;
- Test points are less likely to suffer from disturbance from their 'pair', providing the CPT test is undertaken first;
- Accuracy and repeatability of CPT tests are reported to be good, making it theoretically possible to use the CPT as a 'reference' value when compared against the significantly less accurate/repeatable SPT;
- Variations arising from the use of different drilling methods or drilling/testing equipment can be compared more readily.

2.3 *Evaluation of CPT test repeatability*

2.3.1 *Selection of pairs*

Prior to embarking on comparative analyses we first sought to investigate our 'pair' selection criteria (the level of repeatability in CPT q_c and equivalent N_{60}') in Christchurch by comparing a selection of paired CPT tests. A similar selection process was undertaken to that employed for BH/SPT tests. From the approximately 11,500 CPT tests currently available, ten tests were selected within a proximity of '*d*' where 3 m > *d* > 1 m, resulting in a total of five pairs.

2.3.2 *Correction to CPT tests*

All CPT tests used in this study have been carried out using 10 cm^2 cones and are assumed to have been carried out in accordance with the relevant standard (ASTM 2012). The value of q_c is corrected to q_t where $q_t = q_c + u_2(1 - a)$ and '*a*' assumed to be 0.8.

2.3.3 *CPT q_c - N_{60} correlation*

Robertson (1983) originally proposed a correlation between CPT q_c and SPT *N* as a simple q_c/N_{60} ratio that varies with grain size. Jefferies and Davies (1993) updated the correlation to utilise the soil behavior type index, I_c as a proxy for grain size resulting in the following relationship:

$$\frac{(q_t/p_a)}{N_{60}} = 8.5\left(1 - \frac{I_c}{4.6}\right) \qquad (1)$$
$$I_c = ((3.47 - \log Q_t)^2 + (\log F_r + 1.22)^2)^{0.5}$$

where Q_t = normalized cone penetration resistance (dimensionless)
$= (q_t - \sigma_{vo})/\sigma'_{vo}$
F_r = normalized friction ratio, in%
$= (f_s/(q_t - \sigma_{vo})) \times 100\%$

Total and effective stress determined assuming an average unit weight of 18 kN/m^3 and a groundwater table at 1.0 m.

2.4 *Results of paired CPT/CPT comparison*

Figure 5 contains a plot of cone resistance vs depth for four CPT tests conducted by the same contractor with the same cone at '*d*' less than 3 m to provide an indication of repeatability using one set of equipment. Figure 6 presents the plot in terms of Equivalent N_{60} (termed N_{60}'). The potential for ground variability is illustrated by CPT 21577 (blue line) which is at a greater distance (*d* = 2.6 m) from its pair compared to CPT 24536 (*d* = 1.7 m) and CPT 25096 (*d* = 2.0 m).

Figure 7 present five pairs of CPT test results expressed as a ratio of 'equivalent' SPT N_{60}, Figure 8 presents the ratio between each pair as a frequency distribution. Predrill and variable soils in upper 1.5 m have been removed.

Results of analysis of selected CPT pairs/groups are summarised in Table 3.

The level of variation within this data is higher than the ±1% of instrument range (1% of 150 MPa = 1.5 MPa) suggested Robertson (2012), perhaps reflecting the highly variable stratigraphy encountered within surficial deposits beneath Christchurch. Based on the sample tests evaluated, a standard deviation of 3 N_{60}' might be expected from SPT N correlated from CPT q_c for pairs at close spacing. This is an order of magnitude better than the equivalent BH/ST dataset and supports the use of CPT derived N_{60}' to assess factors influencing the repeatability in SPT derived N_{60}.

2.5 *CPT to SPT comparison*

2.5.1 *Selection of suitable test pairs*

CPT and BH/SPT pairs for this study have been identified as follows:

- Tests within at a proximity of '*d*' where 1 m < *d* < 3 m;
- Available SPT hammer efficiency values;

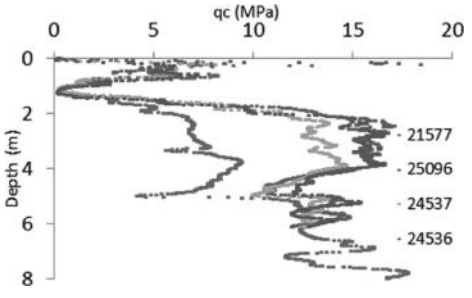

Figure 5. Cone resistance vs depth.

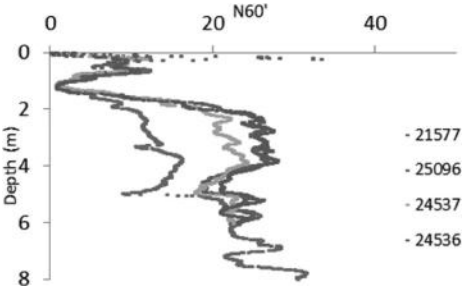

Figure 6. N60' vs depth.

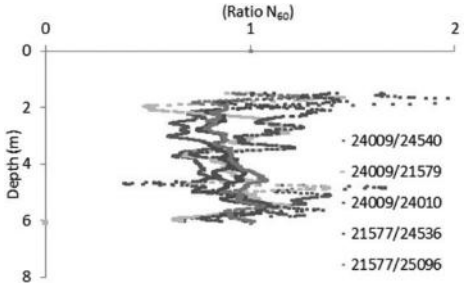

Figure 7. Ratio N60' vs depth 'paired' CPT's.

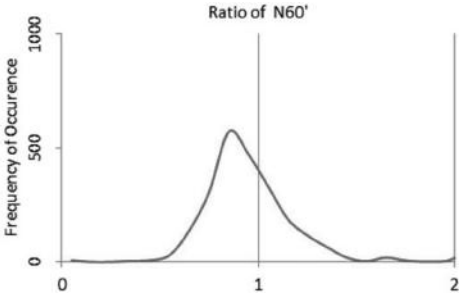

Figure 8. Ratio CPT frequency distribution.

Table 3. Summary N_{60}' from CPT correlation.

		Ratio (N_{60}'$_1$/N_{60}'$_2$)		Difference (N_{60}'$_1$–N_{60}'$_2$)	
n	Range N_{60}' (from CPT)	Mean	Standard Dev.	Mean	Standard Dev.
2313	0–33	0.95	0.23	–1.7	3.1

- Adequate information available on type of drilling equipment used;
- Records of borehole heave.

2.5.2 *Borehole/SPT methods to be compared*

Our sample includes SPT tests undertaken within boreholes drilled using the following equipment:

- HQTT
  'H' series triple tube rotary cored boreholes with SPT tests undertaken within the core barrel. In accordance with standard NZ practice it is assumed that the core barrel remains at the base of the borehole during the test (in lieu of casing). Automatic drop hammer used.
- LFS
  Low frequency sonic cored borehole. Typically comprising a top drive rotary rig converted to sonic drilling by the addition of a low frequency (<100HZ) vibratory drive head. Automatic drop hammer used.
- HFS
  High frequency sonic. Purpose built top drive high frequency (>100HZ) High efficiency Automated hammer used.
- Percussion/Direct Push
  Also known as double tube direct push. High efficiency automated hammer used.

Note, unlike international practice AW rods are rarely used for SPT testing in NZ. SPT tests are typically carried out using N-series drill rods which might be expected to transfer more energy to the sampler than AW rods, particularly if rods are 'well used'.

2.6 *Results of CPT/SPT comparison*

N_{60} from SPT testing/CPT derived correlated N_{60}' are compared against a number of potential indicators of factors likely to influence SPT test repeatability.

2.7 *Apparent influence of drilling method*

Figure 9 presents a general plot of SPT N vs N_{60}'for all results combined. Figure 10 presents a plot of SPT N_{60} vs N_{60}' to illustrate any potential influence of the different type of drilling rig used.

2.8 *Apparent influence of penetration resistance*

Figure 11 presents a plot of SPT N_{60}/N_{60}' vs N_{60}' and Figure 12 a plot of SPT $N_{60} - N_{60}$' to illustrate the any apparent influence of soil density on the scatter in N_{60}.

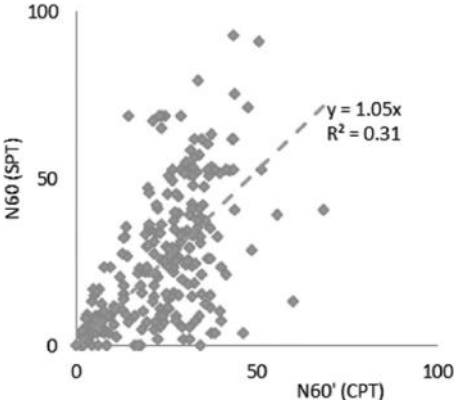

Figure 9. N_{60} (SPT) vs N_{60}' (CPT).

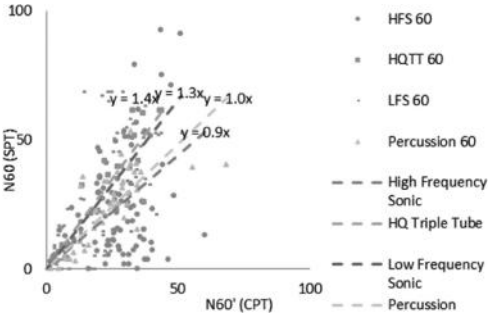

Figure 10. N_{60} (SPT) vs N_{60}' (CPT).

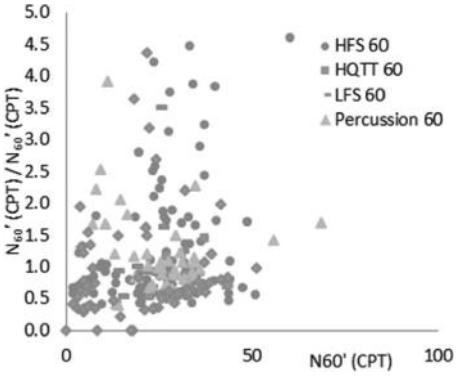

Figure 11. N_{60} (SPT)/N_{60}' (CPT) vs N_{60}'.

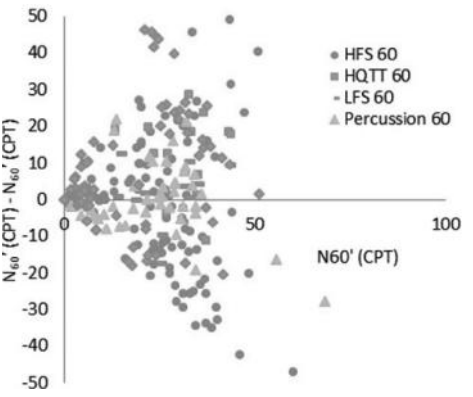

Figure 12. N_{60} (SPT)–N_{60}' (CPT) vs N_{60}'.

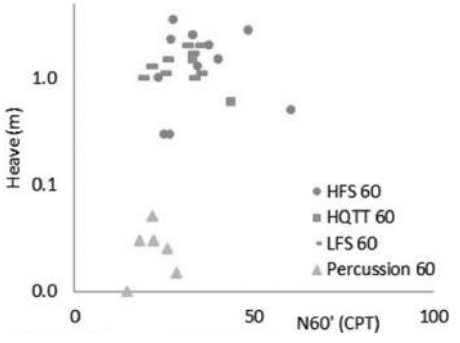

Figure 13. Heave vs N60' (CPT).

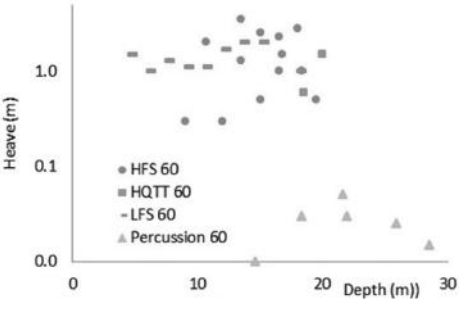

Figure 14. Heave vs depth (m).

2.9 *Occurrence of heave*

Observations of borehole disturbance are recorded as 'heave' of the base of the borehole. Figure 13 presents a plot of recorded heave against N_{60}', while Figure 14 Presents recorded borehole heave plotted against borehole depth.

3 DISCUSSION

Ten pairs of side by side (within 1 and 3 m c–c) BH/SPT tests drilled using High Frequency Sonic, Rotary Mud (HQTT) and Percussion/Dual Tube, were identified from the Canterbury Geotechnical Database (CGD). These borehole pairs amount to 139 pairs of SPT tests undertaken using a combination of automatic SPT and modern automated SPT equipment. The tests have been corrected from raw N values to N_{60} in a manner typically recommended for liquefaction analysis (Idriss and Boulanger 2008). The correlation between adjacent tests is poor, with a standard deviation in the ratio between tests in the order of 30.

A similar exercise carried out on ten CPT tests yielding six pairs for comparison and 2313 paired data points indicated variability in q_c with a standard deviation of 1.9 MPa. When q_c is converted to equivalent N_{60} this returned a standard deviation of 3.1N. While the scatter is higher than the accuracy of <1% (<1.5 MPa for a 150 MPa cone) suggested by Robertson (2012), in comparison to that observed in the SPT tests results this value could be considered minor. The greater scatter in CPT test results compared to that reported by Robertson is considered likely a consequence of the highly variable nature of Christchurch soils, particularly

in some layers. Where identified, these layers (typically gravelly) have been filtered from the data used in the comparisons.

On the basis that CPT tests appear to offer an order of magnitude better repeatability than SPT tests, and that many more CPT/SPT than SPT/SPT test pairs are available, a brief study was undertaken of factors such as drilling method, observed heave and soil grain size that may contribute to the observed poor repeatability of SPT tests in Christchurch.

The observations made from the comparison undertaken are as follows:

- Overall the correlation proposed by Jeffries and Davies (1993) appears valid with an average 1:1 correlation considering all N_{60} and N_{60}'data points combined.
- There appears to be considerable scatter in the N_{60} and N_{60}'comparison, consistent with that observed in the SPT: SPT pairs.
- There appears to be a greater scatter in the High Frequency Sonic data compared to other methods (R^2 of around 0.2 for HFS compared to around 0.5 for LFS/HQTT/Percussion). This was hypothesized as being related to increased soil disturbance resulting from the vibratory drilling method, however this remains unproven as there is no clear reduction in the variation, as might be expected in this case, with increasing N_{60}' (as a proxy for soil strength). This may also be influenced by the greater dataset considered for HFS. This requires addressing in further study.
- HQ Triple Tube data appears to have a relative bias toward recording higher SPT N; while this could be an indication of less ground disturbance it is noteworthy that Low Frequency Sonic has a similar bias. One aspect of the test both these methods have in common, in this dataset, is the use of traditional automatic drop SPT hammers. Note however that this effect has already been incorporated into the analysis in generating the N_{60} values used in the analysis. Further research may be warranted in this area, noting that the automated hammers used in the HFS and Percussion rigs have the potential to deliver blows at a faster rate than traditional drop hammers.
- There does not appear to be a strong correlation between the apparent error and soil density suggesting, contrary to the author's expectations, that drilling induced disturbance is likely to be a more significant factor in loose soils compared to medium dense of dense soils.
- Similarly, there does not appear to be a strong correlation between the reported occurrence of heave and N_{60}.
- There appears to be a positive correlation between heave and depth, possibly associated with coarser/gravelly layers at depth and increased potential for large hydraulic gradients.
- There appears to be a correlation between recorded heave and drilling method although consideration of a larger sample is required in order to draw conclusions.

The observed poor repeatability in SPT testing in Christchurch soils has significant implications for liquefaction analysis. In engineering practice liquefaction potential is generally assessed using semi empirical methods as a ratio between liquefaction resistance, derived empirically in correlation to SPT N, and seismic cyclic stress. The difference between soil considered likely to liquefy ($F_L < 1.0$) and unlikely to liquefy ($F_L > 1.5$) can occur with a difference of less than ± 15% in N_{60} (Idriss and Boulanger 2006, Figure 14, $N = 20$–26, $CRR = 0.2$ to 0.3). The likely error in SPT N identified by the preceding study has the potential to cause significant errors in the reliable assessment of liquefaction potential.

Similarly significant is the potential for incorrectly predicting liquefaction induced settlement. Using a commonly applied method for estimating liquefaction induced settlement (Tokimatsu and Seed 1987 Figure 3–proposed tentative relationship between cyclic stress ratio, $(N_1)_{60}$ and volumetric strain for saturated clean sand) the sensitivity of settlement predictions to even a single erroneously low N_{60} value can be illustrated. Considering a single SPT test undertaken within a sequence of otherwise medium dense soil, an erroneous value of $(N_1)_{60} = 3$ results in a predicted post liquefaction volumetric strain of 5%. At a test interval of 1.5 m this corresponds to a total predicted post liquefaction consolidation settlement of 75 mm.

Sites within Christchurch are commonly classified under guidance from the Ministry of Business and Innovation into Technical Categories (MBIE 2012). Technical Categories 1 to 3 are a range of site seismic behavior and corresponding recommendations for development, ranging from TC1: 'Liquefaction damage is unlikely in future large earthquakes. Standard residential foundation assessment and construction is appropriate' to TC3: 'Liquefaction damage is possible in future large earthquakes. Individual engineering assessment is required to select the appropriate foundation repair or rebuild option.' One of the more commonly applied differentiators in the determination of the relevant TC is the predicted liquefaction induced settlement. According to the liquefaction settlement limits set out in Table 3.1 of 'Technical categorization of the Green Zone on the flat' TC1 (0–25 mm ULS Liquefaction) and TC3 (>100 mm ULS Liquefaction Settlement) the single erroneous test could, theoretically, have the potential to change the site categorization from TC1 to TC2.

4 CONCLUSIONS

Internationally and in New Zealand the SPT test is progressively being superseded by the CPT tests as the geotechnical practitioner's preferred in-situ testing method. Numerous researchers have discussed the shortcomings of the Borehole/SPT test citing poor test repeatability.

However SPT tests remain widely used in Christchurch, with a similar expenditure as on CPT tests for a number of reasons including:

- Shallow gravel interbeds generally prevent adequate penetration of CPT tests;
- CPT tests are unable to penetrate to 'prove' deeper gravel founding layers, refusing close to their surface;
- Preference for soil descriptions based on physical samples rather than CPT derived soil behavior indices and limited availability/familiarity/use of CPT based sampling equipment;
- Familiarity with SPT based empirical correlations and design 'rules of thumb'.

Given the ongoing widespread use of SPT tests and the implications of variability on liquefaction analyses it was considered worthwhile to undertake an assessment of repeatability of SPT tests in the Christchurch area. The assessment was undertaken initially by comparison of paired bores, however when the number of suitable bores was found to be limited, by comparison against bores paired with CPT tests using q_t to N_{60} correlation.

An assessment was carried out between the closest ten pairs of BH/SPT tests from the Canterbury Geotechnical Database. The correlation was found to be poor, with a standard deviation in the tests results in the order of 30 N_{60}. A similar exercise carried out on ten CPT tests indicated a significantly lower variability, which when correlated to N_{60} corresponds to a standard deviation of $3.1N_{60}$.

In an effort to identify uncorrected factors which might affect SPT repeatability we have compared paired SPT N_{60} and CPT correlated N_{60}' for a range of drilling methods, a range of soil penetration resistances and for observed borehole heave. Scatter appears similarly large for all methods, with perhaps a slightly larger scatter with sonic drilling, contrary to what might otherwise be expected, correlation or the recorded incidences of heave do not improve noticeably in denser soils at depth.

The large uncertainty in SPT N_{60} has significant implications in terms of the validity of SPT based liquefaction assessment. The importance of reliability is illustrated by an example calculation where it is noted that a single erroneous N_{60} value of 3bl/300 mm could theoretically increase the predicted post liquefaction settlement sufficient for a property otherwise categorized as TC1 to be re categorized as TC3.

Given the observed variability in SPT tests, CPT tests are recommended wherever practical for liquefaction analysis, where CPT tests cannot be undertaken for reasons of gravel beds, consideration might be given to other methods such as downhole shear wave velocity measurement.

ACKNOWLEDGEMENTS

The author would like to thank Gavin Alexander at Beca for valuable review comments and Tony Fairclough and Darren Ashfield from Tonkin and Taylor Christchurch for assistance in compiling some of the data used in this paper.

REFERENCES

ASTM D1586–11 2011. *Standard method for Standard Penetration Test (SPT) and Split-Barrel Sampling of soil*, ASTM International. www.astm.org.

ASTM D5778–12 2012. *Standard Test Method for Performing Electronic Friction Cone and Piezocone Penetration Testing of Soils*, ASTM International. www.astm.org

Canterbury Earthquake Recovery Authority, CERA 2013. Canterbury Geotechnical Database. https://canterburygeotechnicaldatabase.projectorbit.com

Idriss I.M. & Boulanger R.W. 2006. Semi-empirical procedures for evaluating liquefaction potential during earthquakes. *Soil Dynamics and Earthquake Engineering,* Vol. 26, 115–130.

Idriss, I.M. & Boulanger, R.W. 2008. *Soil liquefaction During Earthquakes*, Monograph series, No. MNO-12, Earthquake Engineering Research Institute

Jefferies, M.G. & Davies, M.P. 1993. Use of CPTu to Estimate Equivalent SPT N_{60}. *ASTM Geotechnical Testing Journal*, Vol. 16, No. 4, pp. 458–468.

Ministry of Business Innovation and Employment 2012. *Guidance: Repairing and rebuilding houses affected by the Canterbury earthquakes* http://www.dbh.govt.nz/canterbury-earthquake-residential-building

Robertson, P.K. & Cabal, K.L. 2012. *Guide to Cone Penetration Testing for Geotechnical Engineering*, Prepared for Gregg Drilling & Testing Inc., 5th Edition, 2012.

Robertson, P.K., Campanella, R.G. & Wightman, A. 1983. SPT-CPT Correlations. *Journal of Geotechnical Division*, ASCE, Vol. 109, pp. 1449–1459.

Rogers, J.D. 2006. Subsurface Exploration Using the Standard Penetration test and the Cone Penetrometer Test. *Environmental & Engineering Geoscience*, Vol. XII, No. 2, pp. 161–179.

Tokimatsu, K. & Seed, H.B. 1987. Evaluation of settlements in sands due to earthquake shaking. *Journal of Geotechnical Engineering*. 113(8), 861–878.

Soil Liquefaction during Recent Large-Scale Earthquakes – Orense, Towhata & Chouw (Eds)
© 2014 Taylor & Francis Group, London, ISBN 978-1-138-02643-8

Analysis of liquefaction characteristics at Christchurch strong motion stations

L. Wotherspoon & R.P. Orense
Department of Civil and Environmental Engineering, University of Auckland, Auckland, New Zealand

R. Green
Department of Civil and Environmental Engineering, Virginia Tech, USA

B. Bradley
Department of Civil and Natural Resources Engineering, University of Canterbury, Christchurch, New Zealand

B. Cox
Department of Civil, Architectural and Environmental Engineering, The University of Texas, USA

C. Wood
Department of Civil Engineering, University of Arkansas, USA

ABSTRACT: The city of Christchurch and its surrounds experienced widespread damage due to soil liquefaction caused by the Canterbury earthquake sequence that began in September 2010 with the M_w7.1 Darfield earthquake. Prior to the start of this sequence, the city had a large network of Strong Motion Stations (SMSs) installed, which recorded a vast database of strong ground motions. This paper uses this database of strong ground motion recordings, observations of liquefaction manifestation at the ground surface, and data from a recently completed extensive geotechnical site investigation program at each SMS to assess a range of liquefaction evaluation procedures at the four SMSs in the Christchurch Central Business District (CBD). In general, the characteristics of the accelerograms recorded at each SMS correlated well with the liquefaction evaluation procedures, with low liquefaction factors of safety predicted at sites with clear liquefaction identifiers in the ground motions. However, at sites that likely liquefied at depth (as indicated by evaluation procedures and/or inferred from the characteristics of the recorded surface accelerograms), the presence of a non-liquefiable crust layer at many of the SMS locations prevented the manifestation of any surface effects. Because of this, there was not a good correlation between surface manifestation and surface manifestation indices, namely the Liquefaction Potential Index (LPI) and the Liquefaction Severity Number (LSN).

1 INTRODUCTION

The city of Christchurch is located on the east coast of the South Island of New Zealand, on the edge of the Canterbury Plains, a large area (approximately 160 km long and up to 60 km wide) formed by the overlapping alluvial fans of glacier-fed rivers. The surface geology within the city consists primarily of the Springston Formation Holocene alluvial gravels, sands and silts that are highly susceptible to liquefaction, and the Christchurch Formation dense dune and beach sands that are less susceptible to liquefaction (Brown & Weeber 1992).

The city and some surrounding towns experienced widespread damage due to soil liquefaction induced by seismic shaking during the Canterbury earthquake sequence, beginning

in September 2010 with the M_w7.1 Darfield earthquake. The other most notable earthquakes in this sequence were the 22 February 2011 M_w6.2 Christchurch earthquake, and the two twin earthquake events on 13 June 2011 and 23 December 2011. Each resulted in widespread liquefaction induced damage.

Prior to the start of this sequence, the city had a large network of strong motion stations (SMSs) installed, which recorded a vast database of strong ground motion recordings. Within Christchurch there were seven SMSs as part of the National Strong Motion Network and nine that were part of Canterbury regional strong motion network (Avery et al. 2004). Additionally, there were SMSs located in both Lyttelton (LPCC) and Kaiapoi (KPOC), and all are part of the GeoNet project (GNS Science 2013).

This paper uses this database of strong ground motion records, the observations of liquefaction manifestation at the ground surface, and data from a recently completed extensive geotechnical site investigation program at each SMS to assess a range of liquefaction evaluation procedures that are based on various site investigation techniques. The focus of this paper is on the SMSs located in the Christchurch CBD, namely Christchurch Botanical Gardens (CBGS), Christchurch Cathedral College (CCCC), Christchurch Hospital (CHHC), and Christchurch Resthaven (REHS). These sites are all within 2.5 km of each other, and have very diverse soil profile characteristics. Results of the evaluation procedures were compared against the observed liquefaction surface manifestations and the characteristics of the accelerograms recorded at each SMS during the Darfield and Christchurch earthquakes.

2 GEOTECHNICAL DATA

Prior to 2011, little information regarding the subsurface geotechnical characteristics of the strong motion station locations in and around Christchurch was available. As noted by Cousins & McVerry (2010), the soil profiles and site classes at each SMS were assumed from well logs and regional geological knowledge. Therefore, as part of this study CPT, SPT and borehole data, shear wave velocity (V_s) profiles, and horizontal to vertical spectral ratio measurements (H/V) in close vicinity to the SMS were used to develop detailed soil profiles at each site.

Initially, the authors collected existing CPT, borehole and SPT data in the vicinity of each SMS from available sources (CERA 2012). At locations with a paucity of data, an additional program of subsurface site investigations was carried out using CPT and borehole methods where appropriate. At each site, CPT data was used to calculate the soil behaviour type index (I_c) as a function of depth, to enable qualitative comparisons with the borehole log data where available (Robertson & Wride 1998). Shear wave profiles were developed using dispersion data from the study summarised by Wood et al. (2011) and additional surface wave testing. A combination of active-source and passive-source surface wave techniques were used to resolve the shear stiffness and layering beneath each SMS. Towards this end, layering characteristics at each site from the subsurface investigations were used to help constrain the layering of the shear wave velocity profile. A summary of the data collated at the CBGS SMS is outlined in Figure 1. Regional geotechnical investigations have shown little change in CPT sounding characteristics before and after major events in the earthquake sequence (Orense et al. 2011). Therefore, although site investigations were carried out following these earthquakes, it can be reasonably assumed that they provide a good representation of the pre-sequence soil profile characteristics.

At each location where borehole cores were available, samples were taken from each of the soil layers to define their grain size distribution and fines content (*FC*). At the time of writing, the grain size distribution testing of all sand and silty sand layers were completed, but grain size analyses still needed to be carried out on other soil types. At sites where no borehole data was available, the fines content was estimated using the generic correlation between *FC* and I_c proposed by Robertson & Wride (1998).

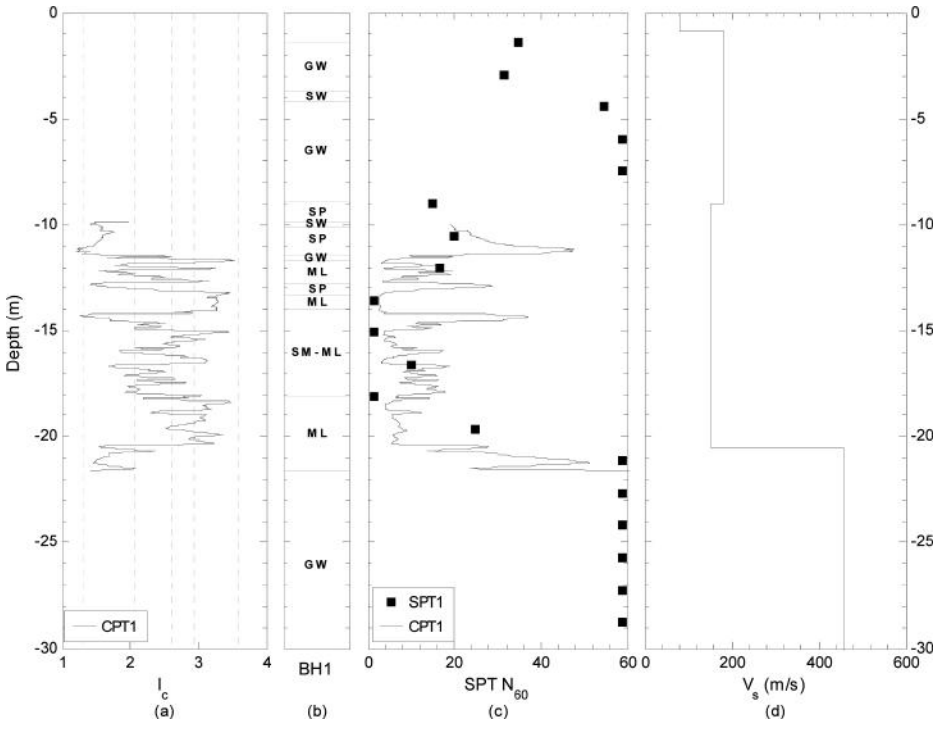

Figure 1. CBGS geotechnical site investigation summary. (a) soil behaviour type index, (b) borehole BH1 log, (c) SPT and CPT equivalent blow counts, (d) shear wave velocity.

3 LIQUEFACTION EVALUATION PROCEDURES

Multiple deterministic liquefaction evaluation procedures were applied to each of the site investigation methods available at the four SMS locations studied herein. Calculations were performed using the geometric mean of the horizontal PGA recorded at each SMS for the M_w7.1 2010 Darfield earthquake and the M_w6.2 2011 Christchurch earthquake. The PGA values prior to any manifestation of liquefaction in the accelerograms were used in these calculations. The following procedures were investigated:

- CPT based methods—Robertson & Wride (1998)/Youd et al. (2001), Moss et al. (2006), Idriss & Boulanger (2008)
- SPT based methods—Youd et al. (2001), Cetin et al. (2004), Idriss & Boulanger (2008)
- V_s based methods—Andrus & Stokoe (2000), Kayen et al. (2013)

4 LIQUEFACTION EVALUATION PROCEDURES

Multiple deterministic liquefaction evaluation procedures were applied to each of the site investigation methods available at the four SMS locations studied herein. Calculations were performed using the geometric mean of the horizontal PGA recorded at each SMS for the M_w7.1 2010 Darfield earthquake and the M_w6.2 2011 Christchurch earthquake. The PGA values prior to any manifestation of liquefaction in the accelerograms were used in these calculations. The following procedures were investigated:

- CPT based methods—Robertson & Wride (1998)/Youd et al. (2001), Moss et al. (2006), Idriss & Boulanger (2008)

- SPT based methods—Youd et al. (2001), Cetin et al. (2004), Idriss & Boulanger (2008)
- V_s based methods—Andrus & Stokoe (2000), Kayen et al. (2013)

A probability of liquefaction (P_L) of 15% was used to represent a deterministic liquefaction evaluation for the procedures of Moss et al, Cetin et al. and Kayen et al. The middle of the range of magnitude scaling factors (MSFs) recommended for the Youd et al. methods were used in this study. The rest of the procedures used the MSF (or Duration Weighting Factor, DWF) detailed in the respective references. The relative densities (D_r) were estimated using the relationship given in Robertson and Cabal (2012) for use in the Youd et al. and Cetin et al. procedures. Ground water levels for each event were defined using the guidelines from the Canterbury Geotechnical Database (CERA 2012). At these locations, no potentially liquefiable layers were present above these water table levels. Soil unit weight was assumed to be 17 kN/m^3 above the water table, and 19.5 kN/m^3 below the water table.

For the CPT evaluations, layers having I_c<2.6 were assumed to be potentially liquefiable. The potentially liquefiable layers for the SPT analyses were defined based on the soil type encountered in the borehole and the *FC* data from laboratory analysis, with only sand and silty sand layers considered in the analyses. At SMS locations with borehole and SPT data, the potentially liquefiable layers for the V_s based methods were the same as those assumed liquefiable for the SPT based methods. At SMS locations with CPT data only, the potentially liquefiable layers for the V_s based methods were the same as those assumed for the CPT based methods.

Data from the liquefaction evaluation procedures were used to define two indicators of the severity (or damage potential) of liquefaction, the Liquefaction Potential Index (LPI) (Iwasaki 1984), and the Liquefaction Severity Number (LSN), (van Ballegooy et al. 2012). An approximate relationship between surface manifestation severity and the LPI and LSN values is summarized in Table 1. Work by Toprak & Holtzer (2003) suggested that there is unlikely to be any surface manifestations for an LPI less than 5.

These evaluation procedures were compared against two physical indicators of liquefaction: 1) the observed severity of liquefaction surface manifestations following the Darfield and Christchurch earthquakes, defined using both post-event site visits by the authors and high aerial and satellite imagery taken soon after each earthquake; 2) the characteristics of the accelerograms recorded at the SMSs, with liquefaction indicated by acceleration spikes characteristic of cyclic mobility, and reduced high frequency content in the latter part of the record. A summary of the observed liquefaction surface manifestations and the surface ground motion characteristics at each SMS is provided in Table 2.

Table 1. Liquefaction surface manifestation severity as a function of LPI and LSN.

Severity	None	Minor	Moderate	Major
LPI	0	0–5	5–15	15+
LSN	0	0–20	20–50	50+

Table 2. Summary of the evidence of liquefaction from observed ground motions, surface manifestations and CPT based liquefaction indicators.

	Darfield earthquake				Christchurch earthquake			
SMS	Ground motions	Surface evidence	LPI	LSN	Ground motions	Surface evidence	LPI	LSN
CBGS	N	N	0–1.1	0.1–0.2	Y	N	0.3–3.6	0.2–0.3
CCCC	N	N	1.7–7.7	10.8–16.1	Y	Y	1.8–7.5	7.1–16.4
CHHC	N	N	0.4–2.8	4.4–7.4	Y	Y	2.7–14.1	10.1–16.9
REHS	N	N	3.4–6.6	15.2–28.0	Y	N	7.0–11.1	17.3–32.3

5 CASE STUDIES

Two case studies of the liquefaction characteristics and evaluations at two SMS locations are described in detail in this section.

5.1 *Christchurch Botanical Gardens (CBGS)*

The CBGS SMS is located in the Christchurch Botanical Gardens (Figure 2) on the western edge of the Christchurch CBD. The soil profile characteristics at the CBGS SMS are summarized in Figure 1. Borehole logs indicate approximately 9 m of gravels at the surface with SPT N_{60} values of 30 and above. Beneath these surface gravels are interbedded layers of sands, sandy silts and silts down to 21 m. I_c values from CPT data also indicate the variability of deposits within the 9–21 m depth range. The fines content for the sand and silty sand layers from lab testing ranged from 1.1 to 15.3%. Below this the dense Riccarton Gravel deposits were encountered.

There was no clear manifestation of liquefaction effects at the ground surface in the immediate vicinity of the SMS or evidence of liquefaction in the accelerogram from the Darfield earthquake (Figure 3a). Also, there was no clear manifestation of liquefaction effects near the CBGS SMS following the Christchurch earthquake. Aerial views of the CBGS location are shown in Figure 2 for both these events. The lighter spots in the grass surrounding the SMS in Figure 2b were confirmed as dry grass areas and not surface ejecta by ground reconnaissance following the Christchurch earthquake. A few hundred metres to the north of the SMS, significant volumes of ejecta were evident at the ground surface in North Hagley Park following the Christchurch earthquake. However, the accelerogram from the Christchurch earthquake in Figure 3b showed a clear indication of liquefaction of the underlying soils, with characteristic acceleration spikes and reduced high frequency content in the latter part of the record (Bradley & Cubrinovski 2011). This indicates that liquefaction likely triggered during the Christchurch earthquake, but, the thick gravel layer near the surface inhibited surface manifestation of liquefaction near the SMS.

Using the CPT, SPT and V_s data summarized in Figure 1, all the liquefaction evaluation procedures outlined in the previous section were applied. The geometric mean PGA was equal to 0.16 g and 0.33 g for the Darfield and Christchurch earthquakes, respectively. For the Darfield earthquake only a small number of very thin layers were shown to have a factor of safety slightly less than one throughout the soil profile. For the Christchurch earthquake multiple layers up to 40 cm in thickness were predicted to liquefy throughout the soil profile, with the factors of safety of these layers being as low as 0.5 for some of the methodologies. These predicted liquefied layers sit below the approximately 9 m of surface gravels. These predictions correlate well with the accelerogram characteristics for each event. The significant

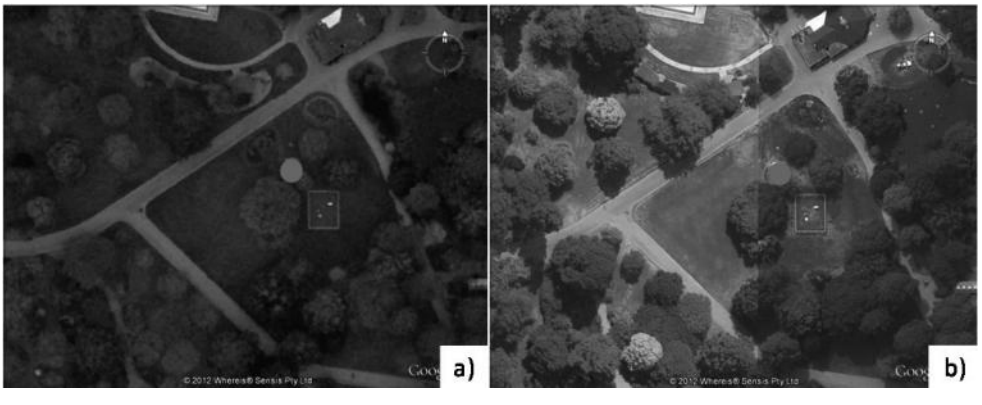

Figure 2. CBGS liquefaction surface manifestation a) Darfield earthquake; b) Christchurch earthquake.

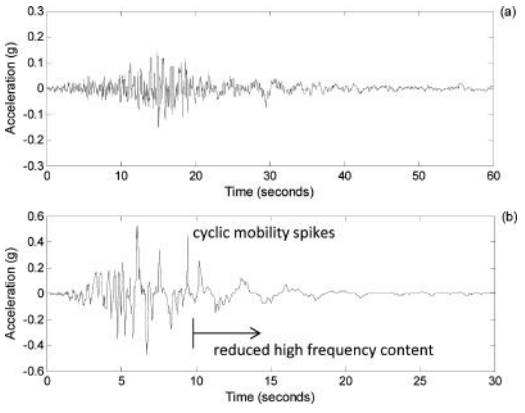

Figure 3. CBGS accelerogram for the a) Darfield earthquake; b) Christchurch earthquake (note the different scales in each plot).

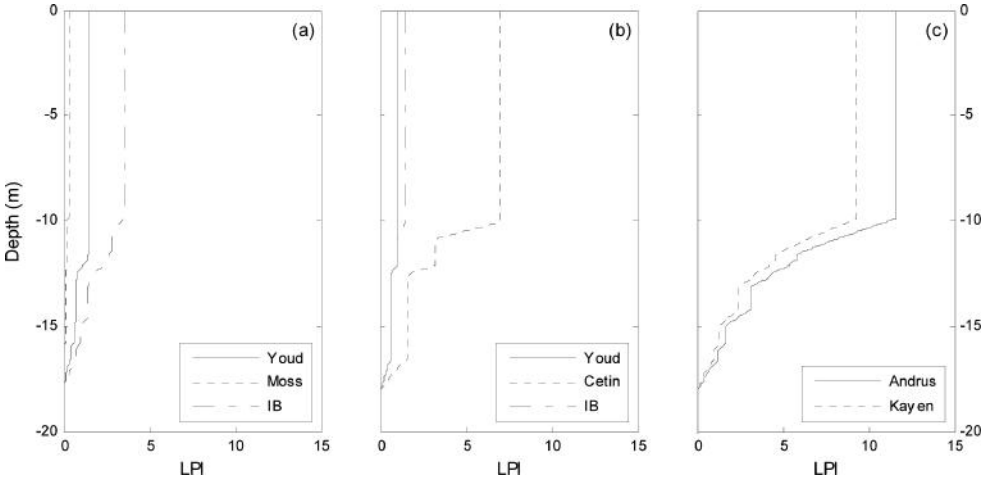

Figure 4. CBGS LPI calculations for the Christchurch earthquake a) CPT based methods; b) SPT based methods; c) V_s based methods.

interbedding below the gravels meant that the SPT was not able to accurately characterize the properties of each layer, with most test depths passing through different soil layers. The only potentially liquefiable layer characterized with any confidence using the SPT was the sand directly below the gravels.

The LPI values for each site investigation method and liquefaction evaluation procedure for the Christchurch earthquake are summarized in Figure 4. There is range in the LPI values for each site investigation method and across each of the methods. Similar layers were shown to liquefy using all of the CPT and SPT based methods, with LPI values suggesting minor surface liquefaction manifestations. This has a reasonable correlation with the observed surface manifestations. Using the CPT evaluation procedures, the LSN was equal to 0.2–0.3 for the Christchurch earthquake, a range that correlates to no surface effects. This compares well with the lack of surface manifestations, as only the top 10 m of the soil profile is included in the calculation of LSN. Clearly the crust thickness is important as it has an influence on the presence of any surface manifestations, and if the LPI was computed using only the top 10 m of the soil profile the calculated surface manifestation severities would be similar to those suggested by the LSN calculations.

The V_s based methods in Figure 4c predicted liquefaction would have triggered in most of the sand and silty sand layers, with the final LPI value indicating moderate liquefaction surface manifestations, clearly not correlating well with what was observed. However, this method predicted very low factors of safety in the liquefiable layers, which correlates well with the observed ground motion characteristics.

5.2 *Christchurch Hospital (CBGS)*

The CHHC SMS is located at the south western corner of the Christchurch CBD. Borehole logs indicate layered deposits of sands and gravels to a depth of between 10 and 15 m (Figure 5). A stiff sand layer is located beneath these interbedded layers, varying in thickness by between 4 and 8 m. A soft, 4 m thick layer of silts and organics sits between the sand layer and the stiff Riccarton Gravels below. The Riccarton Gravels are located at a depth of approximately 22 m.

There was no clear manifestation of liquefaction at the ground surface in the immediate area surrounding the SMS following the Darfield earthquake (Figure 6a), and moderate volumes of ejecta were present in the area immediately adjacent and surrounding the SMS following the Christchurch earthquake (Figure 6b). The acceleration record from the Christchurch earthquake in Figure 7 clearly indicates liquefaction was triggered in the underlying soils, with characteristic acceleration spikes and reduced high frequency content in the latter part of the record (Bradley & Cubrinovski 2011). In contrast, the acceleration record from the Darfield earthquake showed no indication of the occurrence of liquefaction in the underlying soils.

The liquefaction evaluation procedures for CPT and V_s mentioned in the previous section were used to compute the factors of safeties against liquefaction triggering at CHHC SMS site, which in turn were used to compute LPI and LSN. The geometric mean PGA was equal

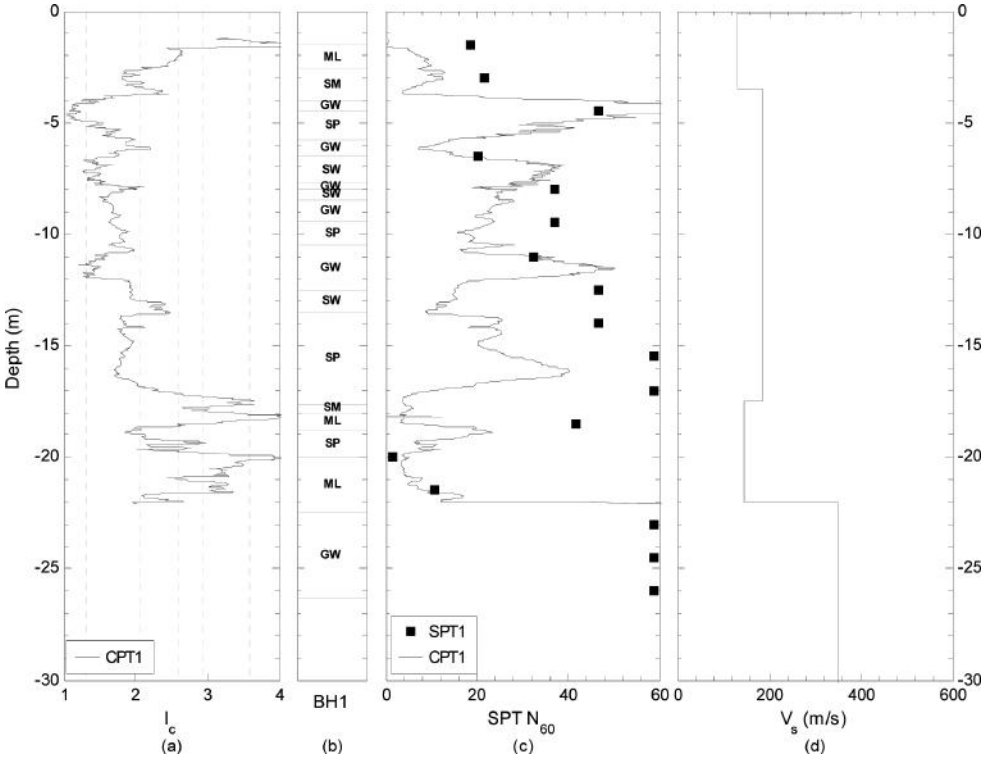

Figure 5. CHHC geotechnical site investigation summary (a) soil behaviour type index, (b) borehole BH1 log, (c) SPT and equivalent CPT blow counts, (d) shear wave velocity.

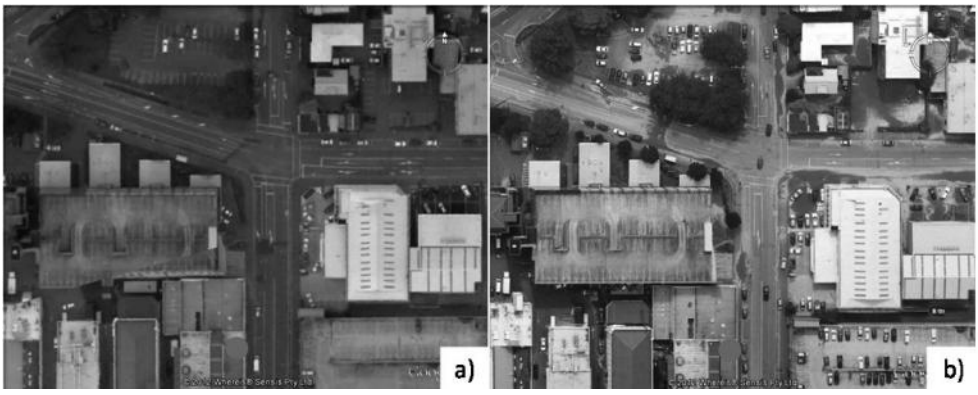

Figure 6. CHHC liquefaction surface manifestation a) Darfield earthquake; b) Christchurch earthquake.

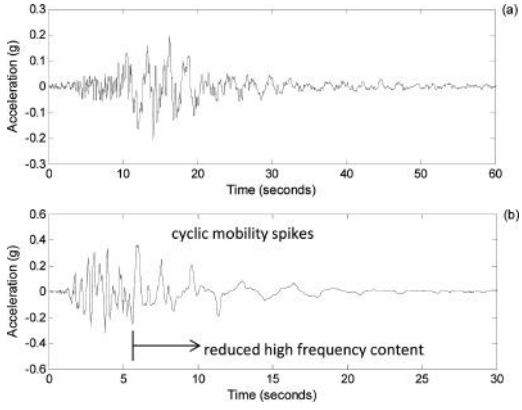

Figure 7. CHHC accelerogram for the a) Darfield earthquake; b) Christchurch earthquake (note the different scales in each plot).

to 0.17 g and 0.37 g for the Darfield and Christchurch earthquakes, respectively. For the Darfield earthquake only a small number of thin layers were shown to have a factor of safety less than one throughout the soil profile for the majority of the evaluation procedures. For the Christchurch earthquake much thicker layers were predicted to liquefy throughout the soil profile, with much lower factors of safety. The CPT calculations generally correlate well with the accelerogram characteristics recorded during each event.

A summary of the LPI and LSN calculations for the CHHS SMS site are presented in Figure 8. The range for the CPT based LPI for the Darfield earthquake was 0.4–2.8, and the range for LSN was 4.4–7.4, both suggesting that there would be minimal surface manifestation effects, correlating well with what was observed. For the Christchurch earthquake there was a significant increase in these values, with the range for LPI equal to 2.7–14.1 and the range for LSN equal to 10.1–16.9. There is a large range in the LPI values, with the lower end of the scale suggesting surface manifestation effects less severe than what was observed. The LSN values have a smaller range and also suggest surface manifestations less severe than what was observed. The LPI calculated using the V_s data were again very similar, with the liquefiable layers were defined using the CPT I_c values. These both suggest surface manifestation effects that were similar to what was observed. The LPI value for the V_s procedures are developed in two main layers, while the CPT based methods show a gradual increase through multiple thinner layers.

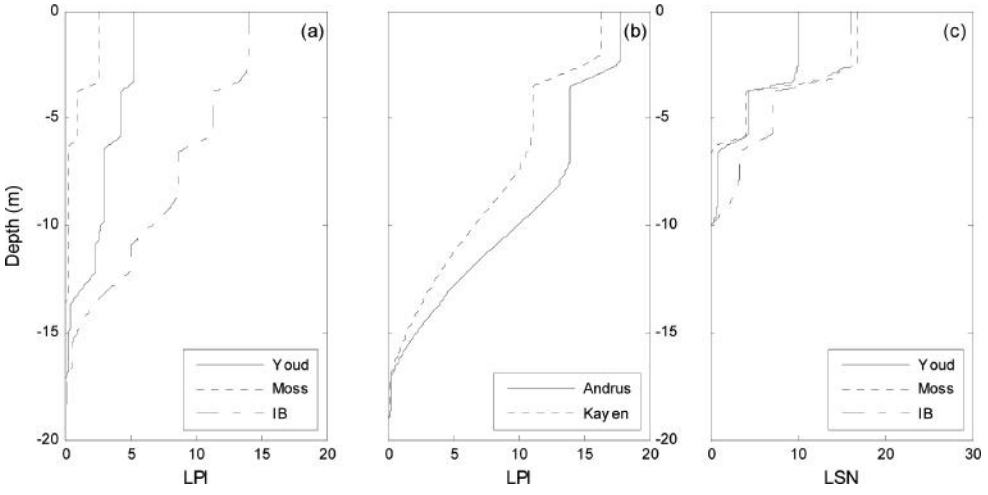

Figure 8. CHHC calculations for the Christchurch earthquake a) CPT based LPI; b) V_s based LPI; c) CPT based LSN.

6 SUMMARY

A summary of the CPT based LPI and LSN outlined in the previous section and those at the two remaining Christchurch SMSs is provided in Table 2. These are compared against any evidence of liquefaction triggering in the ground motion records and at the ground surface for the Darfield and Christchurch earthquakes. In general, the predicted factor of safety against liquefaction triggering a good correlation to the sites where the recorded ground motions showed evidence of liquefaction, with factors of safety less than one.

At REHS there was no manifestation of liquefaction effects at the ground surface in the immediate area surrounding the SMS following any of the major earthquakes in the Canterbury earthquake sequence. The indicator values calculated for both the Darfield and Christchurch earthquakes did not correlate well with these observations, with both the LPI and LSN values predicting minor severity during the Darfield earthquake, and moderate severity during the Christchurch earthquake. However, this lack of surficial surface manifestations may be due to the presence of a thin gravel layer at the ground surface at this location.

Minor volumes of ejecta were evident in the area surrounding the CCCC SMS following the Christchurch earthquake, with a few isolated sand boils approximately 50 m from the SMS location. The severity of the surface manifestation at CCCC was much less that that at CHHC for this event, however the LSN values for both sites were very similar. For the Darfield earthquake the LPI and LSN values predicting minor-moderate surface manifestations, while in reality there was no manifestation and no evidence of liquefaction in the ground motion records.

For sites that had no liquefaction manifestations at the ground surface, and no evidence of liquefaction being triggered in the accelerograms, the LPI values ranged from 0 to 7.7, and the LSN values ranged from 0.1 to 28. This is a large range of values for these sites with no surface manifestation, with the lack of evidence from surface acceleration records also suggesting that the triggering of liquefaction would only be marginal. For multiple sites there may have been severe liquefaction of a layer at depth, as indicated by liquefaction evaluation analyses and/or inferred from the characteristics of the recorded surface acceleration time series, however due to a non-liquefiable crust layer, liquefaction was unable to manifest itself at the ground surface. This lack of surface manifestation was not in accord with the prediction using either the LPI or LSN methodologies across all the SMS locations.

7 CONCLUSIONS

Using the database of strong ground motion recordings from the Canterbury earthquake sequence, the observations of liquefaction manifestation at the ground surface, and data from a recently completed extensive geotechnical site investigation program at each SMS, a range of liquefaction evaluation procedures for multiple site investigation techniques were assessed.

In general, the characteristics of the recorded accelerograms at each SMS correlated well with the liquefaction evaluation procedures, with lower liquefaction factors of safety predicted at sites with clear liquefaction identifiers in the ground motions. However, at sites that likely liquefied at depth (as indicated by evaluation procedures and/or inferred from the characteristics of the recorded surface acceleration time series), the presence of a non-liquefiable crust layer at many of the SMS locations prevented the manifestation of any surface effects. This meant that there was not a good correlation between surface manifestation and two surface manifestation indices, the Liquefaction Potential Index (LPI) and the Liquefaction Severity Number (LSN).

ACKNOWLEDGEMENTS

This primary support for this research project was provided by Earthquake Commission (EQC) Biennial Grant 12/629. L. Wotherspoon's position at the University of Auckland is funded by the EQC. The primary support for the US authors was provided by the U.S. National Science Foundation (NSF) grant CMMI-1306261. However, any opinions, findings, and conclusions or recommendations expressed in this material are those of the authors and do not necessarily reflect the views of the National Science Foundation. We acknowledge the Canterbury Geotechnical Database for some of the site investigation data used in this study. EQC, CERA, their data suppliers and their engineers, Tonkin & Taylor, have no liability to any user of this data or for the consequences of any person relying on them in any way. We acknowledge the New Zealand GeoNet project and its sponsors EQC, GNS Science and LINZ, for providing accelerograms used in this study. We also thank the land owners at all SMSs for their cooperation during this study, and the support of McMillans Drilling.

REFERENCES

Andrus RD and Stokoe II, KH. 2000. Liquefaction resistance of soils from shear wave velocity. *Journal of Geotechnical and Geoenvironmental Engineering*, ASCE, 126(11), 1015–1025.

Avery HR, Berrill JB, Coursey PF, Deam BL, Dewe MB, Francois CC, Pettinga JR, and Yetton MD. 2004. The Canterbury University strong-motion recording project. *Proc. 13th WCEE*, *Vancouver, 2004*.

Bradley BA and Cubrinovski, M. 2011. Near-source strong ground motions observed in the 22 February 2011 Christchurch earthquake. *Seismological Research Letters*, 82, 853–865.

Brown LJ and Weeber JH. 1992. *Geology of the Christchurch urban area.* Institute of Geological and Nuclear Sciences, Lower Hutt.

Canterbury Earthquake Recovery Authority (CERA). 2012. *Geotechnical database for Canterbury earthquake sequence*. https://canterburygeotechincaldatabase.projectorbit.com.

Cetin KO, Seed RB, Der Kiureghian A, Tokimatsu K, Harder LF, Kayen RE and Moss RES. 2004. Standard penetration test-based probabilistic and deterministic assessment of seismic soil liquefaction potential. *Journal of Geotechnical and Geoenvironmental Engineering*, ASCE, 130(12), 1314–1340.

Cousins J and McVerry G. 2010. Overview of strong motion data from the Darfield earthquake. *Bulletin of the NZSEE*, 43(4), 222–227.

GNS Science. 2013. *GeoNet* http://www.geonet.org.nz (accessed June 15, 2013)

Idriss IM and Boulanger RW. 2008. *Soil liquefaction during earthquakes*. Monograph MNO-12, Earthquake Engineering Research Institute, Oakland, CA, 261 pp.

Iwasaki T, Arakawa T and Tokida KI. 1984. Simplified procedures for assessing soil liquefaction during earthquakes. *International Journal of Soil Dynamics and Earthquake Engineering*, 3, 49–58.

Kayen RE, Moss RES, Thompson EM, Seed RB, Cetin KO, Der Kiureghian A, Tanaka Y and Tokimatsu K. 2013. Shear-wave velocity-based probabilistic and deterministic assessment of seismic soil liquefaction potential. *Journal of Geotechnical and Geoenvironmental Engineering*, ASCE, 139(3), 407–419.

Moss RES, Seed RB, Kayen RE, Stewart JP, Der Kiureghian A, and Cetin, KO. 2006. CPT-based probabilistic and deterministic assessment of in situ seismic soil liquefaction potential. *Journal of Geotechnical and Geoenvironmental Engineering*, ASCE, 132(8), 1032–1051.

Orense RP, Pender MJ and Wotherspoon LM. 2011. Analysis of soil liquefaction during recent Canterbury (New Zealand) earthquakes. *Geotechnical Engineering Journal SEAGS & AGSSEA*, 42(3), 8–17.

Robertson PK and Cabal KL. 2012. *Guide to Cone Penetration Testing for Geotechnical Engineering, 5th edition*, Gregg Drilling & Testing, 131pp.

Robertson PK and Wride CE. 1998. Evaluating cyclic liquefaction potential using the cone penetration test. *Canadian Geotechnical Jnl.*, 35, 442–459.

Toprak S and Holtzer TL. 2003. Liquefaction potential index: field assessment. *Journal of Geotechnical and Geoenvironmental Engineering*, ASCE, 129(4), 315–322.

Van Ballegooy S, Malan PJ, Jacka ME, Lacrosse VIMF, Leeves JR and Lyth JE. 2012. Methods for characterising effects of liquefaction in terms of damage severity. *Proc. 15th World Conference of Earthquake Engineering*, Lisbon, Portugal.

Wood CM, Cox BR, Wotherspoon LM and Green RA. 2011. Dynamic site characterization of Christchurch strong motion stations. *Bulletin of the NZSEE*, 44(4), 195–204.

Youd TL, Idriss IM, Andrus RD, Arango I, Castro G, Christian JT, Dobry R, Finn WDL, Harder LF, Hynes ME, Ishihara K, Koester JP, Liao SSC, Marcuson III WF, Martin GR, Mitchell JK, Moriwaki Y., Power MS, Robertson P.K, Seed RB, and Stokoe II KH. 2001. Liquefaction Resistance of soils: Summary report from the 1996 NCEER and 1998 NCEER/NSF workshops on evaluation of liquefaction resistance of soils. *Journal of Geotechnical and Geoenvironmental Engineering*, 127(4), 297–313.

This page intentionally left blank

Soil Liquefaction during Recent Large-Scale Earthquakes – Orense, Towhata & Chouw (Eds)

Geophysical survey of two piers affected by liquefaction-induced lateral spreading for the 2010 Maule earthquake

E. Sáez, C. Ledezma, G. de la Maza, M. Cortés & S. Brunet
Department of Structural and Geotechnical Engineering, Pontificia Universidad Católica de Chile, Santiago, Chile

ABSTRACT: The February 27, 2010 Mw 8.8 Chile earthquake caused significant damage to ports and bridges, severely disrupting transportation links and the economy of the country. In many cases, the infrastructure damage was associated with liquefaction-induced lateral spreading, in which large blocks of soil slid on top of liquefied sandy layers impacting pile-supported wharfs and bridges. The main objective of this paper is to understand the key reasons behind the seismic behavior of two pile-supported wharfs: southern and northern piers in the Port of Coronel. With this purpose, a surface-wave based geophysical survey was conducted in this area to characterize shear wave velocity profiles and fundamental natural periods of soil deposits. This collected data was analyzed with standard liquefaction potential methodologies to identify liquefaction potential.

1 INTRODUCTION

Ports are Chile's preferred means for importing and exporting large quantities of goods. Early in the 21st century, 95% of Chilean exports and almost 90% of imports traveled through port facilities. The more important ports are located in Valparaíso, San Antonio, Concepción, and Coronel. Liquefaction-related damage after the Feb 27, 2010, Mw 8.8 event was relatively minor at both the Valparaíso and San Antonio ports; however, lateral spreading and ground settlement (with displacements reaching up to 1 m) damaged quay walls and pile-supported wharves in older sections of these ports (Brunet, 2012).

The port of Coronel is located in the town of Coronel, in the Bio-Bio Region, 30 km south of the city of Concepción and 545 km from Santiago (capital of Chile). Cargo is stored onshore, in a relatively-level open area and in a warehouse behind a 9 m deep sheetpile wall (1.6 m above ground). The sheetpile wall was driven into the sand beach and shallow water fronts the wall.

Cargo is transferred to ships via two pile-supported piers, which extend 500 to 600 m out into the ocean as shown in Figure 1. The northern pier was constructed in 1998, and it is supported by battered and vertical steel pipe piles. The southern pier was constructed in 2008 using a base-isolation system. Lead-core rubber bearings sit atop four battered piles connected together by steel beams. The base-isolation system was designed to work in concert with additional long, flexible vertical piles, which are able to move with the deck during an earthquake. There was no evidence of damage to the base-isolated pier, although some pounding occurred at the joint with the conventional pile-supported abutment.

As indicated by Bray et al. (2012), the port experienced significant lateral spreading during 2010 Mw 8.8 Chile earthquake. Evidence of lateral spreading was greatest in the northern part of the port where the surface was paved with asphalt underlain by a 0.2 m thick layer of compacted gravel fill. Movement was less obvious in the southern part of the port where the surface was paved with bricks underlain by a 0.8 m thick layer of gravel. Black sand ejecta obtained from cracks in the lateral spread was similar to the beach sand. The poorly graded

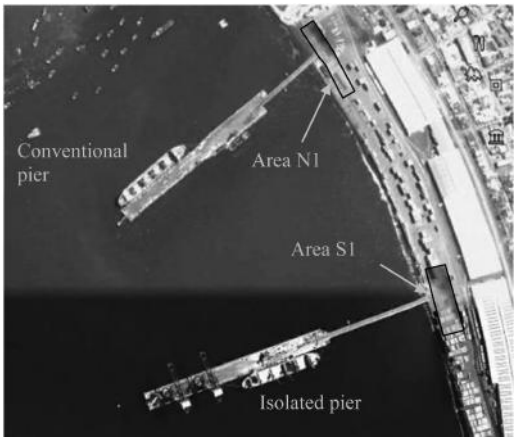

Figure 1. Location of both piers and geophysical surveyed areas.

beach sand (SP) found had a mean diameter of ~0.5 mm and a fines content of about 2%. Cumulative horizontal displacements behind the sheetpile wall were measured by summing the crack widths in the pavement along two lines. Maximum lateral movement at the wall was between 1.0 and 1.2 m, and relatively little movement occurred beyond a distance of 25 m behind the wall. Lateral spreading caused the 0.5 m-diameter steel pipe piles supporting the northern pier to rotate 14º from vertical; however, there were no obvious signs of distress along the pile surface. Pile rotation due to lateral spreading caused buckling of the stiffeners on the compression side and yielding of the stiffeners on the tension side of the support beam. Additional details regarding observed evidence of lateral spreading can be found in Bray et al. (2012).

The shear wave velocity profile is a fundamental parameter to evaluate the dynamic response of a site (Tokimatsu, 1997). In-hole tests are commonly used to evaluate this parameter, but the required borehole is not available for all projects. There are several approaches to estimate the soil shear-wave velocity profile through the analysis of surface wave propagation; however, as in any geophysical-indirect method, there is an important degree of uncertainty that needs to be quantified and eventually reduced. These geophysical methodologies involve a larger volume of soil, and therefore they are probably more representative of the seismic behavior of a site than local in-hole measurements. In this paper, shear wave velocity profile were used to quantify liquefaction potential.

As it is well known, Rayleigh waves are dispersive, i.e., the phase propagation velocities are a function of frequency (Okada, 2003). Surface wave methods use this property to characterize soils since their dispersion properties depend on the stratigraphy, particularly on the shear wave velocity profile. The procedure consists of three phases (Tokimatsu, 1997; Foti, 2000): (a) observation and recording of surface waves, (b) determination of dispersion curves, and (c) estimation of a shear wave velocity profile compatible with the observations through an inversion procedure.

The Spectral Analysis of Surface Waves (SASW) is one of the most known surface wave methods and has been widely studied by different authors (Nazarian and Stokoe, 1984; Sanchez-Salinero, 1987). This method uses a pair of receivers to record a signal generated from an active controlled source aligned with the receivers, thus, data gathered from different spacing layouts is required to build the dispersion curve. Multi-channel methods record the signal with multiple receivers simultaneously, decreasing the time of execution with respect to the SASW approach (Park et al., 1999). The seismic source can be either active (i.e., a sledgehammer or a weight drop, or mechanical oscillators), or passive (Bonnefoy-Claudet et al., 2006). Compared against active sources, ambient vibrations allow the inference of deeper layers properties, due to their low-frequency content.

Once a dispersion curve is obtained, the inversion must generate a model of horizontal soil layers with elastic properties compatible with field observations in terms of the dispersive characteristics (dispersion or autocorrelation curves). The Neighborhood Algorithm (NA; Sambridge, 2001) is a global optimization method that, unlike iterative methods, does not require an initial model and widely explores the space of parameters. The NA generates random initial models with uniformly distributed parameters. The mismatch of each model is evaluated, and the best model is selected to generate new random models. The difference between the analytical model and the empirical data (misfit) is evaluated, and the process is repeated until the misfit reaches a minimum. Wathelet (2008) proposed an improvement to NA, allowing the introduction of certain conditions among the parameters of models. This last improvement has been implemented in the version of the GEOPSY package, the software that was used in this study (Wathelet, 2002–2011).

In-situ geophysical seismic surveys, using active and passive measurement-based analysis of surface wave dispersion, along with fundamental period measurements, were conducted in two zones of the port area (N1 and S1 on Figure 1). These techniques were selected instead of conventional refraction due to the high level of ambient noise due to operation of the port and a velocity inversion beneath the pavement-base which can't be detected with refraction. The active tests were analyzed using the f-k active procedure considering that the direction of the waves is known; on the other hand, passive tests using a 2D array were analyzed using the f-k passive method. These tools are implemented in the GEOPSY package software (Wathelet 2002–2011). Passive measurements using linear arrays were analyzed using the Roadside MASW method implemented in the SeisImager/SW software (Geometrics Inc. 2005–2006).

In general terms, the ambient noise shows a variable amplitude with time, and it can be treated as a stochastic signal coming from a great number of processes of different origin (antropic or natural). Nevertheless, knowing the ratio between the amplitudes of the horizontal (H) and the vertical (V) components of ambient noise allows the estimation of the natural frequency of the ground vibration (Nakamura, 1989). Additional to natural frequency estimation, H/V curve could be used directly in the inversion process as ellipticity curves in order to complement geophysical data.

2 SOIL GEOPHYSICAL SURVEY

In this investigation we used a GEODE-24 (Geometrics®) seismograph, connected to 24 evenly spaced geophones (4.5 Hz natural frequency). The source used in the active test was an 18 pounds sledgehammer. The distance between the receivers and the source determines the range of frequencies where the dispersion curve is valid (Foti, 2001); hence, tests were conducted with different spacings between the source and the receivers to get as much information as possible. Since we have no control on the generated wavefield or its frequency range, the test must be repeated a number of times to ensure that reliable dispersion properties are obtained. In addition, to improve the results of the active experiments, we stacked the active signals to increase the signal-to-noise ratio. We used linear arrays for the f-k active and the MASW Roadside techniques, while 2D "L-shape" arrays were used for the f-k passive method. Since the fundamental assumption in the passive methods is that ambient vibrations are a superposition of surface waves that propagate with random directions (Tokimatsu, 1997), a longer recording time is required (Wathelet, 2005). The minimum recording was 20 minutes for all cases, sampling at 62.5 Hz.

Figure 2 depicts the geophone arrays that were used in each area. In Area N1, three linear arrays, LN1, LN2 and LN3, were used. A spacing of 2.5 m between geophones was used for arrays LN1 and LN3, while 2 m was used for line LN2 and L-shaped TN1 arrays. For the circular array CN1, a separation of 2.5 m between neighboring geophones (secant) was used. In Area S1, two linear–2.5 m spaced LS1 and LS2 were used. A variable separation of 2.0 and 2.5 m between geophones was used for L-shaped TS1 and TS2 arrays.

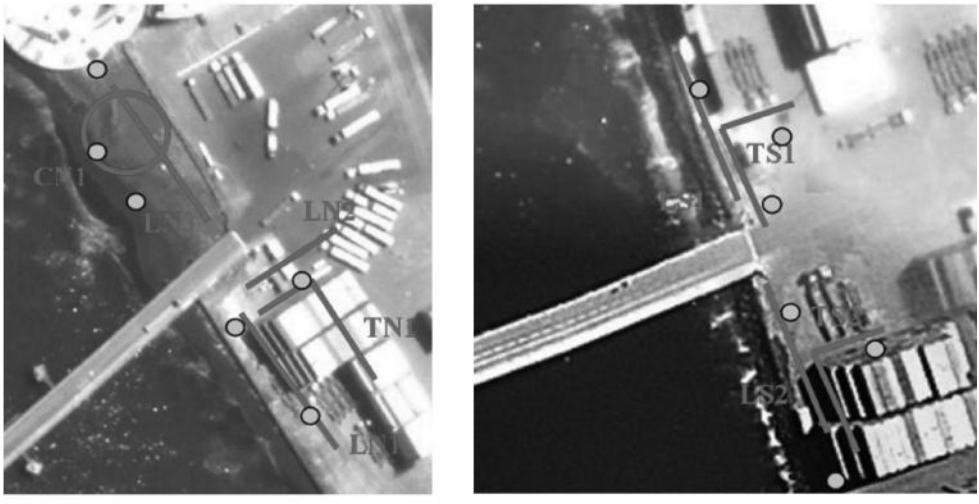

Figure 2. Location of geophone's arrays used in both surveyed areas.

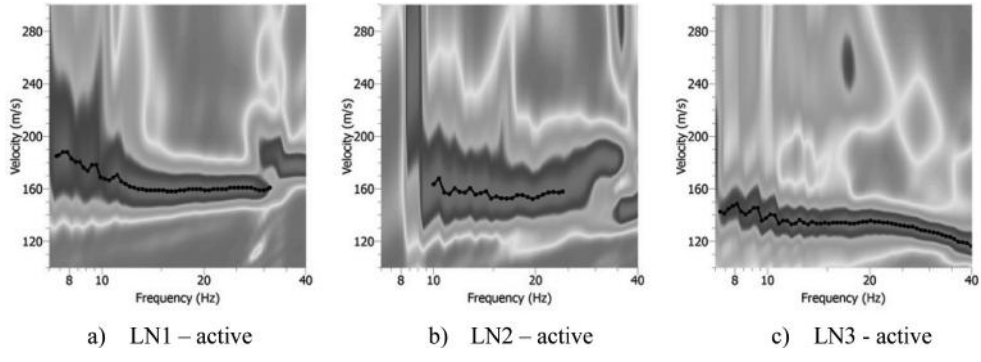

Figure 3. f-k active analysis for linear arrays of geophones. Area N1.

2.1 *Dispersive characteristics of soils: Area N1*

Figure 3 displays empirical dispersion curves obtained from active experiments using LN1, LN2 and LN3 arrays. In these three cases, a very low and uniform phase velocity of around 150 m/s was obtained. For longer arrays (LN1 and LN3), a minimum reliable frequency of 8.5 Hz was explored, whereas for the short array (LN2) a minimum frequency of around 10 Hz was satisfactorily explored. LN2 dispersion curve is slightly stiffer than the other profiles. LN2's curve exhibits a small phase-velocity increase between 18 and 25 Hz approximately. To complete a deeper soil profile description (lower frequencies), active tests were combined with ambient noise recording during about 20 minutes. These records were analyzed using the Roadside MASW method.

Figure 4 displays dispersion curves obtained using ambient noise analysis of data recorded in three linear arrays of geophones. The straight blue lines indicate geometrical limits of reliable exploration due to spatial sampling (resolution and aliasing). Additionally, as 4.5 Hz geophones were used, only dispersive data over this frequency value must be considered. According to these limits, the resulting dispersion curves are reliable between 4.5 and 13 to 15 Hz approximately.

Regarding the bi-dimensional arrays used to record ambient noise, Figure 5 displays the dispersion curves obtained using the f-k passive technique. As the predominant incident direction of surface waves is unknown in this case, the dispersion curve (bold black curve) is displayed with standard deviation. Ascending black curves from left to right on Figure 5 define reliable geometrical limits of the used arrays related to spatial sampling (minimum and maximum reliable wavelength). Data from TN1 arrays is robust between 5.5 to 15 Hz, whereas CN1 information is reliable between 5 to 15 Hz approximately. It is interesting to note that the dispersion variability of CN1 array is less than that observed for the TN1 array using exactly the same recording time. This variability reduction is related to the improved spatial sampling of circular arrays due to the several combinations of distance between pairs of geophones, which allows this array to properly identify intermediary wavelengths.

2.2 *Fundamental periods: Area N1*

To evaluate the soil's resonance frequency, several measurements using a portable three-component seismograph Tromino® were done in the studied area. Some of these measurements are qualitatively displayed on Figure 2 as yellow dots. The recorded data was analyzed using standard Nakamura's technique, with windows 20 s long and a total recording time of 20 minutes. Abnormal high amplitudes were removed using an anti-triggering filter.

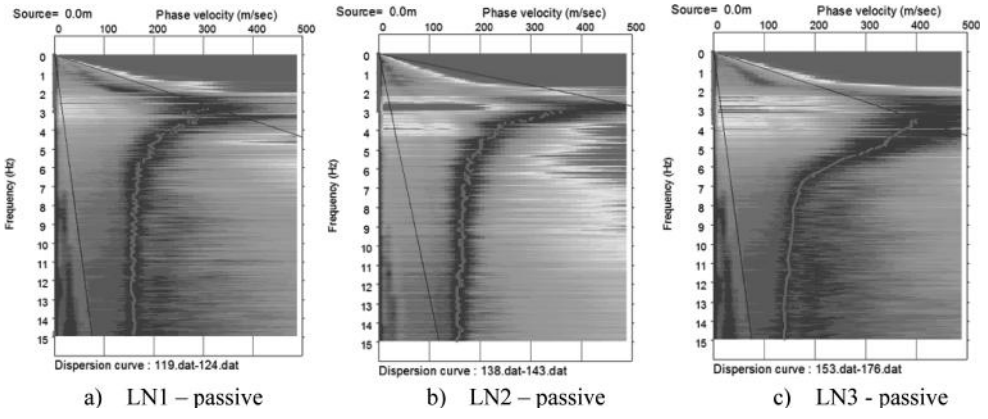

Figure 4. MASW Roadside analysis for linear arrays of geophones. Area N1.

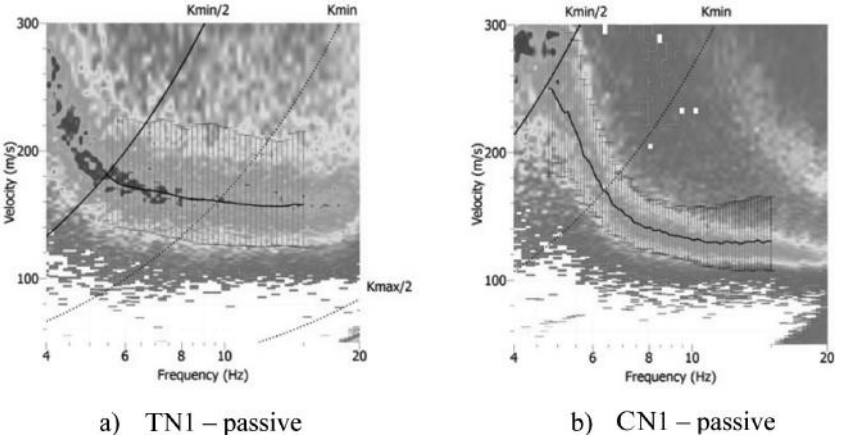

Figure 5. f-k passive analysis for circular and triangular arrays of geophones. Area N1.

A representative result of the zone covered by arrays LN1, LN2 and TN1 is displayed on Figure 6a, while Figure 6b displays a typical result of the zone explored by arrays CN1 and LN3 (beach). In general terms, a resonance frequency F_0 very close to 2 Hz was clearly identified in all cases with maximum amplitude A_0 of about 9. Amplitudes on the southern side of the pier access were approximately 90% of the amplitudes obtained in the beach because the seismograph was placed over the pavement instead of natural soil.

2.3 *Inversion: Area N1*

Dispersion information displayed on Figures 3 to 5 and ellipticity curves on Figure 6 are combined to characterize each explored zone. In general terms, dispersive information arising from each analysis is very consistent and overlaps satisfactorily across common explored frequency range. Two inversions were performed in Area N1: combining data from LN3 and CN1 arrays, and combining dispersive characteristics from LN1, LN2 and TN1. For both inversions, corresponding ellipticity curves are directly included in the inversion procedure. As previously indicated, the inversion problem consists of obtaining a horizontally stratified soil profile that closely matches the empirical data.

Figure 7 displays the results of inversions in Area N1. During the inversion, more than 100,000 models were generated. Figure 7a presents the obtained profile using arrays LN1, LN2 and TN1. In this case, a maximum reliable depth of about 22 m was obtained. Below this depth, the shear wave velocity is highly variable without an important variation of the error

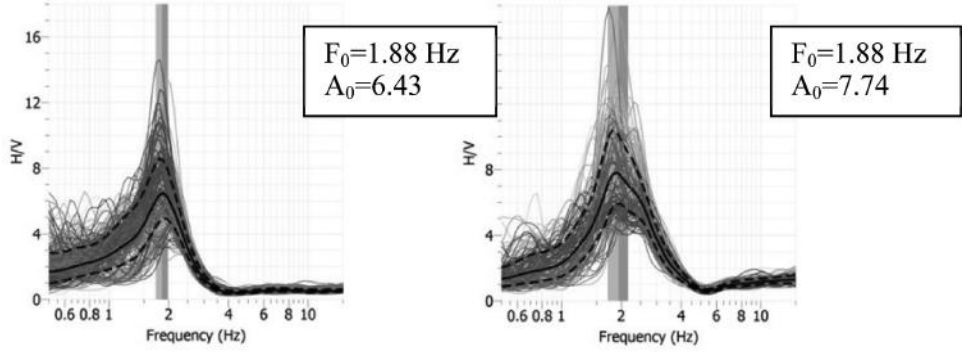

Figure 6. Representative resonance frequencies using Nakamura's technique. Area N1.

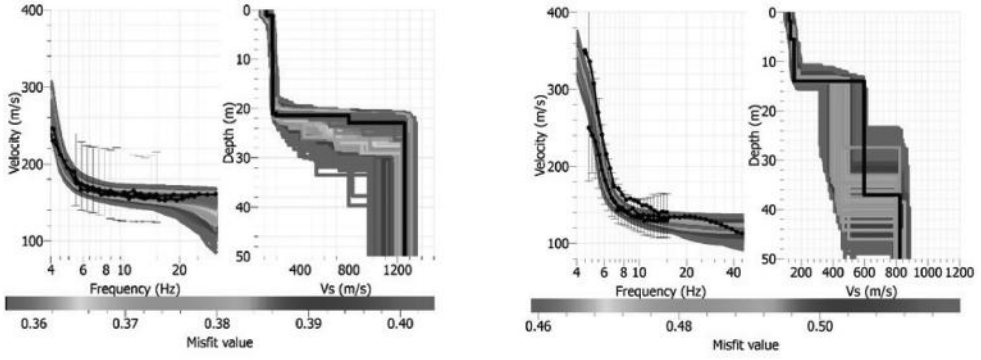

Figure 7. Inversion procedure results. Area N1.

indicator (misfit). Indeed, the minimum observable frequency of the geophones (4.5 Hz) was reached but the exploration does not reach bedrock depth and velocity satisfactorily. This Figure displays approximately 80% of valid models visited. The best inversion in terms of minimum misfit is displayed with a black line in the figure showing the shear wave profile. The adjustment between the empirical data and the theoretical inversion is displayed on the left-side. Regarding the beach zone, the best inversions are displayed in Figure 7b. In this case, the maximum reliable explored depth is about 34 m and 23% of the valid visited models are displayed The best inversion locates the bedrock level at approximately 42 m but its shear wave velocity is not properly defined. As ellipticity curves were directly included in the inversion, this bedrock level was obtained by the inversion algorithm to fit the measured resonance frequency. Detailed shear wave profiles and standard V_{s30} values are indicated in Table 1.

2.4 *Dispersive characteristics of soils: Area S1*

Using the same procedure described previously, Figure 8a summarizes soil dispersion properties obtained for the Area S1 using arrays LS1 and TS1. In this case, active experiments provided information between 9 to 40 Hz, while the MASW Roadside technique using passive LS1 recording provided information between 4.5 to 15 Hz approximately. Using the f-k passive technique on the TS1 arrays provides reliable information between 6 to 15 Hz. These three sets of data are very consistent and produce a rather flat dispersion curve with an almost constant phase-velocity of about 180 m/s. Figure 8b provides a representative result of H/V technique on this area. A representative fundamental period of 1.1 s (or F_0 = 0.82 Hz) was found with a very clear amplitude of at least A_0 = 12. In comparison with the results obtained for Area N1, shear wave velocities are very similar, but the soil deposit is certainly deeper.

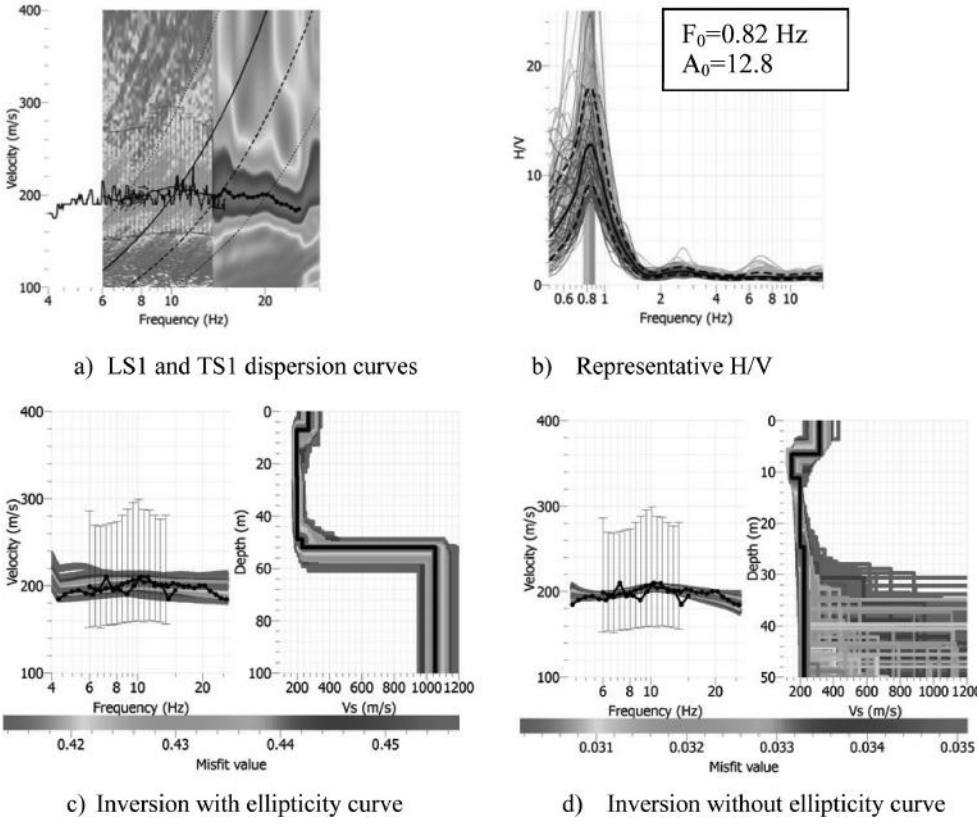

Figure 8. Results: Area S1, arrays LS1 and TS1.

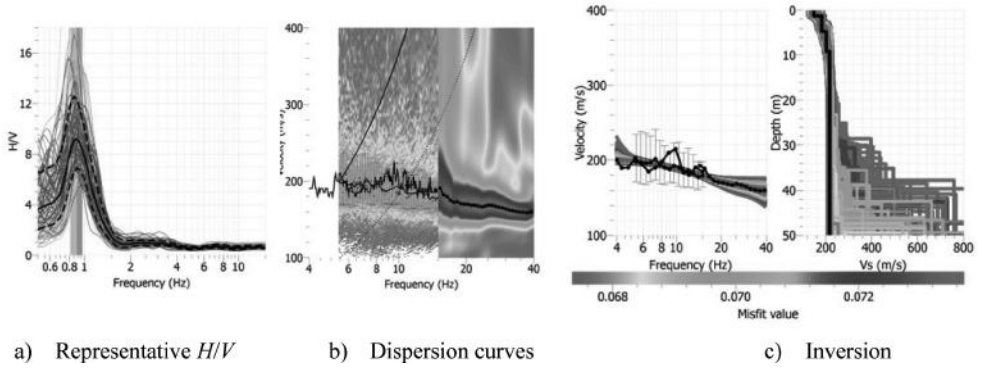

Figure 9. Results: Area S1, arrays LS2 and TS2.

Two kinds of inversion were performed to verify the acquired data. Figure 8c displays an inversion using the dispersion curves presented in Figure 8a and the ellipticity curve associated to Figure 8b. With this combination, an apparent reliable profile down to ~50 m is obtained, but it is clear that this inversion does not fit the empirical information below 6 Hz. Indeed, the inversion algorithm favors the fundamental period fitting by placing the bedrock at approximately 50 m deep to satisfy the ellipticity curve's amplitude and peak. This inversion cannot be considered reliable in the authors' opinion. To obtain a more reliable profile, the ellipticity curve was removed and the inversion procedure was repeated. A result of this combination is displayed on Figure 8d. It is evident in this figure that the dispersion curve provides reliable information only down to ~25 m; below this depth, the inversion is highly uncertain. Indeed, there are infinite combinations of shear wave velocity and depth below this level that could provide exactly the same fundamental period. Table 1 displays the shear wave profile adopted for this zone based on the inversion displayed in Figure 8d.

Finally, Figure 9 displays the results obtained using arrays LS2 and TS2. In this case, active experiments were not well defined between 15 and 20 Hz approximately (Figure 9b). The minimum frequency properly explored with TS2 was 5 Hz, while the application of the MASW Roadside technique to LS2 array provides information down to 4 Hz. Application of Nakamura's techniques indicates a resonance frequency of 0.89 Hz with an amplitude of 9.9. Similar to the previous case, including the ellipticy curve in the inversion procedure enforces a high impedance contrast close to 50 m depth which cannot be considered reliable. For this reason, Figure 9c displays the inversion obtained using only dispersion curves. The inversion produces a very homogenous profile with a V_s value close to 200 m/s down to 25 m depth. Below this level, the inversion is highly uncertain. The adopted profile is displayed on Table 1.

3 LIQUEFACTION POTENTIAL ASSESSMENT

Shear-wave velocity (V_s) offers a mean to evaluate liquefaction potential using a fundamental soil property. In this study, the procedure proposed by Kayen et al. (2013) was used for this purpose, considering that M_w = 8.8 and $a_{max} \approx 0.4$ g, and assuming a saturated density of 1.9 tonf/m^3 for the sandy soils (fine contents less than 5%). The results from Table 1 show that the average shear wave velocity of the upper 12 m ($V_{s,12}$ in the Kayen et al. (2013) procedure) is 155 m/s for Area N1, and 219 m/s for Area S1, which gives rather high Cyclic Stress Ratios (*CSR* values) ranging from 0.29 to 0.55 for Area N1, and from 0.40 to 0.55 for Area S1, for the explored depths. As Figures 10 and 11 show, the associated probabilities of liquefaction are, for Area N1, essentially 1.00 down to a depth of 20 m, and, for Area S1, larger than 0.8 for depths between 5 m and 30 m, which is consistent with the observed occurrence of liquefaction at these sites. More detailed analyses will be performed in a following phase of this project, using the results from SPTs, CPTs, cyclic triaxial, and resonant column tests.

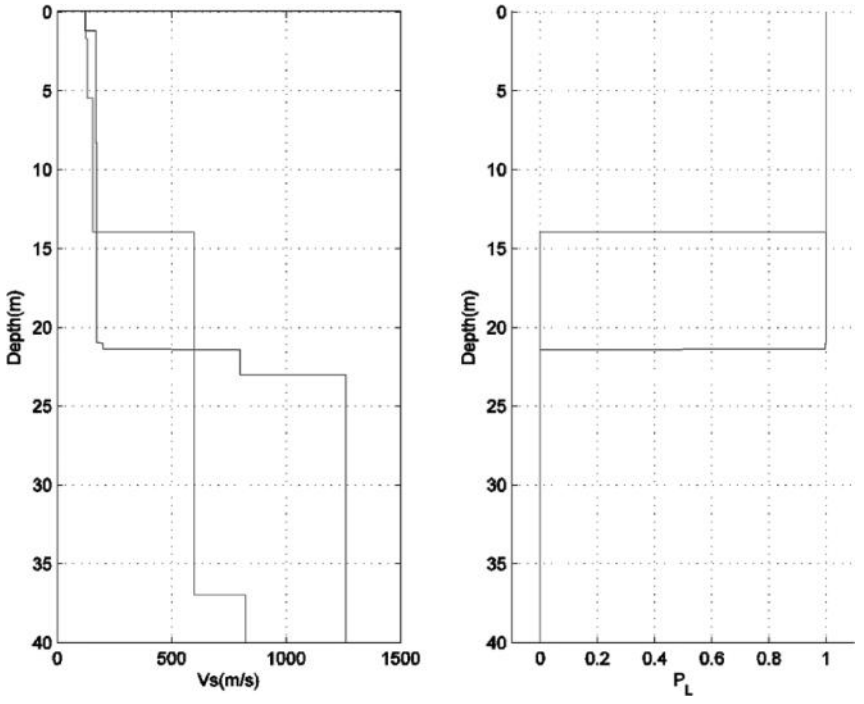

Figure 10. Shear-wave velocity profiles (left) and associated probabilities of liquefaction (right) for area N1.

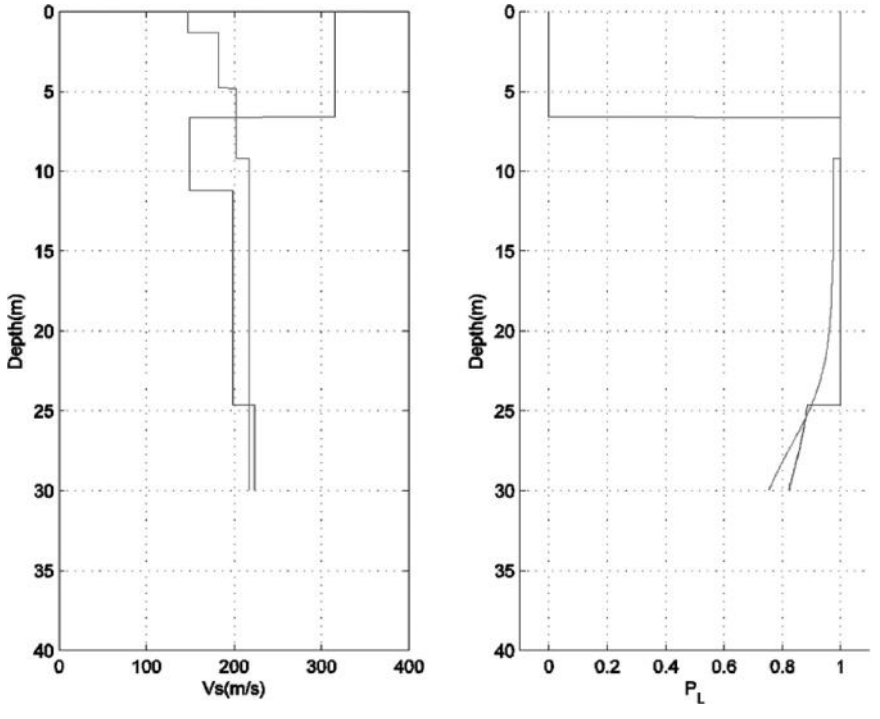

Figure 11. Shear-wave velocity profiles (left) and associated probabilities of liquefaction (right) for area S1.

4 CONCLUSIONS

A surface-wave based geophysical survey was conducted in a port where significant lateral spreading was observed during the 2010 Mw 8.8 Chile earthquake. An approximately uniform soil profile, with an average shear wave velocity of about 210 m/s, was determined using Rayleigh's wave dispersive properties and fundamental period estimation. A variable bedrock depth was also detected based on the application of Nakamura's technique. The collected data was analyzed using the liquefaction potential methodology proposed by Kayen et al. (2013), obtaining a probability of liquefaction essentially equal to one, which is consistent with the observed occurrence of liquefaction at these sites. It can be concluded that the application of a geophysical-based methodology was good enough to anticipate the liquefaction occurrence in this case. This initial geophysical survey will be complemented with *in-situ* and laboratory tests in future stages of this research to derive correlations between non-invasive geophysical survey results and invasive geotechnical exploration data.

ACKNOWLEDGEMENTS

Support for this work was provided by the Comisión Nacional de Investigación Científica y Tecnológica de Chile (CONICYT) under Award No. USA2012–0007. The authors would like to thank Mr. Francisco Echeverria, Technical Department Head of Puerto de Coronel, for all the valuable information and help on the field work. Any opinions, findings, conclusions and/or recommendations expressed in this material are those of the authors.

REFERENCES

Bonnefoy-Claudet, S., Baize, S., Bonilla, L., Berge-Thierry, C., Pasten, C., Campos, J., Volant, P. & Verdugo, R. 2008. Site effect evaluation in the basin of Santiago de Chile using ambient noise measurements. *Geophysical Journal International* 176: 925–937.

Bray, J.D., Rollins, K., Hutchinson, T., Verdugo, R., Ledezma, C., Mylonakis, G., Assimaki, A., Montalva, G., Arduino, P., Olson, S.M., Kayen, R., Hashash, Y.M.A. & Candia, G. 2012. Effects of Ground Failure on Buildings, Ports, and Industrial Facilities. *Earthquake Spectra*, Vol. 28, No. S1, pp. S97–S118.

Brunet, S. 2012. Comportamiento Sísmico de Estructuras de Puerto. *M.Sc. thesis*, Pontificia Universidad Católica de Chile (in Spanish).

Foti, S. 2000. Multistation Methods for Geotechnical Characterization using Surface Waves. *Ph.D. thesis*, Politecnico di Torino.

Geometrics Inc. 2005–2006. *SeisImager/SWTM Manual* Version 2.2.

Kayen, R., Moss, R., Thompson, E., Seed, R., Cetin, K., Kiureghian, A., Tanaka, Y. & Tokimatsu, K. 2013. Shear-Wave Velocity–Based Probabilistic and Deterministic Assessment of Seismic Soil Liquefaction Potential. *J. Geotech. Geoenviron. Eng.*, 139(3), 407–419.

Nakamura Y. 1989. A method for dynamic characteristics estimation of subsurface using microtremor on the ground surface. *Q. Rept. Railway Tech. Res. Inst.,* 30, 25–33.

Nazarian, S. & Stokoe II, K.H. 1984. In situ shear wave velocities from spectral analysis of surface waves. In: *Proc. 8th Conf. on Earthquake Eng*. (pp. 31–38). San Francisco: Prentice-Hall.

Okada, H. 2003. The Microtremor Survey Method. *Geophysical Monographs Series*, no.12. Society of Exploration Geophysicists.

Park, C., Miller, R. & Xia, J. 1999. Multichannel analysis of surface waves. *Geophysics* 64: 800–808.

Sambridge, M. 2001. Geophysical inversion with neighborhood algorithm—I. Searching the parameter space. *International Geophysical Journal* 138: 479–494.

Sanchez-Salinero, I. 1987. Analytical investigation of seismic methods used for engineering applications. *Ph.D. dissertation*, University of Texas at Austin.

Tokimatsu, K. 1997. Geotechnical site characterization using surface waves. In: Ishihara (Ed.) Balkema. *Proc. 1st Intl. Conf. Earthquake Geotechnical Engineering*. 1333–1368.

Wathelet, M. 2008. An improved neighborhood algorithm: Parameter conditions and dynamic scaling. *Geophysical Research Letters* 35: L09301.

Wathelet, M. 2002–2011. *GEOPSY packages (Version 2.5.0)* [software]: retrieved from http://www.geopsy.org/download.php.

Liquefaction triggering

This page intentionally left blank

Soil Liquefaction during Recent Large-Scale Earthquakes – Orense, Towhata & Chouw (Eds)

The influence of near-fault motions on liquefaction triggering during the Canterbury Earthquake Sequence

L. Carter & R. Green
Department of Civil and Environmental Engineering, Virginia Tech, Blacksburg, Virginia, USA

B. Bradley & M. Cubrinovski
Department of Civil and Natural Resources Engineering, University of Canterbury, Christchurch, New Zealand

ABSTRACT: The objective of this study is to examine the influence of near-fault motions on liquefaction triggering in Christchurch and neighboring towns during the 2010–2011 Canterbury Earthquake Sequence (CES). The CES began with the 4 September 2010, M_w7.1 Darfield earthquake and included up to ten events that triggered liquefaction. However, most notably, widespread liquefaction was induced by the Darfield earthquake and the M_w6.2, 22 February 2011 Christchurch earthquake. Of particular relevance to this study is the forward directivity effects that were prevalent in the motions recorded during the Darfield earthquake, and to a much lesser extent, during the Christchurch earthquake. A 2D variant of the Richart-Newmark fatigue theory was used to compute the equivalent number of cycles (n_{eq}) for the ground motions, where volumetric strain was used as the damage metric. This study is unique because it considers the contribution and phasing of both the fault-normal and fault-parallel components of motion on n_{eq} and the Magnitude Scaling Factor (*MSF*). It was found that when the fault-normal and fault-parallel motions were treated individually, the former yielded a lower n_{eq} than the latter. Additionally, when the combined effects of fault-normal and fault-parallel components were considered, it was found that the *MSF* were higher than those commonly used. This implies that motions containing near-fault effects are less demanding on the soil than motions that do not. This may be one of several factors that resulted in less severe liquefaction occurring during the Darfield earthquake than the Christchurch earthquake.

1 INTRODUCTION

The objective of the study presented herein is to examine the influence, if any, of near-fault ground motion effects on liquefaction triggering in Christchurch, New Zealand, and neighboring towns during the 2010–2011 Canterbury Earthquake Sequence (CES). The Christchurch area experienced widespread liquefaction as a result of the CES. However, of the 10 events in the CES that are known to have caused liquefaction, the 4 September 2010, M_w 7.1 Darfield and 22 February 2011, M_w 6.2 Christchurch earthquakes were the most significant (Figure 1). Of particular relevance to this study is the forward directivity effects, a near-fault phenomenon, that were prevalent in the ground motions recorded during the Darfield earthquake, and to a much lesser extent, during the Christchurch earthquake (e.g., Bradley and Cubrinovski, 2011; Bradley, 2012a,b; Shahi and Baker, 2012). Forward directivity is a Doppler-type phenomenon resulting from the approximate equality of the fault rupture and shear wave velocities and can result in a double-sided velocity pulse in the fault-normal component of motion. The strike slip rupture mechanism of the Darfield earthquake and the orientation of the causative fault relative to Christchurch resulted in forward directivity effects to manifest throughout much of the city. In contrast, the predominantly reverse rupture mechanism

of the Christchurch earthquake and the causative fault orientation only resulted in forward directivity effects in areas south of the city along the Port Hills. Several studies have examined the detrimental effects of near-fault motions on building structures (e.g., Hall et al., 1995; Alavi and Krawinkler, 2001; and Luco and Cornell, 2007), but relatively little attention has been given to near-fault effects on liquefaction, hence the objective of this study.

The present study differs from previous ones that examined the influence of directivity on liquefaction triggering (e.g., Green et al., 2008) because it considers the contribution and phasing of both the fault-normal and fault-parallel components of motion on the equivalent number of uniform cycles (n_{eq}) and corresponding Magnitude Scaling Factors (MSF). Towards this end, a variant of the macro cumulative damage fatigue theory proposed by Richart and Newmark (1948) (i.e., R-N fatigue theory) was used to compute n_{eq} for the earthquake motions, wherein volumetric strain was used as the damage metric. The R-N fatigue theory was extended to two-dimensional (2D) motions using numerical element tests, where the response of a finite element subjected to the 2D motions was defined by the reduced-order bounding-surface hypoplasticity constitutive model proposed by Li et al. (1992). The constitutive model was calibrated using published seismic compression data from strain-controlled cyclic simple shear tests performed on dry sand samples (Stewart et al., 2004; Duku et al., 2008).

In total, ten sets of fault-normal and fault-parallel components of near-fault motions recorded on rock (V_{S30} > 600 m/s) were selected, with one of the sets being recorded during the CES. These motions were used as rock outcrop input motions in equivalent linear site response analyses, and shear strain time histories were computed at a reference depth that is approximately the modal depth to the center of the critical layers determined from the liquefaction case history database. These strain time histories were the motions used in conjunction with the R-N fatigue theory discussed above to compute n_{eq}. The resulting n_{eq} values were then used to compute near-fault MSF, which were compared with those used in simplified liquefaction evaluations (i.e., Youd et al., 2001) and do not account for near-fault effects.

In the following, an overview of the selection of ground motions and site response analyses is presented, followed by an outline of the 2D variant of the R-N fatigue theory used to compute the neq for the near-fault and reference Mw7.5 motions. Finally, trends in the

Figure 1. Aerial image of Christchurch and neighboring towns. The areas bounded in red liquefied during the 4 September 2010, M_w7.1 Darfield earthquake and the areas highlighted in yellow liquefied during the 22 February 2011, M_w6.2 Christchurch earthquake.

computed n_{eq} and MSF for the near-fault motions are discussed and compared to the conventional relationships for n_{eq} and MSF.

2 SELECTION OF "NEAR-FAULT" MOTIONS

As stated above, ten sets of fault-normal and fault-parallel near-fault rock motions ($V_{S30} > 600$ m/s) were used in this study; Table 1 lists the selected near-fault motions. Nine of the ten motions were taken from the NGA 1 database and one from a collection of near-fault CES motions (NGA Sequence number 6928). Other near-fault motions recording during the CES were not used in this study because the site conditions of the recording stations were other than rock. All the selected motion sets are considered to have forward directivity effects, manifested as "pulse-like" behavior in the fault-normal component, identified by Shahi and Baker (2012), and no observable velocity pulse in the fault-parallel component, consistent with the forward directivity phenomenon.

3 SITE RESPONSE ANALYSES

A series of site response analyses were performed using the selected sets of "near-fault" motions listed in Table 1. As shown in Figure 2, the profile assumes a constant soil unit weight of 18.9 kN/m^3 (≈ 120 pcf), a ground water table depth of 1.5 meters, and shear wave velocities, V_S, that increase exponentially with depth given by the following equation:

$$V_S(z) = (V_S)_{z_{ref}} \left(\frac{z}{z_{ref}} \right)^{0.15} \tag{1}$$

where: $(V_S)_{Zref}$ is the shear wave velocity at the reference depth (z_{ref}) of 4 m; and z is depth from the ground surface in the same units as z_{ref}; and the power of 0.15 is typical for sand profiles (e.g., Lee, 2009). $(V_S)_{Zref}$ was estimated using the correlation proposed Andrus et al. (2004):

$$(V_S)_{z_{ref}} = 87.8 \cdot N_{1,60}{}^{0.253} \left(\frac{Pa}{\sigma'_v} \right)^{-0.25} \tag{2}$$

where: $(V_S)_{Zref}$ is in m/s; $N_{1,60}$ is the Standard Penetration Test (SPT) blow count normalized/corrected to 1 atm of vertical effective confining stress and 60% hammer energy efficiency;

Table 1. Near-fault motions.

NGA sequence no.	Event	Year	Station	Mw	Distance* (km)
77	San Fernando	1971	Pacoima Dam (upper left abut)	6.61	1.81
150	Coyote Lake	1979	Gilroy Array #6	5.74	3.11
459	Morgan Hill	1984	Gilroy Array #6	6.19	9.86
828	Cape Mendocino	1992	Petrolia	7.01	8.18
879	Landers	1992	Lucerne	7.28	2.19
1013	Northridge – 01	1994	LA Dam	6.69	5.92
1051	Northridge – 01	1994	Pacoima Dam (upper left)	6.69	7.01
1511	Chi-Chi, Taiwan	1999	TCU076	7.62	2.76
1529	Chi-Chi, Taiwan	1999	TCU102	7.62	1.51
6928	Darfield, New Zealand	2010	LPCC	7.10	22.4

*Closest distance to ruptured area on fault.

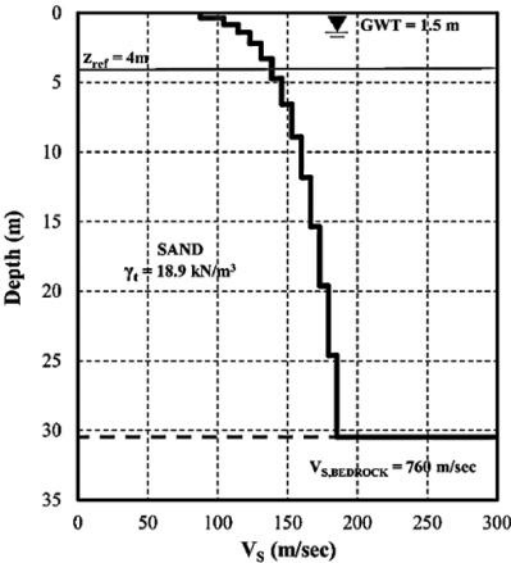

Figure 2. Shear wave velocity profile used in the site response analyses.

P_a is atmospheric pressure; and σ'_v is the vertical effective stress at z_{ref} in the same units as P_a. In using Eqn 2, $N_{1,60}$ was assumed to be 12 blows/0.3 m (or 12 blows/ft), which is approximately the modal blow count for the liquefaction case histories listed in Cetin's (2000) database, consistent with assuming z_{ref} = 4 m, which is approximately the modal depth to the center of the critical layers in Cetin's (2000) liquefaction case history database.

To ensure consistency of the degraded shear wave velocity profiles used in the site response analyses for a given set of near fault motions, the analyses were performed in two stages. In the first stage, site response analyses were performed treating each component in the set individually (i.e., for each analysis the shear wave velocities were allowed to degrade in accord with the shear strains induced in the profile for that motion). Next, the two degraded shear wave velocity profiles for a given set of near-fault motions were compared, and the profile that had the overall lowest degraded velocities was used in the second stage of site response analyses. In these latter analyses, the shear wave velocities and damping ratios were set to those determined from the first stage and were not allowed to degrade, and the shear strain time histories were computed at a reference depth, z_{ref}, of 4 meters for both fault-normal and fault-parallel components of motions. As outlined in the next section, these time histories were then used in conjunction with the R-N fatigue theory to compute n_{eq}.

4 EQUIVALENT NUMBER OF UNIFORM CYCLES

The concept of converting a random load to an equivalently damaging number of sinusoidal cycles has its roots in metal fatigue theory. One of the earliest approaches was proposed by Palmgren (1924) and further developed by Miner (1945), with the approach commonly referred to as the Palmgren-Miner (P-M) fatigue theory. In the late 1960's to early 1970's, Professor H.B. Seed and colleagues adopted Miner's implementation procedure for the P-M theory, with slight modifications, to compute n_{eq} for evaluating the liquefaction triggering in soil (e.g., Seed et al., 1975a and Annaki and Lee, 1977). The Seed et al. variant of the P-M theory is still commonly used in geotechnical earthquake engineering studies today (e.g., Liu et al., 2001). However, several significant shortcomings of this procedure have been identified by Green and Terri (2005) and Green and Lee (2006), among others. Namely, the P-M theory, as adopted by Seed et al., applies to high cycle fatigue, which is characterized by a large number of load cycles (thousands to millions) wherein the material being loaded

remains in the elastic range. As a corollary, the Seed et al. variant of the P-M theory fails to account for the absolute amplitude and sequencing of peaks in earthquake-induced ground motions, both of which are known to significantly influence excess pore pressure generation in saturated sands subjected to cyclic motions (Martin et al., 1975; Ishihara and Yasuda, 1973; Ishihara and Nagase, 1988).

As a result of the above limitations of the P-M theory, Green and Lee (2006) proposed the use of the R-N fatigue theory (Richart and Newmark, 1948) for computing n_{eq} for evaluating seismic compression in dry and partially saturated sands. The R-N theory can be applied to high and low cycle fatigue analyses, where the latter is characterized by a few load cycles (one to hundreds) and plastic deformations in the material being loaded (consistent with earthquake induced liquefaction). Furthermore, the R-N theory can account for both the absolute amplitude and sequencing of peaks in earthquake ground motions. As outlined in Green and Lee (2006), the Martin et al. (1975) procedure, and the Byrne (1991) simplified variant thereof, for computing volumetric strains in freely draining soils subjected to earthquake motions is an alternative form of the R-N fatigue theory. It is the Byrne (1991) formulation of the R-N theory that was adopted in this study, wherein volumetric strain is used as the damage metric to compute n_{eq} for strain time histories obtained from the site response analyses.

4.1 *Volumetric strain model & equivalent number of cycles—one-directional loading*

The incremental volumetric strain induced in freely draining soil by each peak (or half cycle) in a shear strain time history is computed, per Byrne (1991), using the following relation:

$$\left(\Delta\varepsilon_v\right)_i = 0.5\left(\left|\gamma_i\right| - \gamma_{thresh}\right) C_1 \exp\left(-C_2 \cdot \frac{\left(\varepsilon_v\right)_i}{\left(\left|\gamma_i\right| - \gamma_{thresh}\right)}\right) \tag{3}$$

where $(\Delta\varepsilon_v)_i$ is the incremental volumetric strain induced by the i^{th} peak in the shear strain time history; γ_i is the amplitude of the i^{th} peak in the shear strain time history; γ_{thresh} is the threshold shear strain below which no volumetric strain will occur (taken as 0.01% in this study); $(\varepsilon_v)_i$ is the cumulative volumetric strain before the i^{th} peak in the shear strain time history is applied; and C_1 and C_2 are the material parameters. Assuming $(\varepsilon_v)_i = 0$ for $i = 1$, the cumulative volumetric strain is incrementally computed by summing the incremental volumetric strain induced by successive peaks in the shear strain time history from the beginning to the end (i.e., for $i = 1$ to n, where n is the total number of peaks in the shear strain time history):

$$\left(\varepsilon_v\right)_{i+1} = \left(\varepsilon_v\right)_i + \left(\Delta\varepsilon_v\right)_i \tag{4}$$

Byrne (1991) proposed the following generic relations for C_1 and C_2 for sands:

$$C_1 = 7600 \cdot D_r^{-2.5} \tag{5a}$$

$$C_2 = \frac{0.4}{C_1} \tag{5b}$$

where D_r is the relative density of the soil in percent.

The Byrne model is used to compute n_{eq} for a random load by equating the cumulative volumetric strains induced by the random load to that induced by n_{eq} of a sinusoidal load. In geotechnical engineering applications, the amplitude of the sinusoidal load is traditionally set equal to 0.65 times the absolute value of the maximum amplitude pulse in the earthquake motion (e.g., Seed et al., 1975a).

Inherent to the above approach is the assumption that volumetric strain in dry sand is a valid damage metric for computing n_{eq} for use in liquefaction evaluations. At first glance, excess pore pressure ratio (r_u) would be a seemingly more applicable damage metric for computing

n_{eq} for liquefaction evaluations. However, a limitation of r_u is that it has the potential to reach a limiting value (i.e., $r_u = 1$) prior to the end of shaking, beyond which point subsequent motions do not contribute to the computed n_{eq}. As a result, several investigators have scaled the amplitude of the ground motions so that $r_u = 1$ at the end of shaking (e.g., Ishihara and Nagase, 1988; Wer-Asturias, 1982). However, as mentioned previously, the absolute amplitude of the pulses in a ground motion are known to influence the liquefaction response of soil (e.g., Ishihara and Yasuda, 1974), and as a result, scaling of the ground motion amplitude is not desirable. Using the volumetric strain of dry sand as the damage metric avoids the ground motion scaling issue, and as discussed in Martin et al. (1975) and Byrne (1991) relates to excess pore pressure response in saturated sands.

4.1.1 *Model calibration*

Although Byrne (1991) provides generic relations for estimating the material parameters C_1 and C_2 (i.e. Eqn 5), for this study, C_1 was determined using published seismic compression data from strain-controlled cyclic simple shear tests performed on dry sand (Stewart et al., 2004). Eqn 5b was then used to determine C_2. Specifically, C_1 was calibrated to the volumetric strains induced in dry Silica #2 sand samples having $D_r = 45\%$ and subjected to 15 cycles of loading, for a range of shear strain amplitudes. However, the data from Stewart et al (2004) were based on tests conducted having an effective overburden pressure of 1 atm (~101.3 kPa), which differs from the vertical effective stress ($\sigma'_{v,z_{ref}}$) at the reference depth used in this study (i.e., z_{ref}; Figure 2). Accordingly, before C_1 was determined, the volumetric strains from Stewart et al. (2004) were adjusted to $\sigma'_{v,z_{ref}}$ by applying the overburden correction factor ($K_{\sigma,\varepsilon}$) proposed by Duku et al. (2008):

$$K_{\sigma,\varepsilon} = \left(\frac{\sigma'_v, z_{ref}}{P_a} \right)^{-0.29} \tag{6}$$

$$\left(\varepsilon_v\right)_{\sigma'_v, z_{ref}} = \left(\varepsilon_v\right)_{1atm} \cdot K_{\sigma,\varepsilon} \tag{7}$$

where: $(\varepsilon_v)_{\sigma'_v, z_{ref}}$ is volumetric strain corrected to $\sigma'_{v,z_{ref}}$, and $(\varepsilon_v)_{1\ atm}$ is the volumetric strain obtained from the cyclic simple shear tests performed using a vertical effective confining stress of 1 *atm*. C_1 was determined to be 0.51 and C_2 was computed to be 0.78. Figure 3 shows a comparison between the Byrne model predictions and $\left(\varepsilon_v\right)_{\sigma' v, z_{ref}}$.

4.2 *Volumetric strain model & equivalent number of cycles—multi-directional loading*

A limitation of the R-N fatigue theory, and hence a limitation of the Byrne model, is that it was developed for one-dimensional (1D) loading. However, both horizontal components of earthquake shaking contribute to the breakdown of the soil skeleton and commensurate

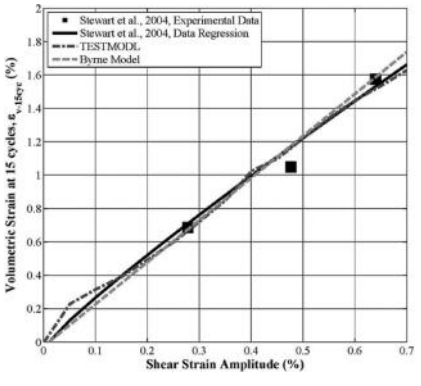

Figure 3. Model predictions and Stewart et al. (2004) test data.

triggering of liquefaction in saturated sands. In previous studies, the multi-directional loading commonly has been accounted for subsequent to the computation of n_{eq}, e.g., increasing the estimated volumetric strain caused by n_{eq} cycles of loading (Pyke et al., 1975) or reducing the cyclic resistance required to trigger liquefaction in n_{eq} cycles of 1D loading (e.g., Seed et al., 1975b). This approach is better suited for situations where the characteristics of the two horizontal components of motion are similar, or at least do not differ significantly. On the contrary, the fault-normal and fault-parallel components of near-fault motions have very different characteristics, as discussed previously. Accordingly, the authors opted to extend the R-N fatigue theory to 2D using numerical element tests, where the volumetric strain response of a finite element subjected to the 2D motions was defined by the reduced-order bounding-surface hypoplasticity constitutive model proposed by Li et al. (1992). The numerical element tests were performed using the utility program, TESTMODL, that is part of the multi-directional site response finite element code SUMDES (Li et al., 1992).

4.2.1 *TESTMODL*

The reduced-order bounding-surface hypoplasticity constitutive model proposed by Li et al. (1992) is built into TESTMODL and can be used to predict the non-linear, inelastic behavior of a soil specimen under a variety of multi-directional loading conditions. TESTMODL can apply the general six component loading paths (three normal and three shear), where loads can be either stress- or strain-controlled, and the soil element can be modeled as either drained or un-drained. Following the coordinate convention shown in Figure 4, a single horizontal component of motion (e.g., fault-normal or fault-parallel) can be applied in either *13 or *23 directions as a shear strain-time history to compute the vertical strain in the *33 direction. To simulate a horizontal soil profile of infinite lateral extent, strains in the *11 and *22 directions can be forced to be zero. Thus, the vertical strain in the *33 direction is equal to the volumetric strain in the element. The volumetric strain in the soil element resulting from being subjected to a set of motions individually in the *13 or *23 direction, not simultaneously, are referred to herein as $(\varepsilon_{v,1D\text{-}X})_{TESTMODL}$ and $(\varepsilon_{v,1D\text{-}Y})_{TESTMODL}$, while the volumetric strain resulting from the simultaneous application of a set of fault-normal and fault-parallel motions in the *13 and *23 directions are denoted as $(\varepsilon_{v,2D})_{TESTMODL}$.

4.2.2 *Model calibration*

The reduced-order bounding-surface hypoplasticity constitutive model in TESTMODL was calibrated using the shear modulus and damping degradation curves proposed by Ishibashi and Zhang (1993) in conjunction with the seismic compression data mentioned above (Stewart et al., 2004). Figure 3 shows a comparison between the TESTMODL model predictions and $\left(\varepsilon_v\right)_{\sigma'v,z_{ref}}$.

4.2.3 *n_{eq} for multi-directional loading*

As stated above, TESTMODL was used to compute the volumetric strains induced in a soil element subjected to the fault-normal and fault-parallel components of motion, individually

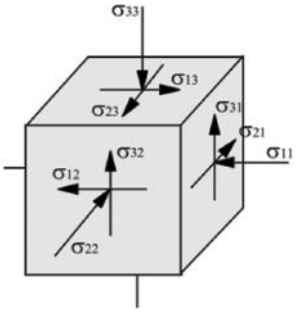

Figure 4. TESTMODL coordinate convention.

and simultaneously, resulting in $(\varepsilon_{v,1D\text{-}X})_{TESTMODL}$, $(\varepsilon_{v,1D\text{-}Y})_{TESTMODL}$, and $(\varepsilon_{v,2D})_{TESTMODL}$ for each set of near-fault motions. To ensure consistency with previous studies that used the Byrne (1991) model to compute n_{eq} for 1D loading (e.g., Green and Lee, 2006; Lee, 2009), the following relation was used to obtain volumetric strains for computing the number of equivalent cycles for 2D loading ($n_{eq,2D}$):

$$\varepsilon_{v,2D} = \left[\frac{\left(\varepsilon_{v,2D}\right)_{TESTMODL}}{\left(\varepsilon_{v,1D-X}\right)_{TESTMODL} + \left(\varepsilon_{v,1D-Y}\right)_{TESTMODL}}\right] \times \left[\left(\varepsilon_{v,1D-X}\right)_{Byrene} + \left(\varepsilon_{v,1D-Y}\right)_{Byrne}\right] \tag{8}$$

where: $(\varepsilon_{v,1D\text{-}X})_{Byrne}$ and $(\varepsilon_{v,1D\text{-}Y})_{Byrne}$ are volumetric strains computed using the Byrne model for the fault-normal and fault-parallel components of motion individually, not simultaneously.

The Byrne model was used to compute $n_{eq,2D}$, which is the number of cycles of a 1D sinusoidal load required to induce $\varepsilon_{v,2D}$ in the soil, where the amplitude of the sinusoidal load (γ_{eff}) was 0.65 times the geometric mean of the peak shear strains in the fault-normal and fault-parallel motions (i.e., $\gamma_{max,X}$ and $\gamma_{max,Y}$):

$$\gamma_{eff} = 0.65\sqrt{\gamma_{\max,X} \cdot \gamma_{\max,Y}} \tag{9}$$

Figure 5 shows the resulting number of equivalent cycles for the fault-parallel and fault-normal components of motion computed individually ($n_{eq\gamma,1D}$) and simultaneously ($n_{eq\gamma,2D}$). Also shown in this figure is the number of equivalent cycles correlation developed by Seed et al. (1975a), wherein the motions (non near-fault) were treated individually.

From Figure 5, it can be seen the fault-parallel component tends to yield a greater $n_{eq\gamma,1D}$ than its respective fault-normal counterpart. Because n_{eq} and significant duration of a motion are related (e.g., Green and Terri, 2005), this phenomenon can be explained by the relationship between duration and rupture directivity noted in previous studies (e.g., Somerville et al., 1997; Green et al., 2008). That is, due to the way the near-fault effects manifest in the ground motions, the fault-normal component tends to have a shorter significant duration than the fault-parallel component.

Also from Figure 5, it may be observed that the $n_{eq\gamma,1D}$ values for this study plot below the mean of the Seed et al. (1975a) regression. This is likely due to the site-to-source distances of the motions used in the two studies. Seed et al. (1975a) used non near-fault motions (i.e., motions that are further from the fault rupture), while the study presented herein is focusing on near-fault motions. As shown in Lee (2009), the number of equivalent cycles tends to

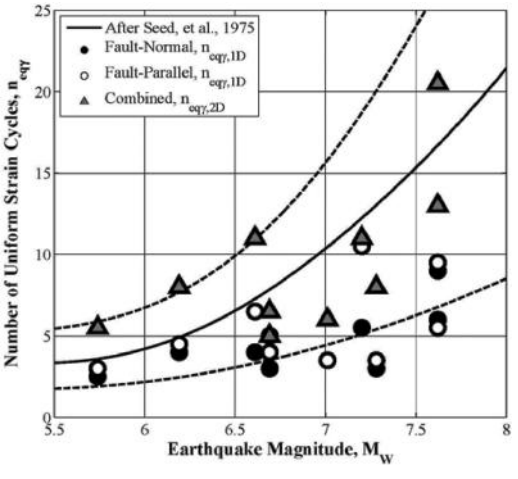

Figure 5. Number of equivalent strain cycles for near-fault 1D and 2D loading conditions.

increase with increased site-to-source distance. Finally, as expected, the $n_{eq,2D}$ values are generally greater than the $n_{eq,1D}$ values, with the average ratio of $n_{eq,2D}/n_{eq,1D}$ for the fault-normal and fault-parallel components being 2.2 and 1.7, respectively.

5 MAGNITUDE SCALING FACTORS FOR MULTI-DIMENSIONAL SHAKING

To assess the influence of near-fault motions on liquefaction triggering, $n_{eq,2D}$ values were used to compute MSF for the motions. As shown in Idriss (1997) and Green (2001), n_{eq} and MSF are related by:

$$MSF = \left(\frac{n_{eq,M7.5}}{n_{eq}} \right)^m \tag{10}$$

where $n_{eq,M7.5}$ is the number of cycles for a reference earthquake magnitude of 7.5, traditionally taken as 15 cycles (Seed and Idriss, 1982), and m is the negative of the slope of a log-log plot of Cyclic Stress Ratio (CSR) versus number of cycles to liquefaction for a soil having a given relative density and confined at a given effective stress. For the study presented herein, m was set equal to 0.35, which falls within the range of published values and is approximately equal to that determine by Yoshimi et al. (1984) from cyclic triaxial tests performed on high-quality, undisturbed samples obtained by frozen sampling.

As mentioned above, $n_{eq,M7.5}$ is traditionally assumed to be 15 cycles. However, this value is for 1D loading (i.e., $n_{eq,M7.5\_1D}$). Accordingly, the approach outlined above to compute $n_{eq,2D}$ for near-fault motions was applied to sets of horizontal components of non near-fault rock motions (V_S > 600 m/s) recorded during earthquakes having M_w7.5 ± 0.3 and site-to-source distances less than 70 km. In total 14 sets of motions were used to compute $n_{eq,M7.5\_2D}$, all of them coming from the NGA 1 database, with the average $n_{eq,M7.5\_2D}$ equal to 23.0. Figure 6 depicts the number of equivalent cycles as a function of site to source distance for both horizontal components of motion of the reference magnitude 7.5 dataset computed individually ($n_{eq\gamma,1D}$) and simultaneously ($n_{eq\gamma,2D}$).

The resulting near-fault MSF that accounts for the contributions of both the fault-normal and fault-parallel components of motions (i.e., MSF_{2D}) is plotted in Figure 7. For reference, MSF_{2D} for non near-fault motions computed using the approach outlined in this study are also shown in this figure, as is the range of MSF recommended by Youd et al. (2001). As may be observed from this figure, the near-fault MSF_{2D} are generally higher than the non near-fault MSF_{2D} and the MSF recommended by Youd et al. (2001), implying that near-fault

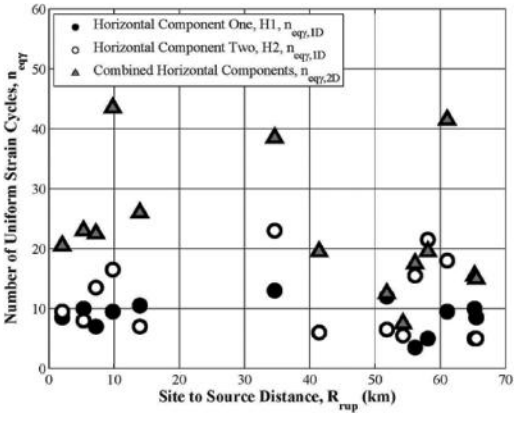

Figure 6. Number of equivalent strain cycles for reference M_w 7.5 1D and 2D loading conditions.

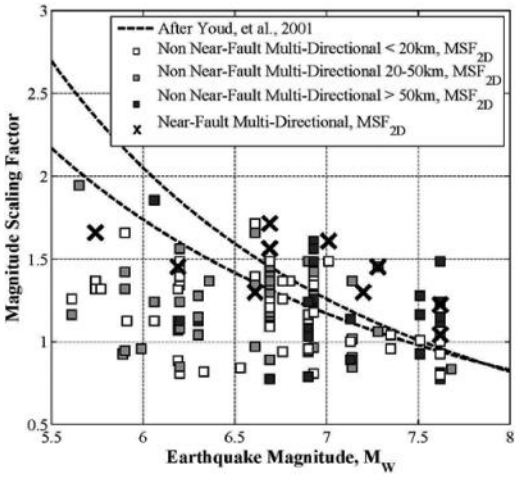

Figure 7. Magnitude scaling factor for near-fault and non near-fault for 2D loading.

motions are less demanding, from a liquefaction triggering perspective, than non near-fault motions having equal amplitudes. This may be one of several factors that resulted in less severe liquefaction occurring during the Darfield earthquake than the Christchurch earthquake (Figure 1).

6 CONCLUSION

Based on the analysis of the ten fault-normal and fault parallel near-fault ground motion sets, the influence of rupture (forward) directivity on liquefaction triggering was evaluated. Using a 1D variant of the R-N fatigue theory wherein volumetric strain was used as the damage metric, it was determined that the fault-normal components of motion (i.e. motions containing a pronounced velocity pulse) resulted in a lower number of uniform strain cycles than the fault-parallel counterpart. This finding is consistent with that of Green et al. (2008) who used a low cycle variant of the P-M fatigue theory to analyze near fault motions. To determine the combined influence of both the fault-normal and fault-parallel components, a 2D variant of the R-N fatigue theory was developed as part of this study, wherein volumetric strain was again used as the damage metric. To assess the influence on liquefaction triggering, MSF were computed for the combined near-fault components of motions and compared with ones developed for non near-fault motions that are commonly used in practice. The near-fault MSF were generally higher than both the non near-fault MSF commonly used in practice and computed as part of this study, implying that near-fault motions are less demanding, from a liquefaction triggering perspective, than non near-fault motions. This may be one of several factors that resulted in less severe liquefaction occurring during the Darfield earthquake than the Christchurch earthquake.

ACKNOWLEDGEMENTS

Primary support for the US authors was provided by the U.S. National Science Foundation (NSF) grants CMMI-1030564 and CMMI-1306261 and an NSF EAPSI Fellowship awarded to L. Carter. However, any opinions, findings, and conclusions or recommendations expressed in this material are those of the authors and do not necessarily reflect the views of the National Science Foundation.

REFERENCES

Alavi, B. and Krawinkler, H. 2001. Effects of Near-Fault Ground Motions on Framed Structures. *Blume Center Report 138*, Stanford, CA, USA.

Andrus, R.D., Piratheepan, P., Ellis, B.S., Zhang, J., and Juang, C.H. 2004. Comparing liquefaction evaluation methods using penetration-Vs relationships. *Soil Dynamics and Earthquake Engineering*, 24(9–10), 713–721.

Annaki, M. and Lee, K.L. 1977. Equivalent Uniform Cycle Concept for Soil Dynamics. *Journal of the Geotechnical Engineering Division*, ASCE, 103(GT6), 549–564.

Bradley, B.A. 2012a. Strong ground motion characteristics observed in the 4 September 2010 Darfield, New Zealand earthquake. *Soil Dynamics and Earthquake Engineering*, *42*, 32–46.

Bradley, B.A. 2012b. Observed Ground Motions in the 4 September 2010 Darfield and 22 February 2011 Christchurch Earthquakes. *Proc. 2012 New Zealand Society of Earthquake Engineering Conference* (2012 NZSEE), 13–15 April 2012, Christchurch, New Zealand, Paper No. 037.

Bradley, B.A. and Cubrinovski, M. 2011. Near-Source Strong Ground Motions Observed in the 22 February 2011 Christchurch Earthquake. *Bulletin of the New Zealand Society for Earthquake Engineering*, 44(4), 181–194.

Byrne, P.M. 1991. A cyclic shear-volume coupling and pore pressure model for sand. *Proc. 2nd International Conference on Recent Advances in Geotechnical Earthquake Engineering and Soil Dynamics*, Paper No. 1.24, St. Louis, Missouri.

Cetin, K.O. 2000. Reliability-Based Assessment of Seismic Soil Liquefaction Initiation Hazard. *PhD. Dissertation*. Department of Civil Engineering, University of California, Berkeley.

Duku, P.M., Stewart, J.P., Whang, D.H., and Yee, E. 2008. Volumetric strains of clean sands subject to cyclic loads. *Journal of Geotechnical and Geoenvironmental Engineering*, ASCE, 134(8), 1073–1085.

Green, R.A. 2001. Energy-Based Evaluation and Remediation of Liquefiable Soils. *Ph.D. Dissertation* (J.K. Mitchell, Advisor), Department of Civil and Environmental Engineering, Virginia Polytechnic Institute and State University (Virginia Tech), Blacksburg, VA, 397pp. http://scholar.lib.vt.edu/theses/available/etd-08132001–170900/.

Green, R.A. and Lee, J. 2006. Computation of Number of Equivalent Strain Cycles: A Theoretical Framework. *Geomechanics II: Testing, Modeling, and Simulation* (P.V. Lade and T. Nakai, eds.), ASCE Geotechnical Special Publication 156, 471–487.

Green, R.A. and Terri, G.A. 2005. Number of Equivalent Cycles Concept for Liquefaction Evaluations–Revisited. *Journal of Geotechnical and Geoenvironmental Engineering*, ASCE, 131(4), 477–488.

Green, R.A., Lee, J., White, T.M., and Baker, J.W. 2008. The significance of near-fault effects on liquefaction. *Proc. 14th World Conference on Earthquake Engineering*, Beijing, China.

Hall, J.F., Heaton, T.H., Halling, M.W., and Wald, D.J. 1995. Near-Source Ground Motions and Its Effects on Flexible Buildings. *Earthquake Spectra*, 11(4), 569–605.

Idriss, I.M. 1997. Evaluation of Liquefaction Potential and Consequences: Historical Perspective and Updated Procedures. *Presentation Notes: 3rd Short Course on Evaluation and Mitigation of Earthquake Induced Liquefaction Hazards*, 13–14 March 1997, San Francisco, CA, 16pp.

Ishibashi, I. and Zhang, X. 1993. Unified dynamic shear moduli and damping ratios of sand and clay. *Soils and Foundations*, 33(1), 182–191.

Ishihara, K. and Nagase, H. 1988. Multi-directional irregular loading tests on sand. *Soil Dynamics and Earthquake Engineering*, 7(4), 201–212.

Ishihara, K. and Yasuda, S. 1973. Sand Liquefaction Under Random Earthquake Loading Condition. *Proc. 5th World Conference on Earthquake Engineering*, Rome, Italy, 1, 329–338.

Joshi, V.A., Bradley, B.A. 2013. Empirical Analysis of Near-Fault Forward-Directivity Effects in the 2010–11 Canterbury Earthquakes. *Proc. 2012 New Zealand Society of Earthquake Engineering Conference* (2013 NZSEE), 26–28 April 2013, Wellington, New Zealand.

Lee, J., 2009. Engineering Characterization of Earthquake Ground Motions. *PhD. Dissertation*. Department of Civil Engineering, University of Michigan.

Li, X.S., Wang,Z.L., and Shen, C.K. 1992. *SUMDES: A Nonlinear Procedure for Response Analysis of Horizontally-layered Sites Subjuected to Multi-directional Earthquake Loading.* Department of Civil Engineering, University of California, Davis, 88p.

Liu, A.H., Stewart, J.P., Abrahamson, N.A., and Moriwaki, Y. 2001. Equivalent Number of Uniform Stress Cycles for Soil Liquefaction Analysis. *Journal of Geotechnical and Geoenvironmental Engineering*, ASCE, 127(12), 1017–1026.

Luco, N. and Cornell, C.A. 2007. Structure-Specific Scalar Intensity Measures for Near-Source and Ordinary Earthquake Ground Motions. *Earthquake Spectra*, 23(2), 357–392.

Martin, G.R., Finn, W.D.L., and Seed, H.B. 1975. Fundamentals of liquefaction under cyclic loading. *Journal of the Geotechnical Engineering Division*, ASCE, 101(GT5), 423–438.

Miner, M.A. 1945. Cumulative Damage in Fatigue. *Transactions*, ASME, 67, A159-A164.

Palmgren, A. 1924. Die Lebensdauer Von Kugella Geru. *ZVDI*, 68(14), 339–341.

Pyke, R., Seed, H.B., and Chan, C.K. 1975. Settlement of Sands Under Multidirectional Shaking. *Journal of the Geotechnical Engineering Division*, ASCE, 101(GT4), 379–398.

Richart, F.E. and Newmark, N.M. 1948. An Hypothesis for Determination of Cumulative Damage in Fatigue. *ASTM Proceedings*, 48, 767–800.

Seed, H.B. and Idriss, I.M. 1982. *Ground Motions and Soil Liquefaction During Earthquakes*, Earthquake Engineering Research Institute, Oakland, CA, USA.

Seed, H.B., Idriss, I.M., Makdisi, F., and Banerjee, N. 1975a. Representation of Irregular Stress Time Histories by Equivalent Uniform Stress Series in Liquefaction Analysis. *Report No. EERC 75-29*, Earthquake Engineering Research Center, College of Engineering, Univ. of California, Berkeley, California, United States.

Seed, H.B., Lee, K.L., Idriss, I.M., and Makdisi, F.I. 1975b. The Slides in the San Fernando Dams during the Earthquake of February 9, 1971. *Journal of the Geotechnical Engineering Division*, ASCE, 101(GT7), 651–688.

Shahi, S., Baker, J., 2012. November 1st, *2012 Pulse Classifications from NGA West2 database*, Stanford University, CA, http://www.stanford.edu/~bakerjw/pulse_classification_v2/Pulse-like-records.html.

Somerville, P.G., Smith, N.F., Graves, R.W., and Abrahamson, N.A. 1997. Modification of Empirical Strong Ground Motion Attenuation Relations to Include the Amplitude and Duration Effects of Rupture Directivity. *Seismological Research Letters*, 68(1), 199–222.

Stewart, J.P., Whang, D.H., Moyneur, M., and Duku, P.M. 2004. Seismic Compression of As-Compacted Fill Soils with Variable Levels of Fines Content and Fines Plasticity. *Earthquake Damage Assessment and Repair Project,* CUREE.

Tokimatsu, K., and Seed, H.B. 1987. Evaluation of settlement in sands due to earthquake shaking. *Journal of Geotechnical Engineering*, ASCE, 113(8), 861–878.

Wer-Asturias, R. 1982. The equivalent number of cycles of recorded accelerograms for soil liquefaction studies, *MS thesis*, Rensselaer Polytechnic Institute, Troy, N.Y.

Yoshimi, Y., Tokimatsu, K., Kaneko, O., and Makihara, Y. 1984. Undrained Cyclic Shear Strength of a Dense Niigata Sand. *Soils and Foundations*, 24(4), 131–145.

Youd, T.L., Idriss, I.M., Andrus, R.D., Arango, I., Castro, G., Christian, J.T., Dobry, R. Finn, W.D.L., Harder, L.F., Hynes, M.E., Ishihara, K., Koester, J.P., Liao, S.S.C., Marcuson III, W.F., Martin, G.R., Mitchell, J.K., Moriwaki, Y., Power, M.S., Robertson, P.K., Seed, R.B., and Stokoe II, K.H. 2001. Liquefaction Resistance of Soils: Summary Report from the 1996 NCEER and 1998 NCEER/NSF Workshops on Evaluation of Liquefaction Resistance of Soils. *Journal of Geotechnical and Geoenvironmental Engineering*, ASCE, 127(4), 297–313

Soil Liquefaction during Recent Large-Scale Earthquakes – Orense, Towhata & Chouw (Eds)
© 2014 Taylor & Francis Group, London, ISBN 978-1-138-02643-8

Rate of dissipation of excess pore water pressure in a liquefiable sand deposit

S. Iai & K. Nagaura
Disaster Prevention Research Institute, Kyoto University, Kyoto, Japan

ABSTRACT: Rate of dissipation of excess pore water pressure in a liquefiable sand deposit is governed by a highly non-linear behavior of soil following liquefaction. A series of one dimensional effective stress analyses of a liquefiable sand deposit is performed to identify a governing factor on the rate of dissipation of excess pore water pressure. The first series of analyses demonstrates that rate of dissipation at smaller excess pore water pressure ratio is faster than that at larger excess pore water pressure ratio. This fact is due to the non-linear relation between the mean effective stress and volumetric strain. Tangential bulk modulus at lower confining stress (i.e. larger excess pore water pressure ratio) is smaller than that at higher confining stress (i.e. smaller excess pore water pressure ratio). The second series of analyses implies that, despite the complexity of non-linear behavior, the governing factor is a time factor, which is similar to that appearing in linear one dimensional consolidation analysis of clay ground.

1 INTRODUCTION

As is well known in soil mechanics learned by undergraduate students, the rate of dissipation of excess pore water pressure in a linear elastic porous material follows the solutions of Terzaghi's one dimensional consolidation equation. Time history of dissipation is given by a superposition of exponential functions with higher modes more rapidly disappearing and later phase of dissipation is governed by the fundamental mode of an exponential function.

Soil in general does not behave like a linear elastic material. Soil liquefaction is a typical example of non-linear behaviour of soil. Thus, the rate of dissipation of excess pore water pressure following liquefaction can be different from that of a linear elastic material. With the involvement of non-linearity, the dissipation behaviour can be highly complex.

A governing factor for the rate of dissipation of excess pore water pressure in a linear elastic material is time factor T given by

$$T = \frac{k}{m_v \gamma_w H^2} t \tag{1}$$

where k: coefficient of permeability, m_v: compressibility coefficient, γ_w: unit weight of water, H: thickness of a layer, and t: time.

A question may arise whether or not a governing factor exists for the rate of dissipation in a highly non-linear behavior following liquefaction of sand.

In this study, a series of one dimensional effective stress analyses of a liquefiable deposit are performed to discuss the above mentioned non-linear behavior and answer the question raised above. A strain space multiple mechanism model (Cocktail glass model) is used for the analyses (Iai et al., 2011).

2 A STRAIN SPACE MULTIPLE MECHANISM MODEL

In the strain space multiple mechanism model, the effective stress, defined as extension positive, is given based on a dyad defined by the unit vector **n** along the direction of the branch between the particles in contact with each other and the unit vector **t** normal to **n** as follows:

$$\boldsymbol{\sigma}' = -p\mathbf{I} + \frac{1}{4\pi}\iint q\langle \mathbf{t}\otimes\mathbf{n}\rangle \mathrm{d}\omega\mathrm{d}\Omega \tag{2}$$

$$\langle \mathbf{t}\otimes\mathbf{n}\rangle = \mathbf{t}\otimes\mathbf{n} + \mathbf{n}\otimes\mathbf{t} \tag{3}$$

where p denotes effective confining pressure (compression positive), $\mathbf{I}$ denotes second order identity tensor, q denotes micromechanical stress contributions to macroscopic deviator stress due to virtual simple shear mechanism (called virtual simple shear stress), and $\langle \mathbf{t}\otimes\mathbf{n}\rangle$ denotes second order tensor representing the virtual simple shear mechanism. Out of the double integration, the integration with respect to $\omega(=0$ through $\pi)$ is taken over a virtual plane spanned by the direction vectors **n** and **t** with $\omega/2$ being the angle of **n** relative to the reference local coordinate defined in the virtual plane, while the integration with respect to the solid angle Ω is taken over a surface of a unit sphere to give a three dimensional average of two dimensional mechanisms.

The integrated form of the constitutive equation, i.e. direct stress strain relationship, is derived by relating the macroscopic strain tensor ε to the macroscopic effective stress σ' through the structure defined by Equation (2). The first step to derive this relationship is to define the volumetric strain ε (extension positive) and the virtual simple shear strains γ as the projections of the macroscopic strain field to the second order tensors representing volumetric and virtual simple shear mechanisms as follows:

$$\varepsilon = \mathbf{I} : \boldsymbol{\varepsilon} \tag{4}$$

$$\gamma = \langle \mathbf{t}\otimes\mathbf{n}\rangle : \boldsymbol{\varepsilon} \tag{5}$$

where the double dot symbol denotes double contraction. In order to take into account the effect of volumetric strain due to dilatancy ε_{d}, effective volumetric strain ε' is introduced by

$$\varepsilon' = \varepsilon - \varepsilon_{\mathrm{d}} \tag{6}$$

where the rate of volumetric strain due to dilatancy is given by the projection of strain rate field to a second order tensor $\mathbf{I}_{\mathrm{d}}$ as

$$\dot{\varepsilon}_{\mathrm{d}} = \mathbf{I}_{\mathrm{d}} : \dot{\boldsymbol{\varepsilon}} \tag{7}$$

The scalar variables defined in Equations (5) and (6) as the projection of macroscopic strain field are used to define the isotropic stress p and virtual simple shear stress q in Equation (2) through path dependent functions as

$$p = p(\varepsilon') \tag{8}$$

$$q = q(\gamma) \tag{9}$$

In the strain space multiple mechanism model, the virtual simple shear mechanism is formulated as a non-linear hysteretic function, where a back-bone curve is given by the following hyperbolic function;

$$q(\gamma) = \frac{\gamma/\gamma_{\mathrm{v}}}{1+|\gamma/\gamma_{\mathrm{v}}|} q_{\mathrm{v}} \tag{10}$$

The parameters q_v and γ_v defining the hyperbolic function are the shear strength and the reference strain of the virtual simple shear mechanism, respectively.

The isotropic component in Equation (8) is defined by a hysteretic tangential bulk modulus depending on the loading/unloading (L/U) condition as

$$K_{\mathrm{L/U}} = -\frac{\mathrm{d}p}{\mathrm{d}\varepsilon'} = r_K K_{\mathrm{U0}} \left(\frac{p}{p_0} \right)^{l_K} \tag{11}$$

where p_0: initial confining pressure, K_{U0}: tangential bulk modulus at initial confining pressure. Figure 1 shows the relationship, obtained by integrating Equation (11), between effective volumetric strain (normalized by the reference volumetric strain $\varepsilon'_{\mathrm{m0}} = p_0/K_0$) and confining pressure (normalized by p_0). The relationship is significantly affected by power index l_K in the vicinity of $p/p_0 = 0$ but not in the vicinity of $p/p_0 = 1$. The parameter r_K is also introduced in Equation (11) to add flexibility in the model for practice application. The smaller r_K gives smaller tangential bulk modulus, simulating more compressible materials.

Dilatancy in Equation (6) in the Cocktail glass model is decomposed into contractive component ε_d^c and dilative component ε_d^d as

$$\varepsilon_d = \varepsilon_d^c + \varepsilon_d^d \tag{12}$$

The contractive component of dilatancy is given by the simple hypothesis in that the macroscopic component is given from those of microscopic counterparts associated with the virtual simple shear strain rate as follows:

$$\dot{\varepsilon}_{\mathrm{d}}^{\mathrm{c}} = -\frac{1}{4\pi} \iint r_{\varepsilon_{\mathrm{d}}} \mathrm{M_v} \left| \dot{\gamma}_{\mathrm{p}} \right| \mathrm{d}\omega \mathrm{d}\Omega \tag{13}$$

where γ_{p} denotes irreversible (plastic) portion of virtual simple shear strain, being defined by

$$\dot{\gamma}_{\mathrm{p}} = \dot{\gamma} - c_1 \dot{\gamma}_{\mathrm{e}} \tag{14}$$

The parameter $r_{\varepsilon_{\mathrm{d}}}$ is introduced for controlling the degree of dilatancy. The larger $r_{\varepsilon_{\mathrm{d}}}$ generates larger dilatancy if other conditions, such as rate of shear strain and the parameter $\mathrm{M_v}$, which is related to the phase transformation angle, are the same.

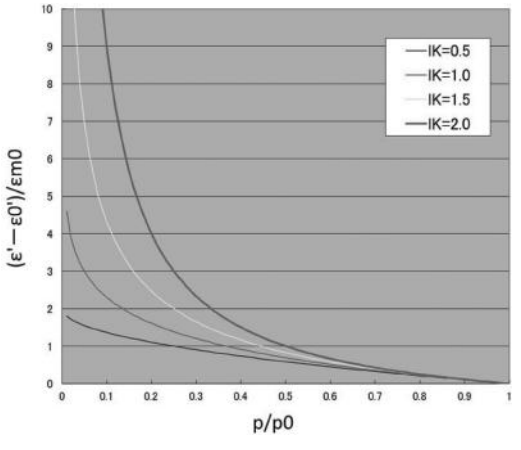

Figure 1. Volumetric mechanism (for $r_K = 1$).

The dilative component of dilatancy is idealized based on the concept of energy less strain component. See Iai et al. (2011) for details.

3 RATE OF DISSIPATION OF EXCESS PORE WATER PRESSURE

In order to study the effect of non-linearity in volumetric mechanism of soil such as shown in Figure 1, two cases of one dimensional analyses were performed on Port Island Site, Kobe, Japan using the earthquake motion during 1995 Hyogoken Nambu earthquake. Case-1 assumes very high liquefaction resistance and the computed acceleration at the ground surface and excess pore water pressures are shown in Figures 2 and 3. Case-2 assumes liquefaction resistance with a stress ratio of 0.25 at 20 cycles and the computed results are shown in Figures 4 and 5. As shown in these figures, Case-1 does not reach state of liquefaction during shaking and excess pore water pressure dissipation curve resembles that of typical curve for consolidation of clayey ground.

Case-2 does reach the state of liquefaction during shaking and excess pore water pressure dissipation at each layer does not begin before the excess pore water pressure at lower level of ground reaches the same level of excess pore water pressure at that layer. In Case-2, dissipation is completed at about 7000 seconds whereas, in Case-1, dissipation is completed at about 700 seconds, about one tenth of that in Case–2.

The dissipation in Case-1 takes place close to the region of $p/p_0 = 1$ in Figure 1. In this region, soil behaves similar to linear material because the tangential bulk modulus basically remains constant. Dissipation in Case-2 takes place initially from the region of $p/p_0 = 0$ and eventually move to the region of $p/p_0 = 1$. At the region close to $p/p_0 = 0$ (at the state of liquefaction), tangential bulk modulus of soil is close to zero and thus the dissipation behavior is completely different from that at $p/p_0 = 1$. Thus, the difference in dissipative behaviors in Cases-1 and 2 is attributed to the non-linear volumetric mechanism shown in Figure 1.

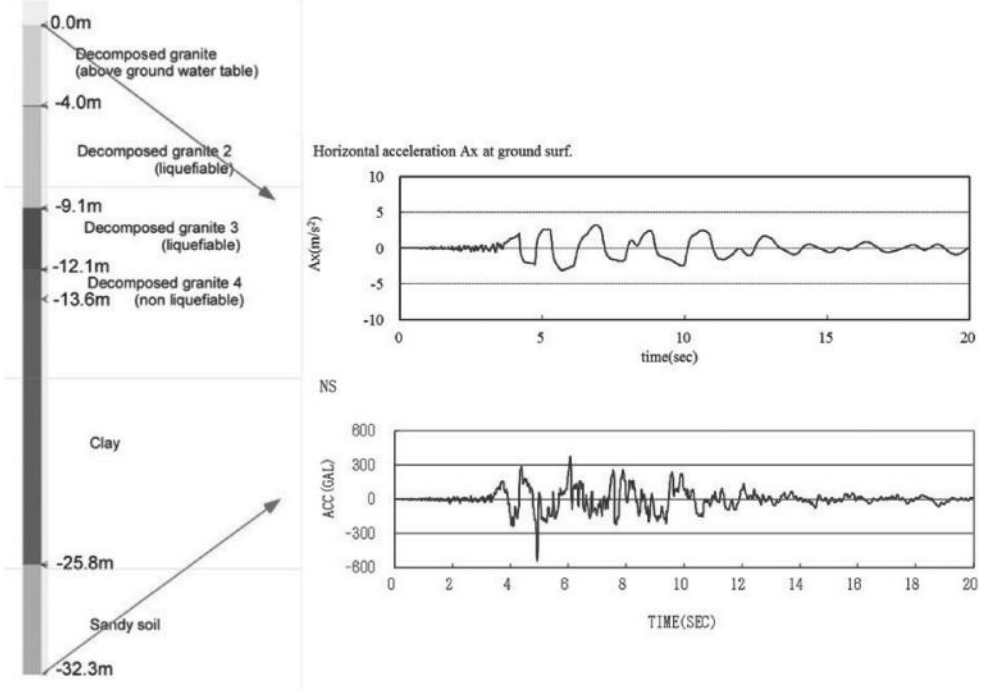

Figure 2. Computed acceleration at ground surface (Case-1).

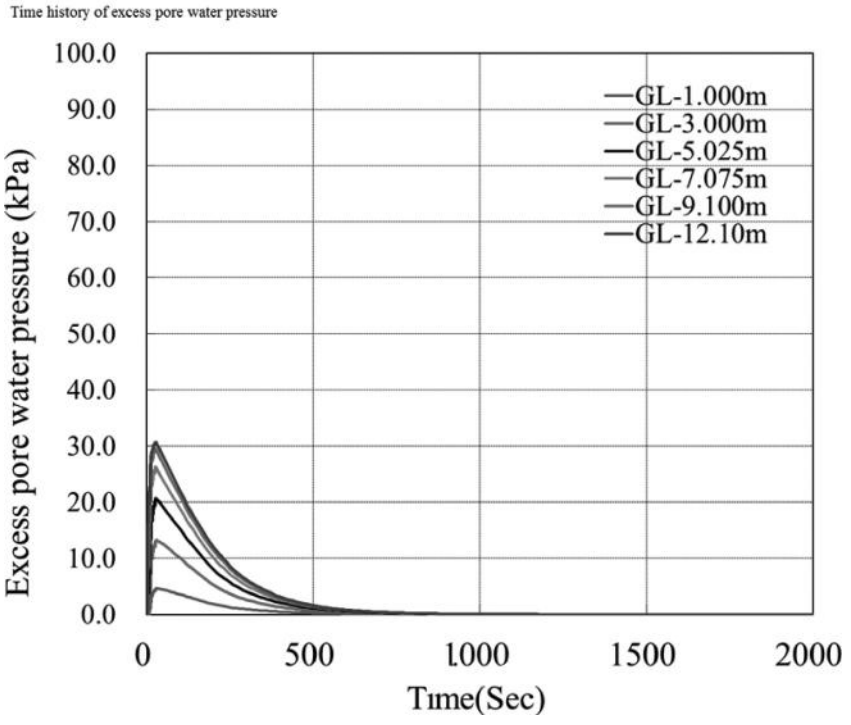

Figure 3. Computed excess pore water pressures (Case-1).

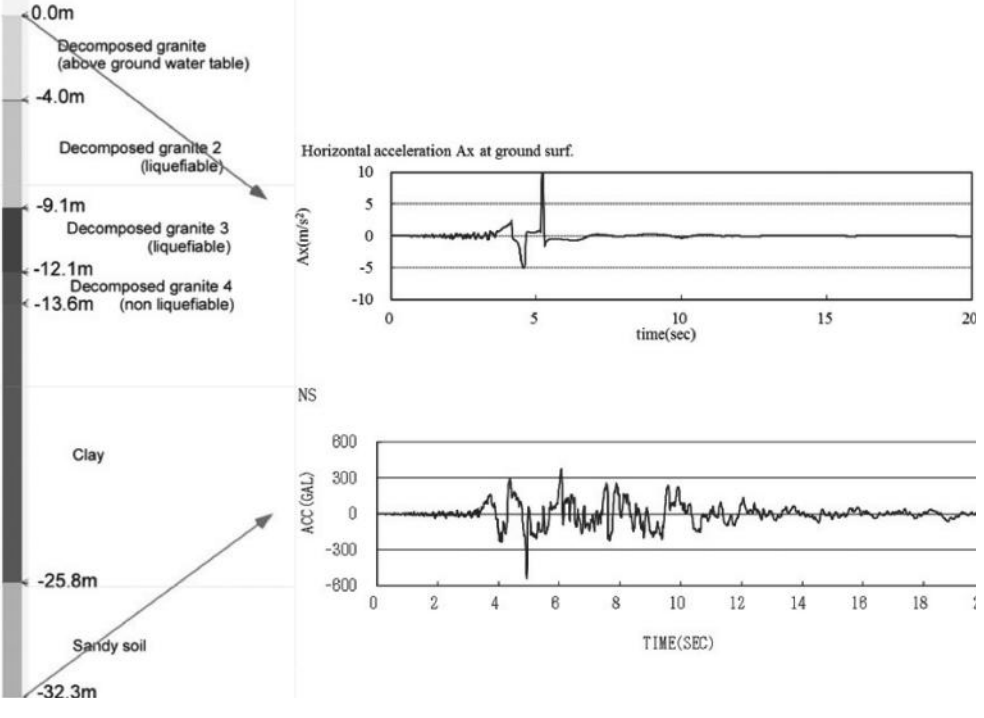

Figure 4. Computed acceleration at ground surface (Case-2).

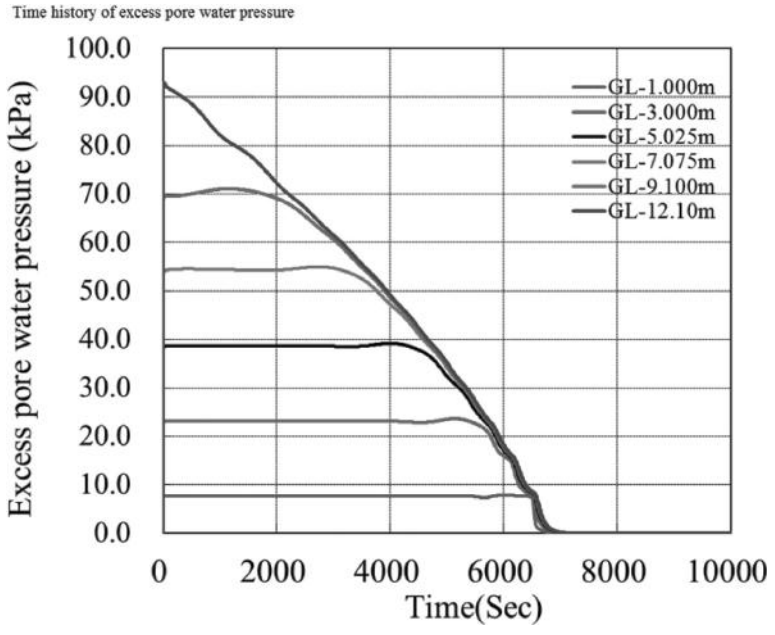

Figure 5. Computed excess pore water pressures (Case-2).

4 GOVERNING FACTOR ON DISSIPATION OF EXCESS PORE WATER PRESSURE

In order to identify a governing factor on dissipation of excess pore water pressure following liquefaction, a parameter study was performed on uniformly deposited sand with a thickness of 20 m shown in Figure 6. In this study, the coefficient of permeability k and the parameter for adjusting tangential bulk modulus r_K appearing in Equation (11) are varied as shown in Table 1. Other parameters such as r_{ε_d} appearing in Equation (13) are varied in order to keep the liquefaction resistance the same throughout the Cases A through E of the parameter study. As shown in Table 1, tangential consolidation coefficient C_v at a confining pressure of $p = p_0$ can be written by using the bulk modulus K at a confining pressure of $p = p_0$ by

$$C_v = \frac{k(r_K K)}{\gamma_w} \tag{15}$$

Figure 7 shows the computed results of undrained cyclic loading test in terms of liquefaction resistance for Cases-1 through 3. As shown in this figure, the liquefaction resistance curves remain the same throughout these cases as intended.

Figure 8 shows the computed dissipation of excess pore water pressure for the uniform sand deposit 20 m deep with varying tangential bulk modulus by varying the parameter r_K in Equation (11) (Cases-B and C) and varying coefficient of permeability (Cases-D and E) with Case-A as reference. The rate of dissipation is higher with a larger coefficient of permeability and a larger tangential bulk modulus.

In order to identify a governing factor for the rate of dissipation, a time factor is introduced as follows:

$$T = \frac{C_v}{H^2} t \tag{16}$$

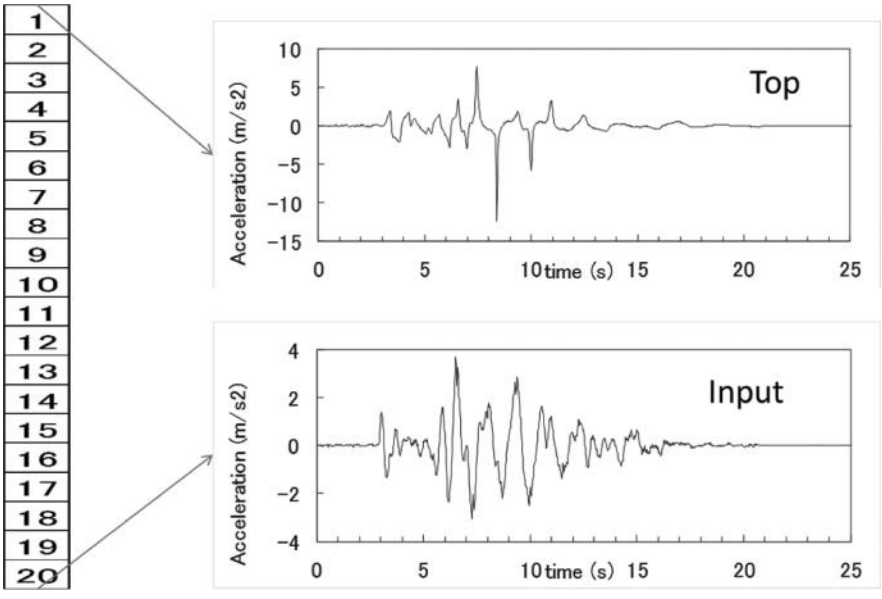

Figure 6. Computed ground surface acceleration for a liquefiable uniform sand deposit.

Table 1. Model parameters.

	k (m/s)	ε_d^{cm}	$r_{\varepsilon d}$	r_k	$r_k \times r_{\varepsilon d}$	C_v
Case A	1.64×10^{-5}	0.2	0.15	0.3	0.045	4.32×10^{-2}
Case B	1.64×10^{-5}	0.6	0.45	0.1	0.045	1.44×10^{-2}
Case C	1.64×10^{-5}	0.04	0.03	1.5	0.045	0.216
Case D	5.47×10^{-6}	0.2	0.15	0.3	0.045	1.44×10^{-2}
Case E	8.2×10^{-5}	0.2	0.15	0.3	0.045	0.216

where C_v is defined by Equation (15). By using this time factor, the computed results shown in Figure 8 are re-plotted as shown in Figure 9. The results shown in this figure indicate that the time factor introduced by Equations (15) and (16) is indeed the governing factor for the rate of dissipation. Despite the complex behaviour due to the effect of non-linearity in volumetric mechanism, the governing factor is identified and can be used for controlling the numerical analysis of liquefaction.

In order to generalize the results of the rate of dissipation obtained for a homogenous deposit to a non-homogenous deposit, Equation (15) is substituted to Equation (16) to give

$$t = \frac{T}{r_K \left(\dfrac{kK}{\gamma_w H^2} \right)} \tag{17}$$

Equation (17) implies that time (for dissipation) is affected by the parameter r_K in inversely proportional manner provided that other material properties, with respect to k, K, H, are the same for a homogenous deposit.

For a non-homogenous deposit, time (for dissipation) is generally affected by each parameter r_K for each layer so that is it not possible to obtain a simple conclusion as for a homogenous deposit. However, if the same parameter r_K is applied for all the layers in

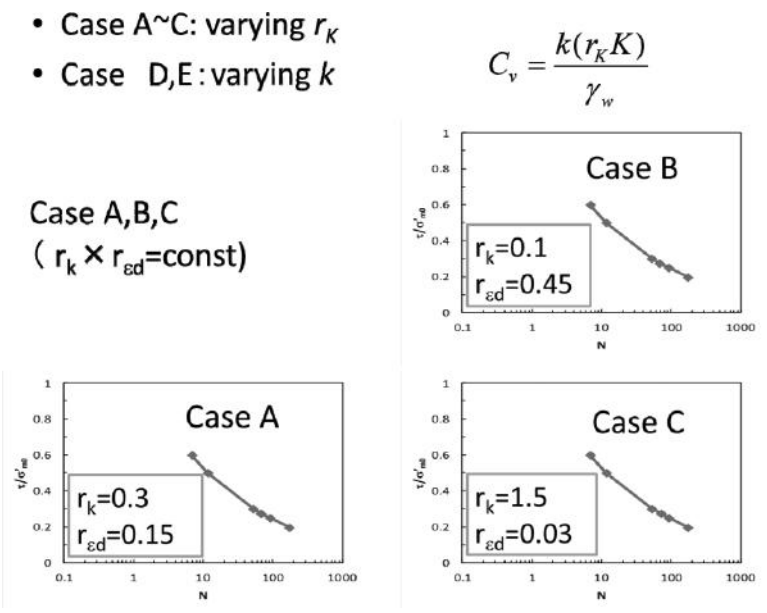

Figure 7. Computed liquefaction resistance curves for Cases A through C.

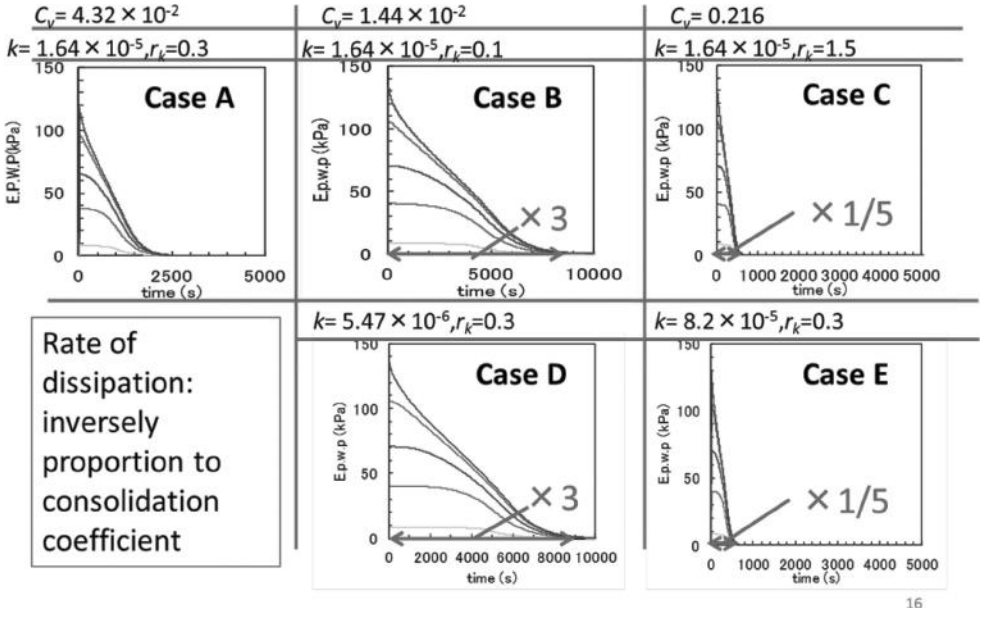

Figure 8. Computed dissipation of excess pore water pressure.

a non-homogenous deposit, time (for dissipation) for the non-homogenous deposit will be controlled by the parameter r_K in inversely proportional manner, provided that all other material properties, with respect to k, K, H in each layer, remain the same. Numerical analysis to confirm this statement is yet to be done in future.

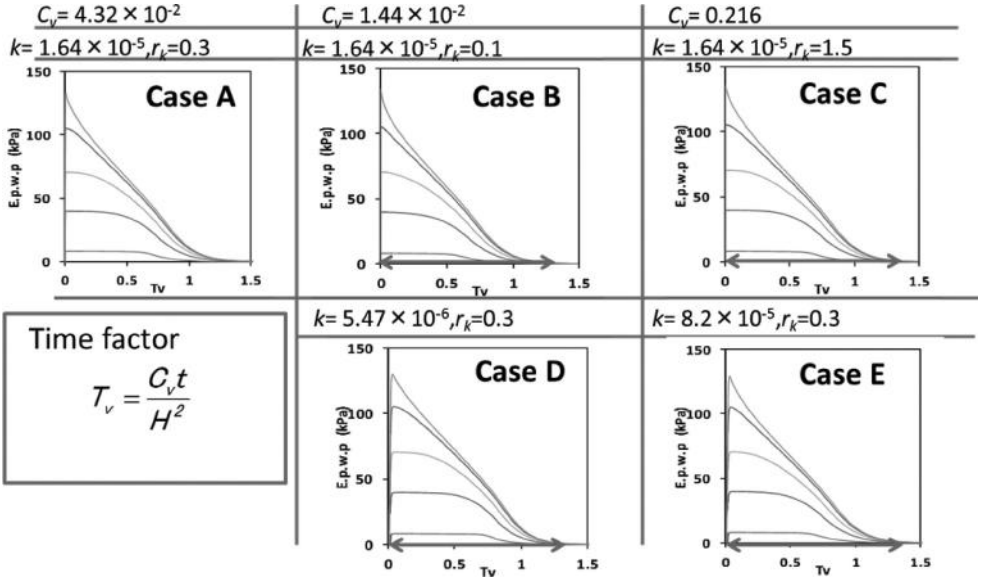

Figure 9. Computed dissipation of excess pore water pressure plotted with time factor.

5 CONCLUSIONS

A series of one dimensional effective stress analyses of a liquefiable sand deposit was performed to identify a governing factor on the rate of dissipation of excess pore water pressure. The first series of analyses demonstrated that the rate of dissipation at smaller excess pore water pressure ratio is faster than that at larger excess pore water pressure ratio. This fact is due to the non-linear relation between the mean effective stress and volumetric strain. Tangential bulk modulus at lower confining stress (i.e. larger excess pore water pressure ratio) is smaller than that at higher confining stress (i.e. smaller excess pore water pressure ratio). The second series of analyses implied that, despite the complexity of non-linear behavior, the governing factor is a time factor, which is similar to that appearing in linear one dimensional consolidation analysis of clay ground.

REFERENCE

Iai, S., Tobita, T., Ozutsumi, O. & Ueda, K. 2011. Dilatancy of granular materials in a strain space multiple mechanism model. *International Journal for Numerical and Analytical Methods in Geomechanics,* 35(3), 360–392.

This page intentionally left blank

Soil Liquefaction during Recent Large-Scale Earthquakes – Orense, Towhata & Chouw (Eds)

Laboratory tests on cyclic undrained behavior of loose sand with cohesionless silt and its application to assessment of seismic performance of subsoil

I. Towhata, K. Gunji & Y.A. Hernandez
Department of Civil Engineering, The University of Tokyo, Japan

S. Yamada
Department of Urban Design and Engineering, Osaka City University, Japan

ABSTRACT: Geotechnical earthquake engineering in the recent times has been paying its special attention to such themes as performance-based design, liquefaction of sand with cohesionless fines, and seismic mitigation measures for residential areas. Because recent earthquakes in Japan and New Zealand caused many liquefaction problems in residential areas, the above-mentioned themes have become even more important than before. The present study conducted laboratory tests on sand with cohesionless fines in order to show how the seismic performance of loose subsoil is assessed, thus developing a practical methodology of performance-based mitigations. Most experimental data thus obtained is presented together with interpretations, and the mathematical framework for the performance assessment is described together with an example of specified mitigation methods.

1 INTRODUCTION

The major point of discussion in geotechnical earthquake engineering in the recent times lies in the development of performance-based design in which the seismic factor of safety does not necessarily have to be greater than unity, if the induced damage is within an acceptable limit (Finn and Wu, 2013; Iai and Tobita, 2010; JGS, 2006; Kramer et al., 2006; Murakami et al., 2004; Sendir Torisu et al., 2010; Towhata, 2010 and 2012; Wieland, 2012a and b). One of the reasons for this trend is the increasing intensity of seismic load for design due to the people's desire for safety. Obviously it is difficult to maintain with reasonable budget the seismic factor of safety greater than unity under a significant intensity of seismic actions. Hence, the idea of seismic performance has emerged in which the seismic performance is synonymous with the residual displacement/deformation being less than the allowable limit at the end of a seismic event. Therefore, it is essential to be able to assess the residual displacement and deformation in a practical manner in both technical and financial senses.

Another point of argument is the liquefaction behavior of loose sand with cohesionless (non-plastic) silt (Adachi et al., 1998; Adalier et al., 2003; Galandarzadeh and Ahmad, 2012; Hwang et al., 1993; Polito and Martin, 2003; Sato et al., 1997; Yamamuro and Lade, 1997; Yamamuro and Covert, 2001). In contrast with the cohesive fines content in sand that has been regarded in many design codes to increase the liquefaction resistance of subsoil, sand with cohesionless silt developed liquefaction disasters during such recent earthquakes as the 1999 Chi Chi earthquake of Taiwan (Lee et al., 2012), the 2001 Tottoriken-Seibu earthquake (Towhata, 2008), the 2010–2011sequence of earthquakes in Christchurch (Cubrinovski et al., 2012) and the 2011 Great earthquake in East Japan. In spite of such liquefaction vulnerability, the experimental studies as cited above present contradictory remarks such as liquefaction

resistance of sand being increased or reduced by adding a certain amount of cohesionless silt. Hence, this controversial issue needs to be examined in a more rational manner.

The third issue is the mitigation of liquefaction effects in residential areas. Because the financial ability of people is small, the available mitigation measure is limited. Moreover, the Japanese people in liquefaction-hit areas in 2011 chose to improve the liquefied subsoil while keeping their affected houses untouched. This means that vibratory compaction or other technologies that may damage the fragile houses are impossible. This situation is in clear contrast with the situation in Christchurch in New Zealand where the liquefaction-prone areas are declared to be dangerous and residents are advised to move out of the area, leading to demolition of affected houses.

With these situations in mind, the authors made an attempt to propose some solutions to the current controversial issues by running field investigations, carrying out laboratory tests, and developing analytical/numerical methods of seismic performance assessment.

2 FIELD INVESTIGATION

The first stage of the present study addressed the situation of real liquefaction of sand with silt of little cohesion. The selected sites were in Christchurch, New Zealand, where significant liquefaction affected the residential areas. In December 2012, portable Dynamic Cone Penetration Tests (DCPT) were conducted to comprehend the stiffness of the ground around the Avon River where significant damage was observed. The DCPT is similar to the Standard Penetration Test (SPT) except that resistance is measured continuously in the vertical direction. It is performed by dropping a 5 kg hammer from 50 cm height and counting the number of blows per 10 cm penetration. This blow count is called N_d.

Figure 1 shows the test points and Figure 2 compares the results of DCPT with the static Cone Penetration Test (CPT), which comes from "Canterbury Geotechnical Database". Although units are different, results of DCPT reasonably correspond to those of CPT in depth. This N_d was then converted to SPT-N value by Eq. 1.

$$\begin{aligned} N &= 1.1 + 0.30 N_d \quad (N_d > 4) \\ N &= 0.66 N_d \quad (N_d \le 4) \end{aligned} \tag{1}$$

Figure 3 shows the factor of safety against liquefaction (F_L) from B7 to B11 in Figure 1. F_L was calculated by the Japanese Architectural Standard "Recommendations for Design of Building Foundations" for which the design ground motion was 200 Gal and the earthquake magnitude was $M_w = 7.5$. $F_L > 1.0$ is required for safety but, in most areas, $F_L \leqq 1.0$ down to 5.0 m depth (Figure 3). Thus, the risk of liquefaction is still high in this zone and countermeasures are necessary for future earthquakes.

Figure 1. The studied area in Christchurch, New Zealand (from Google Map).

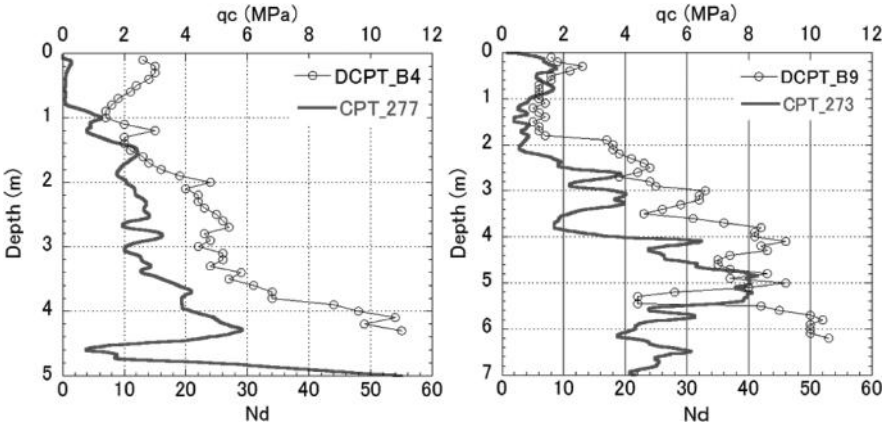

Figure 2. The soil profiles obtained by dynamic cone penetration and conventional CPT.

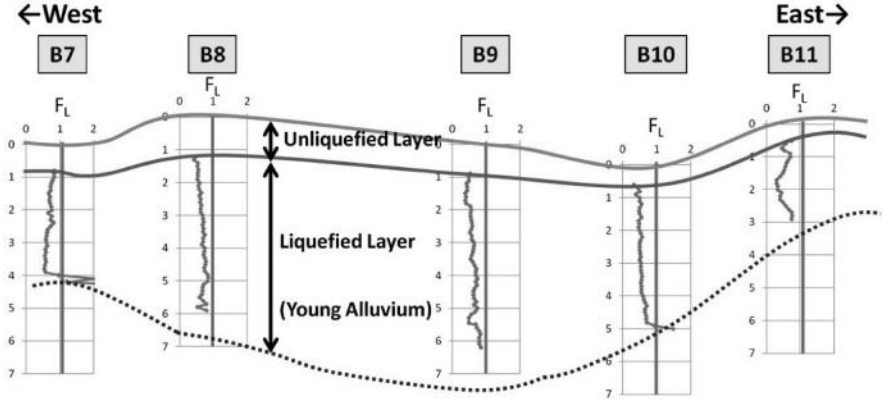

Figure 3. The assessed cross section of the studied area in terms of factor of safety against liquefaction.

3 CHARACTERISTICS OF LIQUEFIED SAND IN CHRISTCHURCH

The particle size distributions of the boiled sand along the Avon River (Figure 4) were examined and Figure 5 shows the results. The soil at each point contains 5~20% silty fines and the fines are slightly or non-plastic. This characteristic is similar to sand ejecta in the Tokyo Bay area where severe liquefaction occurred during the Great East Japan Earthquake on March 11, 2011. Figure 6 shows the particle size distribution of the sand ejecta which also contains 30% non-plastic fines. Because the quarantine control made it very difficult to run tests in Tokyo on the New Zealand soil, the sand ejecta from the Tokyo Bay area was used for laboratory test in place of Christchurch soil.

4 TORSIONAL SHEAR TESTS

4.1 *Aims*

Liquefaction of silty sand has been an important problem for seismic design engineers since current design criteria do not clearly recognize the difference between plastic and non-plastic fines and seems to be in disagreement regarding the role of non-plastic fines in liquefaction

Figure 4. Sites of sand in Christchurch where grain size distribution was studied.

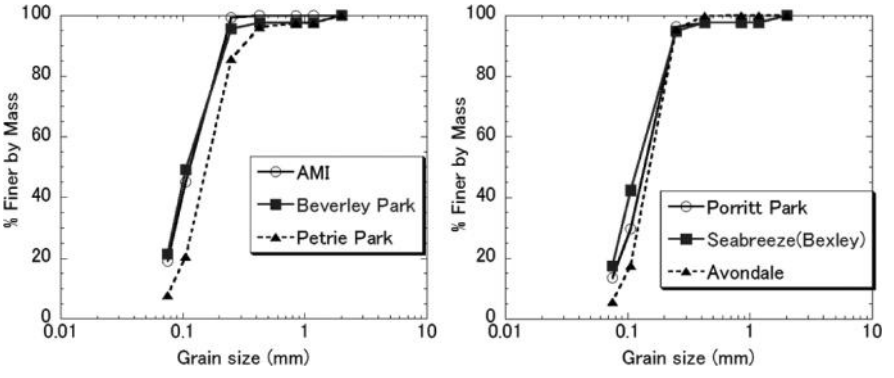

Figure 5. Grain size distribution of sand ejecta in Christchurch.

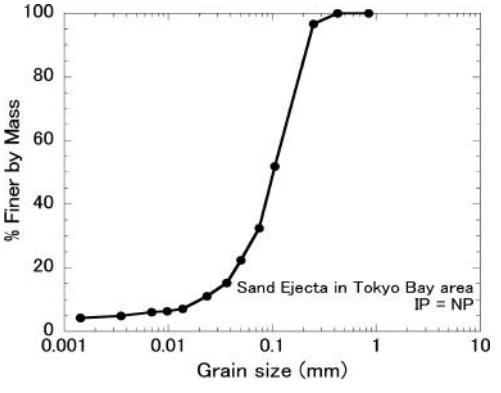

Figure 6. Grain size distribution of sand ejecta in Tokyo Bay area.

resistance. To account for this, many researchers have tried to comprehend the effects of non-plastic fines on the potential of liquefaction.

Carraro et al. (2003) conducted cyclic triaxial tests on reconstituted specimens of Ottawa sand with non-plastic silt content ranging from 0 to 15% and found that, for a given relative density, the liquefaction resistance of sand increases when small amounts of non-plastic silt are added. Huang et al. (2004) performed cyclic triaxial tests on Mai Liao sand with non-plastic fines content of 0, 15, and 30% and discovered that the liquefaction resistance seems to decrease with increasing fines content at the same void ratio. Polito and Martin (2001) performed a series of cyclic triaxial tests on two sands, varying non-plastic fines content from 0 to 20%, while keeping the sand skeleton void ratio constant. The skeleton void ratio is the ratio of the volume of space among coarse sand grains and the volume of these coarse grains. The liquefaction resistance of Monterey sand was nearly constant as more fines were added to clean sand, but on the other hand, the liquefaction resistance of Yatesville sand seems to increase as fines content increases. Thus, a consensus has not been reached regarding the effects of non-plastic fines.

In the present study, torsional shear tests were conducted to understand the effects of non-plastic fines on the liquefaction resistance and, besides, degradation of shear modulus in the course of cyclic undrained shear towards liquefaction for carrying out the deformation analysis.

4.2 *Tested material and experimental procedure*

The sand ejecta in Tokyo Bay area was used for the experiments as mentioned before. To observe the effect of fines, fines contents were varied. Sand was sieved to separate fines from coarser sand grains. After washing and drying, both sand and fines were thoroughly mixed together, varying the amount of fines from 0 to 80%.

A hollow cylindrical torsional shear device was used. The device subjects a thin hollow cylindrical specimen (190 mm height, 60 mm internal diameter and 100 mm external diameter) to a combination of axial and torsional stresses in addition to the fluid cell pressures on inside and outside faces of a cylindrical specimen. In this device, torque, vertical force, inner and outer cell pressures can be controlled independently which allows the control of the direction of principal stresses.

Minimum and maximum void ratios vary as more fines are added, making it difficult to select both void ratio and relative density as the constant parameters. To avoid this concern, constant energy for sample preparation which seems to be most similar to natural process is used in this study as the comparison parameter for several fines contents. The samples were prepared by Air Pluviation (AP), keeping a constant height of fall which, in this study, has been set at 5 cm and 50 cm.

After preparing samples, saturation was completed using the double vacuum method. Because specimen saturation is essential in such tests, the degree of saturation was measured in terms of Skempton's B-value and all samples achieved $B \geqq 0.95$. Once satisfactory B-values were achieved, samples were isotropically consolidated under the effective confining stress of 100 kPa. After consolidation, cyclic shear tests were conducted in an undrained strain-control manner (in this case, a strain rate of 0.12%/min). Note that this cyclic loading maintained the stress amplitude constant equal to the specified value.

4.3 *Test results and liquefaction curves*

Figures 7, 8, 9 and 10 demonstrate typical results of cyclic shear tests with 30% non-plastic fines (AP-5 cm) and 80% non-plastic fines (AP-50 cm). The 5% double amplitude shear strain was the criterion of liquefaction. The number of cycles needed for this criterion was measured for each fines content and plotted against the shear stress ratio. The liquefaction curves of AP-5 cm and AP-50 cm are depicted respectively in Figures 11 and 12. Cyclic resistance ratio (CRR_{20}) is the shear stress ratio at which samples reach the liquefaction criterion of 5% DA strain at 20 cycles. Figure 13 plots the CRR_{20} against the change of fines content. For the AP-5 cm set, it is observed that there are three different groups. From 0 to 20% of

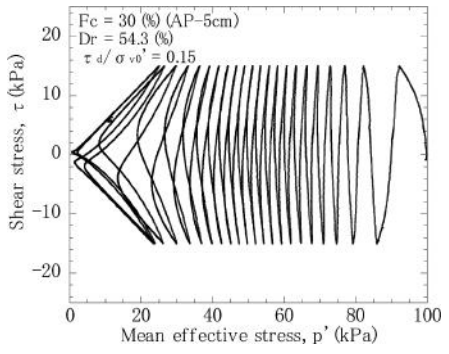

Figure 7. Stress path of Tokyo Bay sand ejecta. (AP-5 cm)

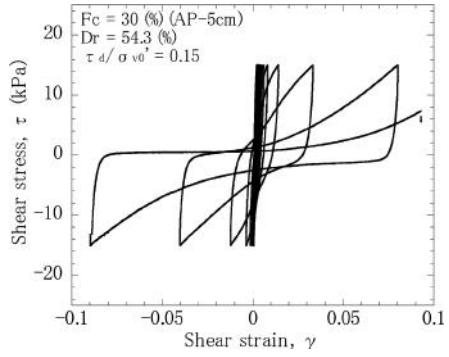

Figure 8. Undrained stress-strain behavior of Tokyo Bay sand ejecta (AP-5 cm).

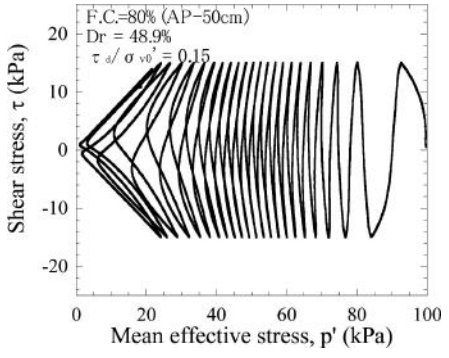

Figure 9. Stress path (AP-50 cm).

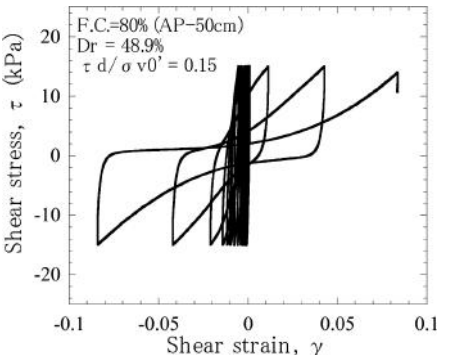

Figure 10. Undrained stress-strain behavior (AP-50 cm).

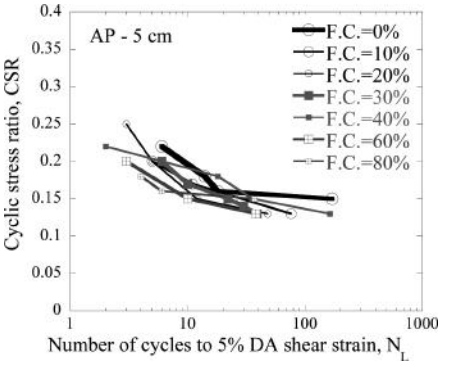

Figure 11. Liquefaction curves of Tokyo Bay sand ejecta with different non-plastic fines content.

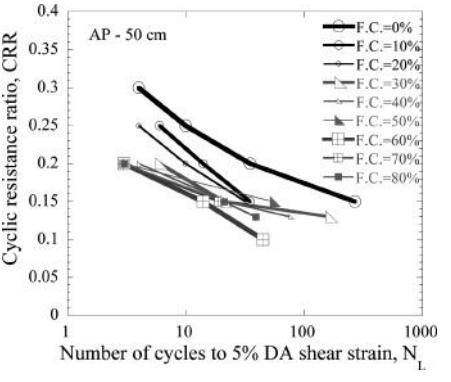

Figure 12. Liquefaction curves of Tokyo Bay sand ejecta with different non-plastic fines content (AP-50 cm).

fines content, there is a slight decrease, while there is an increase from 20 up to 40% of fines content. Then, CRR_{20} decreases but increases again from 60 to 80% of fines content. For the AP-50 cm, there is a decrement in resistance as the fines content increases from 0 to 30%, and then there is reversal in the behavior from 40 to 50%. The last group from 60 to 80% shows a rise in the resistance as more fines are added. In both cases the increment of non-plastic fines

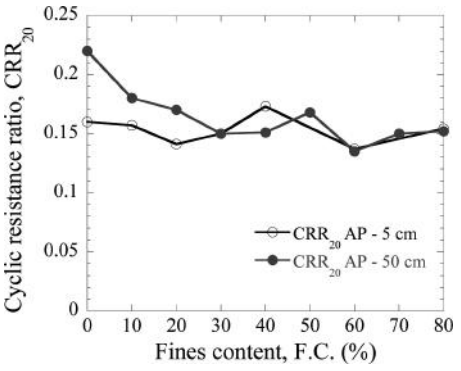

Figure 13. Variation of liquefaction resistance at 20 cycles with non-plastic fines content.

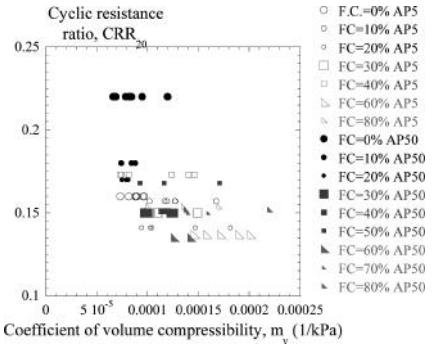

Figure 14. Undrained stress-strain behavior of Tokyo Bay sand ejecta.

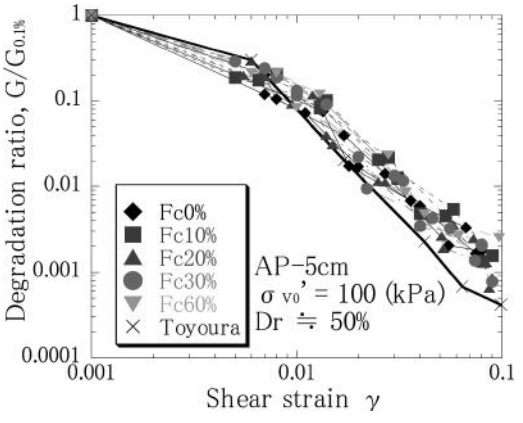

Figure 15. Decay or reduction of secant shear modulus with the progress of undrained cyclic shear toward liquefaction.

reduces the liquefaction resistance within 30~40% of fines content and then small increment is observed around 50%. Thereafter, the CRR_{20} soon decreases to 60% and the resistance increases again as fines content grows to 80%. The obtained CRR_{20} of AP-50 cm is larger than that of AP-5 cm within small fines content range due to bigger sample preparation energy, but the two values of CRR_{20} are almost same over 60% of fines content.

As mentioned before, different opinions come from different testing schemes that keep constant void ratio, matrix void ratio, relative density etc. From the view point of practice, people are keen to know how the liquefaction resistance of clean sand based on SPT-*N* values should be modified or affected by non-plastic fines: increase or decrease. Therefore, we keep the compaction energy constant and then compare the liquefaction resistance for m_v parameter (Figure 14). The unit of the reciprocal of m_v is "kPa" so it could be acceptable as a mechanical property of sand which is a laboratory alternative of SPT-*N* values. Detailed inspection of Figure 14 may suggest that the cyclic resistance at constant m_v decreases as fines content increases, although the trend is not very obvious.

4.4 *Degradation of shear modulus during undrained cyclic shear*

Secant and tangent shear modulus was measured during cyclic shearing to draw a shear modulus degradation curve. The value of the initial secant shear modulus at 0.1% shear strain was

taken from the first cycle of shearing. This shear strain of 0.1% represents situation of null damage from the liquefaction viewpoints, which is the pre-earthquake situation where no damage has occurred yet. Then all the following cycles were studied to determine the tangent shear modulus in accordance with the softening of the stress-strain behavior.

The results are shown in Figure 15. The figure illustrates that fines content does not seem to have a clear influence on the degradation of shear modulus ratio ($G/G_{0.1\%}$) during the progress of cyclic loading. Same tests were conducted on Toyoura sand as well but the degradation of this clean sand was more significant than that of the Tokyo Bay ejected sand.

5 ANALYSIS ON RESIDUAL DEFORMATION OF GROUND CAUSED BY SEISMIC LOADING AND LIQUEFACTION

Seismic performance–based design is one of the hot topics in the recent times, and the practical assessment of ground deformation is a key issue. Deformation analysis is proposed for comprehending to what extent countermeasures should be conducted for future earthquake. In particular, the proposed methods are analytical solutions and can be used without running computer codes, and, therein, the meaning of individual input parameters is clearly understood. Note further that the proposed method is valid on both liquefied and unliquefied subsoil.

5.1 *On lateral displacement of a sloping ground*

Figure 16 shows the model of this analysis. The slope is tilted at the constant degree θ and the thicknesses of liquefied and unliquefied layers are constant in the slope direction in the selected range.

In order to obtain the ground surface displacement distribution F at the ultimate equilibrium state, variation of the total energy due to deformation, q, was integrated over the entire length of liquefied ground and minimized;

$$q = \frac{\pi^2 G_L}{16 H_2} F(x)^2 + \left(\frac{E_L H_2}{4} + \frac{E_S H_1}{2} \right) \left(\frac{dF}{dx} \right)^2 - \sin\theta \left\{ \frac{2\gamma_L H_1}{\pi} + \gamma_s H_1 \right\} F(x) \tag{2}$$

where E_L and G_L are the Young's modulus and the shear modulus of the liquefied soil layer respectively at the time of liquefaction. The relation of $E_L = 2(1+\nu)\, G_L$ was used, and Poisson ratio was assumed to be $\nu = 0.5$ because of undrained condition. E_S is the Young modulus of the unliquefied surface layer, while γ_L and γ_S are the unit weights of the liquefied and the unliquefied soil layers, respectively. Degradation of shear modulus, G_L, during cyclic loading is the cause of lateral flow. For the mathematical background of this theory, refer to Towhata et al. (1999).

According to the variational principle of mathematics, the equivalent Euler equation is given by:

$$\frac{\partial q}{\partial F} - \frac{d}{dx} \left\{ \frac{\partial q}{\partial \left(\frac{dF}{dx} \right)} \right\} = 0 \tag{3}$$

It is possible to obtain analytical solutions with the following two boundary conditions:

$$[1]\ F_0 = 0 \ at\ x = 0, \quad \frac{dF_L}{dx} = 0 \ at\ x = L \ or$$

$$[2]\ \frac{dF_0}{dx} = 0 \ at\ x = 0, \quad F_L = 0 \ at\ x = L$$

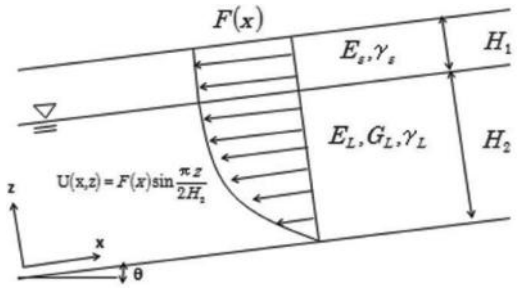

Figure 16. Parameters as employed in the analytical solution of slope displacement.

In which $x = 0$ and $x = 1$ designate the bottom and top of a slope, respectively. Solutions for these two boundary conditions are then given by

$$\mathrm{F}(x) = \frac{c_2}{c_1}\left[1 - \frac{\cosh\left\{\sqrt{c_1}(L-x)\right\}}{\cosh(\sqrt{c_1}L)}\right] \quad [2]\ F(x) = \frac{c_2}{c_1}\left[1 - \frac{\cosh(\sqrt{c_1}x)}{\cosh(\sqrt{c_1}L)}\right] \tag{4}$$

where constants c_1 and c_2 depend on the geometry and soil properties in the slope;

$$c_1 = \frac{\pi^2 G_L}{(4E_L H_2 + 8E_s H_1)H_2}, \quad c_2 = \frac{2\sin\theta\left(\frac{2\gamma_L H_2}{\pi} + \gamma_s H_1\right)}{E_L H_2 + 2E_s H_1}$$

The meanings of parameters are illustrated in Figure 12.

5.2 *On subsidence of house caused by earthquake shaking and liquefaction*

The house lying on an unliquefied surface layer subsides due to reduction of rigidity in the liquefiable layer. Figure 17 illustrates a two-dimensional cross section of a house and its foundation which is actually three-dimensional in the proposed analysis. For simplicity, the plan of a house is assumed to be square with B on each side and the distance to the fixed lateral boundary, b, is symmetrical with isotropic conditions. Although the vertical stress under a house decreases with depth, a uniform stress distribution, q, is assumed atop the liquefiable layer. This assumption is not too bad because the non-liquefied layer is not very thick as compared with the house width.

Being similar to the aforementioned lateral displacement analysis, the variation of total energy due to house subsidence, S, is minimized. The variation of the total energy, Q, is composed of the variation of gravity potential energy, strain energy and energy loss due to friction caused by subsiding foundation of a house:

$$Q = \frac{B^2\left\{E_L\left(4B^3 + 19B^2 b + 28Bb^2 + 12b^3\right) + 2\gamma_L\left(B^3 + 5B^2 b + 8Bb^2 + 4b^3\right)\right\}H_2}{16b(B+b)^2 H_2}S^2 + \left[2K_0 \ddagger BH_1^2 \tan\phi\left\{1 + \frac{B^2}{4b(B+b)}\right\} - qB^2\right]S \tag{5}$$

The minimum value of Q occurs when $dQ/dS = 0$. Accordingly,

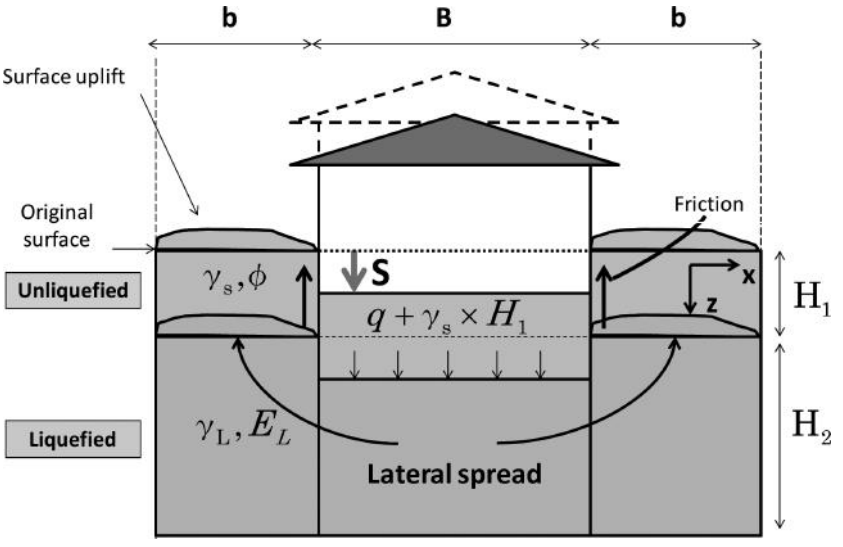

Figure 17. Idealization of a house with shallow foundation resting on surface of liquefaction-prone ground (two-dimensional cross section of a three-dimensional idealization).

$$S = -\frac{d_2}{2d_1} \tag{6}$$

in which constants d_1 and d_2 depend on the geometry and soil properties in the subsoil:

$$d_1 = \frac{B^2\left\{E_L\left(4B^3+19B^2b+28Bb^2+12b^3\right)+2\gamma_L\left(B^3+5B^2b+8Bb^2+4b^3\right)H_2\right\}}{16b\left(B+b\right)^2 H_2}$$

$$d_2 = 2K_0\gamma_s BH_1^2\tan\phi\left\{1+\frac{B^2}{4b\left(B+b\right)}\right\}-qB^2$$

6 ASSESSMENT OF SEISMIC DEFORMATION OF GROUND

The analytical solutions of ground deformation were employed to evaluate the effects of soil improvement that reduces the thickness of liquefiable subsoil and increases the thickness of the surface unliquefied soil. It was therein aimed to determine the thickness of the surface unliquefied soil that is needed to satisfy the safety requirements.

First, the effects of soil improvement in the liquefiable ground were examined. An example of CPT data of the original ground was taken from the Canterbury Geotechnical Database (CPT_273) which is close to B1 point in Figure 1, and the CPT parameters were converted to SPT-N values as described herein. First, Robertson (1990) defined the soil behavior index (I_c) by

$$I_c = \left\{\left(3.47-\log_{10}Q_t\right)^2+\left(\log_{10}Fr+1.22\right)^2\right\}^{0.5} \tag{7}$$

where Q_t is the normalized CPT penetration resistance and F_r is the normalized friction.

$$Q_t = \frac{q_t-\sigma_v}{\sigma'_v} \tag{8}$$

$$F_r = \frac{f_s}{q_t - \sigma_v} \times 100\,(\%) \tag{9}$$

in which σ_v is the total vertical stress, σ_v' is the effective stress, q_t is the corrected cone tip resistance considering water pressure and f_s is the measured sleeve friction. Second, Suzuki et al. (2003) suggested the following relationship between SPT-N and the tip resistance (q_t) of CPT by using I_c:

$$\begin{aligned} N &= 0.341 I_c \left(q_t - 0.2\right)^{(1.34-0.0927Ic)} \quad \left(q_t > 0.2\,MPa\right) \\ N &= 0 \qquad\qquad\qquad\qquad\qquad\quad \left(q_t \le 0.2\,MPa\right) \end{aligned} \tag{10}$$

The converted SPT-N is shown in Figure 18. Then the factor of safety against liquefaction (F_L) was calculated by using the Japanese Architectural Design Code assuming maximum design acceleration 350 Gal (Figure 19).

For the current analyses, the Young's modulus and the shear modulus of the liquefiable layer, E_L and G_L, have to be determined for different extents of pore pressure rise (or F_L values). The general procedure for this is summarized as what follows;

i. The factor of safety against liquefaction, F_L, is calculated by considering the maximum ground acceleration A_{max} and the seismic magnitude, M_w together with the SPT-N values for the liquefiable and un-liquefiable layers, which is a common practice.
ii. Once the seismic stress ratio and the SPT-N values are obtained, the corresponding maximum shear strain, γ, is determined graphically by the Japanese Architectural Design Code.
iii. On the other hand, the shear wave velocity in soil is assessed by $V_s = 80N^{1/3}$ (m/s) (Highway Bridge Design Code of Japan) for sand and then, the maximum shear modulus of small strain is determined by $G_{max} = \rho V_s^2$.

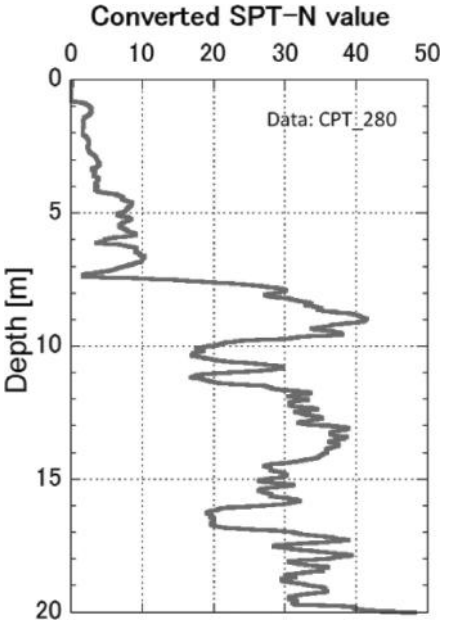

Figure 18. SPT-N profile of a studied subsoil after conversion from CPT data.

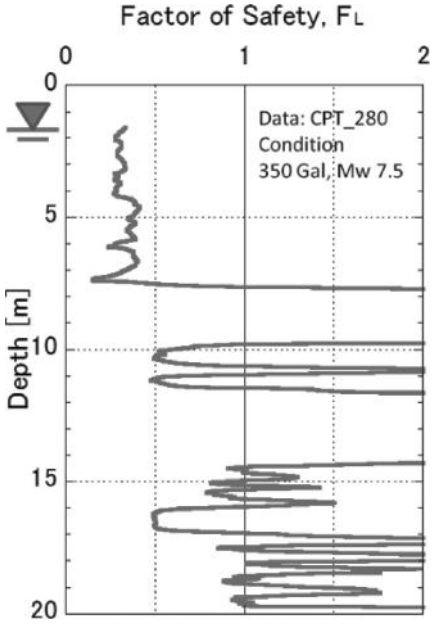

Figure 19. Factor of safety against liquefaction as assessed from SPT-N.

iv. The degradation curve for the normalized shear modulus $G_L/G_{0.1\%}$ was obtained from the laboratory tests (Figure 15). However, $G_{0.1\%}$ corresponds to the cyclic shear strain amplitude of 0.1%, while G_{max} mentioned above corresponds to typically 0.0001%. To account for this issue, data measured in Urayasu City during the post-earthquake period was summarized and a typical result is shown in Figure 20. The relation between maximum shear modulus at 0.0001% shear strain and the shear modulus for 0.1% strain is $G_{0.1\%}/G_{max} = 0.44$, which is consistent with data on many cohesionless soils.

v. With the strain level γ from step (ii), the corresponding ratio $G_L/G_{0.1\%}$ is read from Figure 15 and it is multiplied by $G_{0.1\%}/G_{max} = 0.44$ to determine G_L/G_{max}. As G_{max} has already been obtained in step (iii), G_L can be determined. Finally, E_L is determined as well by $E_L = 2(1+\nu)\, G_L$, $\nu = 0.5$.

vi. E_s for the unliquefied surface layer is obtained from the SPT-N value by using an empirical relationship such as $E_s = 2800\, N$ (kPa) from Highway Bridge Design Code of Japan.

Tables 1 and 2 show the values of input parameters estimated by the CPT data for calculation of lateral displacement and subsidence, respectively. As for the slope, the set of boundary conditions where there is no displacement at the bottom of the slope and cracks open at the upper end of the slope was considered and the displacement along the slope length was

Table 1. Parameters for calculation of lateral displacement.

Parameters	Values
Assumed maximum design acceleration, A_{max} [Gal]	350
Standard penetration test blows for the liquefiable layer, SPT-N	5.4
Standard penetration test blows for the un-liquefiable layer, SPT-N	1.8
Assessed shear strain in liquefiable layer, γ	0.06
Assessed degradation ratio, G_L/G_{max}	0.0002
Slope length, L [m]	380
Slope angle θ [%]	0.006
Thickness of unliquefiable layer, H_1 [m]	1.6
Thickness of liquefiable layer, H_2 [m]	5.9
Young modulus of un-liquefiable layer, E_S [kPa]	5030
Young modulus of liquefiable layer at the time of liquefaction, E_L [kPa]	22.3
Shear modulus of liquefiable layer at the time of liquefaction, G_L [kPa]	7.4
Unit weight of un-liquefied soil, γ_S [kN/m^2]	16.5
Unit weight of un-liquefied soil, γ_L [kN/m^2]	18.5

Table 2. Parameters for calculation of subsidence of house.

Parameters	Values
Assumed maximum design acceleration, A_{max} [Gal]	350
Standard penetration test blows for the liquefiable layer, SPT-N	5.4
Standard penetration test blows for the un-liquefiable layer, SPT-N	1.8
Assessed shear strain in liquefiable layer, γ	0.06
Assessed degradation ratio, G_L/G_{max}	0.0002
House width, B [m]	14
Distance to the boundary of next house, b [m]	6
Unit load of the house, q [kPa]	7
Thickness of un-liquefiable layer, H_1 [m]	1.6
Thickness of liquefiable layer, H_2 [m]	5.9
Young modulus of unliquefiable layer, E_L [kPa]	22.3
Unit weight of unliquefiable soil, γ_S [kN/m^3]	16.5
Unit weight of liquefied soil, γ_L [kN/m^3]	18.5
Coefficient of earth pressure, K_0	0.5
Internal friction angle, ϕ [°]	35

calculated. The result is shown in Figure 21. If a representative value of lateral displacement is picked up near the center of the slope at 200 m from the bottom, the lateral displacement is around 35 cm. As for the house foundation, moreover, the subsidence is 12 cm by using the formula as derived above.

Subsequently, the specification of appropriate ground improvement was examined in order to mitigate the calculated deformations. In case of Christchurch, where severe liquefaction hit the residential area, the affected houses are going to be demolished and the house lots will be vacant. With this situation in mind, the present study supposes that the top of the liquefiable layer is compacted. Compaction for soil improvement is effective in an open site and inexpensive as compared with other soil improvement methods. In consequence of soil compaction at shallow depth, the unliquefiable surface layer increases its thickness and SPT-*N* value therein increases as well by, hypothetically, 10 from the original value.

The results of calculation are shown in Figures 18 and 19. Note that the calculated displacement stands for the combined effects of the increased thickness of the surface unliquefied layer (decrease of the thickness of unliquefiable layer) together with the increased SPT-*N* and Young's modulus, E_s, in the unliquefiable layer. With reference to the argument related with architectural engineering, the allowable displacement for the lateral displacement is decided to be 10 cm and for the subsidence it is 5 cm. Accordingly, the thickness of the unliquefiable layer should be more than 5.4 m for reducing the lateral displacement to the allowable limit and should be more than 2.3 m for the allowable house subsidence.

In addition, Figure 24 illustrates the variation of house subsidence with the thickness of unliquefiable layer and liquefiable layer on condition of the Table 2. This figure also plots the empirical curve proposed by Ishihara (1985) for human safety. It deserves attention that

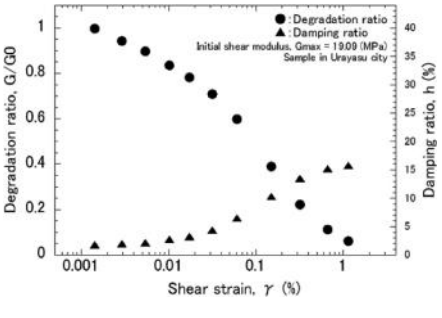

Figure 20. Nonlinear properties of sandy soils in Urayasu City.

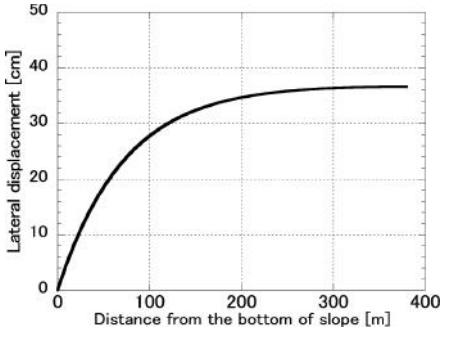

Figure 21. Ultimate lateral displacement of a slope subjected to seismic loading.

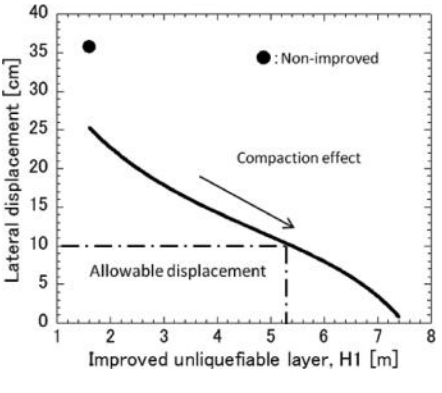

Figure 22. Variation of lateral displacement of slope near its center.

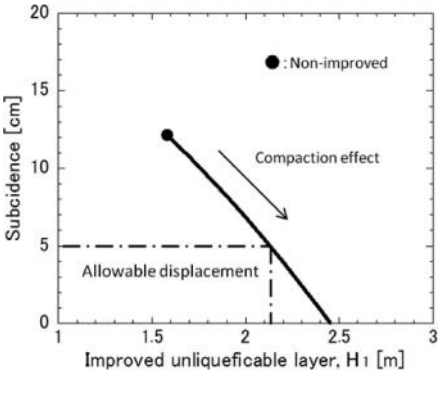

Figure 23. Variation of house subsidence with different extents of surface compaction.

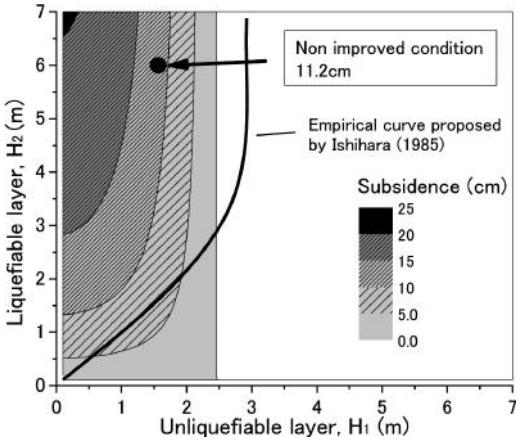

Figure 24. Analysis solution of subsidence against the thickness of unliquefiable soil layer and liquefiable soil layer.

this curve and the product of this paper are consistent with each other in spite of possibly different soil conditions on extent of liquefaction.

7 CONCLUSIONS

The present study addresses the laboratory tests on cyclic behavior of loose sand with non-plastic silt and its application to evaluation of seismic performance of sandy ground. To achieve the second goal, a new mathematical formula was developed by using the principle of minimum potential energy. The major conclusions drawn from this study are as what follows.

1. The current controversy on effects of non-plastic fines content on liquefaction resistance of sand is caused by choices of different constant soil parameters by different researchers. The present study keeps the compaction energy constant for later comparison.
2. Undrained cyclic torsional tests revealed that liquefaction resistance decreases when the fines content increases from 0% to 30%. Beyond 30%, the liquefaction resistance changes in a complicated manner with the further increase of fines content.
3. The secant shear modulus of sand decreases with the progress of cyclic undrained shear. This decrease was related experimentally with the progress of shear strain amplitude.
4. Within the framework of an existing design code, it is possible to assess the reduced shear modulus by using the factor of safety against liquefaction.
5. Closed-form solutions were developed to evaluate the seismic performance of a sloping ground as well as a house with shallow foundation which are subject to effects of pore pressure rise and liquefaction in the subsoil.
6. The developed closed-form solutions were employed to determine the required extent of soil improvement in order to satisfy the allowable level of ground deformation.

ACKNOWLEDGEMENTS

The present study was made possible by the financial support of the Tokyo Gas Company. The subsurface soil data was obtained from the Canterbury Geotechnical Database. During the field investigation, the supports by Prof. M. Cubrinovski of Canterbury University and Dr. R. Orense of University of Auckland were invaluable. Financial support for Japan—New Zealand bilateral scientific collaboration research was supplied by the Ministry of Education,

Sport, Culture, Science and Education. The authors express their sincere gratitude to those supports and assistances.

REFERENCES

Adachi, M., Yasuhara, K. and Shimabukuro, A. 1998. Liquefaction and post-liquefaction recompression characteristics of sand containing non-plastic silt. *Proc. JSCE*, 596/III-43, pp. 29–38.

Adalier, K., Elgamal, A., Meneses, J. and Baez, J.I. 2003. Stone columns as liquefaction countermeasure in non-plastic silty soils, *Soil Dynamics and Earthquake Engineering*, Vol. 23, pp. 571–584

Carraro, J., Bandini, P. and Salgado, R. 2003. Liquefaction resistance of clean and nonplastic silty sands based on cone penetration resistance, *Journal of Geotechnical and Geoenvironmental Engineering, ASCE*, 129(11), pp. 965–976.

Cubrinovski, M., Henderson, D. and Bradley, B.A. 2012. Liquefaction impacts in residential areas in the 2010–2011 Christchurch earthquakes, *One Year after 2011 Great East Japan Earthquake: International Symposium on Engineering Lessons Learned from the Giant Earthquake*, JAEE, Tokyo.

Finn, W.D.L. and Wu, G.X. 2013. Dynamic analyses of an earthfill dam on over-consolidated silt with cyclic strain softening, *7th Int. Conf. on Case Histories in Geotechnical Engineering*, Chicago.

Galandarzadeh, A. and Ahmadi, A. 2012. Effects of Anisotropic Consolidation and Stress Reversal on the Liquefaction Resistance of Sands and Silty Sands, *Geotechnical Engineering Journal of SEAGS & AGSSEA*, 43(2), pp. 33–39.

Huang, Y.-T., Huang, A.-B., Ku, Y.-C. and Tsai, M.-D. 2004. A laboratory study on the undrained strength of a silty sand from Central Western Taiwan, *Soil Dynamics and Earthquake Engineering*, 24 9–10, pp. 733–743.

Hwang, D.J., Yanagisawa, E. and Sugano, T. 1993. Shear characteristics of silt containing sand, *Proc. JSCE, 463/III-22*, pp. 25–33.

Iai, S. and Tobita, T. 2010. Performance-based design of geotechnical structures: recent advances, *5th Int. Conf. on Recent Advances in Geotechnical Earthquake Engineering and Soil Dynamics*, San Diego.

Ishihara, K. 1985. Stability of natural deposits during earthquakes, *11th Int. Conf. on Soil Mechanics and Foundation Engineering*, San Francisco, pp. 321–376

Japanese Geotechnical Society 2006. *Principles for foundation designs grounded on a performance-based design concept*.

Kramer, S.L., Mayfield, R.T. and Anderson, D.G. 2006. Performance-based liquefaction hazard evaluation: implications for codes and standards, *8th U.S. National Conference on Earthquake Engineering*, Paper No. 888.

Lee, W.F., Ishihara, K. and Chen, C.-C. 2012. Liquefaction of silty sand Preliminary studies from recent Taiwan, New Zealand, and Japan earthquakes, *One Year after 2011 Great East Japan Earthquake: International Symposium on Engineering Lessons Learned from the Giant Earthquake*, Tokyo.

Murakami, H., Kaneko, T., Kimura, H., Razavi, S. and Bando, S. 2004. Displacement-based design of reinforcement method for natural slope, *Proc. 11th Int. Conf. Soil Dynamics and Earthquake Engineering and the 3rd Int. Conf. Earthquake Geotechnical Engineering*, Berkeley, Vol. 2, pp. 344–350.

Polito, C.P. and Martin II, J.R. 2001. Effects of nonplastic fines on the liquefaction resistance of sands. *Journal of Geotechnical and Geoenvironmental Engineering*, 127(5), pp. 408–415.

Polito, C.P. and Martin II, J.R. 2003. A reconciliation of the effects of non-plastic fines on the liquefaction resistance of sands reported in the literature, *Earthquake Spectra*, 19(3), pp. 645–651.

Robertson, P.K. 1990. Soil classification using the cone penetration test, *Canadian Geotechnical Journal*, 27(1), pp. 151–158.

Sato, M., Oda, M., Kazama, H. and Ozeki, K. 1997. Fundamental study on the effect of fines on liquefaction strength of reclaimed ground, *Proc. JSCE, 561/III-38*, pp. 271–282.

Suzuki, Y., Tokimatsu, K. and Sanematsu, T. 2003. Correlations between CPT data and soil characteristics obtained from SPT, *Journal of Structural and Construction Engineering*, AIJ, No.566, pp. 73–80.

Torisu, S.S., Sato, J., Towhata, I. and Honda, T. 2010. 1-G model tests and hollow cylindrical torsional shear experiments on seismic residual displacements of fill dams from the viewpoint of seismic performance-based design, *Soil Dynamics and Earthquake Engineering*, 30(6), pp. 423–437.

Towhata, I. 2008. *Geotechnical Earthquake Engineering*, publ. Springer, p. 358.

Towhata, I. 2010. Development towards performance-based design of geotechnical structures subject to seismic action, *Proc. 4th Int. Conf. on Geotechnical Engineering and Soil Mechanics*, Tehran, pp. 73–82.

Towhata, I. 2012. Seismic performance of river levees; experience and prediction, 2nd International Conference on Performance-Based Design in Earthquake Geotechnical Engineering, Taormina, Italy.

Towhata, I., Orense, R.P. and Toyota, H. 1999. Mathematical principles in prediction of lateral ground displacement induced by seismic liquefaction, *Soils and Foundations*, 39(2), pp. 1–19.
Yamamuro, J. and Covert, K.M. 2001. Monotonic and cyclic liquefaction of very lose sands with high silt content, *Journal of Geotechnical and Geoenvironmental Engineering, ASCE*, 127(4), pp. 314–324.
Yamamuro, J.A. and Lade, P.V. 1998. Steady-state concepts and static liquefaction of silty sands, *Journal of Geotechnical and Geoenvironmental Engineering, ASCE*, 124(9), pp. 868–877.
Wieland, M. 2012a. Seismic design and safety aspects of bottom outlets, spillways and intake structures of large storage dams, *15th World Conference on Earthquake Engineering*, Lisbon.
Wieland, M. 2012b. Seismic design and performance criteria for large storage dams, *15th World Conference on Earthquake Engineering*, Lisbon.

Soil Liquefaction during Recent Large-Scale Earthquakes – Orense, Towhata & Chouw (Eds)

Slope failures in residential land on volcanic fills during the 2011 Great East Japan earthquake

M. Hyodo
Department of Civil and Environmental Engineering, Yamaguchi University, Ube, Yamaguchi, Japan

R.P. Orense
Department of Civil and Environmental Engineering, University of Auckland, Auckland, New Zealand

S. Noda
Department of Civil and Environmental Engineering, Yamaguchi University, Ube, Yamaguchi, Japan

ABSTRACT: As a result of the 2011 off the Pacific coast of Tohoku Earthquake, five slope failures occurred in a residential area on artificial valley fills in Taiyo New Town, Yamamoto, Miyagi Prefecture. The fill material is sandy, derived from the weathering of tuffaceous sandstone which formed the natural ground. Cyclic triaxial tests showed that the fill, which has about F_c = 20%, has very low liquefaction resistance, which decreased with application of initial static shear stress. A pseudo-static slope stability analysis, using conventional strength parameters, could not explain the slope failure at one of the sites that failed, but it could explain the slope failure when the dynamic strength was used to represent the soil strength at the slip surface. Thus, the slope failures in Taiyo New Town, at least at the one analyzed in this study, could be attributed to the liquefaction of the fill material induced by the intense shaking.

1 INTRODUCTION

With moment magnitude M_w 9.0, the gigantic 2011 off the Pacific coast of Tohoku Earthquake (also called the 2011 Great East Japan Earthquake) caused extensive damage to life and property in Tohoku and Kanto regions in eastern part of Japan. One of the worst hit areas is the coastal town of Yamamoto on southern part of Miyagi Prefecture. Almost 24 km^2 of the town's 64 km^2 area, or about 38%, was flooded and destroyed by the large-scale tsunami generated by the earthquake (GSI, 2011). Most of the inundated area was on the eastern side of the National Route 6. In addition, several slope failures occurred on the hilly areas located to the west of Route 6. In terms of slope failures, one of the worst-hit areas was Taiyo New Town, a housing site located on artificial valley fill just to the west of Route 6. The site was constructed by leveling the hilly area and using the cut materials as fills for the valleys to provide viable land for residential purposes. Following the earthquake, slope failures occurred in five different sections of the land, damaging houses, roads, park and pipelines. In one of the failed sites, the debris slid and covered a parking lot just on the side of Route 6. Following the earthquake, site investigations were performed at the site in order to clarify the causes(s) of the slope failures. Samples were obtained at several locations adjacent to the failed slopes and laboratory tests were conducted to investigate their geotechnical properties. Finally, slope stability analyses were conducted in order to better understand the response of the embankment to earthquake loading. The results highlighted the seismic vulnerability of residential areas on artificial valley fills like Taiyo New Town that are constructed with weak tuffaceous materials as fill.

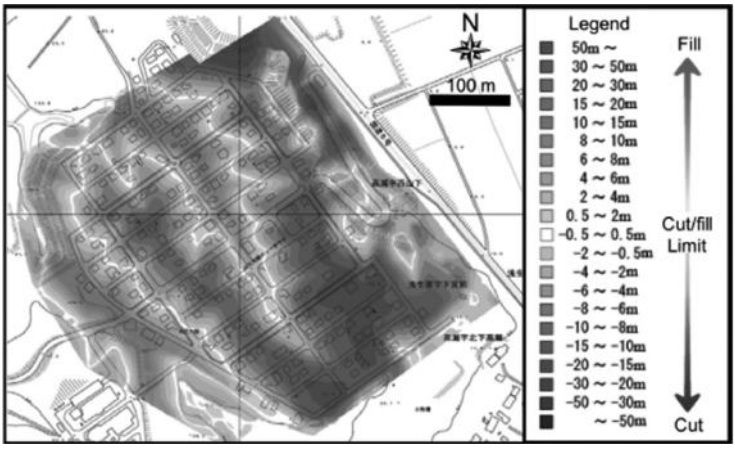

Figure 1. The housing site foundation map of Taiyo New Town, showing the thickness distribution of cut and fill sections (Fukken Gijutsu Consultant, 2008).

2 DESCRIPTION OF THE AREA

The Taiyo New Town housing site is located in the central part of Yamamoto, a coastal town on the southern edge of Miyagi Prefecture. It is located on the hilly region to the west of Route No. 6, which traverses the prefecture in almost northwest-southeast direction. In fact, Route 6 appears to be the dividing line between the coastal plain on the east and the 40–50 m high mountains (Wariyama uplift zone) on the west of the prefecture.

The site of the residential area was developed in the 1970s by cutting and leveling off some parts of the hills and using the materials as fill for the valleys. Figure 1 shows the depth distribution of cuts and fills in Taiyo New Town. To level off the residential land, cuts were made on the hills as high as 8–10 m, while valley floors as deep as 10–15 m were filled up using the same materials that were cut from the elevated regions. It can be observed that deep valleys existed in the central portion and in western boundary of the site. The eastern side of the site adjacent to Route 6 was also filled up, with embankment having slope of 1:1.5. The elevation of the filled-up residential site was about 35 m above mean sea level. It has an area of about 0.12 km2 and when the earthquake struck, more than 200 houses occupied the site.

Investigation of the local geology of the site revealed that the original ground consisted of tuffaceous sandstones of the Yamamoto Formation. Subsequent boring data showed that the sandstones were weakly cemented and exhibited high degree of weathering towards the surface, with the surficial layer appearing like sandy soil. Thus, the material used to fill up the valleys consisted of sandy soils from the weathered tuffaceous sandstones. Standard penetration tests indicated that the sandy material used as fill has an average *N*-value of 5, while the in situ soils, comprising a highly weathered top layer and the weathered layer, the sandstone has average *N*-values of 6 and 16, respectively.

3 STRONG MOTION STATION AND SEISMIC RECORDS

About 2 km to the south of Taiyo New Town, the National Research Institute for Earth Science and Disaster Prevention (NIED) operates a KiK-Net seismic station (MYGH10: Yamamoto Station) with digital strong-motion seismometers installed at the ground surface and at a depth of GL-205 m. The 2011 Tohoku earthquake triggered many seismic stations in the area, including the one in Yamamoto, and recorded strong motions. Figure 2 shows the acceleration time histories recorded at the station, both on the surface and at depth, while Figure 3 illustrates the corresponding Fourier spectra of the acceleration records. The peak accelerations recorded at depth were in the range of 150~220 cm/sec^2 with predominant

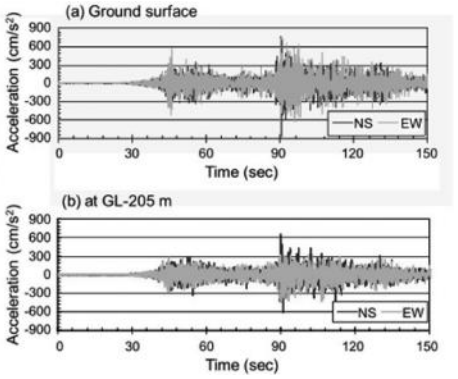

Figure 2. Acceleration time histories obtained from Yamamoto KiK-Net Seismic station: (a) at ground surface; (b) at GL-205 m (data from KiK-Net website).

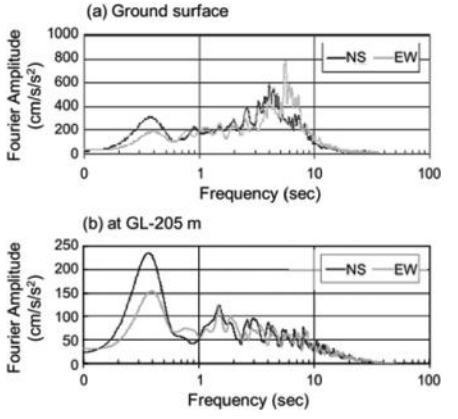

Figure 3. Fourier spectra of acceleration records obtained from Yamamoto KiK-Net Seismic station: (a) at ground surface; (b) at GL-205 m.

Table 1. Soil profile at Yamamoto KiK-Net seismic station (MYGH10) (data from KiK-Net website).

Depth (m)	Thickness (m)	Type of soil/rock	V_p (m/s)	V_s(m/s)
2.0	2.0	Clay	500	110
3.5	1.5	Clay	1750	250
8.0	4.5	Sandstone	1750	390
18.0	10.0	Conglomerate	1750	390
34.0	16.0	Sandstone	1750	390
42.0	8.0	Pumiceous tuff	1830	590
114.0	72.0	Tuffaceous sandstone	1830	590
142.0	28.0	Sanstone	1920	770
178.0	56.0	Tuffaceous sandstone	1920	770
208.0	30.0	silt	1920	770

frequency of 0.35 Hz. The ground level accelerations were much higher, 850~870 cm/sec^2, with the predominant frequency shifting to 4–6 Hz.

The soil profile at KiK-Net Yamamoto station is shown in Table 1. It can be observed that tuffaceous sandstone with shear wave velocity V_s<770 m/sec exists in the vicinity of the

seismometer installed at the bottom of the borehole. Moreover, the upper layer generally consisted of pumiceous tuff and tuffaceous sandstones. This profile generally amplified the seismic motion as it propagates towards the ground surface.

4 OUTLINE OF DAMAGE

Following the 2011 earthquake, slope failures occurred at five sites within the Taiyo New Town housing site. The locations of the slope failure are shown in Figure 4. These failed or slid blocks were sequentially numbered, starting with Failed Block 1 on the eastern boundary of the housing site, going counterclockwise to Failed Block 5 on the western side. Block 1 consisted of two landslides, referred to as Block 1–1 and Block 1–2, respectively. Also shown in the figure are the locations of damaged roads due to the slope failure and damaged road pavements. Extensometers were placed on the eastern boundary to monitor the movement of the fill. In addition, several standard penetrations tests were performed within the fill and adjacent to the failed blocks.

Comparing the locations of the failed blocks in the housing site (Figure 4) with the foundation ground map shown in Figure 1, it is clear that all failed slopes occurred either on the edge of the valley fill or on the shoulder of the embankment. This suggests that the fill material, rather than the natural ground, was involved in the slope failures. Two failed blocks are described in this section.

4.1 *Failed Block 1*

Block 1 consisted of two slope failures. The first sliding block, 1–1, caused settlement at the crest and laterally flowed down the sloping ground, as shown schematically in Figure 5. As a result, a house located on the laterally moving ground tilted and a 1 m high vertical offset

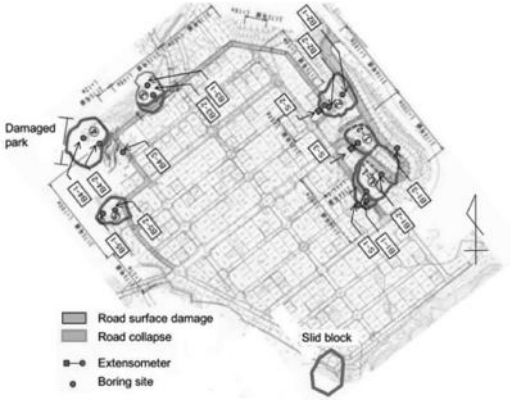

Figure 4. Location of failed slopes in Taiyo New Town.

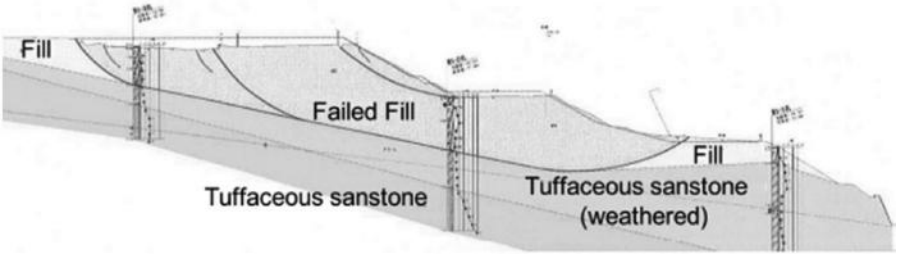

Figure 5. Cross-sectional profile of failed slope in Block 1–1.

was also created. Extensional cracks were also observed on the ground and road pavements. The adjacent failed block, 1–2, was smaller in scope and induced cracking on the road as the sliding mass displaced. In both cases, the surface of the road downslope was pushed up.

4.2 *Failed Block 2*

About 50 m north of failed Block 1, the shoulder of the embankment collapsed, sending debris 15 m below towards the parking lot adjacent to a convenience store. It is apparent that the failure was confined to the upper layer consisting of fill material. A house located at the crest of the sliding mass was partially damaged, while the roads positioned at the top and midway of the slope were totally destroyed, sending cracked pavements downward. Just to the north of the failed slope and down on the main road, a reinforced retaining wall missed the landslide. This retaining wall was constructed in 2008 when the section failed following a heavy rainfall; the retaining wall was not damaged by this earthquake.

5 SOIL CHARACTERISTICS

To understand the characteristics of the fill material, soil samples were obtained adjacent to the failed blocks and geotechnical tests were performed.

5.1 *Geotechnical properties*

Soils samples were obtained near failed Blocks 1, 2, 3 and 5 in order to investigate the geotechnical properties of the soil used as fill. Figure 6 shows the grain size distribution curves for samples from the four sites. It can be seen that the curves were fairly similar at all three locations, indicating that the fill materials were uniform throughout the housing site. The soil have fairly uniform distribution with fines content, $F_c = 20\%$.

Samples obtained from Block 1 site were quite abundant and these were used in most of the geotechnical tests. Index property tests, based on Japanese Geotechnical Society standards (JGS, 2001) showed that the density of the particles was 2.478 g/cm^3, while the maximum and minimum densities were 1.319 and 1.079 g/cm^3, respectively. The compaction curve is shown in Figure 8 where it is seen that the optimum water content is $w_{opt} = 13.8\%$ corresponding to maximum dry density, $\rho_{dmax} = 1.822$ g/cm^3.

5.2 *Triaxial test results*

Next, monotonic drained and cyclic undrained triaxial tests were conducted on the soil samples. In these tests, the reconstituted samples were prepared such that they have dry density equal to 90% of the maximum dry density, i.e., degree of compaction $D_c = 90\%$. Using

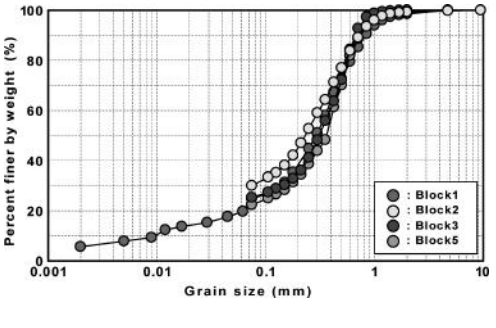

Figure 6. Grain size distribution curves of samples obtained from four sites.

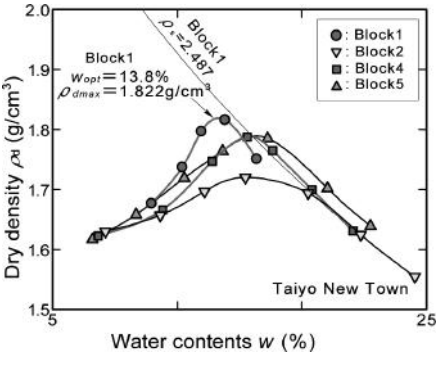

Figure 7. Compaction curves.

the obtained maximum and minimum dry densities, this corresponds to a relative density $D_r = 188\%$. The results of the monotonic drained tests for confining pressure of $\sigma_c' = 50$, 100 and 150 kPa are shown in Figure 8. Undrained shear test was also performed for confining pressure of $\sigma_c' = 100$ kPa and presented in the figure. The soil shows contractive behavior at all levels of applied pressure. This may be due to the collapsible behavior of weathered tuffaceous sandstone. From the stress-strain relations, Mohr circles of stress were drawn at residual state as shown in Figure 9, and the strength parameters were obtained. The results indicate the following values: cohesion, $c = 9$ kPa, and angle of internal friction $\phi = 31.7^{\circ}$. Such internal friction angle is quite low for sandy soils.

Cyclic undrained triaxial tests were performed on reconstituted samples under isotropically consolidated condition, and the liquefaction resistance curve obtained for a double amplitude axial strain $\varepsilon_{DA} = 5\%$ is shown by the solid circles in Figure 10. It is seen that the liquefaction resistance of the material is quite low, indicating the susceptibility of the material to large deformation when shaken under saturated condition. This may be due to the high fines content of the soil and the density used to prepare the reconstituted specimen. Note that for soil specimens with $D_c = 90\%$, the dry density of the soil was taken as 1.64 g/cm^3. According to Yamamoto Town Office, dry densities ranging from 1.44–1.54 g/cm^3 were obtained at the site based on previous site investigations. Thus, although the density of the specimen used in the test was higher than the in-situ values, the liquefaction resistance of the soil was low. Although the location of the water table during the earthquake was not confirmed, this type of material will liquefy easily when subjected to cyclic shearing induced by earthquake, and will fail due to reduction in effective stress.

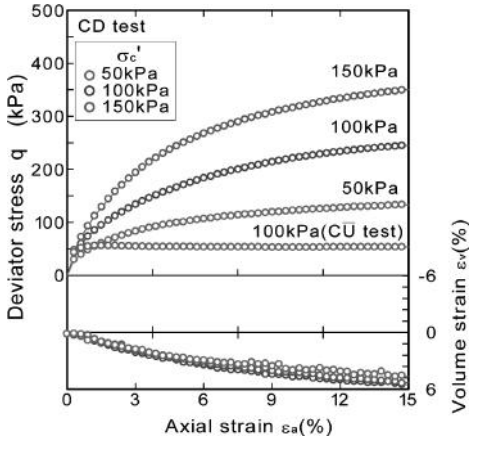

Figure 8. Results of consolidated drained triaxial tests.

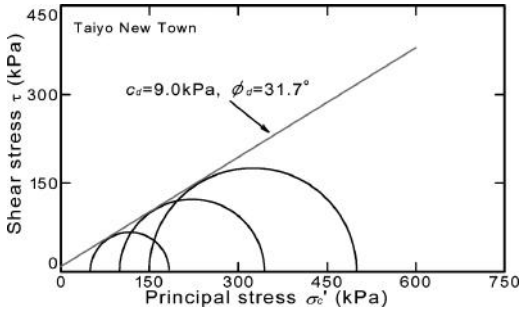

Figure 9. Mohr's stress circles and failure envelope from results by drained triaxial tests.

In order to simulate the presence of initial shear stress in sloping grounds, such as in the present embankment, cyclic undrained triaxial tests were also performed on anisotropically consolidated specimens. Results for cases with initial static shear stress ratio, $\sigma_s/2\sigma_c' = 0.30$, and 0.375 are also indicated in Figure 10. In case of anisotropically consolidated samples, the cyclic failure was defined in terms of peak axial strain $\varepsilon_p = 5\%$. It appears that if the fill material is subjected to initial static stress, the cyclic strength decreases; such behavior is quite different from those observed for other types of granular materials (Vaid, 1983; Hyodo et al., 1991, 1994; Hosono and Yoshimine, 2004). This confirms that the fill material is indeed weak and susceptible to large deformation under earthquake loading. Figure 11 shows the cyclic deviator stress ratio to cause failure after 20 cycles. The results for Toyoura sand with $D_r = 50\%$ and $D_r = 70\%$ are also shown in the figure for comparison. In the case of Toyoura sand, the cyclic strength increases with initial shear stress ratio as expected for medium to dense material. However, in the case of the sampled soil, the cyclic strength decreased with increasing initial shear stress ratio, although it should be noted that the definition of failure changed from $\varepsilon_{DA} = 5\%$ to $\varepsilon_p = 5\%$. Further it should be noted that failure occurred for stress non-reversal condition at the material while stress reversal was necessary to cause failure at dense Toyoura sand.

Figure 12 shows the stress paths and corresponding relationship between cyclic deviator stress and axial strain for both isotropically and anisotropically consolidated samples. Examination of the cyclic stress paths for isotropically consolidated sample shows liquefaction occurring as the stress path cycles through zero effective confining pressure. The development of cyclic strains occurs in both compression and extension. The cyclic failure was defined as a strain double amplitude of 5% ($\varepsilon_{DA} = 5\%$). On the other hand, the cyclic stress paths for anisotropically consolidated samples shows cyclic failure occurring as the stress

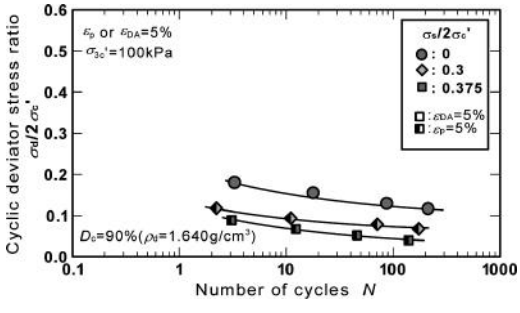

Figure 10. Liquefaction resistance curves of isotropically and anisotropically consolidated samples.

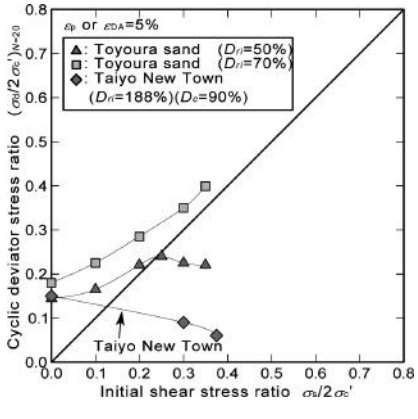

Figure 11. Variation of cyclic strength at $N = 20$ cycles with initial shear stress ratio.

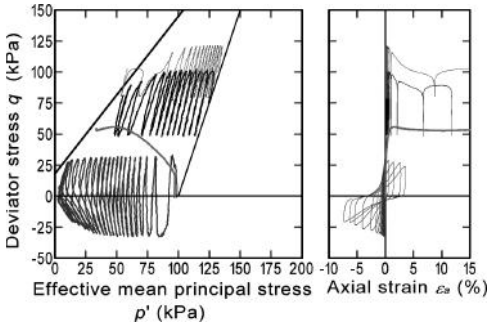

Figure 12. Cyclic stress paths and cyclic stress strain curves for isotropically and anisotropically consolidated samples.

path reaches to the failure envelope developed by monotonic shear tests. The corresponding cyclic stress strain plots are shown taken to peak axial strain of approximately 15%. It should be noted that cyclic strain amplitude becomes larger as the stress path approaches to failure envelope. The cyclic strength for anisotropic samples was defined as the number of cycles to reach peak axial strain $\varepsilon_p = 5\%$.

6 SLOPE STABILITY ANALYSES

To explain the cause of failure, preliminary analyses were conducted considering the stability of the embankments during the 2011 earthquake under different scenarios. For this purpose, pseudostatic analyses were performed. The equivalent strong motion at the top of the embankment was determined through the procedure outlined in Figure 13. Firstly, the model for the 1-D soil profile at the location of the KiK-net seismic station (Table 1) was verified using earthquake recordings obtained during previous smaller earthquakes of 1 September 2010 and 10 February 2011. In both cases, the time history of acceleration recorded on the ground surface was used as input and the acceleration at the bottom of the borehole (GL-205 m) was simulated using the program SHAKE. Next, to incorporate the non-linear response of the soil due to the larger amplitude of motion resulting from the 2011 Tohoku earthquake event, the surface motion (Figure 2a) was used as input to simulate the motion at GL-205 m (Figure 2b). Due to space limitation, the details of the calculations are not presented here. Suffice it to say that the 1-D ground model at the seismic station site was sufficiently validated. From the last analysis, the incident wave (2E) at the engineering bedrock, Point C, was calculated for both N-S and E-W direction.

For the purpose of analysis, the cross-sectional profile for Block 1 shown in Figure 5 was used. Using the boring data obtained from field tests and knowing that the natural period of the site is 0.7 sec, the soil profile and corresponding parameters were established, as summarized in Table 2. The depth of the engineering bedrock from the surface of the fill was 34 m.

Next, the strong motion obtained at Point C was used as input (2E) at Point B to determine the surface acceleration at Point A. Since Point C and Point B are just 2 km apart, attenuation of motion was not considered. Again, seismic response analyses were conducted and the results obtained showed PGAs at point A of 1322.6 and 1171.3 cm/sec^2 in N-S and E-W directions, respectively. Using the equation for lateral seismic coefficient, k_h, proposed by Noda et al. (1975), the obtained PGAs correspond to $k_h = 0.37$ and 0.35, respectively.

In the pseudostatic analysis of slope stability, three cases of ground models and slip failures were considered: Case A, where ground water table is low (effect not considered) with composite slip surfaces; Case B – 1, where ground water table is near the boundary between fill and sandstone with composite slip surfaces; and Case B – 2 where ground water table is near the boundary between fill and sandstone with cylindrical slip surface. In the analyses, the strength parameters obtained from monotonic drained triaxial tests were used. In

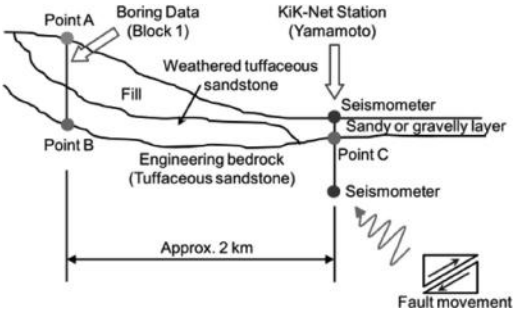

Figure 13. Schematic diagram showing how the PGA on top of the fill was calculated from KiK-Net recorded motions.

Table 2. Soil profile and soil properties for failed Block 1 site used in the analysis.

Soil type	Depth (m)	H (m)	SPT N-value	γ_t (kN/m^3)	γ_{sat} (kN/m^3)	V_s (m/sec)	4H/V_s (sec)
Fill (sandy type)	6	6	4.7	17.5	18.9	128	0.19
Tuffaceous sand stone (strongly weathered)	12	6	6.7	18.6	20.6	149	0.16
Tuffaceous sandstone (weathered)	34	22	32.4	18.6	20.6	252	0.35

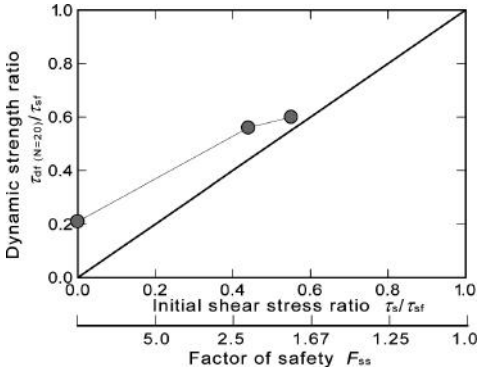

Figure 14. Relation between dynamic strength and initial stress obtained from triaxial test results.

addition to the analyses using conventional strength parameters, a supplementary analysis was performed using the results of cyclic triaxial tests instead. In such analysis, two stages were considered: static analysis prior to the application of the seismic load, and dynamic analysis using pseudo-static approach. In the static analysis, the strength parameters (cohesion c and frictional angle ϕ) obtained from conventional tests were used. Since the calculated factor of safety, F_s, indicates the ratio of the shear resistance, τ_{sf}, and shear stress, τ_s, along the slip surface (i.e., $F_s = \tau_{sf}/\tau_s$), it is possible to estimate the average static shear stress along the slip plane from the known values of F_s and τ_{sf}. From Figure 11, the cyclic shear resistance ratios corresponding to $N = 20$ cycles were read from the curves, and the data were used to plot the dynamic strength ratio, τ_d/τ_{sf}, as a function of the initial shear stress ratio, τ_s/τ_{sf}, as illustrated in Figure 14. Thus, knowing the average static shear stress along a slip plane, the corresponding cyclic resistance (or dynamic strength) can be estimated. The cyclic resistance is added to the initial static shear stresses and then used as strength parameters in performing

Table 3. Results of pseudo-static analysis for the failed embankment in Block 1.

Case	Condition	Strength parameters	Yield acceleration, k_y	
			Slip 1	Slip 2
A	No water table; composite slip surfaces	$c_d = 9$ kN/m^3, $\phi = 31.7^o$	0.46	0.42
B-1	With water table; composite slip surface		0.43	0.39
B-2	With water table; cylindrical slip surface		0.42	
B-2'	With water table; cylindrical slip surface	$c_d = 9$ kN/m^3, $\phi = 31.7^o$; then changed to dynamic strength	0.24	

the pseudo-static analysis to compute the F_s for the specified earthquake load. Note that in this procedure, it is tacitly assumed that the earthquake loading is applied for $N = 20$ cycles.

In all the pseudo-static analysis conducted, the yield acceleration, k_y, corresponding to the limit equilibrium condition $F_s = 1.0$ was calculated. For simplicity, the value of k_y was assumed to be constant throughout the duration of earthquake loading.

The results of the analyses are summarized in Table 3 for all the cases considered in terms of the yield acceleration, k_y, necessary for limit equilibrium condition ($F_s = 1.0$). For cases with composite failure surfaces, the values for the two major slip surfaces considered are also indicated. Considering that the results of SHAKE analysis showed k_h values of 0.35–0.37, the only condition where k_y is less than these values is the case involving the use of dynamic strength at the slip surface; all other cases using conventional strength parameters resulted in higher value of k_y than that induced by the 2011 earthquake. For the conventional analysis to hold, k_h should at least be 0.39, or a PGA of 1,570 cm/sec^2; this value is too large.

Thus, based on the calculations presented above, it appears that the slope failure in Taiyo New Town can be attributed to the liquefaction of the fill, especially near the interface between the top fill layer and the highly weathered tuffaceous sandstone. With the development of excess pore water pressure, the fill underwent large deformation during the shaking induced by the gigantic Tohoku earthquake.

7 CONCLUSIONS

The gigantic 2011 off the Pacific coast of Tohoku Earthquake caused 5 slope failures in Taiyo New Town, a housing site on artificial valley fill in Yamamoto town, Miyagi Prefecture. To understand the mechanism of the slope failures, field inspection, strong motion record analyses, laboratory tests and slope stability analyses were conducted. The following are the major conclusions from this study:

1. The residential site of Taiyo New Town was constructed through cut and fill method. The original hilly ground consisted of weakly consolidated tuffaceous sandstone, which showed high degree of weathering towards the surface and manifested itself as sand on the surface. Thus, the fill material used to fill-up the valleys was generally sandy soil.
2. The maximum surface acceleration recorded in Yamamoto seismic station was 850–870 cm/sec^2 with predominant period of 4–6 Hz. The estimated maximum acceleration on top of the fill based on seismic response analyses was 1170–1300 cm/sec^2.
3. Each of the five slope failures at the housing site was observed to occur at the boundary between the filled-up valley and the fill or on the shoulder of the embankment.
4. The sandy fill material has fines content $F_c = 20\%$. Even when compacted at 90% degree of compaction, the fill material showed very low internal friction angle and low liquefaction

resistance. Moreover, the liquefaction resistance decreased with application of initial shear stress.

5. Pseudo-static slope stability analysis using conventional strength parameters cannot explain the slope failure in Block 1. However, when dynamic strength (or liquefaction resistance) was used to represent the soil strength at the slip surface, the yield seismic coefficient required to induce failure was lower than the estimated seismic coefficient on top of the fill.

The slope failure in Taiyo New Town can be attributed to the liquefaction of the fill material induced by the intense shaking. It was possible that during the earthquake, the ground water level was near the boundary of the original ground and the fill, making liquefaction possible.

ACKNOWLEDGEMENTS

The authors would like to acknowledge the assistance of the engineering staff of Yamamoto Town Office for providing access to the site for inspection and for the valuable information during subsequent meetings. The strong motion data was obtained from K-Net.

REFERENCES

Fukken Gijutsu Consultant Co. Ltd. 2008. *Ground Map of Built-up Residential Land*, 1:25,000 scale.

Geospatial Information Agency of Japan, GSI 2011. *Area Flooded by the Tsunami (Approximate)*, http://www.gsi.go.jp/common/000059734.pdf (in Japanese).

Hosono, Y. and Yoshimine, M. 2004. Liquefaction of sand in simple shear condition. *Proc., International Conference on Cyclic Behaviour of Soils and Liquefaction Phenomena*, Bochum, Germany, 129–136.

Hyodo, M., Murata, H., Yasufuku, N. and Fujii, T. 1991. Undrained cyclic shear strength and residual strength of saturated sand by cyclic triaxial tests. *Soils and Foundations*, Vol. 31, No. 3, 60–76.

Hyodo, M., Tanimisu, H., Yasufuku, N. and Murata, H. 1994. Undrained cyclic and monotonic behavior of saturated loose sand. *Soils and Foundations*, Vol. 34, No. 1, 19–32.

Japanese Geotechnical Society 2001. *Soil Testing Procedure and Commentary*, (in Japanese).

KiK-Net 2011. *Digital Strong Motion Network*, http://www.kik.bosai.go.jp/.

Nakamura, Y. 1989. A method for dynamic characteristics estimation of subsurface using microtremor on the ground surface. *Quarterly Report of Railway Technical Research Institute*, Vol. 30, No. 1, 25 to 33.

Noda, S., Uwabe, T. and Chiba, T. 1975. Relation between seismic coefficient and ground acceleration for gravity quay wall. *Report of the Port and Harbour Research Institute*, 14 (4) (in Japanese).

Vaid, Y.P., Chung, E.K.F. and Kuerbis, R.H. 1990. Stress path and steady state. *Canadian Geotechnical Journal,* 27(1): 1–7.

This page intentionally left blank

Liquefaction effects on structures

This page intentionally left blank

Soil Liquefaction during Recent Large-Scale Earthquakes – Orense, Towhata & Chouw (Eds)

Liquefaction effects in the Central Business District of Christchurch

J. Bray
Department of Civil and Environmental Engineering, University of California at Berkeley, CA, USA

M. Cubrinovski
Department of Civil and Natural Resources Engineering, University of Canterbury, Christchurch, New Zealand

J. Zupan
Department of Civil and Environmental Engineering, University of California at Berkeley, CA, USA

M. Taylor
Department of Civil and Natural Resources Engineering, University of Canterbury, Christchurch, New Zealand

ABSTRACT: The Canterbury earthquake sequence provides an exceptional opportunity to investigate the effects of varying degrees of liquefaction on the built environment. Many multi-story buildings in the Central Business District were heavily damaged by liquefaction-induced ground movements during the Christchurch earthquake, but not by other earthquakes (e.g., Darfield and June 2011 events). CPT-based liquefaction triggering evaluations were conservative. The conservatism in the liquefaction triggering assessments led to post-liquefaction ground settlement estimates that were generally similar for the large events in the earthquake sequence, whereas significant ground settlements and building damage in the CBD were only observed for the Christchurch earthquake. Moreover, the liquefaction-induced ground settlement procedures do not capture important shear-induced deformation mechanisms and the effects of ground loss due to sediment ejecta. Performance-based earthquake engineering requires improved procedures to capture the differing levels of performance observed in Christchurch.

1 INTRODUCTION

The Canterbury earthquake sequence included seven events with $M_w \geq 5.5$, three of which had $M_w \geq 6.0$. Ground shaking was recorded at four Strong Motion Stations (SMS) within the CBD, the locations of which are shown in Fig. 1. The geometric mean horizontal Peak Ground Accelerations (PGA) recorded at the stations are provided in Table 1 for five events. The 22 FEB 11 Christchurch M_w 6.2 earthquake produced the most intense ground shaking in the CBD, because the source-to-site distances (R) were only 3–6 km. Its PGA values were twice those recorded during the larger, but more distant (R = 18–20 km), 4 SEP 10 Darfield M_w 7.1 event. The PGAs recorded in the CBD during the Darfield event are similar to those recorded during the 26 DEC 10 M_w 4.8, 13 JUN 11 M_w 6.0, and 23 DEC 11 M_w 5.9 events. The PGA values of the dozens of other M_w 5^+ events are lower than those recorded during these events. The Canterbury earthquake sequence provides an unparalleled opportunity to investigate the effects of varying degrees of liquefaction on the built environment.

The Christchurch earthquake produced large areas of liquefaction in the CBD as shown in Fig. 1. The Darfield and June 2011 earthquakes also produced localized areas of liquefaction. Hence, these events are explored in more depth. However, examining the less damaging

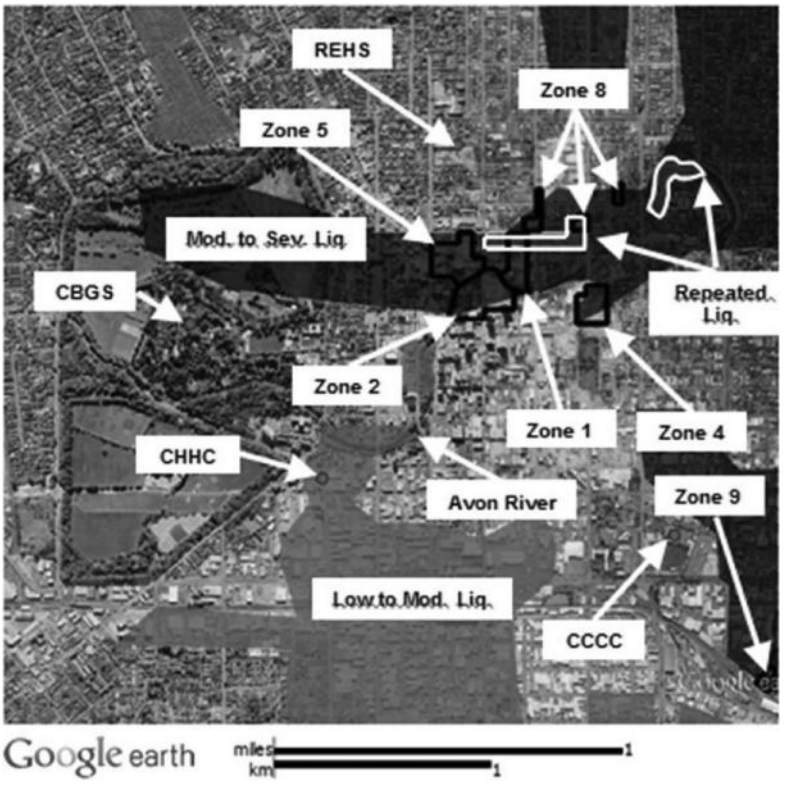

Figure 1. CBD location plan with strong ground motion recording stations and study zones. Shaded zones indicate areas with surficial evidence of soil liquefaction during the 22 FEB 11 event: dark shading indicates moderate-to-severe liquefaction and gray shading indicates low-to-moderate liquefaction (as defined by Cubrinovski et al. 2011b); white outlining indicates areas that also liquefied during the 4 SEP 10 and 13 JUN 11 events.

Table 1. Recorded PGAs in the CBD during five 2010–11 canterbury earthquake events.

Date	M_w	Geometric mean PGA (g) at CBD recording stations				Median PGA (g)
		CBGS	CCCC	CHHC	REHS	
4 SEP 10	7.1	0.17	0.21	0.18	0.25	0.20
26 DEC 10	4.8	0.25	0.22	0.16	0.24	0.21
22 FEB 11	6.2	0.48	0.42	0.35	0.51	0.44
13 JUN 11	6.0	0.16	-	0.21	0.29	0.21
23 DEC 11	5.9	0.20	0.18	0.21	0.30	0.22

events is also important, because it is critical to evaluate if liquefaction evaluation procedures can discern between damaging events and non-damaging events. The 26 DEC 10 earthquake is useful for this purpose, as no liquefaction was observed in the CBD for this event.

Following the 22 February 2011 Christchurch M_w 6.2 earthquake, the UC Berkeley (UCB) – Univ. of Canterbury (UC) research team performed 107 CPTs and 2 boreholes at 23 building sites within 6 study zones to enable detailed subsurface characterizations and simplified seismic evaluations of representative buildings within the CBD (see Figure 1 and Figure 2). These structures consisted of multi-story buildings on shallow and deep foundations and displayed interesting engineering performance characteristics. This subset included buildings that performed well, in addition to buildings that were severely damaged during the

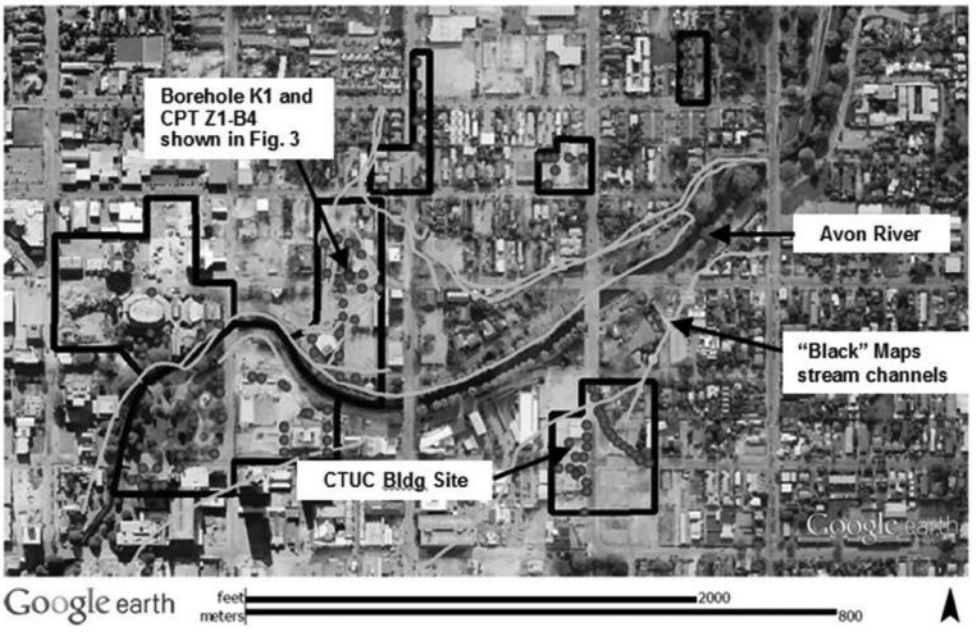

Figure 2. UCB-UC site investigation overview. CPTs are indicated with red dots and boreholes are indicated with blue dots. Locations of buried stream channels from the "Black" Maps are shown with aqua lines. The locations of the CTUC building site, borehole K1, and CPT Z1-B4 are shown for reference. Work in Zone 9 is not shown.

Christchurch earthquake. In this paper, the investigation and evaluation of one of the most insightful building case histories is presented.

2 GENERALIZED SUBSURFACE CONDITIONS IN THE CBD

The Canterbury Plains are composed of complex alluvial fans deposited by eastward-flowing rivers draining the Southern Alps and discharging into Pegasus Bay on the Pacific Coast. Christchurch lies along the eastern extent of the Canterbury Plains, just north of the Banks Peninsula, the eroded remnant of the extinct Lyttelton Volcano, comprised of weathered basalt and Pleistocene loess (Cubrinovski et al. 2011a). The city was built on a historic floodplain of the Waimakiriri River, a large braided river that is now channelized approximately 25 km north of the CBD. The Waimakiriri River regularly flooded Christchurch prior to the construction of levees and river realignment carried out shortly after the city was established in the 1850s (Brown and Weeber 1992; Brown et al. 1995). The "Black" Maps depict several buried stream channels through the CBD, which intersect the study zones (Cubrinovski et al. 2011a). The subsurface conditions in the CBD are highly variable with alternating layers of sands and gravels with overbank deposits of silty soils and some peat pockets, which is indicative of the ephemeral nature of floodplains.

There are three geological formations of primary interest in foundation engineering within the CBD: the Springston Formation, Christchurch Formation, and Riccarton Gravels. The Springston Formation was deposited during the last 3000 years and is the shallowest of the three formations. It consists of three lithologic units (Brown and Weeber 1992): 1) gravels deposited in old flood channels of the Waimakariri River; 2) overbank alluvial silt and sandy silt; and 3) peat deposits formed in marshland. The Christchurch Formation consists of beach, estuarine, lagoon, dune, and coastal swamp deposits composed of gravel, sand, silt,

clay, shells, and peat, and its top is found at a depth of typically 7 to 10 m. Brown and Weeber (1992) describe its age as post-glacial and likely less than 6,500 years old near the maximum inland extent of the post-glacial marine transgression, which likely extended across the CBD based on the presence of shells observed in soil samples (T&T 2011). The Riccarton Gravels are beneath the Christchurch formation and consist of well-graded brown or blue-gray gravels up to cobble size. This 10 to 20 m thick formation is the uppermost confined gravel aquifer in coastal northern Canterbury and is typically about 18 to 30 m below the ground surface in the CBD (Brown and Weeber 1992; T&T 2011).

Two spring fed rivers, the Avon and Heathcote, meander through Christchurch and discharge into an estuary east of Christchurch. The Avon River, labeled in Fig. 1 and Fig. 2, meanders through the CBD, while the Heathcote River flows south of the CBD. Much of the observed moderate-to-severe liquefaction within and to the east of the CBD occurred near the Avon River during the Canterbury earthquakes. The groundwater table is generally within 1 to 3 meters of the ground surface within the CBD.

3 SITE INVESTIGATIONS

Though subsurface conditions within the CBD are variable (Brown and Weeber 1992; T&T 2011), each building study zone has one or two representative soil profiles that reflect the subsurface conditions within a zone. Figure 3 illustrates representative subsurface conditions within Zone 1 with the log of borehole K1 and the adjacent CPT Z1-B4 (locations indicated on Figure 2) with its normalized cone tip resistance (q_{c1N}) and soil behavior type index (I_c) profiles calculated using the procedure described by Robertson and Wride (1998). The soil layer that lies at a depth of about 2 to 8 m has relatively low q_{c1N} values (< 50) and consists of predominantly silty sand (SM), but also sandy silt (ML), with a median fines content (F_C) of approximately 37% (range of 15% to 82% with a standard deviation of 21%) based on 19 laboratory tests performed on retrieved samples. The fines were predominantly non-plastic. Below it, a denser poorly graded sand (SP) extends down to about 20 m. The base silt/clay (ML/MH) layer is the oldest and deepest material of the Christchurch Formation and is typically observed just above the Riccarton Gravels (T&T 2011).

In addition to advancing CPTs adjacent to buildings, a line of 15 CPTs spaced about 10 m apart were advanced in a parking lot at the northeast corner of the intersection of Armagh and Madras streets (S43.5284 E172.6432) to characterize the variability in soil conditions over relatively short distances. At this location within Zone 4, along the southern boundary of the moderate-to-severe liquefaction zone illustrated in Fig. 1, Cubrinovski et al. (2011a)

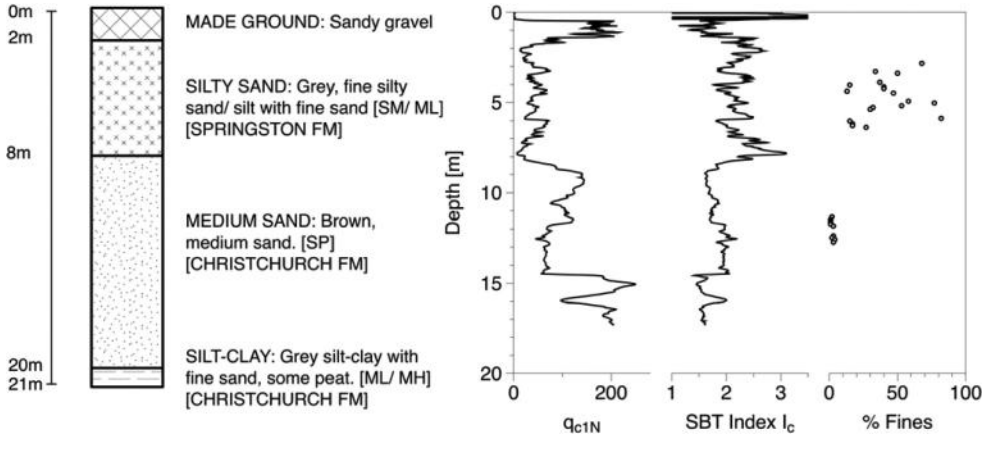

Figure 3. Log of borehole K1 and adjacent CPTZ1-B4 profile in Zone 1. The locations of borehole K1 and CPT Z1-B4 are indicated on Figure 2.

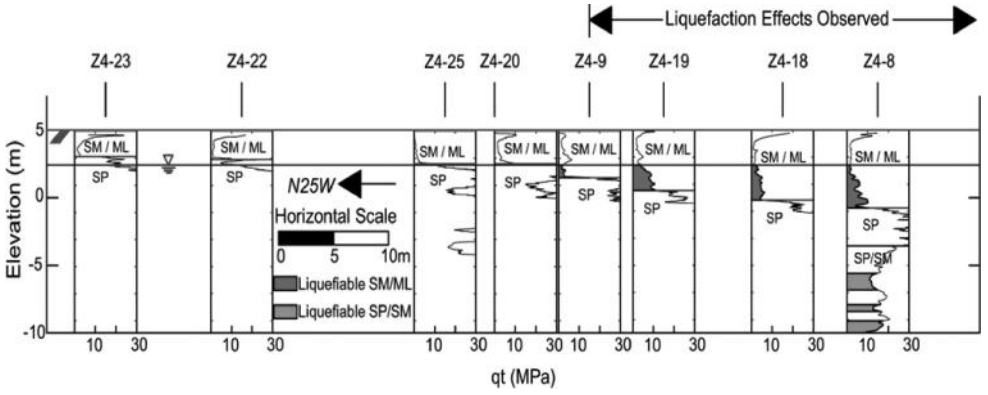

Figure 4. Corrected CPT tip resistance profiles showing variability in the thickness of the shallow SM/ML layer across the Armagh and Madras parking lot.

observed that liquefaction was manifested by a "*well-defined, narrow zone of surface cracks, fissures, and depression of the ground surface about 50 m wide, as well as water and sand ejecta*." A cross section that depicts the cone tip resistance profiles on the north end of the line is shown in Fig. 4. The shallowest layer is composed of silty sand and sandy silt (SM/ ML) with a q_t generally less than 5 MPa and I_c between 2.0 and 2.5. Samples from a nearby borehole indicated a F_C of about 50% for this layer. The next layer was a clean sand to gravelly sand (SP) with q_t greater than 20 MPa and often greater than 30 MPa and I_c between 1.0 and 1.5. Clean to silty sands of varying penetration resistance, but typically with q_t greater than 10 MPa followed the dense SP layer.

Simplified liquefaction evaluations were performed utilizing the CPT-based liquefaction triggering correlations of Robertson and Wride (1998), henceforth RW98; Moss, Seed et al. (2006), henceforth MS06; and Idriss and Boulanger (2008), henceforth IB08. The CPT-based procedure developed by Zhang et al. (2002), henceforth ZR02, was applied to estimate free-field, level ground, surface settlements due to post-liquefaction volumetric strains. For the purposes of applying the ZR02 procedure, the clean sand equivalent, normalized, CPT tip resistance $q_{c1N\text{-}CS}$, as well as the FS_l, were calculated in accordance with RW98.

The portion of the shallowest layer that was below the groundwater table should have liquefied based on the median PGA during the Christchurch earthquake using the RW98, MS06, or IB08 liquefaction triggering procedure. These procedures produced generally consistent results for the shallow liquefiable sandy soils of Christchurch. The resulting post-liquefaction vertical settlement using the ZR02 procedure within this layer decreased from a local maximum of about 10 cm in the middle of the liquefaction feature to zero over a total width of 45 m, which is consistent with the dimensions of the surficial depression in this area documented by Cubrinovski et al. (2011a). Consequently, the shallow liquefiable SM/ML layer, when it existed, was likely a critical layer in the observed liquefaction in Zone 4, and in other zones with similar stratigraphy. Its thickness below the water table could vary considerably over relatively short distances.

4 ILLUSTRATIVE EXAMPLE OF A CBD BUILDING AFFECTED BY LIQUEFACTION

The CTUC Building (S43.5286 E172.6425) is located only 20 m west of the Armagh-Madras parking lot discussed previously. It was a 6-story RC frame structure with RC core walls and block in-fill walls with its roof supported by steel framing (Fig. 5a). Based on its 1974 design drawings, the building frame was largely supported on shallow footings interconnected with tie beams (Fig. 6). Six square footings were 2.44 by 2.44 m and were either 0.46 m or 0.61 m

Figure 5. (a) South end of CTUC building showing tilt to the east (taken July 2011) and (b) Close-up photograph of the SE corner of the building (taken March 2011).

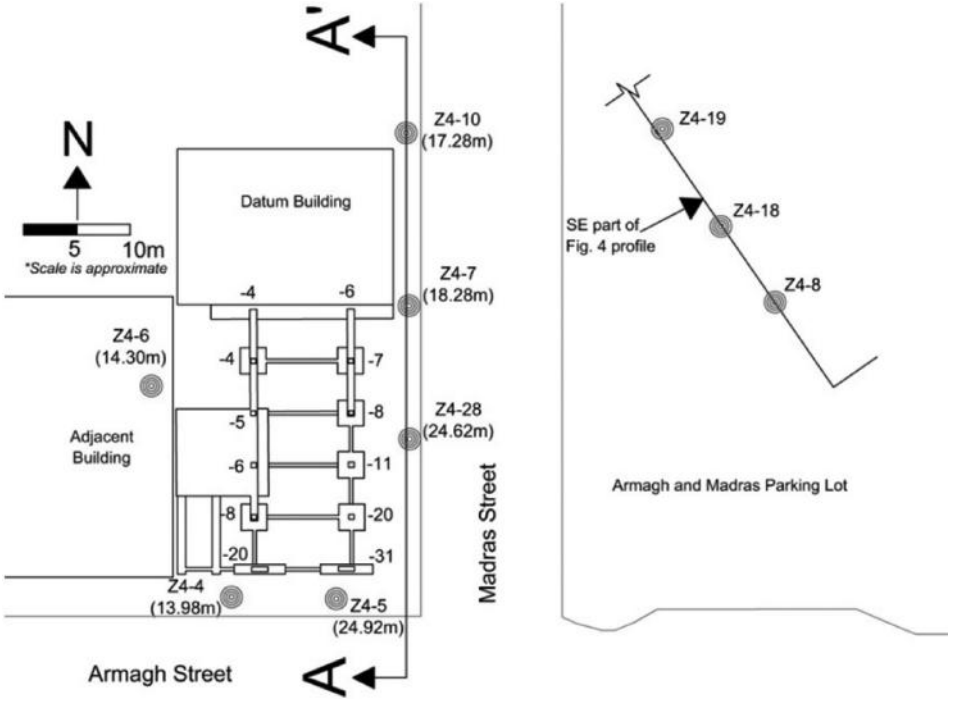

Figure 6. CTUC Building site with its foundation system and CPT locations (with depths). Footing settlements at column locations relative to the datum building are provided in cm. The location of the subsurface profile presented in Figure 4, along with a portion of the profile, are shown for reference.

deep, and the two footings at the south end were 4.88 m by 0.91 m and 0.46 m deep. Each of these footings supported a single, rectangular RC column that were spaced approximately 4.9 m and 9.1 m in the N-S and E-W directions, respectively. A larger footing on the west side of the building supported two rectangular RC columns in addition to the walls associated with the elevator and stair core, and strip footings supported core walls at the SW corner of the building and a block wall on its northern end. Adjacent footings were connected with RC tie beams that had cross sectional areas of either 0.74 m^2 or 0.12 m^2. Floors two through

six were RC and were supported by RC beams 0.41 m wide by 0.61 m deep. Footing contact pressures for the effective seismic building weight were 100–200 kPa.

While damage to the building was negligible during the Darfield and June 2011 events, severe liquefaction of the foundation soils during the Christchurch earthquake induced significant total and differential settlements of the building, leading to structural distortions and cracking (Cubrinovski et al. 2011a). The building tilted to the east 0.4–0.5 degrees. Differential settlement of the SE corner of the building produced most of the structural damage. Several of the exposed beams on the south side of the building were cracked near the beam-column connections (Fig. 5b). Building settlement measurements were performed using the building located just to the north of CTUC Building as the datum, as it did not displace relative to the surrounding ground. The settlement measurements are presented in Fig. 6. The building settled more on its south side than on its north side and more on its east side than its west side. Approximately 20 cm of the 25 cm of differential building settlement along the eastern side of the building was measured across its two southernmost spans (angular distortion ≈ 1/50). Thus, cracking of structural beams in this area is not surprising.

Six (6) CPTs were performed at the CTUC building site, and 15 CPTs were performed at the nearby Armagh-Madras parking lot site, which were used to develop the subsurface profile shown previously in Fig. 4. The generalized subsurface conditions along the east side of the CTUC building are depicted in Fig. 7. The groundwater depth was estimated to be 2.5 m for the Darfield, December 2010, and Christchurch earthquakes, and 2.0 m for the June 2011 earthquake based on the T&T (2012) groundwater model. The shallow SM/ML layer is similar to the upper unit described previously in Fig. 4 and had $q_t < 3$ MPa, $2 < I_c < 2.5$, and nonplastic $F_C \approx 50\%$, which makes it likely to liquefy under strong ground shaking. It is noteworthy that this unit was observed at CPT Z4-5, which is at the SE corner of the building, to a depth of nearly 6 m; whereas it was not observed at CPT Z4-28 near the center of the east side of the building, CPT Z4-7 at the NE corner of the building, or below the groundwater table at CPT Z4-10.

From examining Fig. 7, it is clear that while there are liquefiable soils at each of the CPT locations, the distinguishing difference between them are the shallow liquefiable soils just beneath the building foundation at CPT Z4-5 whereas the liquefiable soils at CPTs Z4-28, Z4-7 and Z4-10 are located primarily at depths below 8 m. The dramatic change in the shallow soil conditions from the building's north end, which did not contain shallow liquefiable

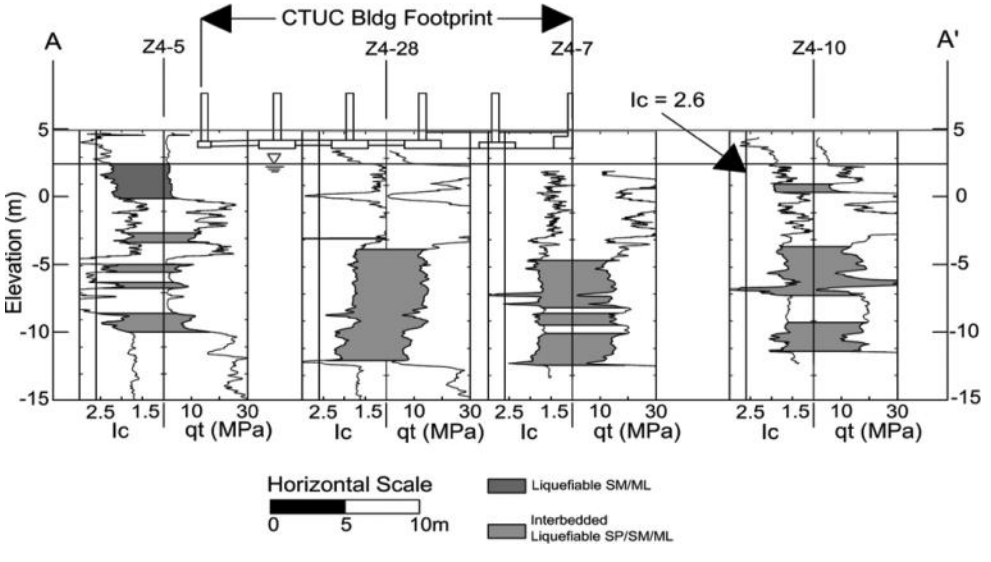

Figure 7. Subsurface conditions at CTUC site showing zones of materials with $FS_{l<}$ 1.0 based on the RW98 procedure using PGA_{50} from Bradley and Hughes (2012) for the Christchurch earthquake.

soils, to its south end, which contained shallow liquefiable soils, led to significant differential settlement over the southernmost spans of the building frame.

The calculated FS_l profiles for four events at CPT Z4-5 are presented in Fig. 8 for the median PGA estimates. As discussed previously, low FS_l values were calculated in the shallow SM/ML layer for the intense Christchurch earthquake, wherein severe liquefaction was observed at the site. However, FS_l values below one are also calculated for the Darfield and June 2011 earthquakes. Although there were no reports of liquefaction at this location after these events, it is possible that a minor amount of liquefaction was unreported or that marginal liquefaction occurred and surface manifestations were not observed. Damage was not reported for these events, so if liquefaction did occur its effects were insignificant. Liquefaction triggering procedures are deliberately conservative, so it is also possible that liquefaction did not occur at this site although the calculated FS_l values were below one.

The post-liquefaction residual shear strength of the shallow SM/ML layer was estimated to be 6 kPa to 10 kPa using the Olson and Stark (2002) and IB08 procedures. The bottom of the SE footing adjacent to CPT Z4–5 was at a depth of about 1.3 m. The static bearing capacity of the foundation soils at this location can be estimated using procedures developed for a two-layer cohesive soil deposit (NAVFACDM 7.02 1986). The *FS* against a bearing capacity failure is 2.1 to 2.3 at the location of the SE corner footing, which was judged to be most critical, using the residual shear strength of the shallow liquefiable SM/ML materials and an equivalent undrained shear strength of the SM/ML materials above the groundwater. If the materials above the groundwater lose strength due to the upward migration of liquefied soil, then the *FS* is below one. The SE footing may have underwent a partial bearing capacity failure, but its differential settlement was largely the result of ground loss due to sediment ejecta and some contribution of other settlement mechanisms described by Bray and Dashti (2010), because bulging of the ground surface was not observed at this site.

Liquefaction-induced free-field level ground settlements at the locations of the CPTs were calculated based on the post-liquefaction volumetric strain ZR02 procedure discussed previously. As is often done in engineering practice, the upper 17 m of the soil deposit was characterized, so liquefaction-induced settlement estimates due to volumetric strains over this thickness were calculated and summarized in Table 2. Calculated settlements due to post-liquefaction volumetric strains during the Christchurch earthquake range from 16 cm to 10 cm across the footprint of the CTUC building (i.e., CPTs Z4–5, Z4–28, and Z4–7). Hence, free-field vertical settlements due to post-liquefaction volumetric strains suggest a differential settlement of only about 6 cm across the building due to the Christchurch earthquake. However, the building actually settled differentially 25 cm more at its south end than at its north end for this event. The presence of the shallow loose SM/ML layer beneath the groundwater table, as

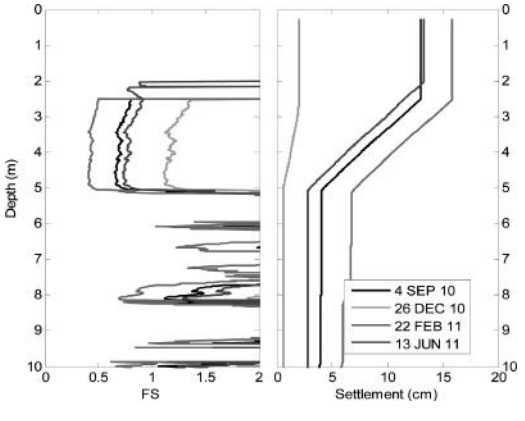

Figure 8. FS against liquefaction triggering and settlement due to post-liquefaction volumetric strain profiles at CPT Z4–5 using ZR02-RW98 and PGA_{50} estimates from Bradley and Hughes (2012).

Table 2. Calculated surface settlements at CPT locations near the CTUC building. Settlements are due to post-liquefaction volumetric strains in the top 17 m based on median PGA estimates.

	Reconsolidation settlement (cm)			
CPT ID	4 SEP 10	26 DEC 10	22 FEB 11	13 JUN 11
Z4–5	13	2	16	13
Z4–28	10	3	16	9
Z4–7	2	0	10	1
Z4–10	2	0	7	1

depicted in CPT Z4–5 at the SE corner of the building, likely led to the significant differential settlement of the building across its two southernmost spans. Ground loss under the shallow foundations due to sediment ejecta and shear-induced mechanisms, such as SSI-ratcheting, likely contributed to larger settlements at the SE corner of the CTUC building. Liquefaction of soils below a depth of 8 m contributed significantly to the amount of calculated settlement, but their impact on the building performance was relatively minor. Thus, the equal weighting of post-liquefaction volumetric strains over all depths of the soil profile in the calculation of free-field vertical settlements can be misleading, because the seismic performance of shallow foundations depends most on seismic response of shallow soil deposits.

Whereas the ZR02 procedure underestimated liquefaction-induced building settlement due to the Christchurch earthquake, it overestimated the observed settlement for the Darfield and June 2011 events. Liquefaction triggering evaluation procedures are typically conservative. The calculation of $FS_l < 1.0$ for the Darfield and June 2011 earthquakes leads to post-liquefaction settlements at CPT Z4–5 that are close to that calculated for the Christchurch earthquake due to the sensitivity of the ZR02 procedure when FS_l is near one. Severe liquefaction and significant damage were observed for the latter event, but not for the former events, so commonly used procedures are not be able to discriminate between these events for this case. Post-liquefaction settlement estimates provide only a rough index of seismic performance. Engineering judgment is required in interpreting their results.

5 CONCLUSIONS

The Canterbury earthquake sequence produced varying degrees of liquefaction with differing effects on buildings with different structural and foundation systems. The CPT proved to be a useful site characterization tool. Its results enabled liquefaction triggering evaluations using prevalent procedures that were found to be conservative. The conservatism in the liquefaction triggering assessments led to post-liquefaction ground settlement estimates that were generally similar for the large events in the Canterbury earthquake sequence, whereas significant building settlements and damage in the CBD were observed for the Christchurch earthquake but not for other earthquakes, such as the Darfield and June 2011 events. Moreover, the liquefaction-induced ground settlement procedures do not capture important shear-induced deformation mechanisms, such as SSI ratcheting and partial bearing failure, and the effects of ground loss due to sediment ejecta. Performance-based earthquake engineering requires improved procedures to discern between the differing levels of performance observed in Christchurch during the Canterbury earthquake sequence. Given the brittle nature of the liquefaction phenomenon as soil transforms from a stiff to a soft response rapidly as the excess pore water pressure rises beyond a threshold value, the development of robust design procedures to evaluate the effects of liquefaction on buildings will be challenging. However, the case histories provided by the Canterbury earthquake sequence provide a comprehensive set of ground and building performance data for developing such methods.

ACKNOWLEDGEMENTS

The primary support for the NZ researchers was provided by the Earthquake Commission New Zealand (EQC) and University of Canterbury. The primary support for the US researchers was provided by grants from the U.S. National Science Foundation (NSF) through CMMI-0825734 and CMMI-1137977 and the U.S. Geological Survey through G12 AP20034. Any opinions, findings, and conclusions or recommendations expressed in this material are those of the authors and do not necessarily reflect the views of the EQC, NSF, or USGS. We would also like to acknowledge the assistance of all NZ and US GEER team members who participated in the reconnaissance of these events, especially Tom O'Rourke, Russell Green, Brendon Bradley, Brady Cox, Simona Giorgini, and Kelly Robinson. Their contributions are noted at: http://www.geerassociation.org/. Site explorations were performed with partial support by Iain Haycock, Nathan Barnes, Richard Wise, and Mike Pickworth of McMillan Drilling Services and Simon Faulkner and John Cresswell of Fugro BTW. Sjoerd Van Ballegooy and Mike Jacka of Tonkin & Taylor shared useful data. Ian McCahon of Geotech Consulting Ltd. shared useful data and insights as well.

REFERENCES

Bradley, B.A., Hughes, M. 2012. Conditional Peak Ground Accelerations in the Canterbury Earthquakes for Conventional Liquefaction Assessment. *Technical Report Prepared for the Department of Building and Housing,* 22 pp.

Bray, J.D., and Dashti, S. 2010. Liquefaction-Induced Movements of Buildings with Shallow Foundations. *Fifth Int. Conf. on Rec. Adv. in Geo. EQ Engrg. & Soil Dyn*., May 24–29, San Diego, CA, Paper No. OSP–2.

Brown, L.J., and Weeber, J.H. 1992. *Geology of the Christchurch Urban Area*. Institute of Geological and Nuclear Sciences, Lower Hutt, New Zealand.

Brown, L.J., Beetham, R.D., Paterson, B.R., Weeber, J.H. 1995. Geology of Christchurch, New Zealand. *Environmental and Engineering Geosciences,* Vol. 1, No. 4, pp. 427–488.

Cubrinovski, M., Bray, J.D., Taylor, M., Giorgini, S., Bradley B.A., Wotherspoon, L., and Zupan, J. 2011a. Soil Liquefaction Effects in the Central Business District during the February 2011 Christchurch Earthquake. *Seismological Research Letters,* 82, 893–904.

Cubrinovski, M., Bradley, B., Wotherspoon, L., Green, R., Bray, J., Wood, C., Pender, M., Allen, J., Bradshaw, A., Rix, G., Taylor, M., Robinson, K., Henderson, D., Giorgini, S., Ma, K., Winkley, A., Zupan, J., O'Rourke, T., DePascale, G. and Wells, D. 2011b. Geotechnical Aspects of the 22 February 2011 Christchurch Earthquake. *Bulletin of the New Zealand Society of Earthquake Engineering*, 44(4): 205–226.

Idriss, I.M, and Boulanger, R.S 2008. *Soil Liquefaction During Earthquakes.* Earthquake Engineering Research Institute, EERIMNO-12, Oakland, CA.

Moss, R.E.S., Seed, R.B., Kayen, R.E., Stewart, J.P., Der Kiureghian, A., and Cetin, K.O. 2006. CPT-Based Probabilistic and Deterministic Assessment of In Situ Seismic Soil Liquefaction Potential. *J. Geotech. Geoenviron. Eng.*, 132(8), 1032–1051

NAVFAC 1986. DM-7.02, *Foundations and Earth Structures*. U.S. Department of Navy, Naval Facilities Engineering Command, 200 Stovall Street, Alexandria, VA 22332–2300.

Olson, S.M., and Stark, T.D. 2002. Liquefied strength ratio from liquefaction flow failure case histories. *Can. Geotech. J.,* 39, 629–647.

Robertson, P.K., and Wride, C.E. 1998. Evaluating cyclic liquefaction potential using the cone penetration test. *Can. Geotech. J.,* 35, 442–459.

Tonkin and Taylor 2011. *Christchurch Central City Geological Interpretive Report*, report prepared for the Christchurch City Council, Dec. (Ver. 1.1).

Tonkin and Taylor 2012. *Groundwater Depth Maps*, preliminary data shared by T&T.

Zhang, G., Robertson, P.K., and Brachman, R.W.I. 2002. Estimating liquefaction-induced ground settlements from CPT for level ground. *Can. Geotech. J.,* 39, 1168–1180.

Soil Liquefaction during Recent Large-Scale Earthquakes – Orense, Towhata & Chouw (Eds)

Effects of lateral spreading on bridges in the 2010–2011 Christchurch earthquakes

M. Cubrinovski, A. Winkley, J. Haskell & K. Robinson
Department of Civil and Natural Resources Engineering, University of Canterbury, Christchurch, New Zealand

L. Wotherspoon
Department of Civil and Environmental Engineering, University of Auckland, Auckland, New Zealand

ABSTRACT: In the 2010–2011 Christchurch earthquakes, the road bridges along the Avon River were subjected to large ground displacements due to spreading of liquefied soils. All bridges affected by lateral spreading exhibited a characteristic deformation (damage) mechanism involving deck-pinning by a strong (rigid) superstructure and inward rotation of the abutments with consequent displacement of the top of the abutment piles towards the river. Two well documented case studies and a series of pseudo-static analyses (PSA) are used to illustrate the characteristic damage mechanism and investigate the response of the bridges and their pile foundations in particular. Key findings for the performance of the bridges and application of PSA to lateral spreading assessment of bridges are summarized.

1 INTRODUCTION

In the period between September 2010 and December 2011, Christchurch was hit by a series of strong earthquakes. The Canterbury Earthquake Sequence, started with the magnitude M_w7.1 Darfield earthquake (4 September 2010) and was followed by the M_w6.2 Christchurch earthquake on 22 February 2011, and magnitude 6 level earthquakes on 13 June and 23 December 2013. The Christchurch earthquake was the most devastating, causing 185 fatalities, collapse of two multi-storey reinforced concrete buildings, and nearly complete destruction of the Central Business District (CBD) of Christchurch. The causative faults of the earthquakes were essentially within the city boundaries, thus generating strong ground motions throughout the city, and extensive liquefaction over approximately one third of the city area. The liquefaction was unprecedented both in scale and severity, causing damage to ~60,000 residential buildings, many multi-story buildings and key lifeline facilities including hundreds of kilometres of roads and buried pipes.

The earthquakes were densely recorded with approximately 15 strong motion stations (SMS) within the city boundaries. The SMS records were then supplemented by massive reconnaissance and damage-inspection efforts resulting in numerous very well documented case studies on the performance of land and engineering structures (residential buildings, CBD buildings, bridges, and potable and wastewater systems). In addition, extensive post-earthquake field investigations were carried out including about 10,000 CPTs, shear wave velocity measurements by various techniques at many sites throughout the city, ground improvement field trials for liquefaction countermeasures, and recovery and laboratory testing of undisturbed (Gel-Push) soil samples, among others. The compiled evidence and data provide an unprecedented opportunity to gain new insights into soil liquefaction, lateral spreading, and their effects on the seismic performance of buildings and infrastructure.

This paper focuses on the performance of road bridges in the 2010–2011 Canterbury earthquakes. It first presents a brief overview of the characteristics of lateral spreading observed in the earthquakes, and then discusses in detail the spreading-induced damage to bridges. A characteristic damage mechanism of short-span road bridges induced by lateral spreading is identified and discussed using two well-documented case studies. Results from a comprehensive analytical study of the ANZAC Bridge are also presented to further elucidate the response of the bridge and its foundations in particular, and to critically assess the use of the pseudo-static analysis for piles in laterally spreading liquefied soils. More details of this study are given in Cubrinovski et al. (2014) and Winkley (2013).

2 CHARACTERISTICS OF LATERAL SPREADING

The Christchurch liquefaction was arguably one of the most extensive and severe liquefaction events in native soils on record. Approximately one third of the city area (predominantly in the eastern suburbs of Christchurch) was affected by moderate to severe liquefaction which was manifested with massive sand boils, large ground distortion, fissures and permanent ground displacements. In the worst hit areas (particularly in the Residential Red Zone along the Avon River) widespread liquefaction occurred in multiple events, with many areas and sites severely liquefying three or four times during the 2010–2011 earthquake sequence. In the zone along the Avon River from the CBD to the estuary (Figure 1), the liquefaction was accompanied by substantial lateral spreading. There are several sources of data available for the interpretation of permanent ground displacements induced by lateral spreading including field measurements of ground displacements by means of the ground surveying (e.g., Robinson et al., 2011), LiDAR data covering most of the city area (CERA, 2012) and aerial photogrammetric interpretation over some areas/suburbs of Christchurch (data not

Figure 1. Observed liquefaction in Christchurch after the 22 FEB 2011 earthquake (red = moderate to severe liquefaction, yellow = low to moderate liquefaction); the CBD and locations of the case study bridges are also indicated.

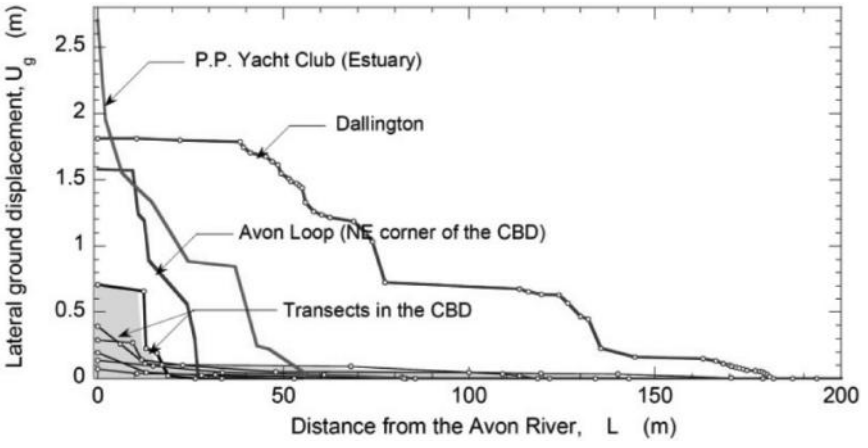

Figure 2. Lateral spreading displacements along the Avon River measured by the ground surveying method after the Christchurch earthquake.

yet published). Based on the ground surveying measurements, the spreading characteristics along the Avon River can be summarized as below:

- The magnitude of spreading displacements and the width of the zone affected by spreading generally increased from the CBD towards the estuary. This is illustrated in Figure 2 where the distribution of permanent lateral ground displacements as a function of the distance from the river is shown for several transects along the Avon River, from the CBD to the estuary.
- In the CBD, the maximum spreading displacements were predominantly between 10 and 30 cm, and the spreading was confined within a distance of about 40–50 m from the river (shaded area in Figure 2). The first more substantial lateral spreads with displacements greater than 1 m were observed at the Avon Loop, at the north-east corner of the CBD.
- Downstream from the Avon Loop, the spreading was more substantial with permanent ground displacements often exceeding 0.5 m or even 1 m, and the zone of spreading extending up to 150 m to 200 m from the river. The largest permanent displacements reached about 3 m at the Pleasant Point Yacht Club where the Avon River discharges into the estuary (Figures 1 and 2).
- The magnitude and spatial distribution of spreading displacements were highly variable even within a given small area, reflecting the complexities of lateral spreads. This was particularly pronounced at the meandering loops of the Avon River where often substantially larger ground displacements were observed in the point bar deposits while much smaller movements were seen in the cut-banks, on the opposite side of the river.

3 SPREADING-INDUCED DAMAGE TO BRIDGES

There are over 800 road, rail and pedestrian bridges in Christchurch and the surrounding region. In the 2010–2011 earthquakes road bridges performed relatively well compared to other engineering structures (Palermo et al., 2011; Wotherspoon et al., 2011). They suffered low to moderate damage and all but one bridge were in service almost immediately after each significant event.

Most of the damage to bridges was due to liquefaction of the foundation soils and lateral spreading in particular. On the Avon River, practically all road bridges downstream from the Avon Loop were affected by substantial lateral spreading. The road bridges of Christchurch are typically two or three span, short—to moderate-length bridges (20 m to 70 m long).

Older bridges constructed before 1960s are integral systems while more recent bridges are commonly segmental precast concrete bridges with movable joints or connections. The bridges have sturdy configurations, with large stiffness and strength in the longitudinal direction provided by a very rigid deck-wall or deck-girder superstructure. Hence, when subjected to large spreading displacements and closing of the banks towards the river, the bridge superstructure resisted the ground movements and prevented any significant displacements occurring in the longitudinal direction at the deck/superstructure level. The deck-pinning in conjunction with the lower lateral resistance and capacity of the abutment piles resulted into a characteristic deformation mechanism schematically illustrated in Figure 3. The mechanism involves deck-pinning, back-rotation of the abutments, consequent displacement and deformation (damage) of the abutment piles, and slumping of the approaches that resulted in large vertical offsets between the approaches and pile-supported deck of the bridge. This deformation mechanism was observed for all road bridges affected by spreading along the Avon River.

3.1 *Two case studies*

Two well documented case studies will be used to illustrate further key features of the spreading-induced damage to the bridges. Figure 4 shows an aerial view of the two case studies: Dallington (Gayhurst) Bridge and ANZAC Bridge. The solid lines indicate the locations of transects along which lateral spreading measurements were carried out using the ground surveying method, with the numbers at the tip of the transects indicating the permanent

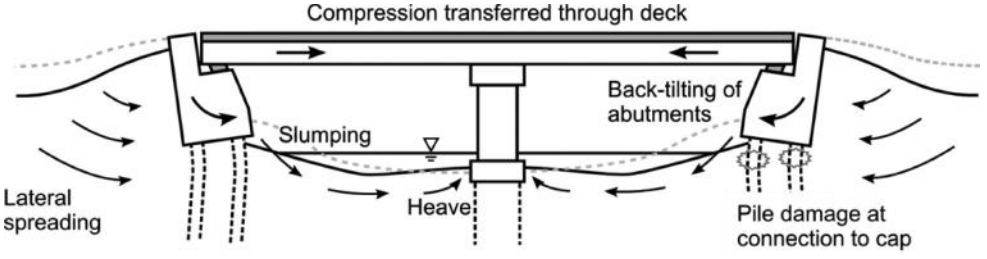

Figure 3. Schematic illustration of the characteristic spreading-induced deformation (damage) mechanism of short-span bridges involving deck-pinning, abutment back-rotation, damage to abutment piles, and slumping of the approaches.

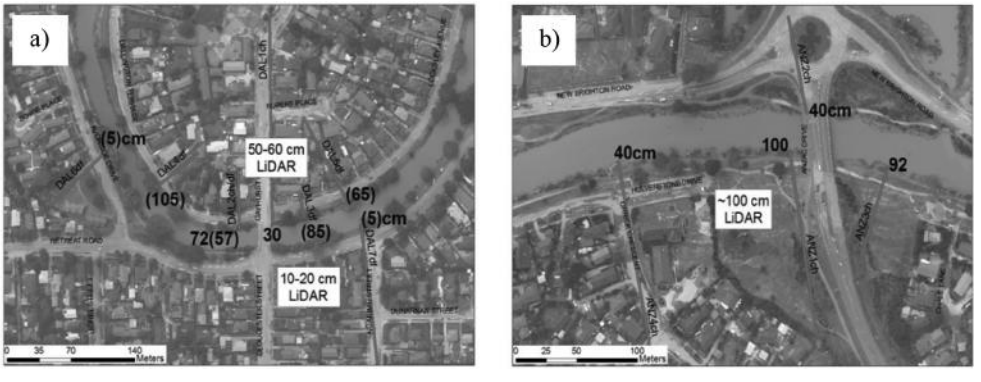

Figure 4. Aerial view of (a) Dallington; and (b) ANZAC bridges; transects of ground surveying measurements are shown with red lines including maximum lateral displacements of the river banks (in cm) for the Christchurch and Darfield (in brackets) earthquakes; also shown are lateral displacements for the Christchurch earthquake estimated from LiDAR data.

horizontal displacements of the river banks measured after the Christchurch earthquake, and Darfield earthquake (in brackets). The range of corresponding ground displacements estimated from LiDAR data (CERA, 2012) is also indicated in the figure. It is apparent that the permanent displacements estimated from the ground surveying are generally consistent with those obtained from the LiDAR data.

3.1.1 *Dallington (Gayhurst) Bridge*

The Dallington Bridge is located approximately 2 km to the east of the Avon Loop (Figure 1). It is an integral bridge consisting of a continuous RC deck, RC piers and RC abutment walls with wing walls, without any expansion joints. The bridge is 26.8 m long and has three spans. The piers and abutments are supported on square reinforced concrete piles 350 mm in width and 10.4 m in length. Seven piles at 4D spacing are used beneath the piers, while six piles at 6D spacing support each abutment. The bridge was constructed in 1954.

The bridge runs approximately in the north-south direction, and spans point bar deposits on the north side and cut-banks on the south side of the bridge (Figure 4a). At the north (point bar) side, the shallow sandy silt is overlying a 2 m layer of peat and clayey soil of very low penetration resistance, then a grey fine sand (with occasional gravelly sands) that extends to about 15 m depth, sandy silt from 15–20 m depth and fine sand from 20–24 m depth. According to a simplified triggering analysis based on the CPT resistance, the shallow silty sand and the sand beneath the peat/clayey soil to approximately 9 m depth should have liquefied during the Darfield and Christchurch earthquakes.

The penetration resistance is much higher at the south side of the bridge, and the simplified liquefaction evaluation procedure predicts that only thin and likely discontinuous lenses should have liquefied during the earthquakes. The CPT profiles and results from the simplified triggering analysis are consistent with the large contrast in liquefaction manifestation, lateral spreading effects and damage observed between the north and south approaches of the bridge. On the north side, severe liquefaction occurred repeatedly during the Darfield, Christchurch and June 2011 earthquakes with permanent spreading displacements of the river banks of about 0.5–1.0 m, and subsidence of the northern approach of the bridge of about 1 m (Figure 5a). Conversely, the permanent displacements on the south (cut-bank) side where much smaller (less than 0.2 m), and there was little evidence of ground distortion and damage to the south approach of the bridge.

The bridge suffered the characteristic damage mechanism involving spreading, deck-pinning and back-rotation of the abutment walls. The effects of this mechanism are evident in Figure 5b where large differential movements and failure of the north wing wall of the bridge are shown. Using the displacement of the wing wall as an indicator for the size of the movement of the foundation soils, one may estimate that the permanent lateral displacement of the foundation soils was approximately 50% of the corresponding free field displacement of

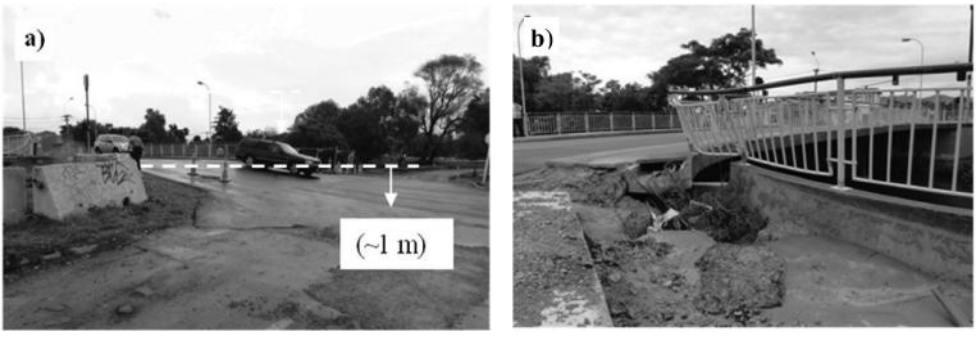

Figure 5. Dallington (Gayhurst) Bridge: (a) subsidence of ~1m at the north approach (point-bar deposit) (b) failure of the north wing wall due to large differential movements between the adjacent river banks and the abutment wall.

the river banks. The north abutment rotated inwards for about 1.2º, and detailed inspections revealed a formation of a wide crack at the connection between the deck and the abutment, and yielding of the top bars of the deck. The bridge was back in service after quick repair works of the north approach.

3.1.2 *ANZAC Bridge*

The ANZAC Bridge runs approximately in the north-south direction and has a roundabout at the north approach (Figure 6a). The 48 m long three-span bridge was constructed in 2000. The superstructure consists of a precast concrete hollow-core (double) deck and precast concrete beams, and is supported on in situ concrete piers and abutments. Each of the four piers is founded on a single circular reinforced concrete pile, 1.5 m in diameter with 8 mm thick permanent steel casing (NZTA, 2011). The piles are 20 m long and at a spacing of 4.7D. The abutments are supported on 22 m long steel "H" piles (310 mm × 137 kg/m), at 1.5 m spacing.

Massive liquefaction occurred in the area of the bridge during the Christchurch earthquake, as illustrated in Figure 6a where large volumes of sand ejecta are seen on the south side of the bridge. There was a clear evidence of substantial lateral spreading towards the river, with large cracks and fissures in the ground running parallel to the river, as illustrated by the alignment of the sand ejecta in Figure 6a. Permanent lateral spreading displacements reached about 1.0 m at the river banks adjacent to the south abutment (Figure 4b). On the north side, the roundabout affected the spreading and obscured its manifestation, thus the magnitude of lateral spreading displacements was inconclusive, but likely ~0.4 m or slightly larger.

Again the same characteristic deformation (damage) mechanism depicted in Figure 3 was evident at the ANZAC Bridge. Figure 6b illustrates the permanent movements observed at the south abutment including an inward tilt of the abutment of about 6 degrees, consequent lateral displacement of the top of the abutment piles towards the river (about 20 cm, i.e. 16 cm due to abutment rotation, and 3–4 cm displacement required to close the gap between the abutment and the deck-girder), displacement of the foundation soils (~40–80 cm), and permanent displacements in the free field (about 1.0 m). Note that the pedestrian underpass shown in Figure 6b was founded on short (6 m long) and rigid piles (1.2 m in diameter RC piles) which were floating in the liquefied soils, and most likely moved together with the surrounding foundation soils. Hence, the detailed permanent displacements shown in Figure 6b provide an excellent evidence for the movement of the foundations soils relative to that of the free field soils. The movement of the foundation soils was not uniform, and on average was approximately 60% of the magnitude of the lateral-spreading displacements in the free field.

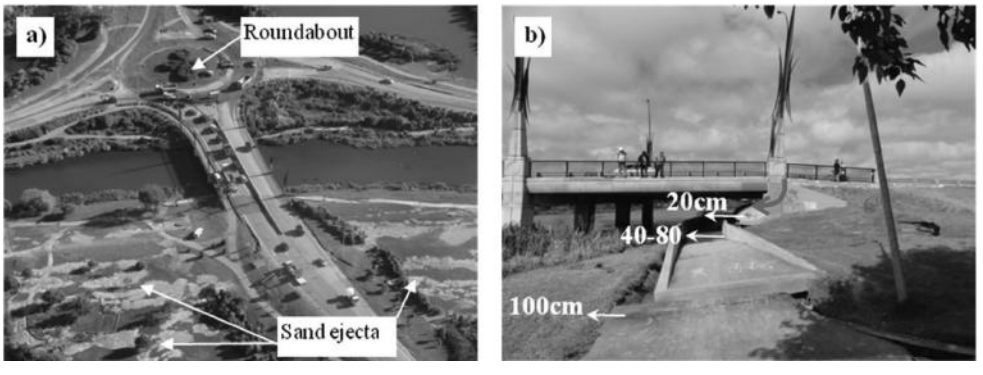

Figure 6. ANZAC Bridge: (a) aerial view towards north (massive sand ejecta on the south banks); (b) back-rotation of the abutment (red arrow) with permanent lateral displacements of the abutment base, adjacent pedestrian underpass and free field soils.

The bridge superstructure sustained some visible damage however, the structural damage was not serious and the bridge remained in service after each earthquake following quick repairs of the approaches and infilling of the large vertical offsets between the deck and the approaches.

4 PSEUDO-STATIC ANALYSIS OF THE ANZAC BRIDGE

A series of Pseudo-Static Analyses (PSA) were conducted to analyze the spreading-induced response and damage of the ANZAC Bridge. The objectives of the analyses were to: (a) assess the capability of the PSA to capture the observed characteristic spreading-induced mechanism of deformation (damage); (b) identify key model/analysis parameters that control the pile response (deformation), and (c) back-calculate best-fit values for the key model (analysis) parameters and hence provide further guidance on the application of PSA.

Two separate series of PSA analyses were conducted targeting the response of the piles (bridge) during the cyclic phase (involving both kinematic and inertial loads) and post-liquefaction lateral spreading phase (involving kinematic loads due to large ground displacements). Here, the lateral spreading analyses are only discussed. Again, two models were employed for the lateral spreading analyses: a single pile model, and a global bridge model. The single pile model was used in the parametric analyses to evaluate the sensitivity of the pile response to various model parameters, then identify the key parameters controlling the pile response, and estimate the best-fit values for these parameters through comparisons of the computed and observed displacements at the top of the abutment piles. The global bridge model was then used to consider the soil-pile-abutment-superstructure interaction including all abutment and pier piles, and non-uniform soil characteristics, spreading displacements and loads on different pier/abutment piles.

4.1 *Single-pile analysis*

In this study, the PSA method summarized in Cubrinovski et al. (2009) was used. It uses a simple beam-spring model, in which the pile (or any other structural member) is represented by a beam element with a nonlinear moment curvature relationship while the soil is modelled by a bi-linear spring. Three types of soil layers are considered in the definition of the springs: a crust of non-liquefied soil at the ground surface, liquefied soil layers with degraded stiffness and strength, and non-liquefied layers at larger depths. The Rankine passive pressure is used as a basis for calculating the ultimate pressure of the springs in the non-liquefied sand layers. The important modelling difference for the crust as compared to deeper non-liquefied layers is that a 'wedge—effect' or an increased pressure on a single pile (as compared to a continuous wall) is considered for the crust through a multiplier α_{crust} with typical values of 3 to 5 for cohesionless soils (Cubrinovski et al., 2006). The effects of liquefaction on the stiffness and strength of the soil springs are accounted for through a stiffness degradation factor (β) and the residual strength of liquefied soils estimated from empirical correlation (e.g. Seed and Harder, 1990, or Idriss and Boulanger, 2008).

While there are a number of uncertainties associated with the stiffness and strength of the soil springs as well as the equivalent kinematic and inertial loads employed in the PSA, previous studies (Haskell et al., 2013) have shown that the pile response is sensitive to only few of these parameters. Hence, only the uncertainties associated with the key parameters controlling the pile response should be considered in the parametric PSA. Note that independent single pile PSAs were conducted for the north abutment and south abutment in which the rigid extension of the pile (modelling the abutment) was fixed in the horizontal direction to simulate the deck-pinning effect. Results and findings from these analyses are briefly summarized below with more details provided in Cubrinovski et al. (2014).

The soil profile generally consists of a 2 m thick fill and then variable top sandy soil to about 4 m depth, overlying a uniform fine to medium sand from ~4 m to 17 m depth (with $q_c < 5$ MPa at shallow depths, and $q_c = 10$–20 MPa at larger depths), and slightly coarser and

denser sands below 17 m depth (with q_c > 20 MPa). The shaded layers in Figure 7a indicate liquefied layers with factors of safety of FS_l < 1.0 in the liquefaction triggering analysis for the Christchurch earthquake. Using the calculated FS_l values, the distribution of lateral spreading displacements throughout the depth was then estimated based on the method of Zhang et al. (2004). The objective of these calculations was to determine the distribution of ground displacements throughout the depth of the profile, as shown in Figure 7b as normalized $U_g/U_{g(max)}$ displacements, where $U_{g(max)}$ is the displacement at the top of the liquefied layer and ground surface. In the PSAs, this distribution of ground displacement was multiplied either by the measured or parametrically estimated lateral spreading displacement and applied at the end of the corresponding soil springs throughout the depth.

Analyses were first performed for each abutment using the reference model (RM) parameters, followed by a sensitivity study in which the value of one parameter was set first at its lower bound (LB) and then at its upper bound (UB) value with all other parameters kept at their RM values. In this way, the sensitivity of the pile response to each particular parameter was examined. Key findings and results from the sensitivity study can be summarized as below:

(a) The response of the pile could be reasonably reproduced using the reference model (RM) values (or similar) for the model parameters with good agreement between the observed and computed displacements at the pile head (Figure 7c). The bending moments (Figure 7d) indicate that the south abutment piles exceeded the yield level and approached the ultimate moment at ~0.5 m to 2 m below the pile head, and also at the interface of the liquefied and non-liquefied layers at ~15 m depth.

(b) In the case of a significant thickness (and load) of the crust layer (such as that for the south abutment), the pile response was very sensitivity to the value of the crust strength parameters and the multiplier α_{crust} in particular. However, the sensitivity of the pile response on the crust strength parameters is conditional on a sufficiently large thickness or load from the crust. For example, the north abutment piles showed no significant sensitivity on the crust strength parameters because the crust was not as thick, and hence the respective load from the crust on the pile was relatively small.

(c) There is a significant influence of the magnitude of the applied ground displacement on the response of the abutment piles, both in terms of the pile displacements and the level of damage to the piles (i.e. whether bending moments reach yield and ultimate levels). When the observed free field lateral spreading displacement at the south river banks (1.0 m) was applied to the pile, the computed pile head displacements were much greater than the observed dis-

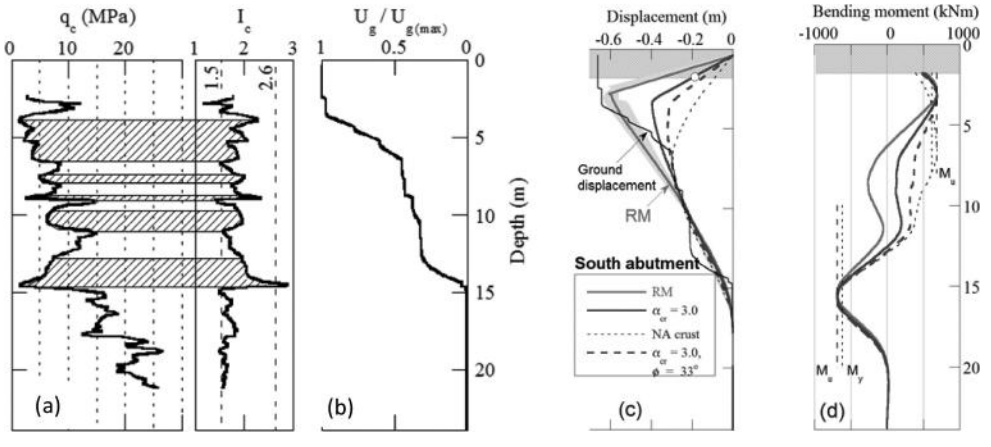

Figure 7. Single-pile PSA of the north abutment of the ANZAC Bridge: (a) subsurface conditions showing layers with FS_l < 1.0 for the Christchurch earthquake; (b) computed distribution of normalized lateral ground displacements; (c) displacements, and (d) bending moments illustrating the reference model (RM) response and effects of crust parameters.

placements. This indicates that the use of free field lateral spreading ground displacements as an input in the PSA might be overly conservative for short-span bridges with stiff and strong superstructure, and further supports the observations that the displacements of the foundation soils (which are more relevant for the piles) were indeed much smaller than the free field displacements (on the order of 50% to 60% from the free field displacements).

(d) There was an insignificant influence of the values of the model parameters for the liquefied and deep non-liquefied layers on the pile response. Also negligible effects were observed on the pile response when varying the stiffness parameters of the crust.

4.2 *Global bridge analyses*

Several global bridge analyses were also conducted to account for the substantial variation in the liquefaction-induced ground displacements acting on the abutment and pier piles, and for the soil-pile-pier/abutment-superstructure interaction. A schematic view of the global bridge model including a summary of the applied ground displacements and computed bridge displacements and bending moments for the piers and pier piles is shown in Figure 8. The analyses were conducted systematically. First, analyses were performed in which lateral ground displacements were applied only to the abutments and abutment piles (A-analysis). The results from the global A-analyses were practically identical to those of the single pile analyses. For reference, Figure 8 shows the displaced shape of the A-analysis using lower-bound values for the crust strength parameters and RM values for all other parameters, and ground displacement of 36 cm and 66 cm at the north and south abutments respectively. Next, ground displacements were also applied to the pier piles (i.e. in addition to the ground displacements at the abutments and abutment piles), as indicated schematically in Figure 8 (referred to as AP-analyses). The ground displacement at the top of the pier piles was assumed to be 50% of that at the respective elevation for the abutment piles while its distribution with depth was evaluated using the triggering and normalized displacement calculation, as previously discussed. The AP-analyses in Figure 8 show that the inclusion of a lateral ground displacement at the pier piles somewhat increased the pier displacements and created bending moments close to the yield moment at the top of the piers. In view of the significant uncertainties associated with the ground displacements at the piers and effects of liquefaction, two additional AP-analyses were conducted. Firstly, the applied ground displacements at the pier

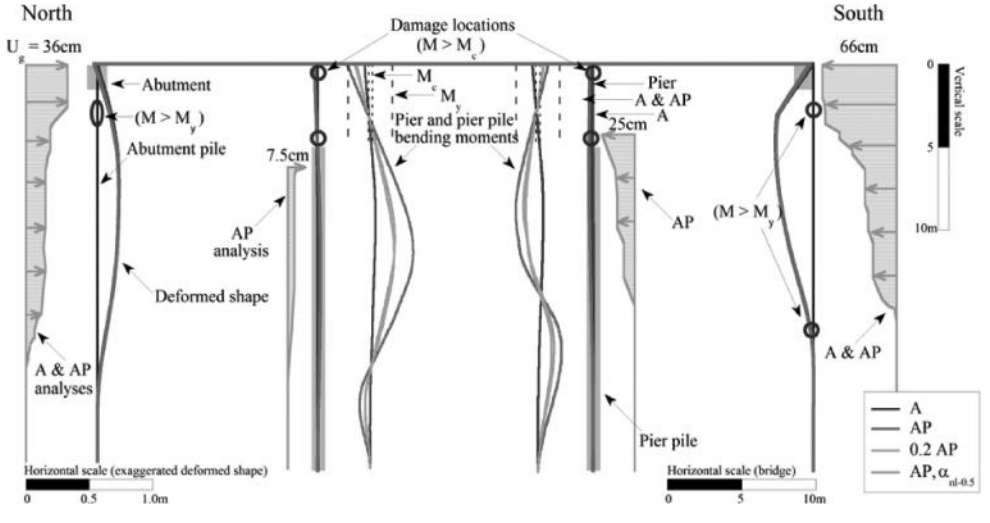

Figure 8. Global bridge model analysis of the ANZAC Bridge showing the applied ground displacement at the abutment piles (applied in all analyses), ground displacements applied along the pier piles (all AP analyses), deformed shape of the bridge, damage locations where $M > M_y$, and bending moments along the piers and pier piles.

piles were reduced to 20% of the initial value (0.2 AP analysis), and secondly, the strength of the non-liquefied layers (springs) was reduced to 50% of its initial value to assess the effects of strength reduction (due to excess pore pressures) in the non-liquefied layers sandwiched between liquefied layers (AP-$\alpha_{nl-0.5}$ analysis). Results from all three AP-type analyses indicate that the pier piles did not suffer any damage. All analyses suggest some damage at the top of the piers corresponding to the cracking moments, and somewhat smaller level of damage at the base of the piers. The computed moments at the top of the pier are probably overestimating the actual pier moments because a fully restrained connection between the deck and the pier-cap was adopted in the analysis. The global analysis also indicated that the whole bridge displaced ~3 cm to the north.

Overall, both single pile and global PSAs produced results consistent with the observed displacements and damage of the ANZAC Bridge. The analyses accurately simulated the observed spreading-induced mechanism and provided additional insight into the response of the pile foundations.

5 CONCLUSIONS

The Canterbury earthquakes triggered widespread liquefaction over approximately one third of the Christchurch area. Along the Avon River, the liquefaction was accompanied by substantial lateral spreads which affected practically all bridges downstream from the CBD. When subjected to large spreading displacements of the river banks, the stiff and robust superstructure of the short-span bridges resisted the ground movement and led to the development of a characteristic damage mechanism involving deck-pinning, abutment back-rotation and damage of the abutment piles. Both segmental and integral bridges exhibited the same characteristic deformation/damage mechanism. Permanent inward tilts of the abutments of ~6 to 8 degrees were observed for segmental bridges, while the back rotation was smaller for integral bridges. The abutment back-rotation resulted in permanent lateral displacements (as large as 20–30 cm) and damage, at the top of the abutment piles.

The damage involved slumping of the approaches and large vertical offsets between the approaches and the pile-supported deck. Large spreading displacements and subsidence of the approaches were observed particularly at point bar deposits on the inside bank of meandering river bends. Well-documented case studies indicate that lateral movements of the foundation soils were greater than the movements of the abutment piles, but substantially smaller than the free field displacements of the spreading river banks. Thus, the commonly adopted use of free field displacements in PSA might be overly conservative for bridges with a sufficient capacity to resist large spreading displacements.

Single pile and global PSAs produced consistent results and accurately simulated the observed deformations and damage of the ANZAC Bridge. The response of the abutment piles was found to be controlled by the magnitude of lateral ground displacement and lateral load from the crust. Good accuracy in the simulations was obtained using measured ground displacements and typical values for the model parameters. The abutment pile response was virtually insensitive to the variation in the properties of the liquefied soil and deeper non-liquefied layers. The global bridge analysis with applied ground displacements at the abutment and pier piles clearly demonstrated the need to consider the response of the bridge and its components using a global interaction model.

ACKNOWLEDGEMENTS

The authors would like to acknowledge the financial support provided by the Earthquake Commission New Zealand (EQC) and Natural Hazards Research Platform (NHRP), and the assistance of all NZ and US GEER team members who participated in the reconnaissance of the 2010–2011 earthquakes. Thanks are extended to the Christchurch City Council, New Zealand Transport Agency and Opus International Consultants engineers for providing

geotechnical data and design drawings for the investigated bridges. The LiDAR data was made available through the CERA geotechnical database (https://canterburygeotechnicaldatabase.projectorbit.com).

REFERENCES

Canterbury Earthquake Recovery Authority [CERA], 2012. *Geotechnical database for Canterbury earthquake sequence*, https://canterburygeotechnicaldatabase.projectorbit.com.

Cubrinovski, M., Ishihara, K. and Poulos, H. 2009. Pseudostatic analysis of piles subjected to lateral spreading. Special Issue, *Bulletin of NZ Society for Earthquake Engineering*, 42(1), 28–38.

Cubrinovski, M., Kokusho, T. and Ishihara, K. 2006. Interpretation from large-scale shake table tests on piles undergoing lateral spreading in liquefied soils. *Soil Dynamics & Earthquake Engineering*, 26, 275–286.

Cubrinovski, M., Haskell, J.J.M., Winkley A., Robinson K. and Wotherspoon L. 2014. Spreading-induced damage to short-span bridges in Christchurch (New Zealand). Special Issue, *Earthquake Spectra* (in print).

Haskell, J.J.M., Cubrinovski, M., Bradley, B. 2012. Sensitivity analysis and its role in pseudo-static design of pile foundations. *Soil Dynamics and Earthquake Engineering,* 42, 80–94.

New Zealand Transport Agency (2011). Private communication.

Palermo, A., Wotherspoon, L., Wood, J., Chapman, H., Scott, A., Hogan, L., Kivell, A., Camnasio, E., Yashinsky, M., Bruneau, M. and Chouw, N. 2011. Lessons Learnt From 2011 Christchurch Earthquakes: Analysis and Assessment of Bridges. *Bulletin of NZ Society for Earthquake Engineering*, 44(4): 319–333.

Robinson, K., Cubrinovski, M., Kailey, P. and Orense, R. 2011. Field Measurements of lateral spreading following the 2010 Darfield earthquake. *9th Pacific Conf. on Earthquake Engineering*, Paper 52, Auckland.

Seed, R.B. and Harder, L.F. 1991. SPT-based analysis of cyclic pore pressure generation and undrained residual strength. *Proc. H. Bolton Seed Memorial Symposium*, 2: 351–376.

Winkley, A. 2013. "*Impacts of liquefaction and lateral spreading on bridge pile foundations from the February 22nd 2011 Christchurch earthquake*," ME Thesis, University of Canterbury.

Wotherspoon, L., Bradshaw, A., Green, R., Wood, C., Palermo, A., Cubrinovski, M. and Bradley, B. 2011. Performance of bridges during the 2010 Darfield and 2011 Christchurch earthquakes. *Seismological Research Letters* 82(6): 950–964.

Zhang, G., Robertson, P.K., and Brachman, R.W.I. 2004. Estimating liquefaction-induced lateral displacements using the standard penetration test or cone penetration test. *ASCE Journal of Geotechnical and Geoenvironmental Engineering*, 130(8), 861–871.

This page intentionally left blank

Soil Liquefaction during Recent Large-Scale Earthquakes – Orense, Towhata & Chouw (Eds)
 ISBN 978-1-138-02643-8

Influence of foundation pinning and deck resistance on the response of a Chilean bridge abutment to lateral spreading

C.R. McGann
Department of Civil and Natural Resources Engineering, University of Canterbury, Christchurch, New Zealand

P. Arduino
Department of Civil and Environmental Engineering, University of Washington, Seattle, Washington, USA

ABSTRACT: The 2010 Maule earthquake in Chile caused extensive lateral spreading at the site of the Mataquito river bridge. The surface soil deformation patterns and relatively minor structural damage to the bridge observed at this site suggest that foundation pinning effects played a prominent role in the overall response of the bridge abutments to the lateral spreading. 3D finite element analysis of a Mataquito river bridge abutment is used to examine the role of foundation pinning, lateral bridge deck resistance, and the deck expansion gap on the response of the abutment and approach embankment to a simulated lateral spreading event.

1 INTRODUCTION

Liquefaction-induced lateral soil deformation is an important design consideration for river crossing bridges in seismically active regions. Observations at numerous bridges affected by lateral spreading (e.g., Youd, 1993; Berrill, 2001; GEER, 2010; Wotherspoon, et al., 2011) suggest that some combination of bridge deck resistance and deep foundation pinning acts to alter the near-field deformation of the laterally spreading soil, leading to potential reductions in foundation demands that may not be considered in simplified design approaches. The Mataquito river bridge near the Pacific coast of Chile is an example of a site where these effects appear to have significantly affected the response of the soil-foundation-bridge system. The 2010 Maule earthquake caused widespread lateral spreading in the soil surrounding the Mataquito river bridge (GEER, 2010; MAE, 2010; FHWA, 2011), with reported surface deformations of up to 2.5 m, however, only relatively minor structural damage was observed in the bridge itself.

Three-dimensional finite element (FE) models of the Mataquito river bridge site are developed and analysed in an effort to identify and quantify the mechanisms that may result in potential reductions in the bridge foundation demands induced by lateral spreading in the surrounding soil. The models are developed using the OpenSees computational framework (McKenna, 1997) and include representations of the southern bridge abutment, grouped shaft foundation, and approach embankment, as well as the surrounding and underlying soil. The 3D models are used to simulate lateral spreading for the Mataquito site in order to assess the influence of the bridge deck and the accompanying expansion gap on the lateral response of the foundation system, and determine the amount of pinning resistance provided by the deep foundations. Comparison to the observed response of the bridge, foundations, approach embankment, and native site soil is used to verify the results of the numerical models.

2 FINITE ELEMENT MODEL

3D FE models are created to analyse the response of the southwest Mataquito bridge approach embankment, abutment, and grouped shaft foundation to the kinematic demands of lateral spreading. Two mesh configurations are considered; (1) a mesh based on the existing 3D embankment geometry, see Figure 1, and (2) a nearly identical mesh (not shown) in which the embankment extends to the boundary of the mesh instead of sloping down to the native soil as in the existing geometry case. This wide embankment geometry is intended to simulate the assumptions made in a plane strain analysis of the site, and is used to evaluate the differences in foundation response resulting from 2D and 3D description of the problem. Symmetry conditions are considered as shown in Figure 1, and each mesh is selectively refined such that the elements are smaller near the important features and larger near the boundaries.

2.1 *Boundary and loading conditions*

The primary goal of the model is to capture the response of the foundations and their immediate surroundings, therefore, the mesh boundaries are defined far enough away from this portion of the model as to minimize their effect on the results. The nodes along the base of the mesh are fixed against vertical translation and elemental body forces are used to simulate the effect of gravity and achieve an appropriate initial state of stress in the soil. The nodes on the symmetry plane are fixed against translation normal to the plane, and the nodes on the vertical boundary opposite the symmetry plane are fixed against all horizontal translation. The nodes on the two remaining vertical mesh boundaries are fixed against out-of-plane translation only.

The kinematic demands of lateral spreading are achieved in the model by gradually imposing a set displacement profile to the non-symmetry mesh boundaries as shown in Figure 2. This displacement profile represents the free-field kinematic demands on the soil system. Applied displacements are constant above the liquefiable material, linearly-increasing across the liquefiable layer, and held at zero below the liquefiable zone. This displacement profile is gradually imposed in a static analysis of the model. The final free-field surface displacement considered in this work is 1.0 m, a value consistent with the magnitude of free-field lateral spreading displacements observed near the Mataquito bridge abutment.

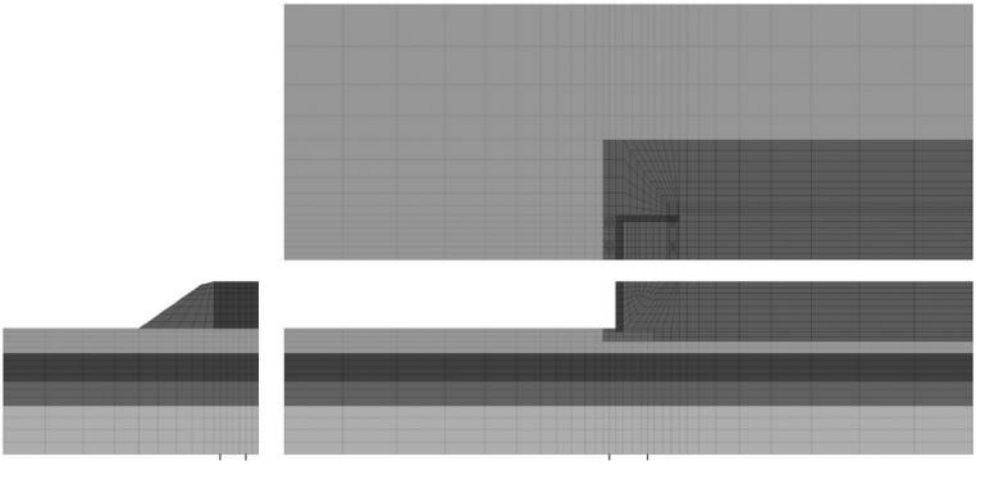

Figure 1. 3D FE mesh for Mataquito bridge abutment site.

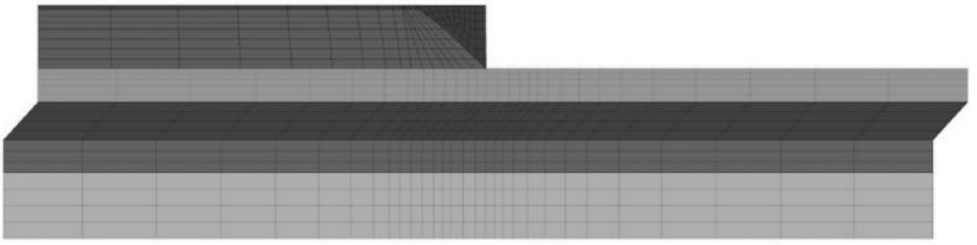

Figure 2. Applied displacement profile used to simulate kinematic demands of lateral spreading.

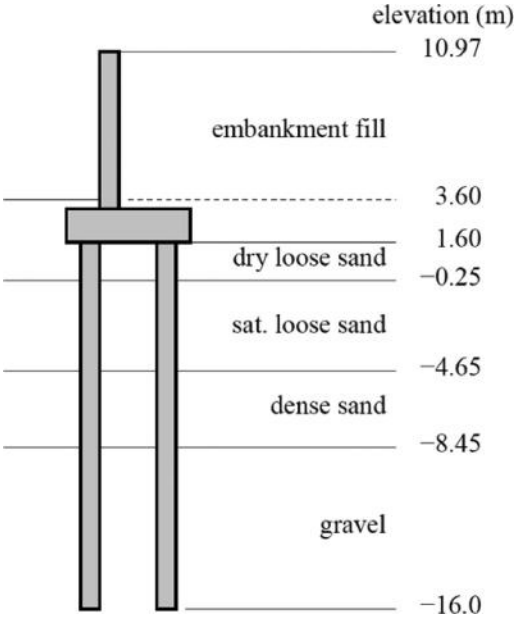

Figure 3. Layout of idealized soil profile near the southwest bridge abutment.

2.2 *Model soil profile*

The finite element model uses an idealized soil profile for the Mataquito bridge site developed from SPT resistance data obtained prior to construction of the bridge and the soil characterization report (Petrus, 2006). The available data sets indicate a predominantly cohesionless soil profile with three general layers: a loose sand layer near the surface, a middle layer of denser sand, and an underlying layer of dense gravel and gravelly sand. For modelling purposes, minor variations in the soil profile are ignored. Figure 3 shows the layout of the idealized soil profile at the location of the southwest bridge abutment.

Representative friction angles are estimated for each layer using the reported SPT resistance data and the correlations of Meyerhof (1956) and Peck et al. (1974). Small strain shear and bulk moduli are estimated from relative densities correlated to the assigned friction angles using the Schmertmann (1978) relation. The properties of the embankment fill are unspecified in the available information, therefore, the fill is given the strength and stiffness properties of the lower soil layer. A 3H:2V embankment side slope is assumed based on Chilean Ministry of Public Works (MOP, 2002) recommendations. The relevant model properties for each layer are listed in Table 1.

Table 1. Model properties for idealized soil profile.

Soil type	ρ (Mg/m^3)	ρ_{sat} (Mg/m^3)	φ (°)	G_{max} (MPa)	K_{max} (MPa)
Loose sand	1.7	2.16	31	60	175
Dense sand	1.7	2.11	36	90	230
Gravel	1.7	2.08	42	130	250
Embankment fill	1.8	–	42	130	250

Ledezma (2012) estimated that sands at the Mataquito site with a normalized SPT N-value < 28 blows/ft are highly susceptible to liquefaction per the Youd et al. (2001) triggering relationship. Of the three layers in the idealized soil profile, only the SPT resistance of the loose sand layer is below this threshold. The portion of this layer below the groundwater table is assumed to be the liquefiable material for the lateral spreading simulations.

The focus of the 3D modelling effort is to assess the response of the soil-foundation-bridge system to the kinematic demands of lateral spreading. It is assumed that effects related to the initiation of liquefaction are irrelevant to this goal; therefore, total stress analysis is considered. The liquefiable saturated loose sand layer is initially defined with residual strength and stiffness properties associated with a liquefied state. This layer is defined using a J2-type multi-surface kinematic plasticity model (Prevost, 1977) with a reduced shear modulus G = 6000 kPa and an undrained shear strength of 18.0 kPa. The remaining soil layers are modelled using a pressure-dependent multi-surface constitutive model (Parra, 1996; Yang, 2000; Elgamal et al, 2003) appropriate for dry and saturated cohesionless soil.

2.3 *Model foundations*

The Mataquito bridge abutments are founded on 1.5 m diameter reinforced concrete shafts grouped in a 4 × 2 layout with the orientation and dimensions shown in Figure 4. The shafts extend 17.6 m below the base of the shaft cap, terminating about 7.5 m into the gravel layer. A template cross-section with a reinforcement configuration typical to the shaft foundations for the bridge is assumed for the definition of shaft cross-sectional models. Details for this template cross-section are available in McGann (2013). Each shaft is loaded vertically with the design axial load, P = 4.12 MN.

Displacement-based beam-column elements are used to model the shaft foundations in the 3D model. Linear elastic shaft behaviour is assumed in order to assess foundation demands independent of strength. Single shaft model properties are based on the gross cross-sectional properties of the shafts (area, A = 1.77 m^2, and second area moment, I = 0.25 m^4), the initial bending stiffness of a single shaft, EI = 5.3 GNm^2, indicated by a moment-curvature analysis of the template reinforced concrete cross-section, and an assumed Poisson's ratio, v = 0.25. Figure 5 shows how the abutment and grouped shaft foundation are incorporated into the 3D models. To consider the physical size of the shafts, a circular space is built into the mesh surrounding the beam-column elements, and the beam-solid contact element of Petek (2006) is used to enforce a contact constraint on the surface of this space. The shafts extend below the base of the gravel soil layer to ensure contact is considered on the mesh boundary, and the shaft elements are supported at the base on Q-z spring (Meyerhof, 1976) elements to consider end bearing effects.

The abutment and shaft cap are modelled using solid elements assigned an isotropic linear elastic constitutive response with shear modulus, G = 1.3 KPa, and bulk modulus, K = 2.5 GPa. An internal frame of beam-column elements is used to rigidly join the shafts within the shaft cap, and this frame is extended into the front wall of the abutment in order to transmit rotations of the upper foundation into the lower portions. These beam-column elements are assigned linear elastic behaviour with a large bending stiffness such that they are rigid relative to the single shaft model.

The bridge deck is incorporated into the model using a linear elastic spring element without tensile stiffness. In order to consider the effects of a deck expansion gap, this spring element includes a compression gap that must be closed prior to activating any lateral resistance.

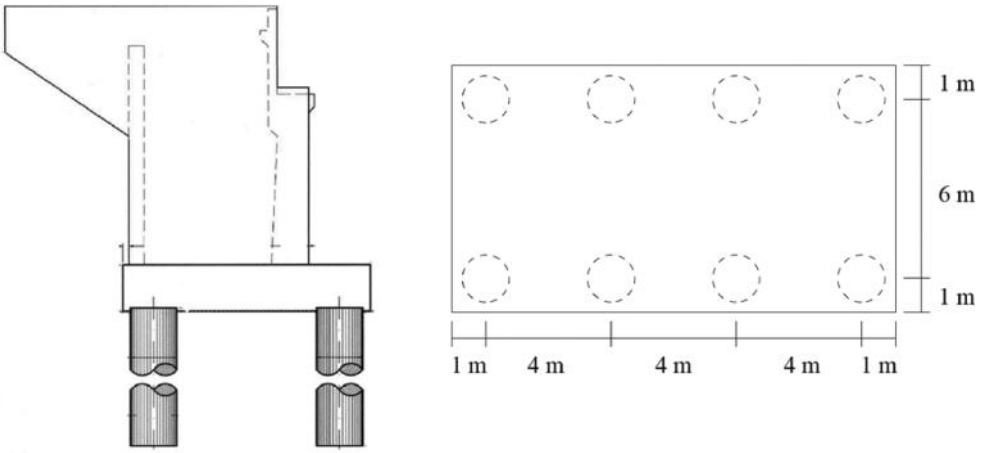

Figure 4. Layout of Mataquito bridge foundation (courtesy Ministerio de Obras Públicas, Chile).

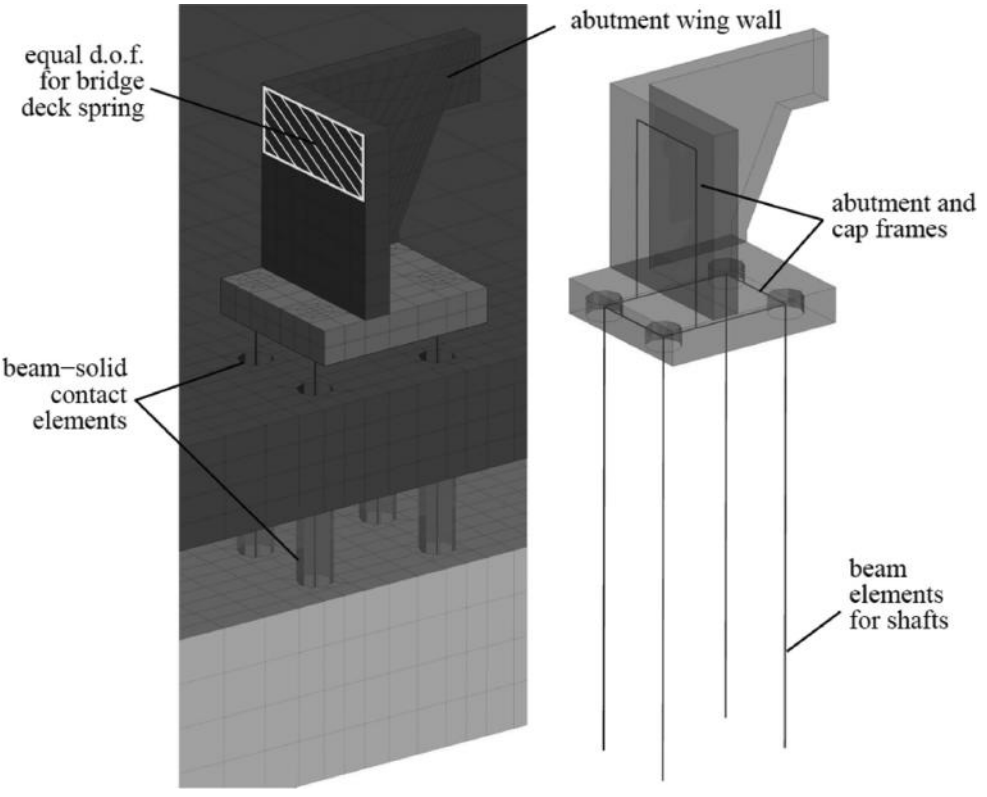

Figure 5. Abutment and grouped shaft foundation in 3D FE model.

The stiffness of the deck spring element is based on the cross-sectional area and length of the bridge deck segment immediately adjacent to the abutment. The nodes on the abutment elements coinciding with the location of the deck connection, see Figure 5, are constrained to have equal degrees-of-freedom in the direction of loading and connected to the free end of the deck spring element. The sensitivity of the lateral abutment response to the magnitude of the expansion gap is assessed by considering two gap values: (1) a 5 cm gap chosen to evaluate

the response of the system when significant deck resistance is mobilized at smaller levels of abutment displacement, and (2) a larger 25 cm gap selected to provide a better assessment of the foundation response in the absence of significant deck resistance.

3 GLOBAL MODEL RESPONSE

Figure 6 shows the deformed mesh with contours of displacement magnitude at the end of the analysis for the existing embankment geometry case with a 5 cm expansion gap. It is difficult to discern from this plot whether deck resistance or foundation pinning is primarily responsible for the observed alterations to the soil deformation field, however, these results confirm the presence of some form of structural resistance at the Mataquito site. The applied free-field displacement (100 cm) essentially exists only on the boundaries of the model, and the surface soil displacements become gradually lower with increased proximity to the bridge abutment.

In contrast, Figure 7 shows the same plot for the wide embankment geometry mesh, also with a 5 cm expansion gap. As shown, the bridge does not provide nearly as much resistance

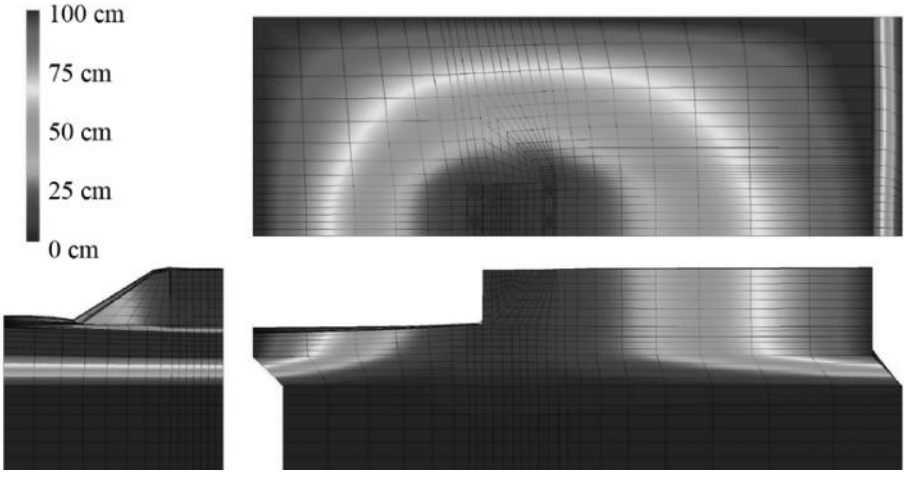

Figure 6. Deformed mesh (magnified 4 times) for existing geometry 5 cm gap model.

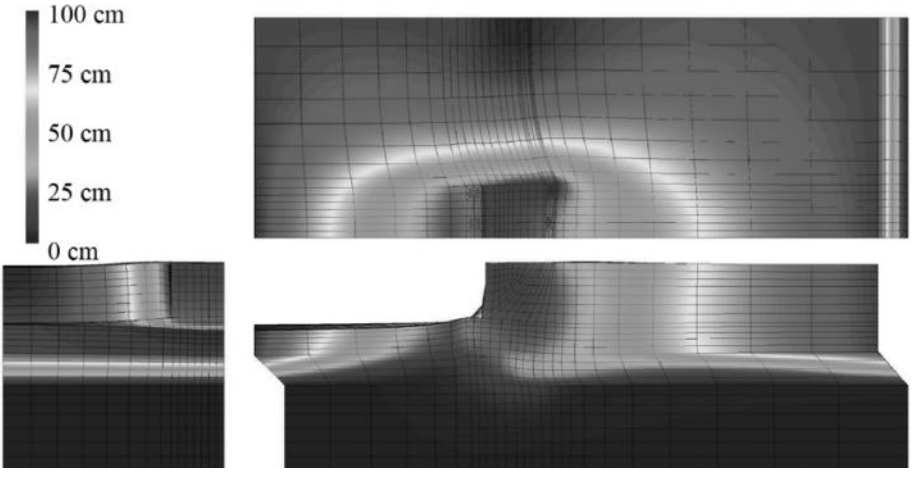

Figure 7. Deformed mesh (magnified 4 times) for wide embankment geometry 5 cm gap model.

to the lateral spreading deformation induced in the soil mesh. This difference in results for the wide embankment geometry makes sense in the context of the pile pinning analysis concept (e.g., Martin et al., 2002; Boulanger et al., 2006), which makes consideration for the effects of 3D embankment geometry on a bridge abutment during lateral spreading, and emphasizes the differences between the foundation demands resulting from 3D and plane strain site descriptions. The moving mass of soil in the wide embankment model is simply too large for the bridge to mount any significant resistance to its lateral movement. The 25 cm gap models naturally display larger lateral displacements across the soil mesh, as the foundation resistance is not sufficient to prevent closure of the expansion gap, however, the relative patterns between the existing and wide geometries are the same as demonstrated in Figures 5 and 6, thus, additional plots are omitted here. See McGann (2013) for further discussion on the global response of the 25 cm gap models.

The overall deformation trends returned by the existing geometry models correspond with physical observations made at the Mataquito site, where the riverward displacement of the approach embankment was less than that in the surrounding native soil and there was significant slumping in the embankment fill immediately adjacent to the abutment along with displacement of the fill out away from the bridge centreline. Outward displacement and minor slumping of the fill are visible in Figure 5, though the magnitude of the slumping is somewhat obscured by the upward heave induced by the lateral displacement applied at the mesh boundary. The magnitude of the slumping in the model is less than that observed at the bridge site; however, the presence of the trend in the model results lends confidence to conclusions drawn from the simulations. The wide geometry cases correspond to a 2D description of the problem, with almost no displacement of the soil perpendicular to the bridge axis.

4 ABUTMENT AND FOUNDATION RESPONSE

The response of the abutment and foundations are isolated from the global model response in order to assess the relative contributions of the bridge deck and deep foundations to the structural resistance evident in Figure 6 (and to a lesser extent, Figure 7). One way in which to determine the relative resistance provided by each structural element is through comparison of the results returned by two considered expansion gap magnitudes. Due to the way deck spring model is defined, prior to gap closure, all of the structural resistance observed in the models is due only to deep foundation pinning. After closure of the gap, the mechanism for structural resistance changes as the deck begins to impede the further deformation of the laterally spreading soil. This change in the resistance mechanism leads to a change in the deformation mode for the foundation system.

4.1 *Foundation pinning resistance*

Figure 8 compares the abutment displacements obtained from both embankment geometries for the two expansion gaps to the free-field displacements applied on the boundary of the mesh. If no pinning resistance was provided by the grouped shaft foundation, the free-field and abutment displacements would coincide at the instant of gap closure. As shown in Figure 8, this is not the case in any of the FE models, though the wide geometry results nearly satisfy this condition. Approximately 8 cm of applied free-field displacement is required to close the 5 cm gap for the existing geometry, while 6 cm is required for the wide geometry. For the 25 cm expansion gap, the free-field displacements at gap closure are 46 and 29 cm, respectively.

These results confirm the observations made from the global model response with respect to the differences between 2D and 3D descriptions of the problem, and also demonstrate the degree of foundation pinning resistance for the Mataquito abutment and approach embankment. For the existing geometry cases, the abutment displacements are approximately 50–60% of the free-field soil displacements up until gap closure at which point the abutment

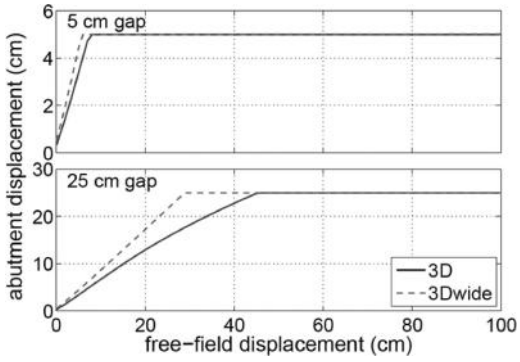

Figure 8. Evolution of abutment displacement in loading direction for 5 and 25 cm gap models.

displacements remain constant with increasing free-field displacement due to the resistance provided by the deck. It also appears that the difference between the abutment and free-field displacements becomes larger with increasing free-field displacement. The abutment displacements are approximately 85% of the free-field levels for the wide geometry cases. The difference between the two displacement sets is relatively constant for these cases.

4.2 *Bridge deck resistance*

After the expansion gap has closed, the lateral resistance provided by the bridge deck is sufficient to essentially hold the top of the abutment stationary as the free-field displacement field continues to increase. The introduction of this additional resistance changes the deformation mechanism for the abutment as the shaft cap and the lower portions of the abutment walls continue to displace in the direction of loading. This change in deformation mechanism is illustrated by Figure 9, which shows the deformed shapes of the model foundation at gap closure and analysis end for the 5 cm expansion gap cases. Up until the deformation of the abutment closes the expansion gap, the displacements of the upper abutment wall and shaft cap are nearly equal, though there is a slight forward lean to the abutment wall. After gap closure, the abutment wall begins to rotate about the bridge deck connection as the lateral movement of the shaft cap continues.

The rotational deformation mechanism is especially apparent for the wide geometry case, where the shaft cap ends up about 15 cm forward of the top of the abutment, indicating an approximately 1.2° rotation of the abutment wall. The existing geometry case displays the same rotational trend; however, the magnitude of the rotation is much less at approximately 0.1°. This type of rotational foundation response is important as it places large bending demands on the upper portions of the shafts. These bending demands can lead to damage of the sort noted by Cubrinovski et al. (2012), potentially resulting in the failure of the piles or shafts that support the abutment.

5 COMPARISON TO PHYSICAL BRIDGE RESPONSE

The overall response of the abutment observed in the lateral spreading simulations corresponds directly with site observations made following the earthquake. The presence of foundation and deck pinning effects are confirmed by the deformation patterns in the embankment fill and immediately surrounding native soils, which were clearly affected by the presence of the bridge structure. It is likely that this implied resistance was due to some combination of the shaft foundations and the bridge deck, though it is difficult to tell for sure which aspect contributed the most to the resultant behaviour. The expansion gap closure predicted by all of the 3D models mirrors the response of the physical bridge abutments, as confirmed by the

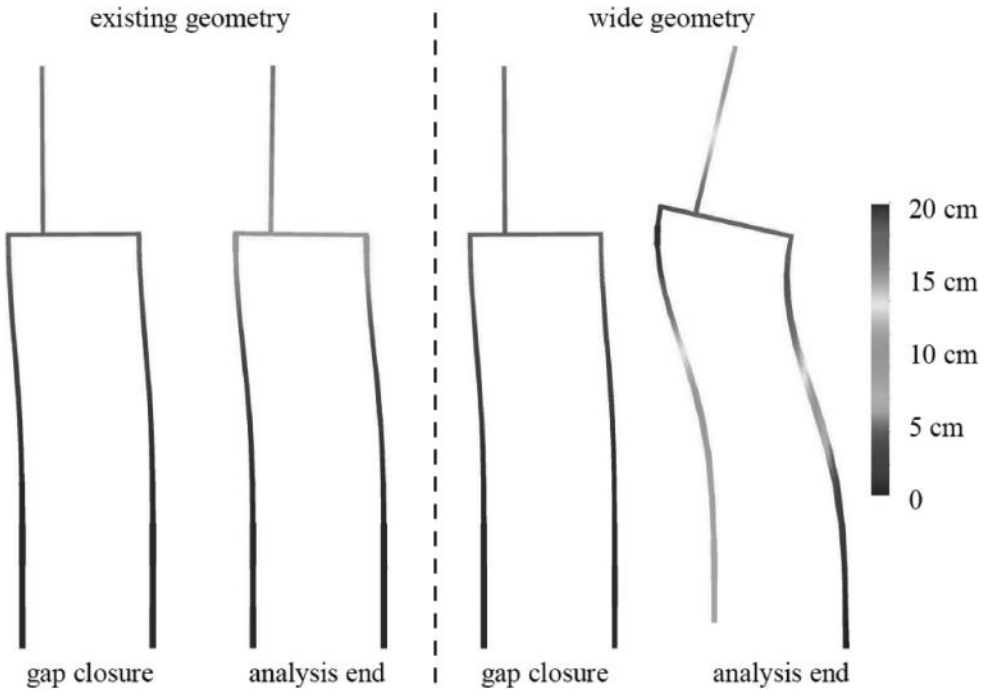

Figure 9. Foundation deformation modes (magnified 15 times) for 5 cm gap models.

Figure 10. Pre- and post-earthquake views of the Mataquito bridge deck expansion gap. Pre-earthquake photo retrieved January 14 2013, www.panoramio.com/photo/8172577. Post-earthquake photo from (GEER, 2010).

pre- and post-earthquake photographs shown in Figure 10. The construction details are such that the expansion gap separates the structural members across the full width of the bridge, thus, this gap is visible from the side in the pre-earthquake configuration of the bridge. After the earthquake and associated lateral spreading, this gap has been closed, resulting in contact between the abutment wall and bridge deck and the concrete spalling visible in Figure 10.

It is unclear whether the Mataquito bridge foundation rotated in a manner similar to that suggested by the FE models, as no obvious physical damage to the abutment or shaft foundations led reconnaissance teams to perform a detailed examination, and rotations on the order of 0.1–1.5° would not be readily apparent if the teams did not specifically look for this type of response. Due to the 20 cm expansion gap for the physical bridge, the forward lean evident in the model results prior to gap closure would be larger than that shown in Figure 9. Such forward rotation may have cancelled out any backward rotation occurring after the gap

was closed, leading to approximately zero net rotation of the abutment wall. The foundation pinning resistance suggested by the FE models would also serve to reduce any rotation of the abutment wall, as the shaft group would continue to resist the spreading-induced deformation after the expansion gap is closed, resulting in less riverward movement of the shaft cap.

6 SUMMARY AND CONCLUSIONS

The response of a bridge abutment, approach embankment, and grouped shaft foundation to lateral spreading was evaluated using 3D FE analysis. The selected site was the Mataquito river bridge, a reinforced concrete structure of recent vintage that was affected by lateral spreading due to the 2010 Maule earthquake in Chile. The results of the 3D analyses were used to gain insights into the mechanisms that govern the response of the abutment and associated deep foundations to the kinematic demands induced by the simulated lateral spreading in the native soils. The completed analyses demonstrated the difference in response returned by 2D and 3D descriptions of the approach embankment geometry. The models based on the existing site geometry demonstrated how the interaction of lateral resistance from the deep foundations and bridge deck leads to a lessening in the magnitude of soil deformation in the near-field, and identified how the interaction between the various structural elements defines the deformation mechanism for the abutment. A marked difference was observed in the model response depending on the state of the deck expansion gap. Prior to gap closure, all structural resistance is provided by foundation pinning. After the gap has been closed, the bridge deck alters the deformation mode for the foundation system, resulting in a tendency for backwards rotation about the connection to the deck. Trends displayed by the 3D FE models were shown to correspond to the physical response at the bridge site as recorded during post-earthquake reconnaissance. The gap-closure response displayed by all of the completed analyses was determined to match the response of the Mataquito bridge abutments. Though the visible structural damage was relatively minor, this finding suggests that the impact of lateral spreading on the bridge was greater than initially thought.

ACKNOWLEDGEMENTS

Funding for this work was provided by the Washington State Department of Transportation. The authors would also like to thank Tony Allen, Christian Ledezma, and Gonzalo Montalva for their input and assistance.

REFERENCES

Berrill, J.B., Christensen, S.A., Keenan, R.P., Okada, W., and Pettinga, J.R. 2001. Case study of lateral spreading forces on a piled foundation. *Géotechnique, 51*(6), 501–517.

Boulanger, R.W., Chang, D., Gulerce, U., Brandenberg, S.J., and Kutter, B.L. 2006. Evaluating pile pinning effects on abutments over liquefied ground. In R.W. Boulanger, and K. Tokimatsu (Ed.), *Seismic Performance and Simulation of Pile Foundations in Liquefied and Laterally Spreading Ground* (pp. 306–318). GSP 145, ASCE.

Cubrinovski, M., Haskell, J., Winkley, A., Robinson, K., and Wotherspoon, L. 2012. Performance of bridges in liquefied deposits during the 2010–2011 Christchurch (New Zealand) earthquakes. *Journal of Performance of Constructed Facilities, ASCE*, Accepted Manuscript.

Elgamal, A., Yang, Z., Parra, E., and Ragheb, A. 2003. Modeling of cyclic mobility in saturated cohesionless soils. *International Journal of Plasticity*, 883–905.

Federal Highway Administration (FHWA). 2011. *Post-Earthquake Reconnaissance Report on Transportation Infrastructure: Impact of the February 27, 2010, Offshore Maule Earthquake in Chile*. Publication No. FHWA-HRT-11-030, U.S. Department of Transportation, McLean, VA.

Geo-Engineering Extreme Events Reconnaissance (GEER) Association. 2010. *Geo-engineering Reconnaissance of the 2010 Maule, Chile Earthquake.* Report No. GEER–022.

Ledezma, C. 2012. Case study of three pile-supported bridges affected by liquefaction-induced lateral spreading after the M8.8 2010 Maule Chile Earthquake. *Second International Conference on Performance-Based Design in Earthquake Geotechnical Engineering.* Taormina, Italy, Paper No. 6.13.

Martin, G.R., March, M.L., Anderson, D.G., Mayes, R.L., and Power, M.S. 2002. Recommended design approach for liquefaction induced lateral spreads. *Proc., 3rd Natl. Seismic Conf. and Workshop on Bridges and Highways.* MCEER-02-SP04, Buffalo, NY.

McGann, C.R. 2013. *Numerical Evaluation of Forces on Piled Bridge Foundations in Laterally Spreading Soil*. Ph.D. Dissertation, University of Washington.

McKenna, F.T. 1997. *Object-Oriented Finite Element Programming: Frameworks for Analysis, Algorithms and Parallel Computing*. Ph.D. Dissertation, University of California, Berkeley.

Meyerhof, G.G. 1956. Penetration tests and bearing capacity of cohesionless soils. *Journal of the Soil Mechanics and Foundations Division, ASCE, 82*(SM1), 1–19.

Meyerhof, G.G. 1976. Bearing capacity and settlement of pile foundations. *Journal of the Soil Mechanics and Foundations Division, ASCE*, 197–228.

Mid-America Earthquake (MAE) Center. 2010. *The Maule (Chile) Earthquake of February 27, 2010 Consequence Assessment and Case Studies.* Report No. 10–04.

Ministerio de Obras Públicas (MOP). 2002. *Manual de Carreteras, Vol. 3, Instrucciones y Criterios de Diseńo*. Santiago, Chile.

Parra, E. 1996. *Numerical Modeling of Liquefaction and Lateral Ground Deformation Including Cyclic Mobility and Dilation Response in Soil System*. Ph.D. Dissertation, Rensselaer Polytechnic Institute.

Peck, R.B., Hanson, W.E., and Thornburn, T.H. 1974. *Foundation Engineering, 2nd Edition.* New York: John Wiley & Sons.

Petek, K.A. 2006. *Development and Application of Mixed Beam-Solid Models for Analysis of Soil-Pile Interaction Problems*. Ph.D. Dissertation, University of Washington.

Petrus Consultores Geotecnicos. 2006. *Informe Complementario de Mecanica de Suelos, Puente Matquito (Ruta Costera), Camino Quivolgo-Iloca (Cruce J-60)*. Santiago, Chile: Informe No. 2619-ING-SGC-150/2006 (Rev 1).

Prevost, J.H. 1977. Mathematical modeling of monotonic and cyclic undrained clay behavior. *International Journal for Numerical and Analytical Methods in Geomechanics*, 195–216.

Schmertmann, J.H. 1978. *Guidelines for Cone Penetration Test Performance and Design.* Washington, D.C.: Report FHWA-TS-78–209, U.S. Department of Transportation.

Wotherspoon, L., Bradshaw, A., Green, R., Wood, C., Palermo, A., Cubrinovski, M., and Bradley, B. 2011. Performance of bridges during the 2010 Darfield and 2011 Christchurch earthquakes. *Seismological Research Letters, 82*(6), 950–964.

Yang, Z. 2000. *Numerical Modeling of Earthquake Site Response Including Dilation and Liquefaction*. Ph.D. Dissertation, Columbia University, New York.

Youd, T.L. (1993). Liquefaction-induced damage to bridges. *Transportation Research Record No. 1411*, 35–41.

Youd, T.L., Idriss, I.M., Andrus, R.D., Arango, I., Castro, G., Christian, J.T., et al. 2001. Liquefaction resistance of soils: Summary report from the 1996 NCEER and 1998 NCEER/NSF workshops on evaluation of liquefaction resistance of soils. *Journal of Geotechnical and Geoenvironmental Engineering, ASCE, 127*(10), 817–833.

This page intentionally left blank

Soil Liquefaction during Recent Large-Scale Earthquakes – Orense, Towhata & Chouw (Eds)
© 2014 Taylor & Francis Group, London, ISBN 978-1-138-02643-8

Piles in liquefiable soil: Kinematic and inertial interaction

M. Pender
Department of Civil and Environmental Engineering, University of Auckland, Auckland, New Zealand

M. Willis
Earthtech Consulting Limited, Auckland, New Zealand

P. Algie
Ports of Auckland Limited, Auckland, New Zealand

ABSTRACT: This paper, based on computational work, presents a comparison of kinematic and inertial interaction for a single pile embedded in a liquefiable soil layer. The question which prompted the work is the relation between the two types of soil-pile interaction for nonlinear soil behavior, particularly as pore water pressures increase with consequent decrease in the stiffness and shear strength of the soil. The software used is OpenSeesPL which includes a model for saturated cohesionless soil which handles cyclic pore pressure build-up as well as cyclic mobility when the phase-change line is crossed. The response of a single pile embedded in a saturated cohesionless soil layer is calculated when a Ricker wavelet, used to represent earthquake input, is applied at the base of the layer. The majority of the results are calculated assuming that the permeability of the cohesionless soil is the same as that of silt. Prior to the calculations with the Ricker wavelet input, pushover calculations were done. The results for both the pushover and dynamic modeling, confirm the validity of the separation of kinematic and inertial responses for an elastic system, but also show that this is a useful way of looking at nonlinear behavior of a pile-soil system. Furthermore the results confirm that the inertial response of the pile shaft and also the push-over response confirm the existence of an active length. A final aspect of the paper looks at the free vibration response of the mass attached to the head of the pile shaft and notes how the damping when nonlinear soil behavior occurs is very different from that of an elastic viscously damped system.

1 INTRODUCTION

This paper, based on computational work, presents a comparison of kinematic and inertial interaction for a single pile embedded in a liquefiable soil layer. The separation of kinematic and inertial pile-soil interaction was explained by Gazetas (1984) for elastic systems. The question which prompted the work reported in the paper is the relation between the two types of soil-pile interaction for nonlinear soil behavior, particularly as pore water pressures increases and the stiffness and shear strength of the soil decreases. The software used is OpenSeesPL which includes a model for saturated cohesionless soil that handles cyclic pore pressure build-up as well as cyclic mobility when the phase-change line is crossed. The response of a single pile embedded in a cohesionless soil layer is calculated when a Ricker wavelet is applied at the base of the layer to represent earthquake input. The results are calculated assuming that the permeability of the cohesionless soil is the same as that of silt. Prior to the calculations with the Ricker wavelet input, pushover calculations were done. The results confirm the validity of the separation of kinematic and inertial responses for an elastic system, but also show that this is a useful way of looking at nonlinear behavior of the pile-soil system. Furthermore the results confirm that the inertial response of the pile shaft and also the push-over response demonstrate the existence of an active length. An important outcome of the

work is the observation that the free vibration of the pile-head mass indicates that the damping associated with nonlinear soil behavior is very different from that of an elastic viscously damped system. The final part of the paper shows that the separation of kinematic and inertial response needs to be based on comparison of pile shaft displacement profiles at the same time step.

Much of the background to the work reported herein is contained in two University of Auckland Master of Engineering theses (i.e. Willis 2012; Algie 2012).

2 SOIL PROFILE, PILE DETAILS, SOFTWARE, AND INPUT MOTION

The soil profile analysed consists of a 10 metre layer of saturated sand overlying much stiffer material. Separate calculations were done for loose, medium and dense sand. The water table was assumed to be at the ground surface and the initial distribution of soil modulus with depth was assumed to be related to the square root of the depth. The pile was 0.6 m in diameter, with an EI value of 190 kNm^2, and a free-head located 1.5 m above the ground surface. For the inertial runs a mass of 10 tonnes is located at the top of the pile shaft. See Figure 1 for details.

OpenSeesPL (Lu et al. 2010) has been developed within the OpenSees (Mazzoni et al. 2009) framework specifically for calculations involving pile-soil interaction. The pile is vertical (but the ground surface does not have to be horizontal), the meshing within the "soil box" is semi-automated so that the element size increases with distance from the pile shaft. Actions can be applied to the pile head, both static and dynamic, earthquake motions can be applied to the base of the finite element mesh, and a range of side boundary conditions is available. Eight node brick elements were used for the soil discretisation. The software also has the facility to account for nonlinear soil and nonlinear pile behaviour. OpenSeesPL differs from OpenSees in that a graphical user interface is provided for input of model details and post-processing is provided for plotting the output data.

The OpenSeesPL software contains a stress-strain model for cohesionless materials (Yang et al. 2003), that can represent build-up in pore water pressure under cyclic loading as well as cyclic mobility, i.e. the reversal of the direction of the undrained effective stress path when the phase transformation line is crossed.

The input ground motion, applied at the base of the soil layer, is in the form of a Ricker wavelet with duration of 1.5 seconds and a digitization interval of 0.01 seconds. The form of the wavelet and the acceleration response spectrum of the motion are shown in Figure 2. The peak ground acceleration is 0.25 g and the Arias Intensity of the motion is 0.2 m/sec.

The following terms require explanation: long pile and active length; total, kinematic, and inertial pile shaft displacement. A pile shaft is said to be long when there is a certain distance, less than the pile shaft length, beneath which pile head shear and moment generate negligible pile shaft deformation. The distance down the pile shaft to negligible deformation is known as the active length. For all the modeling in this paper the active length is less than the embedment depth of 10 m (refer to Figures 3, 4, 8 and 9). If an independently referenced measuring system was available the total displacement at the pile head could be measured. These head displacements would also be associated with a pile shaft displacement profile, such as in Figures 3 a, c, and e. During earthquake excitation part of the pile head displacement is generated by the earthquake induced ground movement. If the pile is sufficiently

Table 1. Soil properties.

	G (MPa at 80 kPa)	ρ (tonnes/m^3)	ϕ' (degrees)	ϕ_{pt} (degrees)	K_o	T_{layer} (sec)
Loose	150	1.7	29	23	0.5	0.31
Medium	200	1.9	33	20	0.7	0.22
Dense	390	2.1	40	16	0.9	0.19

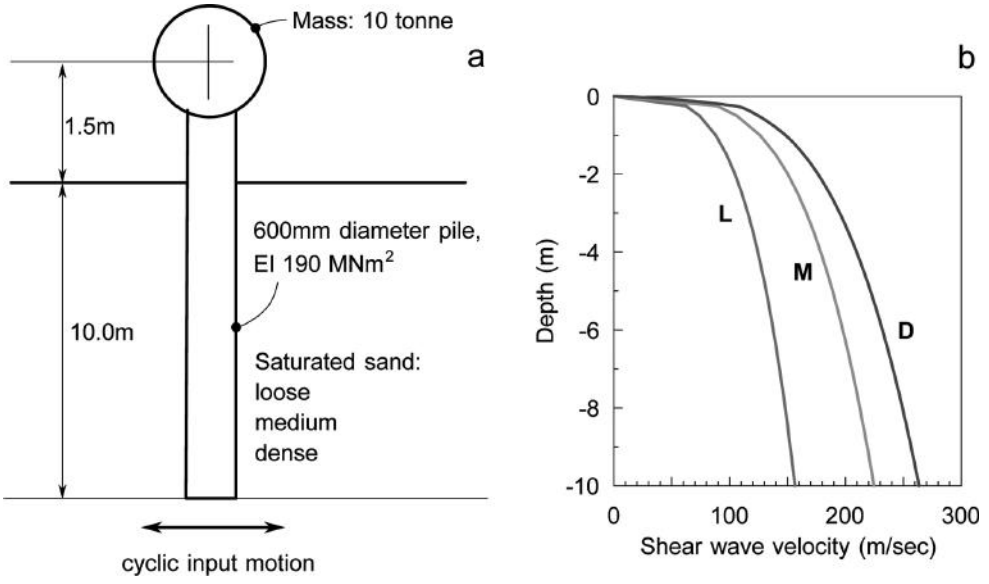

Figure 1. Pile and soil profile details: (a) soil layer and pile dimensions, (b) distribution of shear wave velocities with depth for the loose, medium and dense sand profiles.

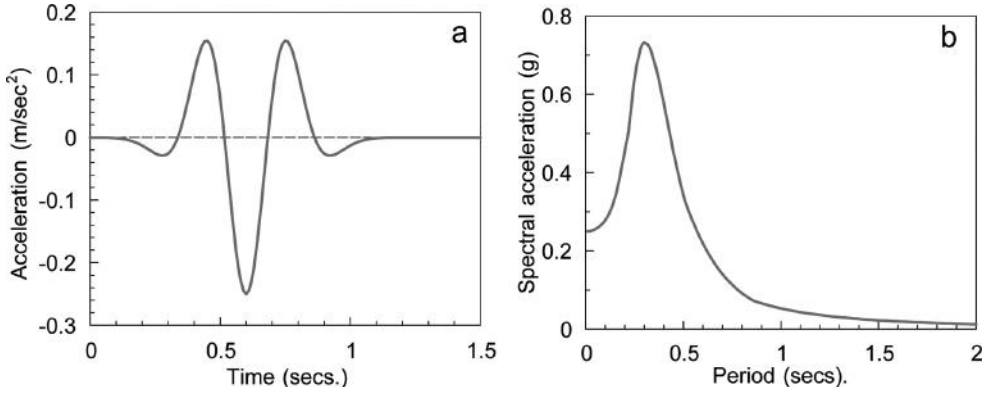

Figure 2. Ricker wavelet details: (a) time history, (b) acceleration response spectrum.

flexible, as is commonly the case, the pile is carried along with the soil; these movements of the pile shaft are known as kinematic interaction (refer to Figures 4 and 8). Usually, when considering kinematic interaction the pile head has no mass or structure attached, so there is no constraint preventing the pile moving with the soil. The inertial interaction, then, is the difference between the total and kinematic pile shaft displacements; inertial displacements are confined to the active length of the pile shaft (as shown in Figures 4, 8 and 9).

3 RESULTS

The first set of calculations considers the push-over response of the pile-soil system. For these calculations a lateral force of 200 kN was applied to the pile head in 1 kN increments over a 2 second period; that is the soil deformation was essentially undrained. Calculations were done for elastic as well as nonlinear soil behavior. The deflected shapes of the pile shaft

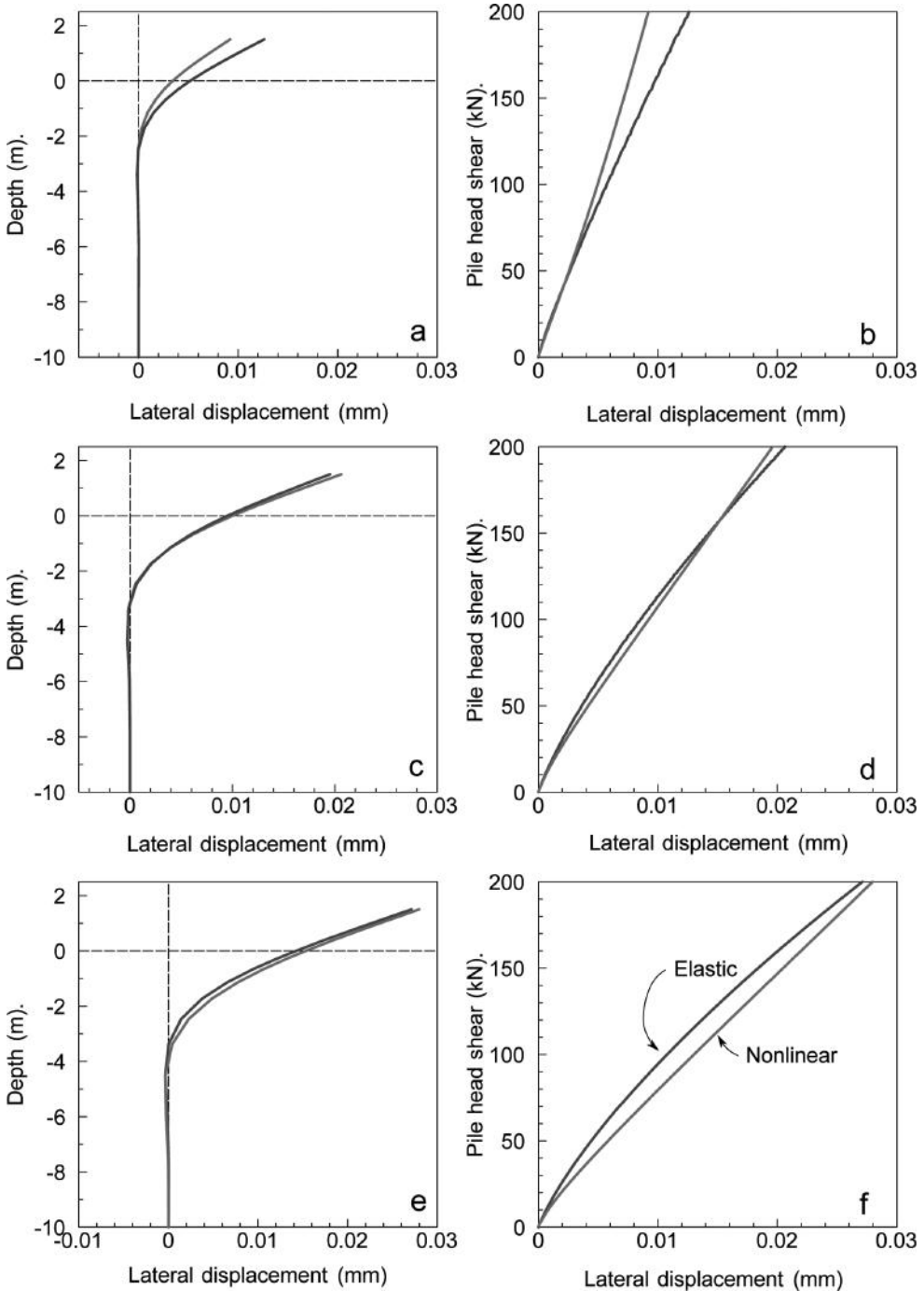

Figure 3. Pile head lateral push-over response. Displacement profile with depth and shear force lateral displacement relationship; dense sand, a and b; medium sand c and d; loose sand e and f. (Blue elastic, red nonlinear.).

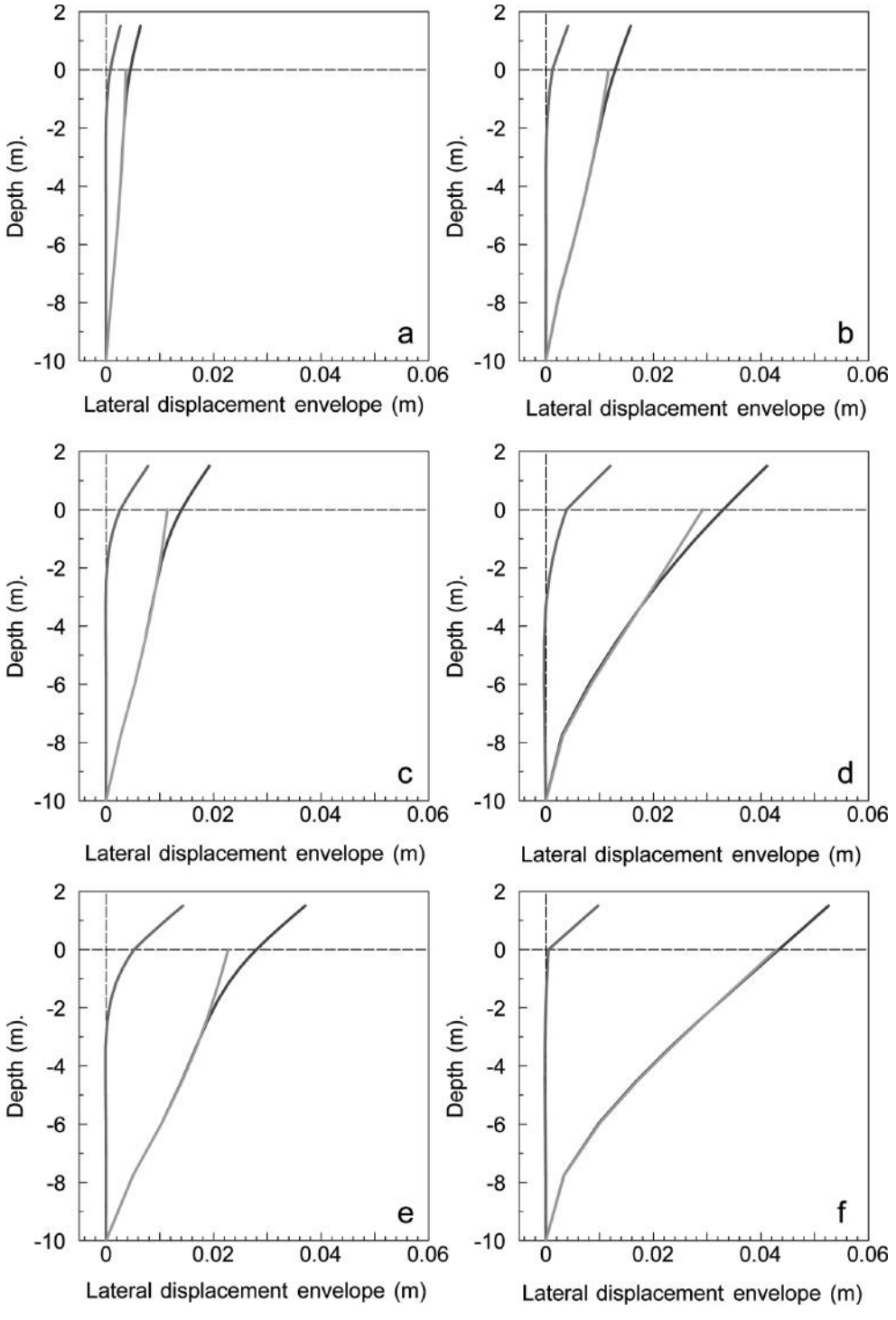

Figure 4. Pile lateral displacement envelopes; separation of inertial and kinematic response based on comparison of maximum displacement profiles (blue total, red inertial response, green kinematic). Left hand side nonlinear, right hand elastic; dense a and b; medium b and c; loose e and f.

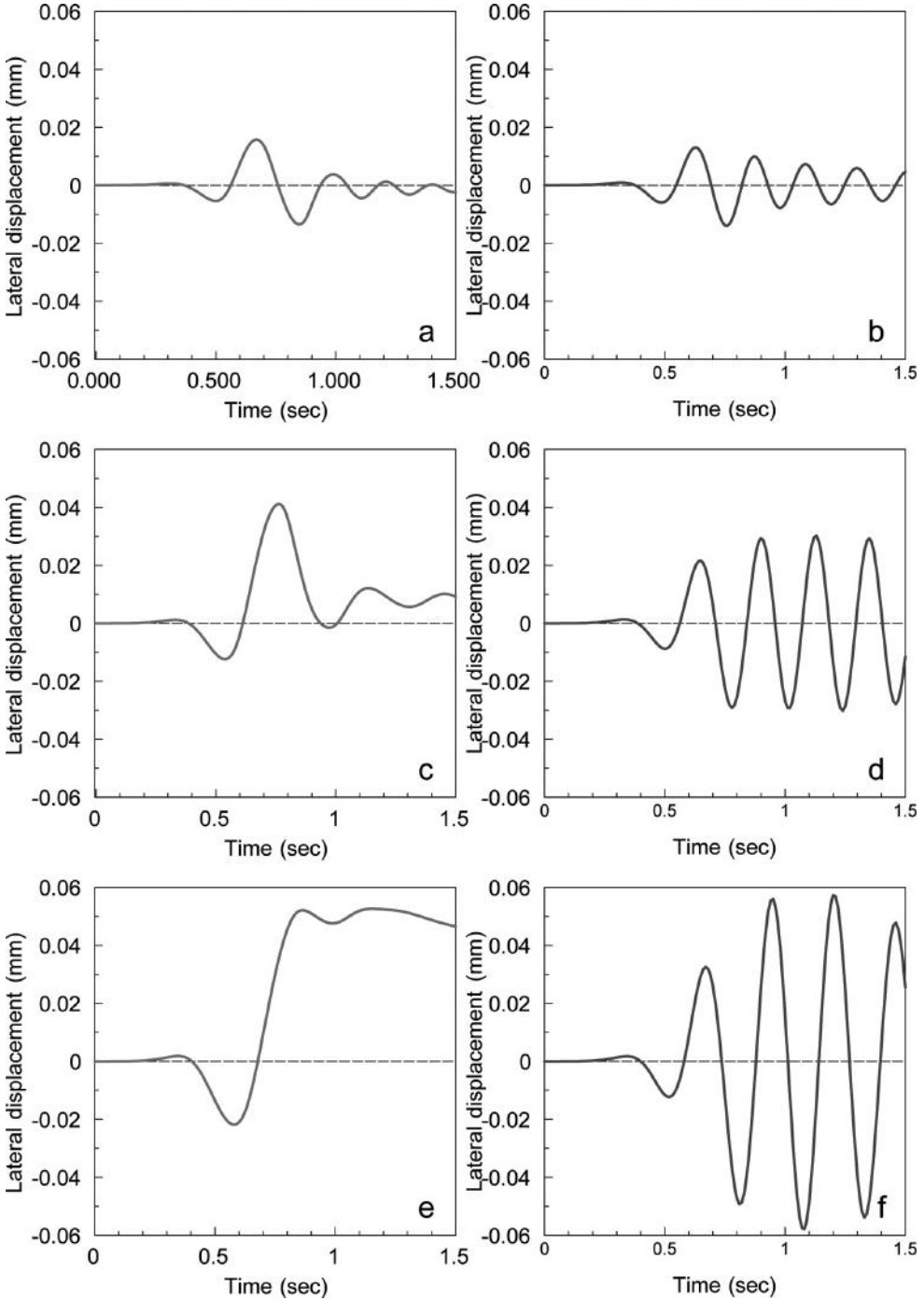

Figure 5. Lateral displacement histories for the pile head mass. Left hand side nonlinear, right hand elastic; dense a and b, medium b and c, loose e and f.

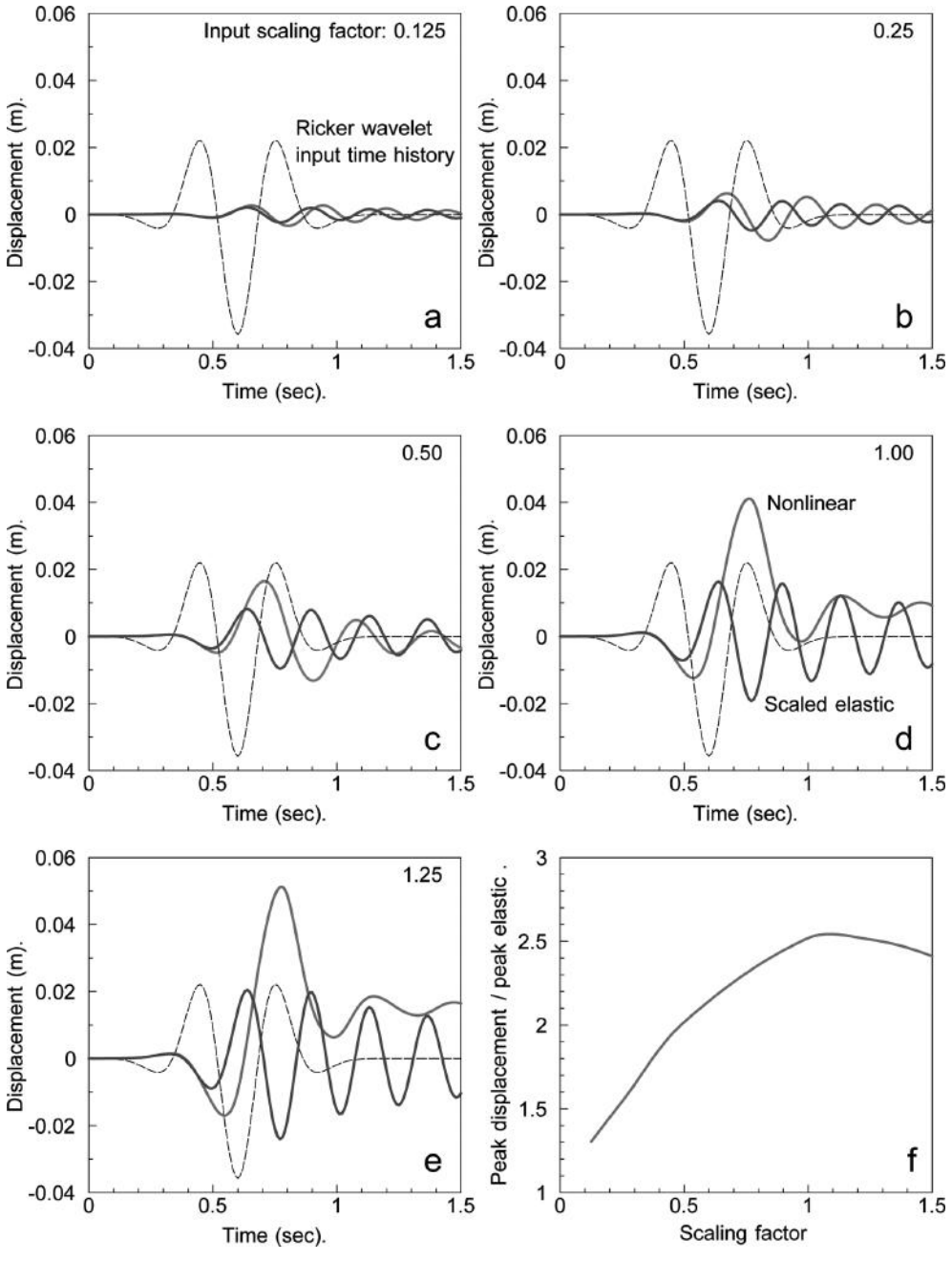

Figure 6. Elastic and nonlinear response to scaled Ricker Wavelet input; medium sand layer elastic period 0.22 seconds, elastic period including pile and mass 0.24 sec.

and the pile head load—deformation results are shown in Figure 3. Figures 3a, c and e indicate that the pile is long.

Figure 4 gives the displacement profiles associated with the maximum pile head displacement for both elastic and nonlinear soil behavior. Kinematic interaction determines the displaced shape of the pile when there is no mass attached to the pile head, that is the pile shaft is installed in the soil profile but there is no structural element attached to the top of the pile

shaft. Thus kinematic interaction considers how the pile shaft interacts with the surrounding soil when there is no shear or moment applied to the shaft at the ground surface. The results plotted in Figure 4 show that for all three soil profiles there are negligible differences between the deflected shape of the pile shaft and the soil profile; in other words the pile shaft simply follows the deformation of the sand layer. In Figure 4 the kinematic displaced shape of the pile shaft is plotted along with the total displacement envelope which includes the effect of the inertial response of the 10 tonne mass attached to the pile head. Subtracting these two gives the inertial displacement envelope for the pile shaft; that is the pile shaft deformation generated by shear and moment applied at the ground surface. It is apparent that the inertial displacements, like the push-over displacements in Figure 3, are confined to the top part of the pile shaft. However, closer examination of Figures 4d and 4f suggests that the approach of simply comparing the peak kinematic and peak total displacement profiles might not always give a clear separation of kinematic and inertial response; more on this below.

Figure 5 shows the free vibration response, induced by the Ricker wavelet excitation, of the 10 tonne pile-head mass which is 1.5 m above the ground surface. The right hand side of the diagram has the response for an elastic pile in an elastic soil layer, whilst the left hand side has the response for nonlinear soil behavior. It is clear that nonlinear soil behavior has a major effect on the apparent damping of the motion.

Figure 6 demonstrates the effect, on the response of a pile embedded in medium dense sand, of scaling the input motion; the wavelet is scaled between 0.125 and 1.25. The diagram also shows the elastic response for each case for reference and also the time signature of the Ricker wavelet is included in the diagram (but the vertical ordinate has no meaning as the units of the wavelet are acceleration, whilst the vertical axis of the diagram is displacement). The figure shows how the 10 fold increase in excitation alters the response. For the lowest scaling value the response is similar to the elastic response. For the higher scaling factors (1.00 and 1.25) it is clear that there is permanent deformation and that the degradation in the motion over the first half cycle after the peak is considerable and thereafter the apparent damping is small. This indicates that when dynamic excitation takes the system into the nonlinear range considerable damping is present. Figure 6e shows the effect of scaling the input motion on the peak lateral displacement. The plot has the scaling factor in the abscissa and the ratio of the peak displacement to the elastic peak displacement for the same input on the ordinate. The diagram shows that the nonlinear system is softer than the elastic one, hence the ratio is greater than unity, but with increasing excitation the ratio decreases, that is the nonlinear effect becomes more significant.

As a preliminary to considering in more detail the separation of kinematic and inertial response, Figure 7 compares the displacement response for linear and nonlinear systems. This shows that for elastic behaviour the peaks in the kinematic response and the total response do not occur at the same time. One the other hand the peaks kinematic and total displacements are nearly coincident when nonlinear soil behaviour occurs.

Our initial approach to separating kinematic and inertial response was very simplistic; just compare the kinematic and total displacement profiles associated with the maximum displacement of each. Figure 4 a, c and d indicate that this was successful and Figure 7b indicates why this is so. However, the elastic case was problematical right from the start; Figures 4 d and 4f hint at underlying problems. To examine these effects in more detail calculations were done with the pile stiffness reduced by a factor of 10, that EI for the pile shaft was now 19 MNm^2. The results are shown in Figure 8; the left hand side has elastic response and the right hand side nonlinear soil behaviour with the pile shaft remaining elastic. A glance at the figure shows that the behaviours for elastic and nonlinear soil are very different.

Figure 8a shows that the very flexible elastic pile in an elastic soil vibrates in a second mode, whilst the kinematic soil profile has a first mode shape. Both of these plots give the maximum responses, thus they make more emphatic the conclusion from Figure 7a. It was this plot that led to the realisation that simply comparing the displaced shapes of the pile corresponding to the maximum lateral displacement to the top is not an appropriate way of separating the kinematic and inertial displacement. Figure 8b indicates a more satisfactory approach. First find at what time step the maximum total displacement occurs, then plot the kinematic response for that same time step. As can be seen from Figure 8b there is a good relation

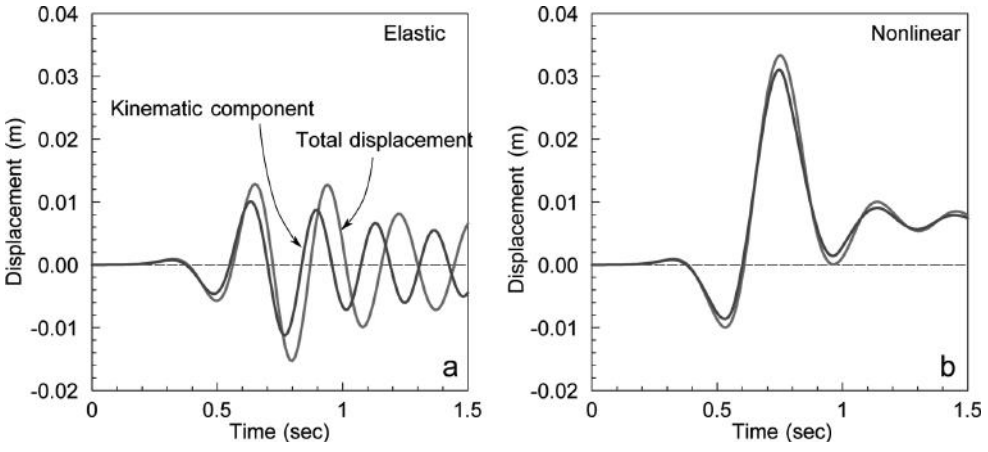

Figure 7. Comparison of total pile head and kinematic ground surface lateral displacement responses for a very flexible pile (EI = 19 MNm^2) in medium sand.

between the two deformation profiles. Having obtained this match the inertial response is then obtained as the difference between these two and is plotted in Figure 8c, from which it is apparent that the inertial deformation occurs only in the upper part of the pile shaft. With this clarification of the way of separating kinematic and inertial response, the situation for nonlinear soil behaviour is presented in Figures 8 d to f. This time the total deformation profile and the kinematic profile are closer than in Figure 8a, but there is still a problem as the kinematic response is greater than the total response. Once again the technique of finding the kinematic profile for the time step corresponding to the maximum total response gives a workable approach, as is shown in Figure 8e. The inertial response so obtained is plotted in Figure 8f. This procedure offers a way of improving the separation in Figures 4d and f. Figures 8c and 8f show that the inertial response is limited to the upper part of the pile shaft; in other words it confirms the validity of the active length concept.

The final step in verifying the active length concept is to apply a sinusoidal cyclic load to the pile head (with the pile head mass at zero). The response to a sinusoidal forcing function of amplitude ±100 kN is shown in Figure 9 in which a number of lateral displacement profiles are plotted. It is apparent that the lateral displacement of the pile shaft occurs in the upper three metres or so of the shaft.

4 DISCUSSION

A valid query, given the difficulty explained above, would be to ask if the separation of total pile response into kinematic and inertial components is worthwhile, particularly as Figures 4 and 8 show that the kinematic displacements are usually much larger than the inertial. Even so, the appealing feature of the separation is that it enables one to consider the earthquake induced deformation of the soil deposit separately from the deformations induced by foundation loading. Also considering inertial response separately means that data on field testing of pile foundations can be applied to earthquake resistant foundation design.

Much more information about the pile—soil interaction is available from the OpenSeesPL output; space precludes including these data here. Available are: stress-strain curves in the soil layer, effective stress paths illustrating cyclic mobility in the dense and medium sand, excess pore water pressure history in the soil layer, data showing high excess pore pressure adjacent to the pile shaft, and acceleration histories through soil layer and pile shaft.

One effect we have not yet considered herein is the role of a transmitting boundary along the bottom of the soil layer—part of our future plans.

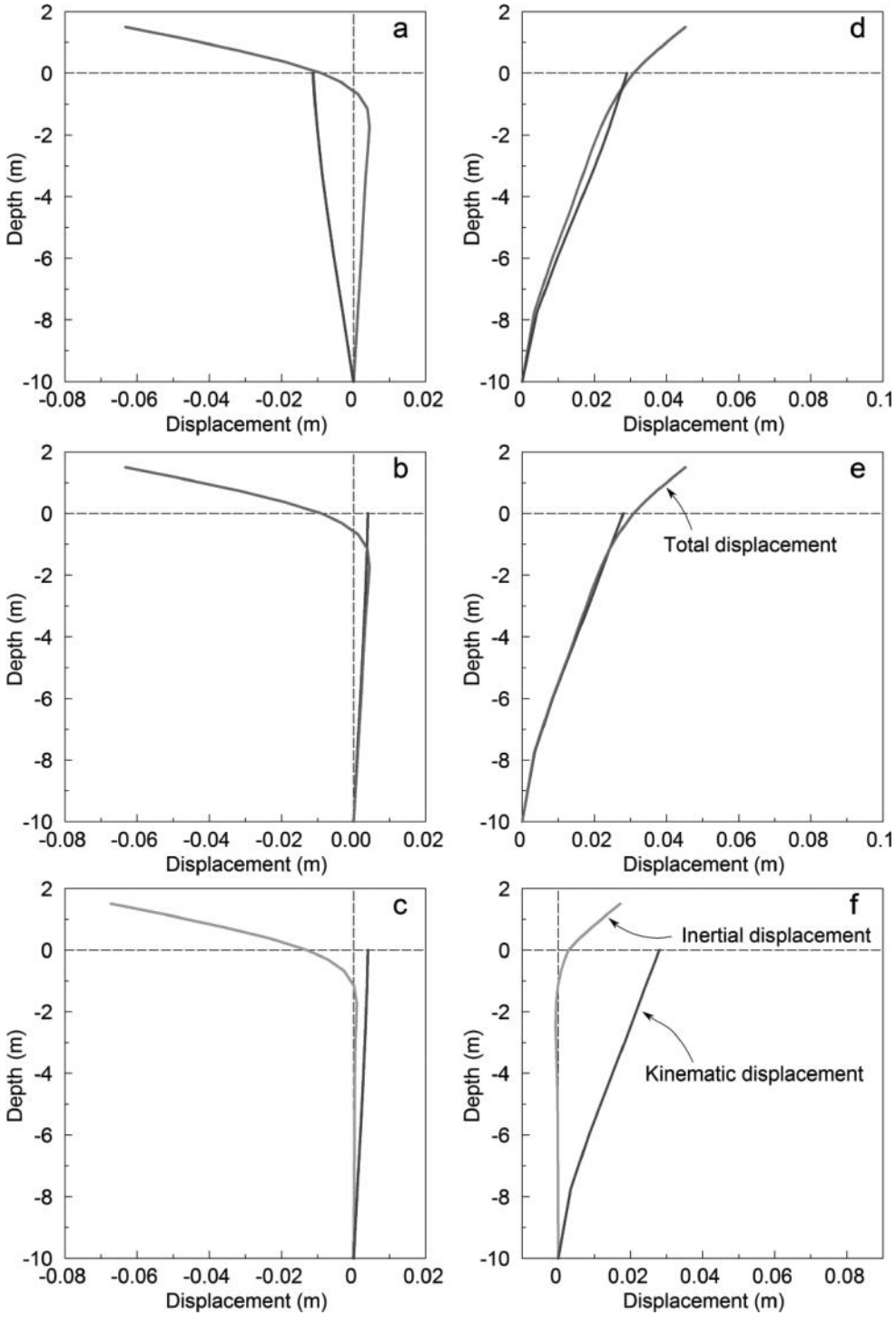

Figure 8. Separation of kinematic and inertial pile response; Elastic—a, b and c; nonlinear—d, e and f nonlinear. (Kinematic profiles in a and d are those for the maximum kinematic displacement. Kinematic profiles in b and e are at the same time step as the maximum total displacement.).

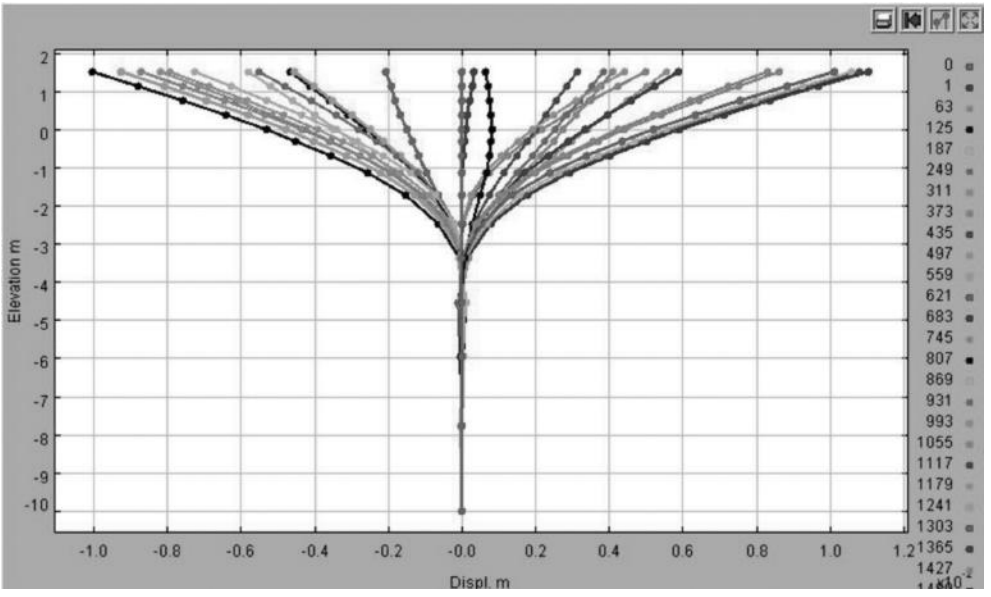

Figure 9. Pile shaft lateral displacement profiles when the pile head is subject to a sinusoidal cyclic shear force of amplitude ±100 kN. (Displacement axis units—cm.).

5 CONCLUSIONS

The following conclusions are obtained:

- One can think of the deformation pattern of a pile shaft during earthquake excitation as the superposition of the response of the soil profile to the base shaking (kinematic interaction) and the at the pile head response generated by the inertial response of the mass attached to the pile (inertial interaction).
- When separating total pile shaft displacement into kinematic and inertial it is important to compare displacement profiles having the same time step (Figures 7 and 8).
- The deflected shape of the pile beneath the ground surface follows that of the soil layer; this is no doubt a consequence of the relative stiffness of the pile and soil profile (Figures 3, 4 and 8).
- The pile deflected shape during pushover is similar to the inertial deflected shape, this holds both for linear and nonlinear soil behaviour and indicates that the active length idea is valid for static loading as well as dynamic loading (Figure 3).
- The dynamic response of the pile head mass to the Ricker wavelet ground motion is heavily damped when nonlinear soil behaviour is mobilised (Figures 6d and e).
- An advantage of separating out the pile head inertial response is that data obtained from pile head lateral test loading may be of use in aseismic foundation design (Figure 9).

ACKNOWLEDGEMENTS

Dr Liam Wotherspoon, University of Auckland, who first drew our attention to the availability of the OpenSeesPL software. Dr Ioannis Anastopoulos, University of Dundee, is the source of the information about the Ricker wavelet seismic input. Our thanks to the teams who developed the OpenSees and OpenSeesPL software packages.

REFERENCES

Algie, P J. 2012. Lateral Response of Piles in Saturated Cohesionless Soils. *University of Auckland Master of Engineering Thesis*.

Gazetas, G. 1984. Seismic response of single end-bearing piles. *Soil Dynamics and Earthquake Engineering*, Vol. 3 No. 2, pp. 82–93.

Lu, J., Yang, Z., and Elgamal, A. 2010. *OpenSeesPL 3D lateral pile-ground interaction: User's manual*. University of California, San Diego. (https://neesforge.nees.org/projects/OpenSeesPL)

Mazzoni, S., McKenna, F., Scott, M.H., and Fenves, G.L. 2009. *Open system for earthquake engineering simulation user manual*, University of California, Berkeley. (http://opensees.berkeley.edu/)

Willis, M L. 2012. The use of vertical timber piles as a liquefaction countermeasure. *University of Auckland Master of Engineering Thesis*.

Yang, Z., Elgamal, A., Parra, E. 2003. Computational Model for Cyclic Mobility and Associated Shear Deformation. *J. Geotechnical and Geoenvironmental Engineering*, ASCE, 129(12), 1119–1127.

Liquefaction countermeasures

This page intentionally left blank

Soil Liquefaction during Recent Large-Scale Earthquakes – Orense, Towhata & Chouw (Eds)

Mitigation of liquefaction-induced damage to residential houses by shallow ground improvement

T. Kiyota
Institute of Industrial Science, The University of Tokyo, Japan

K. Tani
National Research Institute for Earth Science and Disaster Prevention, Japan

K. Matsushita
Misawa Homes Institute of Research and Development Co., Ltd., Japan

T. Hashimoto
Chiyoda Engineering Consultants, Japan

A. Yamamoto
Technical Research Institute, Obayashi Corporation, Japan

H. Takeuchi & J. Ohbayashi
Fudo Tetra Corporation, Japan

T. Noda
Disaster Mitigation Research Center, Nagoya University, Japan

H. Kiku
Department of Civil Engineering, Kanto Gakuin University, Japan

ABSTRACT: A large number of residential houses suffered from liquefaction-induced damage following the 2010–2011 Canterbury earthquakes in New Zealand and the 2011 off Pacific coast of Tohoku earthquake in Japan. In this study, the application of shallow ground improvement for the residential houses was investigated as an economically attractive countermeasure against liquefaction. Based on the case studies after the 2011 Tohoku earthquake in Japan, allowable tilt angles and penetration settlements of houses were proposed for the required level of serviceability against moderate and large earthquakes. The mitigation effect of the shallow ground improvement against liquefaction-induced damage was confirmed by questionnaire survey, airborne LiDAR survey and centrifuge model experiments. The numerical analyses indicated that improvement of shallow layer (below ground water table) by solidification of at least 3 m thick is needed in order to prevent significant damage of houses.

1 INTRODUCTION

On 22nd February in 2011, the Christchurch earthquake with magnitude M6.3, the largest aftershock of the 2010–2011 Canterbury earthquakes, hit the Christchurch city in New Zealand. On 11th March in 2011, the off Pacific coast of Tohoku earthquake (named as 2011 Tohoku earthquake hereafter) with magnitude M9.0 hit the East Japan. These two earthquakes caused significant liquefaction which induced severe damages to residential houses, road facilities and

buried lifelines. High percentage of occurrence of liquefaction was found in areas where relatively new residential lands were developed by reclaiming the swamp and bay areas, thus, linking to the soft subsurface ground condition (Orense et al., 2011; Yasuda et al., 2012).

The Ministry of Land, Infrastructure, Transport and Tourism in Japan reported that more than 25,000 houses suffered liquefaction-induced damage due to the 2011 Tohoku earthquake as of September 2011, and even now, the retrofitting and countermeasure works have been in slow progress. The primary problem on the much needed restoration works on residential houses which suffered from liquefaction-induced damage is the availability of limited personal budget. In addition, there are neither specific regulation nor guideline for the individual residential houses to prevent liquefaction-induced damage in the future.

Based on the above current situation, the authors investigated the application of shallow ground improvement technique for residential houses as an economically attractive countermeasure against liquefaction. The authors firstly proposed the allowable tilt angles and the penetration settlements of houses for the required level of serviceability against earthquake-induced liquefaction. Second, the performance of the shallow ground improvement against liquefaction was investigated by questionnaire survey, airborne LiDAR survey and centrifuge model tests. Finally, FEM analyses were conducted to determine the required thickness of the improved soil layer beneath the residential house necessary to prevent significant damage of houses.

2 EVALUATION OF REQUIRED PERFORMANCE OF RESIDENTIAL HOUSES

In the affected areas, the foundation of individual residential houses have not been well prepared to be resistant against liquefaction. In order to apply liquefaction countermeasure to such residential houses, some guidelines should be set based on an appropriate deformation design criteria of the structure which should be within the required level of serviceability after suffering from liquefaction.

Table 1 shows relationships between tilt angle of house and health problems (after Architectural Institute of Japan, 2003). Residents would recognize the tilting of their house at an angle of 6/1,000 (0.34 degrees). Tilt angle more than 10/1,000 (0.6 degrees) is fatal in their daily lives, causing them disturbance ranging from minor headache to serious health problems. The damage classification of residential houses prepared by Cabinet Office, Japan (2011) indicates that minor restoration is necessary for the residents to return to their previous way of living when the tilt angle exceed 10/1,000 (partially destroyed), and major structural members such as foundation, wall, columns and beams should be repaired when the tilt angle exceed 16.7/1,000 (totally destroyed).

In order to investigate the tilt angle of houses that causes problems in residential life, the authors conducted a questionnaire survey to the house manufacturers which have been involved in the restoration work after the 2011 Tohoku earthquake. In this survey, the tilt angles and differential settlements of 355 repaired houses were collected.

Table 1. Tilt angle of house and health problem (after Architectural Institute of Japan, 2003).

Tilt angle of house			
Degree	Rad.	Inclination	Health disturbance
0.29	1/200	5/1000	Feeling of tilting
0.34	1/167	6/1000	Feeling of differential settlement
0.46	1/125	8/1000	Strong feeling of tilting
0.6	1/100	10/1000	Dizziness and headache. Need leveling retrofitting work
~0.1	~1/60	~16.7/1000	Heaviness of head and feeling of floating
2~3	1/30~1/20	33.3~50/1000	Heavy dizziness, headache, boke and anorexia
4~6	1/15~1/10	66.7~100/1000	Fatigue and disorder of sleep
7~9	1/8~1/6	125~166.7/1000	Heavy fatigue and disorder of sleep

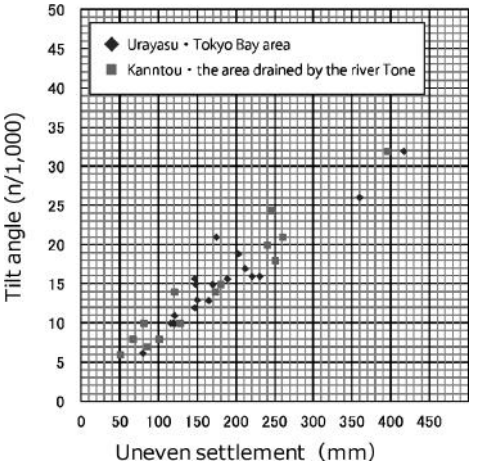

Figure 1. Relationship between tilt angle and differential settlement of repaired houses with strip footing after the 2011 Tohoku earthquake.

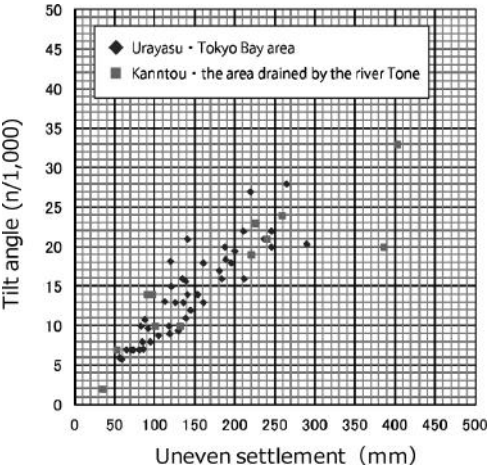

Figure 2. Relationship between tilt angle and differential settlement of repaired houses with mat foundation after the 2011 Tohoku earthquake.

Figures 1 and 2 show relationship between tilt angle and differential settlement of repaired houses with strip footing and mat foundation, respectively. The results indicate that people decide to restore their houses when the tilt angle of house exceeds about 8–10/1,000 for the strip footing, and about 6–8/1,000 for the mat foundation. Based on the above literature and investigation, the design criteria are set for the tilt angle of houses as follows:

1. For moderate earthquake, the liquefaction-induced deformation of house should not pose any problem to people's usual lives. The tilt angle should not exceed 10/1,000.
2. For large earthquake, although some minor damages to the house are admissible, people should be allowed to return to their previous lives by minor restoration work. The tilt angle should not exceed 16.7/1,000.

However, it was difficult to use the tilt angle of house as a design criteria in the verification work because the effectiveness of shallow ground improvement against liquefaction would be confirmed by practical experiment or/and numerical analysis which used simple symmetrical models. We therefore needed to obtain the value of penetration settlement of house which can be correlated with that of tilt angle criteria. In this paper, penetration settlement does not denote an overall (total) settlement of house, but the extent of sinking of house into the ground.

Figures 3 and 4 show relationships between tilt angle and penetration settlement of "partially" and "totally" damaged houses caused by liquefaction during the 2011 Tohoku earthquake in Itako/Kamisu cities in the inland area and in Chiba/Narashino cities in the Tokyo Bay area, respectively. Most of the damaged houses in these areas were found in sites reclaimed in the second half of the 20th century. Refer to Towhata et al. (2013) and Yasuda et al. (2012) for details of the liquefaction-induced damage and the ground condition in these areas.

Although the collected data show significant scatter, the penetration settlement of inland and Tokyo Bay areas corresponding to the prescribed design criteria of tilt angle for the moderate earthquake (10/1000) is found to be roughly 14 cm and 7.5 cm (12.5 cm in total average), while that for the large earthquake (16.7/1000) is about 23 cm and 12.5 cm (21 cm in total average), respectively. In the present stage, however, the authors do not have concrete reason for the different trend between inland and Tokyo Bay areas. Consequently, as summarized in Table 2, the authors adopted fairly safe side values of penetration settlement as design criteria for the moderate and large earthquakes.

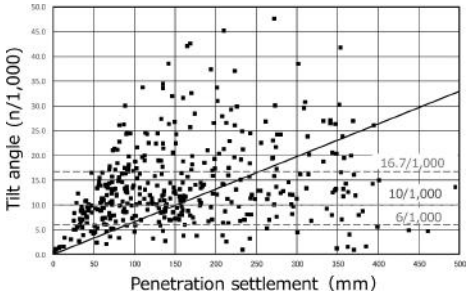

Figure 3. Relationship between tilt angle and penetration settlement of damaged houses by liquefaction in inland areas (Kamisu and Itako cities).

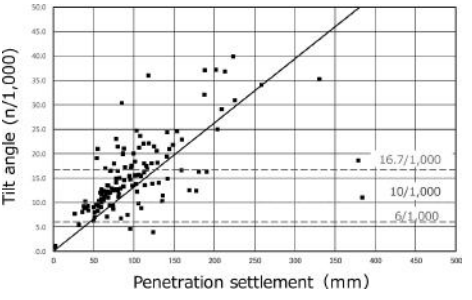

Figure 4. Relationship between tilt angle and penetration settlement of damaged houses by liquefaction in Tokyo Bay area (Chiba and Narashino cities).

Table 2. Design criteria of penetration settlement for moderate and large earthquakes.

		Penetration settlement (cm)			
Seismic levels	Tilt angle	Itako/Kamisu in inland areas	Chiba/Narashino in Tokyo bay area	Average	Adopted
Moderate earthquake	10/1000	14.0	7.5	12.5	10.0
Large earthquake	16.7/1000	23.0	12.5	21.0	15.0

3 SURVEY ON THE MITIGATION EFFECT OF SHALLOW GROUND IMPROVEMENT

3.1 *Questionnaire survey*

In order to investigate the effectiveness of existing liquefaction countermeasures which were constructed for residential houses in the affected area by the 2011 Tohoku earthquake, questionnaire survey was conducted to housing companies that were involved in retrofitting work of the damaged houses. The number of responses were 458. It should be noted that those ground improvements were done to prevent excessive settlement but were not designed to prevent future occurrence of liquefaction.

Figures 5 and 6 show the survey results for tilting angle and differential settlement of houses, respectively. The results indicate that houses on foundation ground without improvement suffered from relatively large titling and differential settlement, as compared to those on improved foundation ground. Although the number of data was limited, the shallow ground improvement was as effective as any other countermeasures stated in the figures.

3.2 *Airborne LiDAR survey*

Airborne LiDAR (Light Detection and Ranging) system is one of the most effective tools to measure the change in ground elevation by comparing two Digital Surface Models (DSMs) of the same area taken at different times. In order to measure liquefied soil subsidence caused by the 2011 Tohoku earthquake, two set of DSMs obtained by airborne LiDAR surveys before and after the earthquake were compared with pile-supported RC buildings as reference for aligning the two sets. The elevation data for DSMs before and after the earthquake were measured from December 2006 to January 2007 (0.792 points/m^2) and in April 2011 (4.089 points/m^2), respectively. Refer to Konagai et al. (2013) for detail on the validation of the accuracy of the obtained results.

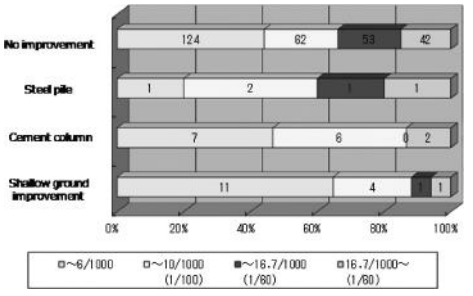

Figure 5. Component ratio of tilt angle of houses with different types of foundation.

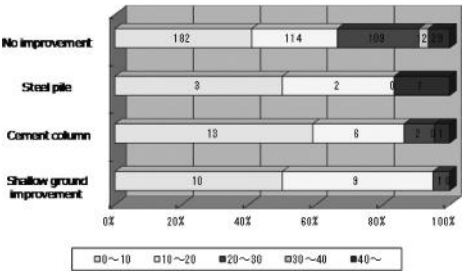

Figure 6. Component ratio of differential settlement of houses with different types of foundation.

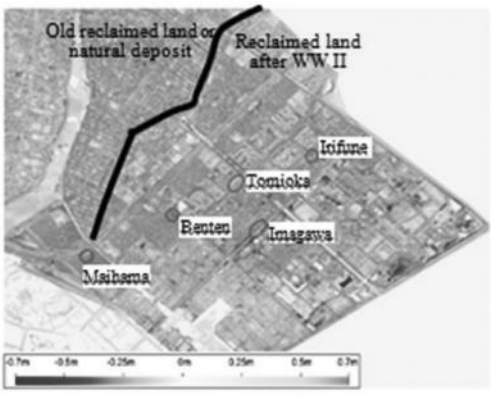

Figure 7. Soil subsidence map in Urayasu city by Airborn LiDAR (Konagai et al., 2013).

Figure 8. Boiled sands observed/non-observed areas in Urayasu city (Kanto Regional Development Bureau, MLIT, 2011).

Figure 7 shows the obtained soil-subsidence map of Urayasu city. Although the subsidence can be seen over the entire stretch of the reclaimed land, the severity of liquefaction within this area was not uniform. In particular, remarkable subsidence is seen in the area reclaimed during the second half of the 20th Century, and it overlaps approximately with the spatial distribution of observed boiled sands (Kanto Regional Development Bureau, MLIT, 2011) in Figure 8.

However, considering the resolutions of the obtained DSMs, it is difficult to accurately read out the values of settlement and tilt angle of each residential house which has complicated roof shape. In this study, therefore, the authors investigated the road deformation which would depend on the thickness of the roadbed. Since the roadbed consists of pavement and subgrade parts which are thought to have not liquefied during the earthquake, it would be reasonable to investigate the relationship between the road deformation and the thickness of roadbed, in order to understand the effectiveness of shallow ground improvement.

The roads studied were selected from five districts in Urayasu city, as shown in Figure 7. We extracted values of tilt angle and total settlement of both residential roads and main roads from each district. Figures 9 and 10 show the effects of thickness of roadbed on the average values of tilt angle and total settlement in each district. These figures clearly indicate that the main roads which have a thicker roadbed resulted in more effective damage mitigation. Although we do not consider the different condition between road and foundation ground beneath the house, the trends of Figures 9 and 10 would imply that the shallow ground improvement is highly effective to prevent liquefaction-induced damage to the ground surface structures.

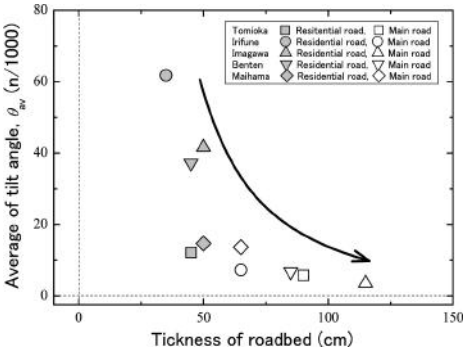

Figure 9. Relationship between road tilting and thickness of roadbed.

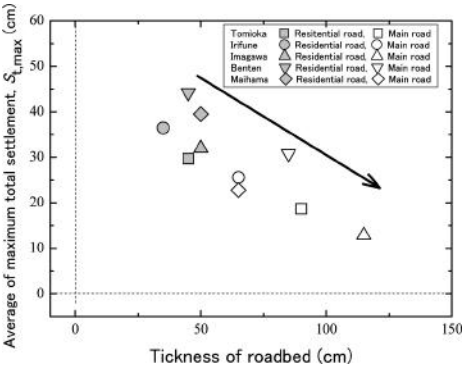

Figure 10. Relationship between road settlement and thickness of roadbed.

4 CENTRIFUGE MODEL TEST

4.1 *Test method*

Centrifuge model tests to evaluate the performance of shallow ground improvement were carried out at the Technical Research Institute of Obayashi Corporation, Japan. Refer to Matsuda and Higuchi (2002) for the details of the centrifuge apparatus. The setup of accelerometers, water pressure gauges and displacement gauges in the ground model are shown in Figure 11. The model ground was prepared using Silica sand No. 7 (D_{50} = 0.15 mm and U_c = 1.6) with D_r = 50–55%. The liquefaction resistance of the tested material was evaluated as liquefaction resistance, R_{L20} = 0.18 by undrained cyclic triaxial tests. The model was subjected to the centrifugal acceleration field of 25 g, and the groundwater table was set at depth of about 1.0 m in terms of the real scale model. The viscosity of the fluid used was about 25 times that of water.

In this model test, the authors adopted solidification method as a shallow ground improvement. The solidified layer was prepared by cement-mixed sand with unconfined compression strength of 400 kN/m^2. A two-story house was modeled by acrylic rectangular block which applied 10 kN/m^2 of pressure on the ground surface. The planar dimension of the house was 7.0 m × 7.0 m, while that of solidified layer beneath the model house was 8.5 m × 8.5 m. A series of model tests with different thickness of solidified layer was performed as shown in Figure 12.

Two levels of input earthquake motion were used: "moderate earthquake, L1", the level of earthquake motion that was observed at Urayasu city during the 2011 Tohoku earthquake and "large earthquake, L2", the level of earthquake motion that was twice the acceleration of L1 associated with rare events that involve strong and long-period ground shaking. The input motion of L1 was estimated by earthquake response analysis (SHAKE) based on the measured surface acceleration record at K-net Urayasu station (CHB008EW) during the 2011 Tohoku earthquake. The maximum value of accelerations, a_{max}, was 1.5 m/s^2 for L1 and 3.0 m/s^2 for L2, respectively. In the test procedure, the authors firstly conducted a test with L1 earthquake motion followed by measuring ground displacement manually, and later on, conducted the test with the same model with L2 earthquake motion.

4.2 *Test results*

As a result of model test with L1 (a_{max} is about 1.5 m/s^2), Figures 13 and 14 show the measured excess pore water pressure at prototype depths of 3.75 m and 8.75 m in the free field far from the house for case 1, and the average values of total settlement of house for all cases. The excess pore water pressures measured at depths of 3.75 m and 8.75 m were reached the initial vertical effective stresses at 120 s and 100 s, which indicate the occurrence of liquefaction.

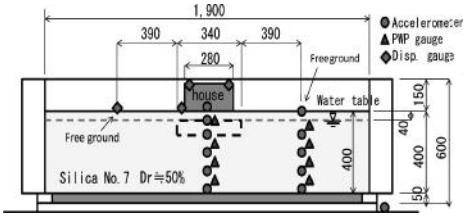

Figure 11. Schematic diagram of centrifuge ground model.

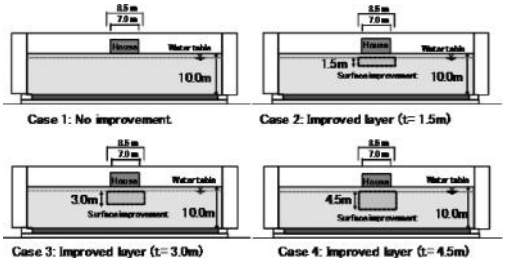

Figure 12. Schematic diagram of experiment cases.

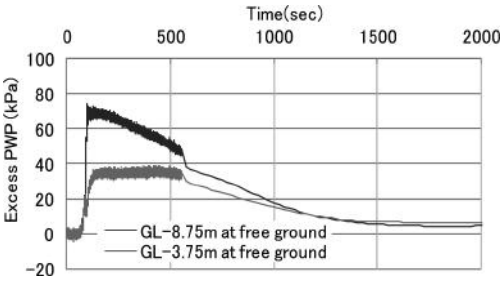

Figure 13. Measured excess pore water pressure at free ground for case 1 (L1).

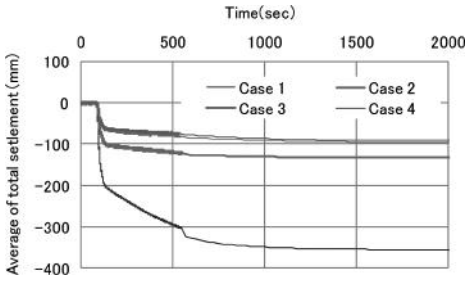

Figure 14. Average values of total settlement of house for all cases (L1).

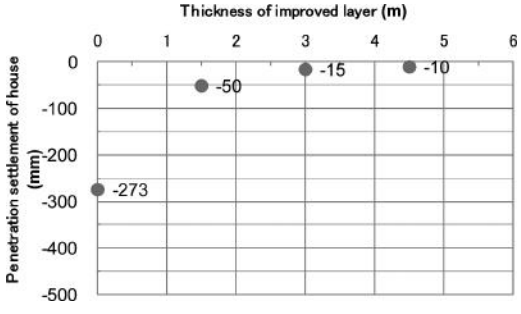

Figure 15. Relationship between penetration settlement and thickness of shallow improvement layer (L1).

The average value of total settlement of house started to increase at 90 s, and significant rate of settlement could be observed until 140 s. The excess pore water pressures dissipated at 1,500 s (25 min), which were almost consistent with the duration time of house settlements. Figure 15 shows the relationship between penetration settlement measured at the end of the experiment and thickness of shallow ground improvement. Larger settlements were observed at smaller improvement depth, and the settlement observed in case 1 (no improvement) was more than five times as large as the other cases.

Figure 16 shows the ground settlement in a longitudinal cross section measured at the end of experiment with L2 (a_{max} is about 3.0 m/s^2). The penetration settlement measured in case 1 was about 40 cm, which is significantly larger than those of the other cases. Since the L2 earthquake motion was successively given after the L1 motion in the same ground model, the evaluation of ground displacement caused by L2 is difficult because it should be affected by the densification of liquefied soil during L1. However, these experiments imply that the shallow ground improvement would be effective to reduce penetration settlement of house during liquefaction.

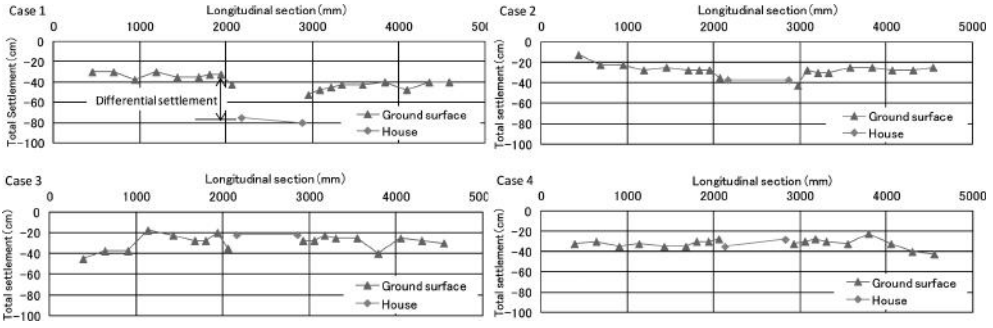

Figure 16. Ground settlement measured at the end of experiment (after L1 and L2).

5 NUMERICAL ANALYSIS

In order to investigate the required thickness of shallow ground improvement which satisfy the design criteria of penetration settlement of the residential house, a series of numerical analyses was conducted by using two different FEM codes, *GEOASIA* (Noda et al., 2008) and *ALID* (Yasuda et al., 1999). Although *GEOASIA* is one of the most sophisticated analytical codes in the geotechnical field, it is rather time consuming. This study, therefore, used *ALID*, one of the simplest codes to simulate liquefied soil behaviour, in order to complement the result from *GEOASIA*. Since the code structure is different from each other, their results cannot be compared directly. Therefore, we preliminarily conducted trial-and-error analysis with *ALID* by changing the value of input ground motion so as to obtain the results consistent with *GEOASIA*.

5.1 *Effect of thickness of improved layer by solidification*

Figure 17 shows the 2D FEM model used in *GEOASIA*. The thickness of loose sand layer (liquefiable layer) was 10 m, and that of the base stratum (non-liquefied layer) was 5 m. Input earthquake motion used in this study was the L1 and L2 motions which were equivalent to those used in the centrifuge model test. As in the model tests, we adopted here the solidification method as a shallow ground improvement. The solidified layer was considered as a permeable elastic body, and its elastic parameters, E and ν, were determined from the previous literature (Public Works Research Center, 2004). Material parameters and initial soil conditions in *GEOASIA* were determined based on the triaxial tests and oedometer tests on the Silica sand No. 7. The applicability of those parameters were preliminarily confirmed through another series of simulations of the model test.

Figure 18 shows the ground deformation caused by L1 motion for the cases of different thickness of the improved layer. It can be clearly seen that the ground settlement becomes smaller with an increase in the thickness of improved layer. Figure 19 shows the relationship between values of penetration settlement of house and thickness of improved layer. The computed penetration settlements of house with three meters improved layer were about 10 cm and 14 cm for the L1 and L2 earthquake motions, respectively. These results imply that the shallow layer (below ground water table) improved by solidification method of three-meter thick is necessary in order to satisfy the design criteria of penetration settlement that was shown in Table 2.

5.2 *Comparison of different improvement methods*

The required thickness of improved layer to prevent significant liquefaction-induced damage of houses may vary when different improvement methods are employed. This section, therefore, discusses the required thickness for compaction and drainage methods which are employed as shallow ground improvement based on the simulation by *GEOASIA* and *ALID*.

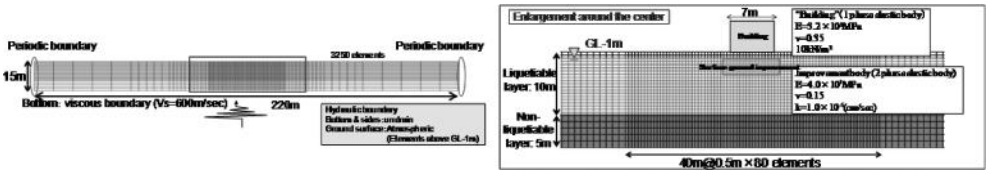

Figure 17. 2D FEM model in *GEOASIA*.

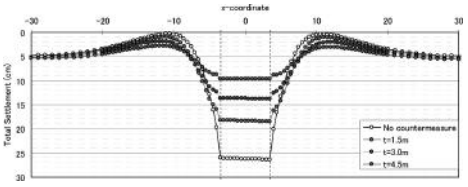

Figure 18. Ground deformation caused by L1 in *GEOASIA*.

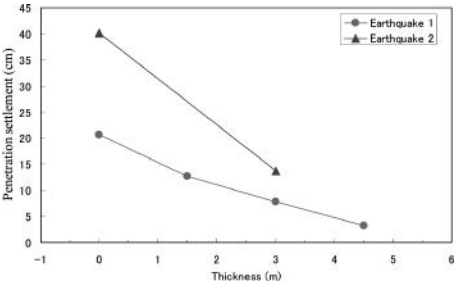

Figure 19. Relationship between penetration settlement of house and thickness of improved layer in *GEOASIA*.

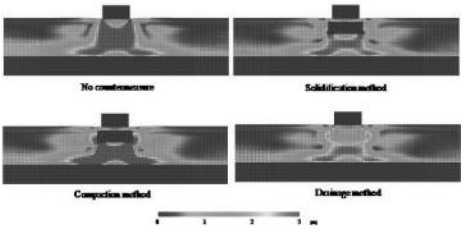

Figure 20. Shear strain distribution by L1 in *GEOASIA*.

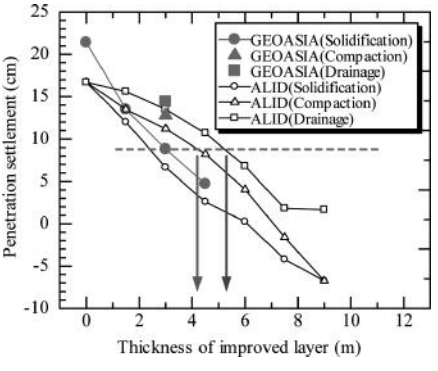

Figure 21. Effect of different types of improvement on penetration settlement by L1.

With regard to the compaction method, the authors considered the improved layer as a sandy soil having $D_r = 95\%$. For the drainage method, in order to avoid occurrence of excess pore water pressure in the improved layer, drainage condition ($\Delta u = 0$) was set at the boundary of improved layer element in *GEOASIA*, while the material properties of the improved layer were calibrated to achieve F_L>1.0 in *ALID*.

Figure 20 shows the shear strain distribution caused by L1 earthquake motion by *GEOASIA*. Although the value of shear strain in the improved layer by compaction method was negligible, that which occurred just beneath the improved layer was significant when compared to those with the solidification and drainage methods. On the other hand, moderate shear strains were found in the layer improved by drainage method.

Figure 21 shows the computed relationship between the penetration settlement and the thickness of layer improved by different methods using *GEOASIA* and *ALID*. The results clearly shows that the value of penetration settlement depends on the improvement method, and the improved effect is higher in the following order of solidification method, compaction method and drainage method. As mentioned above, in the examined ground condition,

the shallow layer (below ground water table) improved by solidification method of three-meter thick is necessary in order to satisfy the design criteria of penetration settlement. On the other hand, about 4.5 m and 6 m is needed when the compaction method and drainage method are employed instead of the solidification method.

6 CONCLUSIONS

This paper summarized the effectiveness of shallow ground improvement as a liquefaction-countermeasure for residential houses. Based on the literature reviews and field damage investigations after the 2011 Tohoku earthquake in Japan, the following design criteria were proposed for required level of serviceability against liquefaction caused by moderate and large earthquakes.

1. For moderate earthquake, the tilt angle of the house should not exceed 10/1,000 which corresponds to 10 cm of penetration settlement.
2. For large earthquake, the tilt angle of the house should not exceed 16.7/1,000 which corresponds to 15 cm of penetration settlement.

The centrifuge model tests with different thickness of improved soil layers clearly showed the effectiveness of shallow ground improvement against earthquake-induced liquefaction, which were also verified by the field investigations including analyses of questionnaire and airborne LiDAR surveys. The relationship between the penetration settlement and the thickness of improved layer with different improvement techniques was investigated by two types of numerical analysis codes, *GEOASIA* and *ALID*. The result showed that the shallow layer (below ground water table) improved by solidification method of at least 3 m thick is needed in order to prevent significant damages of houses, though the analysis condition in this study was limited.

REFERENCES

Architectural Institute of Japan 2003. *Textbook for registered architects* (in Japanese)

Cabinet Office, Government of Japan 2011. http://www.bousai.go.jp/taisaku/unyou.html (in Japanese)

Kanto Regional Development Bureau of the Ministry of Land, Infrastructure, Transport and Tourism 2011. *Liquefaction in Kanto Region caused by the 2011 off Pacific coast of Tohoku Earthquake* (in Japanese)

Konagai, K., Kiyota, T., Suyama, S., Asakura, T., Shibuya, K. and Eto, C. 2013. Maps of soil subsidence for Tokyo bay shore areas liquefied in the March 11th off the Pacific coast of Tohoku earthquake, *Soil Dynamics and Earthquake Engineering* (in press)

Matsuda, T. and Higuchi, S. 2002. Development of the Large Geotechnical Centrifuge and Shaking Table of Obayashi, *Proceedings of International Conference of Physical Modeling in Geotechnics*, pp. 63–68.

Noda, T., Asaoka, A. and Nakano, M. 2008. Soil-water coupled finite deformation analysis based on a rate-type equation of motion incorporating the SYS Cam-clay model, *Soils and Foundations*, Vol. 48, No. 6, pp. 771–790.

Orense, R.P., Kiyota, T., Yamada, S., Cubrinovski, M., Hosono, Y., Okamura, M. and Yasuda, S. 2011. Comparison of liquefaction features observed during the 2010 and 2011 Canterbury earthquakes, *Seismological Research Letters,* 82(6), pp. 905–918.

Public Works Research Center 2004. *Design and construction manual of deep chemical mixing method for works at land*. (in Japanese)

Towhata, I., Maruyama, S., Kasuda, K., Koseki, J., Wakamatsu, K., Kiku, H., Kiyota, T., Yasuda, S., Taguchi, Y. and Aoyama, S. 2013. Liquefaction in Kanto region during the 2011 off the Pacific coast of Tohoku earthquake, *Soils & Foundations*, (in press)

Yasuda, S., Harada, K., Ishikawa, K. and Kanemaru, Y. 2012. Characteristics of liquefaction in Tokyo Bay area by the 2011 Great East Japan Earthquake, *Soils and Foundations*, Vol. 52, No. 5, pp. 793–810.

Yasuda, S., Yoshida, N., Adachi, K., Kiku, H., Gose, S. and Masuda, T. 1999. A simplified practical method for evaluating liquefaction-induced flow, *Journal of Japan Society of Civil Engineers*, No. 638/III-49, pp. 71–89. (in Japanese)

Soil Liquefaction during Recent Large-Scale Earthquakes – Orense, Towhata & Chouw (Eds)

New liquefaction countermeasures for wooden houses

S. Yasuda
Department of Civil and Environmental Engineering, Tokyo Denki University, Saitama, Japan

ABSTRACT: The 2011 Great East Japan Earthquake caused severe liquefaction in a wide area in Japan. About 27,000 wooden houses were damaged due to liquefaction. In the design of wooden houses, liquefaction has not been previously considered, whereas the design code for other buildings has considered liquefaction since 1974. Appropriate countermeasures against the liquefaction of the foundation ground beneath wooden houses were developed soon after the earthquake. In the reconstruction of a house in a narrow space, a compact "gravel drain with compaction" method was applied in Urayasu City. For a wide damaged residential area, the MLIT of Japan established an "Urban liquefaction countermeasure project" to prevent liquefaction during future earthquakes. Two methods, the lowering of the ground water table and surrounding the foundation ground with lattice-type underground walls, are now being used in damaged cities. For a single house, two other methods have been developed, (i) a special compaction grouting method, in which bore holes are dug from outside the house using an inclined bore-hole machine, and (ii) enclosing the house foundation with sheet piles.

1 INTRODUCTION

Many cities, including the Tokyo Metropolitan Area, suffered severe damage due to liquefaction during the 2011 Great East Japan Earthquake. Numerous wooden houses, roads, water pipes, sewage piles and gas pipes were seriously damaged in residential areas. Most houses and lifelines have been repaired, but inhabitants must still reinforce their houses and residential areas to prevent damage due to re-liquefaction during future earthquakes. Several liquefaction countermeasures for wooden houses, developed since the earthquake, are reviewed in this paper.

2 LIQUEFACTION—INDUCED DAMAGE TO WOODEN HOUSES IN KANTO REGION

The 2011 Great East Japan Earthquake caused liquefaction in many places in the Tohoku and Kanto regions. According to the Ministry of Land, Infrastructure, Transport and Tourism (MLIT), about 27,000 wooden houses in Japan were damaged due to liquefaction, as shown in Figure 1. In the design of wooden houses, liquefaction has not been considered, whereas the design code for other buildings has considered liquefaction since 1974. This is the main reason such a large number of houses were damaged. Many houses settled and tilted, though they suffered no damage to walls and windows. In the greatly tilted houses, inhabitants felt giddy, sick and nauseous, and found it difficult to live in their houses after the earthquake. In May 2011, the Japanese Cabinet announced a new standard for the evaluation of damage to houses based on two factors, settlement and inclination, as shown in Table 1. A new class of "large-scale half collapsed house" was also introduced, and houses tilted at angles of more than 50/1,000, of 50/1,000 to 16.7/1,000, and of 16.7/1,000 to 10/1,000 were judged to be totally collapsed, large-scale half collapsed and half collapsed houses, respectively, under the new standard.

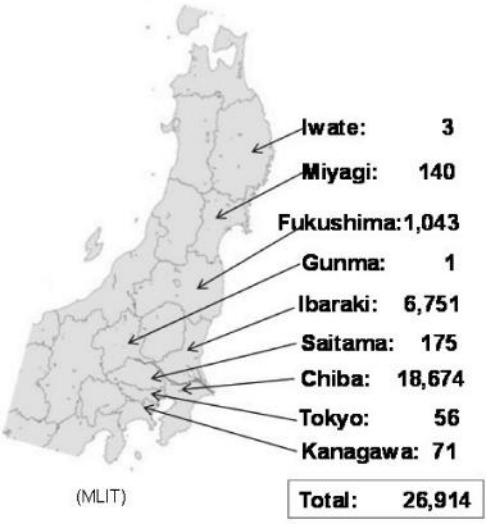

Figure 1. Number of houses damaged by liquefaction.

Table 1. New evaluation standard announced by the Japanese Cabinet.

Grade of damage		Totally collapsed	Large scale half collapsed	Half collapsed	Partially damaged
Evaluation method	Inclination	>50/100	16.7/1000 to 50/1000	10/1000 to 16.7/1000	10/1000
					
	Settlement	1m upper than floor	Upto to floor	25cm to the top of footing	

Figure 2 is a map of the liquefaction sites in the Kanto region. Because of their geomorphologic condition, the following sites liquefied:

a. Artificially reclaimed lands along Tokyo Bay and the Pacific Ocean
b. Filled grounds on former ponds and marshes in lowlands
c. Sites excavated to get iron sand or gravel and then refilled.
d. Filled sloping grounds on hills or terraces

The thickness and inclination of the liquefied layers differ in these geomorphologic conditions, as schematically shown in Figure 3(a) to 3 (d). If the thickness of the liquefied layer was uniform, uniform subsidence occurred due to the volume change of the liquefied layer and houses sank into the ground at some inclination due to the loss of bearing capacity or a decrease in the shear modulus of the liquefied layer, as shown in Figure 3 (a). This type of penetrating settlement of houses following by inclination occurred in artificially reclaimed lands and filled grounds in lowlands. On the contrary, in the excavated and refilled sites, not only did houses settle at an inclination, but non-uniform subsidence also occurred and accelerated the inclination, as shown in Figure 3(b). At a few sites where river walls tilted towards rivers, the ground behind the walls flowed and tore footings of houses, as shown in Figure 3(c). On hills and terraces, the liquefaction of sloping ground caused flow and tore footings as shown in Figure 3(d).

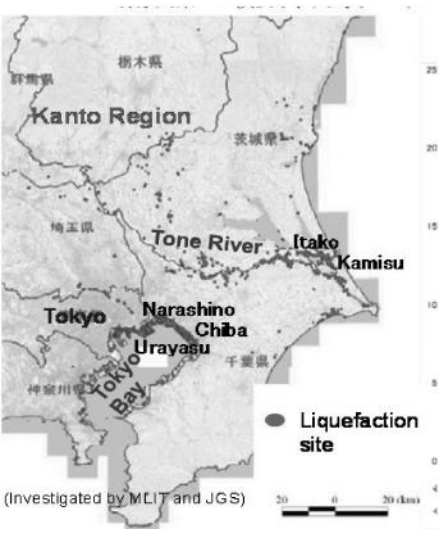

Figure 2. Liquefaction sites in Kanto Region.

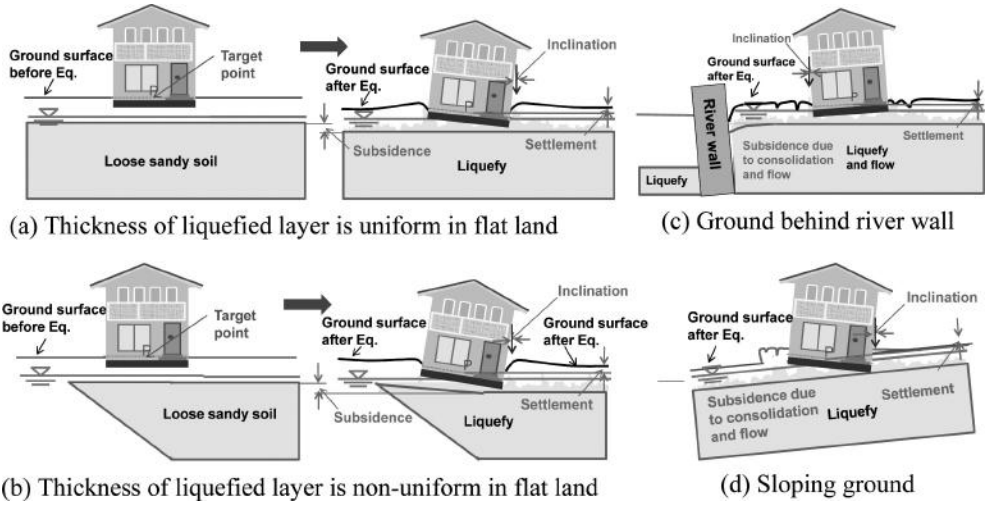

Figure 3. Patterns of liquefaction-induced damage to houses.

The tilting of houses is derived from non-uniform settlement. According to the authors' previous study on the non-uniform settlement of houses, several factors affect non-uniform settlement (Yasuda and Ariyama, 2008). Among them, the effect of adjacent houses was dominant, as schematically shown in Figure 4. If two houses are close to each other, they tilt inward toward each other, and if four houses are close, they tilt toward their common center. Figure 5(a) and 5 (b) show the relationship between the penetrating settlement and the inclination of houses in two cities in which the houses are clustered close together and in two other cities in which the houses are scattered, respectively. Though these data are scattered, inclination increases with penetrating settlement in each figure. And the relationships are different in two sets of cities.

In residential areas where liquefaction occurred, not only houses but also roads, water pipes, sewage pipes and gas pipes were damaged, interrupting daily life (Yasuda et al., 2013). Many houses have been restored by lifting them, repairing their footings, and replacing them

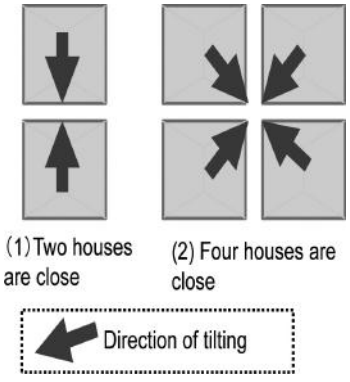

Figure 4. Effect of adjacent houses on the inclination of houses.

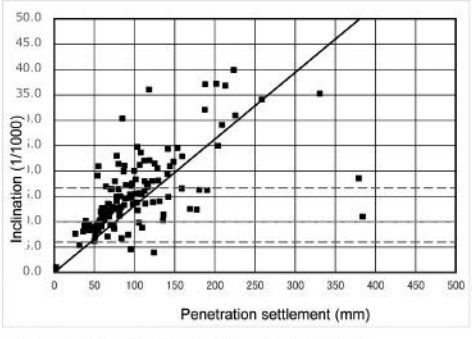

(a) In Chiba and Narashino cities, where houses are clustered close together

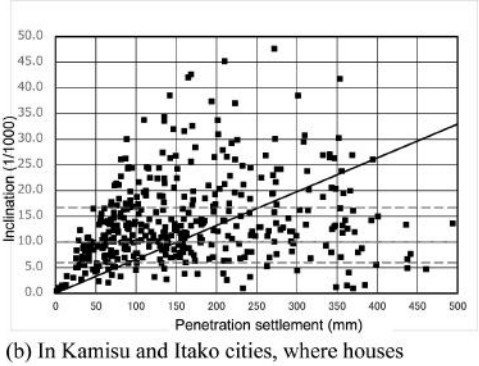

(b) In Kamisu and Itako cities, where houses are scattered

Figure 5. Relationship between penetration settlement and inclination of houses.

on their footings, and lifelines have been repaired in the two and a half years since the earthquake. However, many inhabitants face the serious problem of how to prevent re-liquefaction during future earthquakes. Several organizations have facilitated the development of effective and economic methods of preventing the liquefaction of ground beneath existing or newly constructed houses.

3 PATTERNS TO RECONSTRUCT DAMAGED HOUSES AND/OR RESIDENTIAL AREAS

There are four possible patterns to reconstruct damaged houses and/or areas, as shown in Figure 6 and explained below:

1. **Pattern 1**: If many damaged houses in a residential area are demolished, the best option is to improve the ground in the entire area to prevent re-liquefaction and rebuild houses. Soil in a wide area can be improved easily by current techniques, such as sand compaction piles and deep mixing.
2. **Pattern 2**: If a damaged house is demolished, appropriate countermeasures to liquefaction must be applied before reconstruction. Many old houses in the Kanto Region have been replaced according to this pattern since the 2011 Great East Japan Earthquake.
3. **Pattern 3:** If all or many settled and tilted houses are repaired by uplifting, the ground in the whole area, including lifelines and roads, must be treated by special measures to

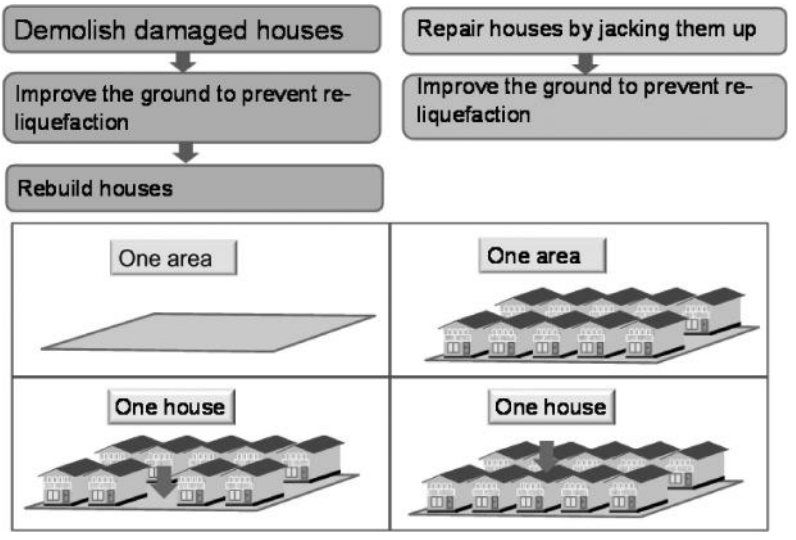

Figure 6. Four patterns to reconstruct damaged houses and/or areas.

prevent re-liquefaction. The Japanese government has launched an "Urban liquefaction countermeasure project" which is now studying possible improvement methods in 12 damaged cities.

4. **Pattern 4**: If a settled and tilted house is repaired by uplifting, the ground beneath it must be treated by some advanced method to prevent re-liquefaction. A few houses have been restored using such a method since the earthquake.

3.1 *Remediation methods for a wide demolished residential area (Pattern 1)*

Many kinds of remediation methods for liquefaction have been developed in Japan since the 1964 Niigata Earthquake, which caused severe liquefaction-induced damage to many structures (Yasuda, 2010). Current countermeasures against liquefaction are classified into two categories (JGS, 1998): (i) methods to improve the liquefiable soil to prevent liquefaction as schematically shown in Table 2; and (ii) methods to strengthen structures to prevent their collapse if the ground should be liquefied. In the first category, liquefaction strength is increased by establishing the following ground conditions: (a) high density; (b) stable skeleton; (c) unliquefiable grain size; or (d) low saturation. Other methods to prevent liquefaction are: (e) immediate dissipation of increased excess pore pressure; (f) reduction of shear stress by increasing confining pressure; and (g) reduction of shear stress by building an underground wall. Among the measures in the first category, the sand compaction method has been most widely used because of its high reliability. Appropriate countermeasures in the second category differ by the type of structure. A typical measure is the pile foundation.

Most of these methods can be applied to wide residential areas. In constructing new houses in Urayasu City from 1975, the Housing Corporation improved the grounds of five residential areas by the sand compaction pile (SCP) and gravel drain (GD) methods to prevent liquefaction. The SCP method was adopted mainly for three-story buildings in order to increase the bearing capacity and to prevent liquefaction. On the other hand, the gravel drain (GD) method was adopted mainly for two-story buildings for the purpose of liquefaction mitigation. Following the 2011 Great East Japan Earthquake, sand boils were observed in unimproved areas around the buildings and in parks within the residential complex. However, no sand boils were seen within the improved area and no damage occurred to buildings constructed on ground improved by either the SCP method or the GD method (Yasuda et al., 2012).

Table 2 (a). Countermeasures against liquefaction for open land (modified from JGS, 1998).

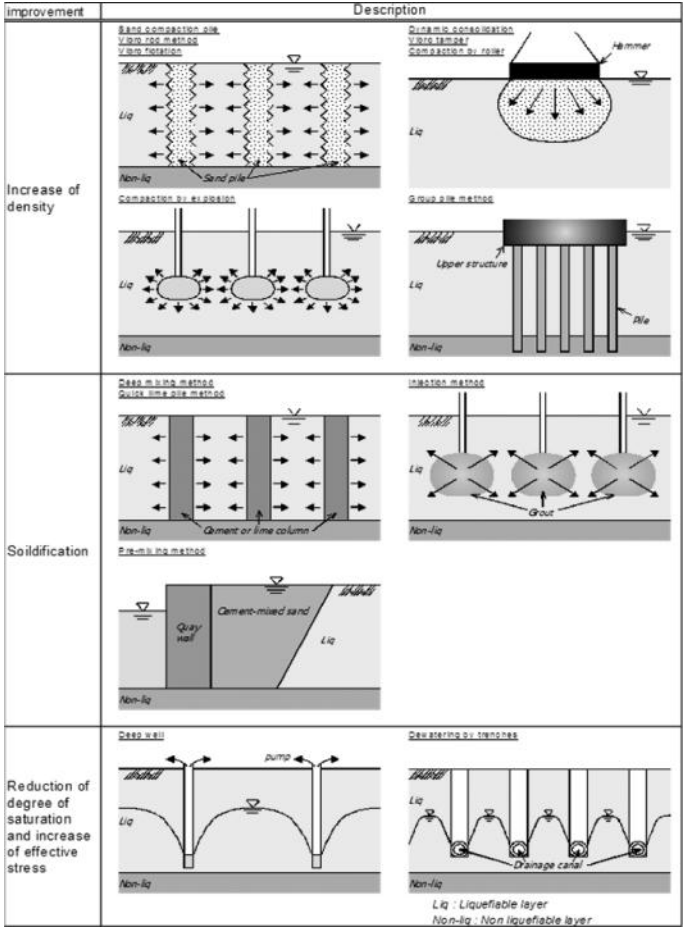

Table 2 (b). Countermeasures against liquefaction for open land (modified from JGS, 1998).

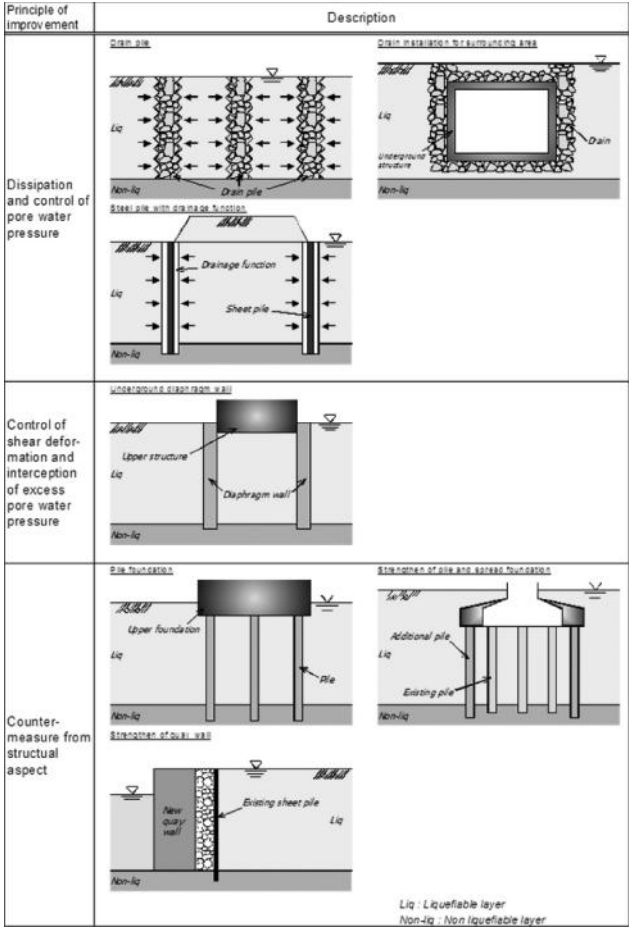

3.2 *Remediation methods for a narrow demolished housing space (Pattern 2)*

One month after the 2011 Great East Japan Earthquake a technical committee was organized in the Kanto Branch of the Japanese Geotechnical Society (JGS) to study the mechanism of the liquefaction-induced damage to houses and discuss appropriate countermeasures. Several possible countermeasures for new houses, including several ideas which have not been confirmed quantitatively, have been proposed, as shown in Figure 7.

Remediation measures for individual houses must be applicable to a narrow space and economical. If penetrated to the depth of the non-liquefiable layer, steel or soil-cement mixed piles satisfy both these conditions for newly constructed houses. Many houses in Japan have been constructed using these methods. Though these methods prevented the settlement of houses during the 2011 Great East Earthquake, sewage pipes around houses were damaged due to the liquefaction-induced subsidence of the surrounding ground. Therefore, steel or soil-cement mixed piles do not prevent all liquefaction-induced damage in a residential area. Current typical soil improvement methods are plotted for economy and area applicability in Figure 8. Normal soil improvement methods, such as SCP and deep mixing, are economical

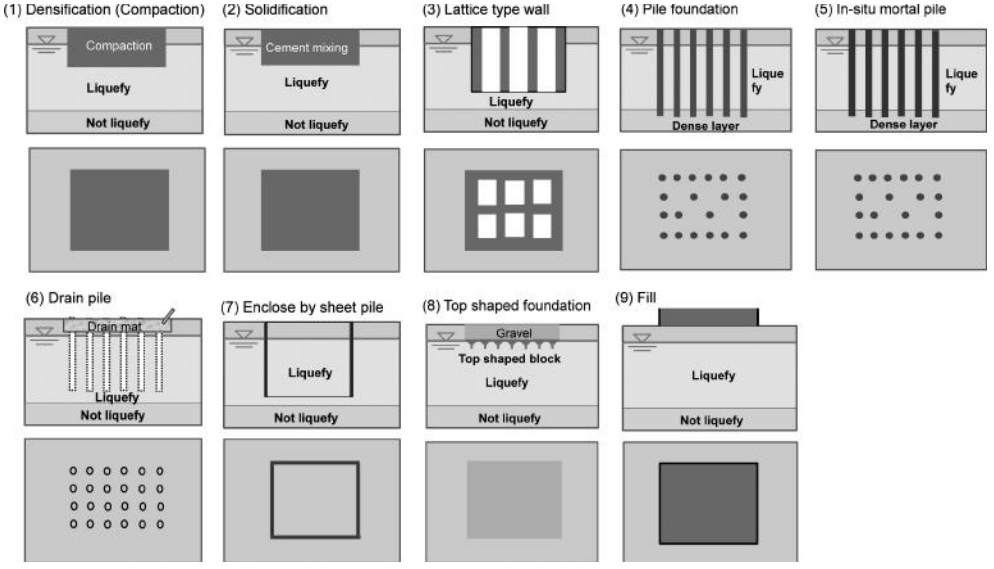

Figure 7. Possible liquefaction countermeasures for constructing new houses, including several ideas which have not been confirmed quantitatively (JGS Kanto, 2013).

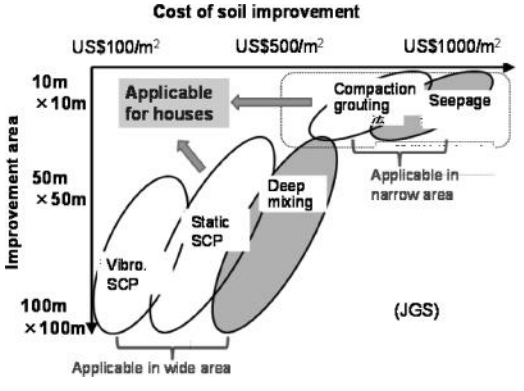

Figure 8. Limitation of current soil improvement methods for individual houses (JGS Kanto, 2013).

but not applicable in a narrow area. To make them applicable in a narrow area would require the development of small, quiet construction machines. On the contrary, compaction grouting and seepage methods are applicable in a narrow area but are not economical. Their cost must be reduced to make them practical. Soon after the 2011 Great East Japan Earthquake, efforts to modify current liquefaction countermeasures for individual new or existing houses started.

One modification, developed by Fudo Tetra Co., is the "gravel drain with compaction" method, in which a compact machine is used, instead of a normal, large machine, as shown in Figure 9 (Harada et al., 2013). This method was applied in 2012 to the ground beneath the site of a house in Urayasu City that was demolished by the Great East Japan Earthquake before a new house was constructed. The area of the site was only 106.8 $m^{2,}$ and the site was surrounded by adjacent houses. The process of the method is: (i) move a machine to the site; (ii) dig a hole using an auger; (iii) remove the auger and fill gravel into the hole; (iv) insert the auger and compress the gravel to expand it horizontally; and (v) repeatedly remove the auger, add gravel, and compress it to densify the foundation ground. Through compaction, the diameter of each gravel layer expanded from 400 mm to about 500 mm. However, the SPT *N*-value of the soil increased by only 5 to 7 after this method had been applied because the ground was very fine silty sand with 42% silt and clay content. The effect of the gravel drain only, neglecting the effect of densification, was considered in the design of gravel piles arranged in square configuration 1.55 m apart to resist liquefaction under a peak acceleration of 200 cm/s^2. Moreover, the penetrating settlement of the newly constructed house during very intense Level 2 shaking of 343 cm/s^2 was estimated using the ALID/Win computer program (Yasuda et al., 1999) at only 3 cm.

3.3 *Remediation methods for a wide existing residential area (Pattern 3)*

In Japan two districts where many houses had been damaged due to liquefaction during past earthquakes were restored by lowering the water table to prevent re-liquefaction during future earthquakes. One is the Tsukiji district of Amagasaki City, built on reclaimed land that was seriously damaged due to liquefaction during the 1995 Kobe Earthquake. Ten houses in this district totally collapsed and 292 houses half collapsed. As the ground water table was shallow, only GL- 0 m to – 1 m, drain pipes were buried to a depth of 2 to 3.5 m to lower the water table (Suwa et al., 2012). Another district is the Yamamoto housing area of Kashiwazaki City, where serious damage occurred during the 2007 Niigataken-chuetsu-oki Earthquake. The ground water table was very shallow because the area is a gently sloping

Figure 9. Compact gravel compaction with drain method applied to a house reconstruction.

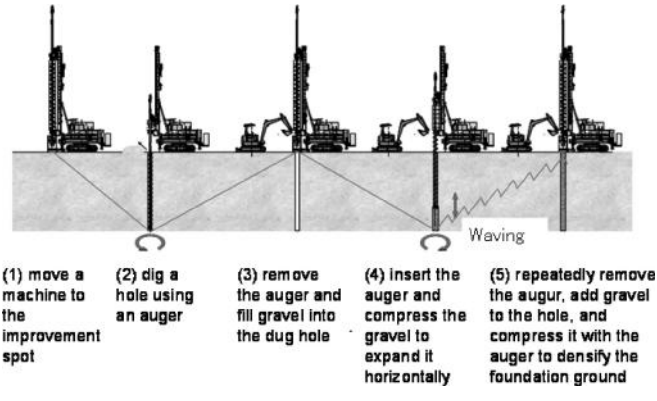

Figure 10. Process of the gravel compaction with drain method (Harada, et al., 2013).

sand dune. Thus, the water table was lowered to a depth of GL – 2 m using drain pipes (JGS, 2009), as shown in Figure 11.

Soon after the 2011 Great East Earthquake, the repair of tilted houses by lifting their superstructure (Figure 12), reconstructing their footings, and replacing the super structures on the new footings, started. More than half of the damaged houses were repaired in two years. However, this kind of repair does not prevent re-liquefaction during a future earthquake. The ground beneath the houses must be improved to prevent liquefaction. Therefore, the Ministry of Land, Infrastructure, Transport and Tourism (MLIT) established a new project eight months after the earthquake, the "Urban liquefaction countermeasure project". In this project, a wide existing residential area of more than 3,000 m^2, including roads, buried pipes and more than 10 houses, is treated by an appropriate countermeasure and its costs are shared by government and inhabitants, as schematically shown in Figure 13. The project aims to select effective countermeasures and determine how to share their cost with inhabitants. Available countermeasures have been compared in 12 damaged cities, and two methods, lowering the water table and surrounding the foundation ground with lattice-type underground walls, as shown in Figure 14 and 15, respectively, have been selected as the most promising. The applicability of these methods is being studied by in-situ tests, centrifuge tests as shown in Figure 16 and analyses.

3.4 *Remediation methods for a narrow existing house space (Pattern 4)*

Figure 17 shows several possible countermeasures to liquefaction applicable to houses built in narrow spaces, including several ideas proposed by the Kanto Branch of the JGS Kanto (2013). Densification and enclosing the foundation ground with sheet pile walls are two effective methods developed after the earthquake.

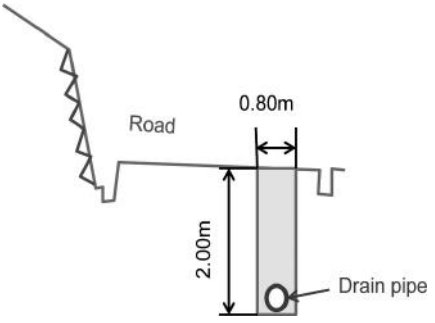

Figure 11. Lowering the ground water table at Yamamoto residential area in Kashiwazaki City.

Figure 12. Lifting house superstructure with jacks.

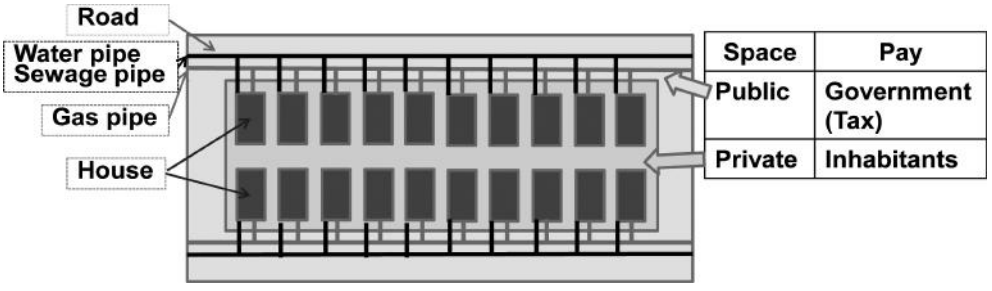

Figure 13. Plan of urban liquefaction countermeasure project.

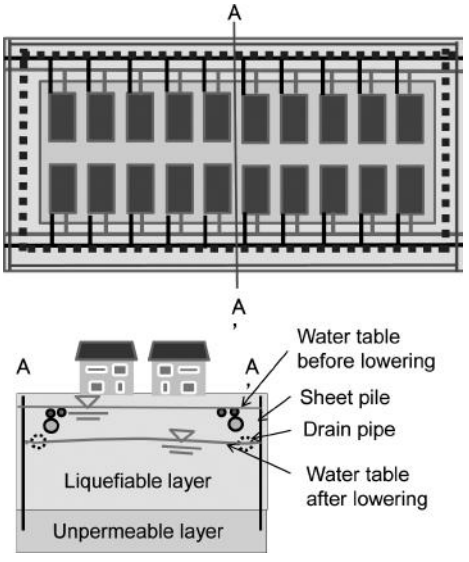

Figure 14. Lowering the ground water table.

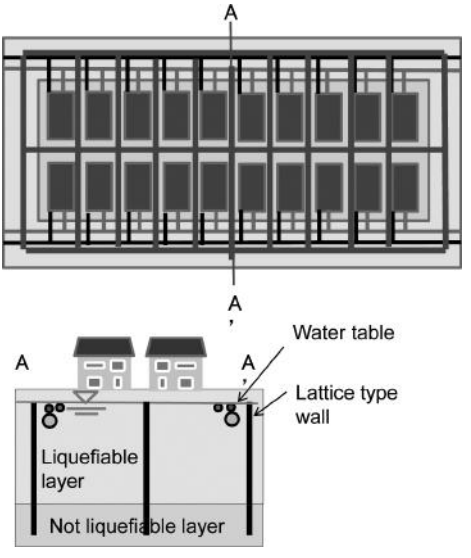

Figure 15. Surrounding foundation soil with lattice type wall.

Figure 16. In-situ test to demonstrate the effect of drain pipes in Kamisu City.

The compaction grouting method could be applied to existing houses by digging holes through floors, as shown in Figure 18 and applied at several sites soon after the 2011 Great East Japan Earthquake. However, it was necessary to cut holes through floor slabs and dig bore holes through these holes in the floor. A more simple technique, in which bore holes are dug from outside a house using an inclined bore-hole machine, was developed by Sanshin Co., as shown in Figure 19. This new technique can be applied to existing houses at moderate cost.

The impact of enclosing the foundation soil of a house with sheet piles on the mitigation of settlement of the house if the foundation ground is liquefied had been studied by small shaking table tests on model houses by the author and his colleagues before the 2011 Great

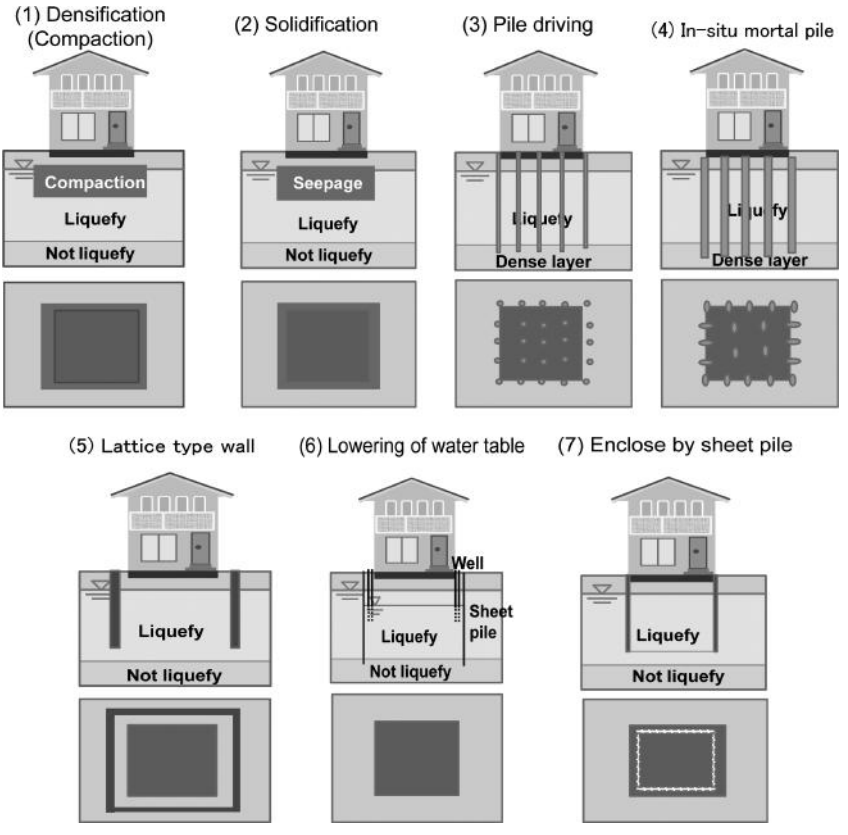

Figure 17. Possible liquefaction countermeasures for existing houses, including several ideas which have not been confirmed quantitatively (JGS Kanto, 2013).

Figure 18. Compaction grouting method applied through floor of an existing house.

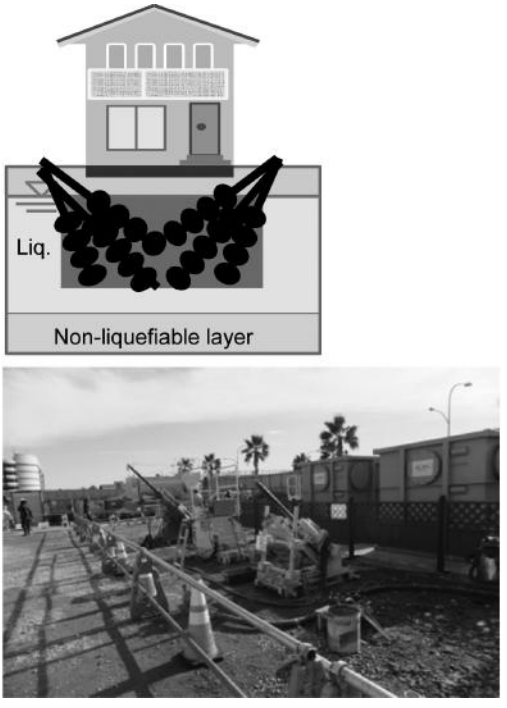

Figure 19. Modified compaction grouting method for existing houses, digging bore holes from outside the houses.

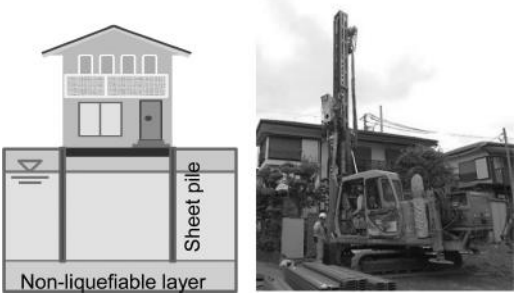

Figure 20. Enclosing foundation soil with sheet pile wall for constructing new houses or for existing houses.

East Japan Earthquake (Yasuda et al., 2005). Immediately after the earthquake, its applicability to actual houses was discussed and additional small-scale and large-scale shaking table tests were conducted. Subsequently, this method was applied to a newly constructed house as, shown in Figure 20, and to an existing warehouse.

4 CONCLUSIONS

As the 2011 Great East Japan Earthquake caused serious damage to wooden houses, appropriate countermeasures to liquefaction were discussed and several new countermeasures were

developed soon after the earthquake. A review of these discussions and developments shows four patterns to reconstruct damaged houses and/or areas:

1. The first pattern is to reconstruct houses in a wide area of demolished houses. Current soil improvement techniques can be applied easily.
2. The second pattern is to reconstruct a house in a narrow space. Countermeasures to liquefaction in this pattern must by applicable in a narrow space and economical. The "gravel drain with compaction" method was developed soon after the earthquake and applied in Urayasu City.
3. The third pattern is to treat a wide existing residential area. The MLIT of Japan established an "Urban liquefaction countermeasure project" to prevent liquefaction damage during future earthquakes. The adaptability of two methods, lowering the water table and surrounding the foundation ground with lattice-type underground walls, is being studied in damaged cities now.
4. The last pattern is to take countermeasures to liquefaction for an existing house. An effective compaction grouting method, in which bore holes are dug from outside a house using an inclined bore-hole machine, and the method of enclosing the foundation soil of a house with sheet piles were developed after the earthquake.

REFERENCES

Harada, K., Ohbayashi, J. and Yoshitomi, H. 2013. Development and application of countermeasures against liquefaction for residential land. *Geotechnical Engineering Magazine*, JGS, Vol. 61, No. 4, pp. 22–25. (in Japanese)

Japanese Geotechnical Society, JGS 1998. *Remedial Measures against Soil Liquefaction*, Balkema.

Japanese Geotechnical Society, JGS Kanto Branch. 2013. *Guideline to Mitigate Liquefaction-induced Damage to Wooden Houses*, p. 209. (in Japanese).

Suwa, S., Fukuda, M, Hamada, T., Hongo, T. and Shigyo, A. 2012. Case study on the effect of dewatering as a liquefaction countermeasure. *Proc. of the 10th Symposium on Soil improvement, The Society of Material Science*, Japan, pp. 213–220. (in Japanese).

Yasuda, S. 2010. Damage to structures due to soil liquefaction. *Proc. of the 11th IAEG Congress*, Geologically Active—Williams et al. (eds), Taylor & Francis Group, pp. 15–52.

Yasuda, S. and Ariyama, Y. 2008. Study on the mechanism of the liquefaction-induced differential settlement of timber houses occurred during the 2000 Totoriken-seibu earthquake. *Proc. of the 14th World Conference on Earthquake Engineering*, Paper No. S26–021.

Yasuda, S., Fukaya, S. and Komori, M. 2005. Shaking table tests on the influence factors and a simple countermeasure for liquefaction-induced settlement of timber houses. *Proc. of the 40th Japan National Conference on Geotechnical Engineering*, pp. 2025–2026 (in Japanese).

Yasuda, S., Harada, K., Ishikawa, K. and Kanemaru, Y. 2012. Characteristics of the liquefaction in Tokyo Bay Area by the 2011 Great East Japan Earthquake. *Soils and Foundations*, Vol. 52, Issue 5, pp. 793–810, 2012.

Yasuda, S., Towhata, I, Ishi, I, Sato, S. and Uchimura, T. 2013. Liquefaction-induced damage to structures during the 2011 Great East Japan Earthquake. *J. of JSCE*, Vol. 1, pp. 181–193.

Yasuda, S., Yoshida, N., Adachi, K., Kiku, H. and Gose, S. 1999. A simplified analysis of liquefaction-induced residual deformation. *Proc. of the 2nd International Conference on Earthquake Geotechnical Engineering*, pp. 555–560.

This page intentionally left blank

Soil Liquefaction during Recent Large-Scale Earthquakes – Orense, Towhata & Chouw (Eds)

Verification of effectiveness of liquefaction countermeasures during past large scale earthquakes in Japan

K. Harada, J. Ohbayashi, J. Matsumoto & H. Yoshitomi
Fudo Tetra Corporation, Tokyo, Japan

S. Yasuda
Tokyo Denki University, Tokyo, Japan

R.P. Orense
University of Auckland, Auckland, New Zealand

ABSTRACT: In this paper, the present state and case histories of liquefaction countermeasures were first presented, and the lessons from past large-scale earthquakes were discussed. Among the ground improvement techniques, compaction method was observed to be very effective against earthquakes characterized by severe shaking, such as the 1995 Hyogo-ken Nambu Earthquake, and those with long duration, such as the 2011 off the Pacific Coast of Tohoku Earthquake. In addition, responses toward Performance-Based Design (PBD) and application to existing structures were introduced as the current trends of liquefaction countermeasure for future earthquakes. Especially in PBD, it is important to set the performance of the target structure and the improvement level required based on prediction of damage to the structure. A simple technique was proposed to estimate the post-liquefaction settlement and its validity was evaluated based on the data from the 2011 off the Pacific Coast of Tohoku Earthquake. The lessons learned and the method developed will be used to further rationalize future ground improvement design.

1 INTRODUCTION

Japan had experienced many earthquakes and, as a result, many types of countermeasures against liquefaction have been developed. The 1995 Hyogoken-Nambu Earthquake (Great Hanshin-Awaji Earthquake) induced extremely intense shaking, but the ground that had been improved by Sand Compaction Pile (SCP) method suffered very little liquefaction-induced damage (Yasuda et al., 1997). In addition, the 2011 off the Pacific Coast of Tohoku Earthquake (The Great East Japan Earthquake) with long shaking duration caused severe liquefaction of reclaimed lands along Tokyo Bay area which was 350 km away from the epicenter. However, reclaimed lands that were remediated by SCP method and Gravel Drain (GD) method did not liquefy (Yasuda et al., 2012).

This paper presents the classification and history of remedial measures against liquefaction in Japan, and introduces some case histories verifying the effectiveness of improvement. In addition, lessons from the past large scale earthquakes, including the 2011 off the Pacific Coast of Tohoku Earthquake, are compiled and analyzed, together with the indication of ground improvement trend against future large scale earthquakes.

2 PRESENT SITUATION OF LIQUEFACTION COUNTERMEASURES IN JAPAN

2.1 *Classification and history of liquefaction countermeasures*

Liquefaction countermeasures are broadly divided into those that prevent liquefaction from occurring through ground improvement and those that minimize damage through structural strengthening (JGS, 2004). Generally, these methods can be classified into six categories depending on the principle involved: (1) compaction (densification); (2) solidification; (3) replacement; (4) groundwater lowering; (5) drainage (pore water dissipation); and (6) shear deformation control. This is illustrated in Figure 1. Among these, the first three methods, i.e. compaction, solidification and drainage, are the main countermeasures employed in Japan.

Table 1 indicates the history of alternative methods for each category. The SCP method as densification technique was the earliest to be developed in which sand piles were installed to reinforce soft clayey ground in the 1950s. In the 1960s, the method was applied as liquefaction countermeasure. The lattice-type Deep Mixing (DM) technique as solidification method and the GD technique as drainage method were developed as liquefaction countermeasure in 1970s and 1980s, respectively.

2.2 *Compaction method as a liquefaction countermeasure*

The proportion of liquefaction prevention projects in Japan for each of the 6 categories is shown in Figure 2. Figure 2(a) covers the approximate 5-year period from 1986 to July 1990 while Figure 2(b) covers a 5-year period after the Hyogoken-Nambu Earthquake, from April 1998 to March 2003. A comparison of the two periods shows that the Hyogoken-Nambu Earthquake prompted an increase in liquefaction prevention projects, and that compaction, solidification and drainage methods are generally the leading countermeasures used in Japan. A comparison of Figures 2(a) and 2(b) indicates no significant change in the proportion of densification projects, but shows a reduction in the proportion of projects based on pore water pressure dissipation while a corresponding growth was observed in the projects based on solidification. This shift may be due to the observed effectiveness of the lattice type DM method applied at Kobe Port during the 1995 Hyogoken-Nambu Earthquake (Suzuki et al., 1996).

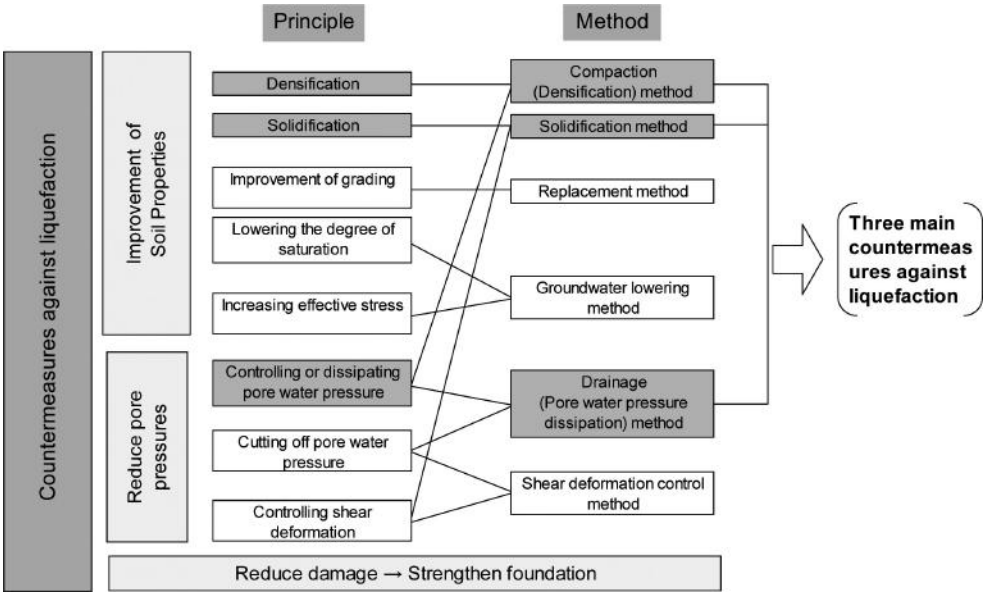

Figure 1. Principles and methods of countermeasures against liquefaction (JGS, 2004).

Table 1. History of countermeasures against liquefaction.

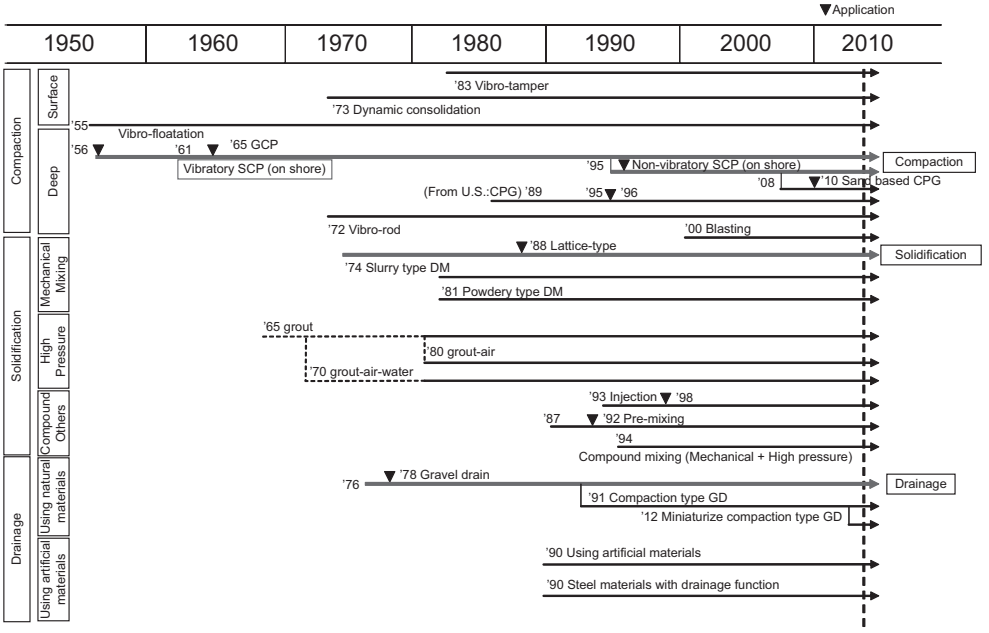

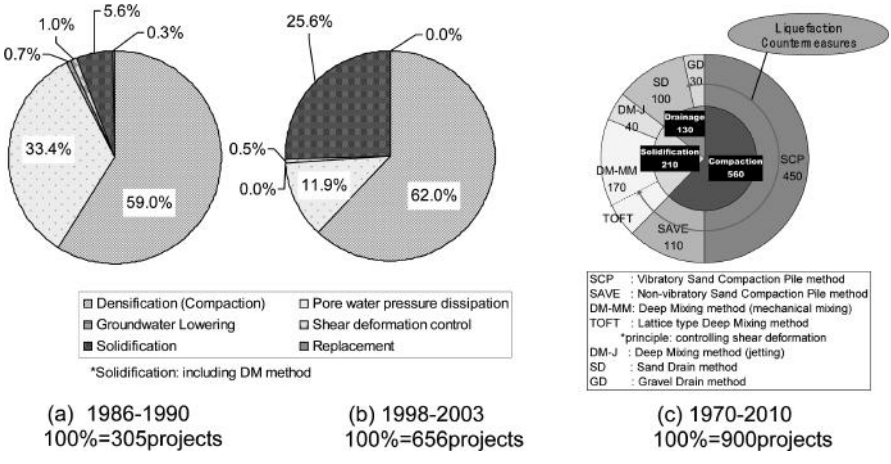

Figure 2. Proportion of countermeasures against liquefaction (JGS, 2004 and Harada, 2011).

Figure 2(c) shows the proportion of various ground improvement methods implemented in areas along Tokyo Bay (Tokyo and Chiba) by Fudo Tetra Corporation over a period of forty years (Yasuda et al. 2012). The figure indicates that a total of 900 ground improvement projects have been implemented, and that 70% of them were liquefaction countermeasure projects, such as vibratory and non-vibratory SCP method, GD method and DM method.

3 CASE HISTORIES OF PERFORMANCE DURING PAST EARTHQUAKES

3.1 *Case histories before the 2011 off the Pacific Coast of Tohoku*

Figure 3 shows the epicenter locations and characteristics of the 1964 Niigata Earthquake and nine other large-scale earthquakes, including the 2011 off the Pacific Coast of Tohoku

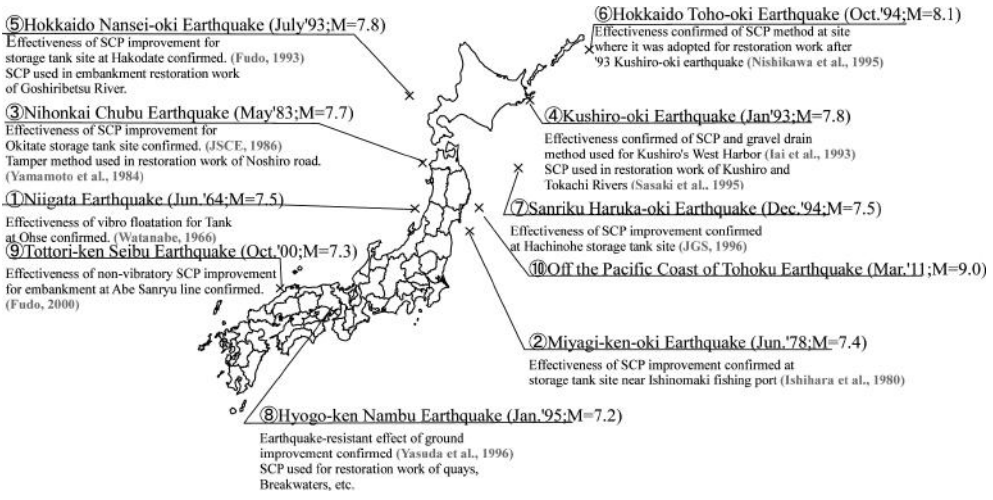

Figure 3. Case histories of compaction method performance through past earthquakes. (modified from Ohbayashi et al., 1998).

Earthquake, as well as information on the performance of compaction-improved grounds during these earthquakes. As shown in the figure, there has been no report of major disruption to structures erected on compacted ground, such as by vibratory and non-vibratory SCP methods, thus confirming in a qualitative sense the effectiveness of compaction-type ground improvement techniques. The detailed information for each case is described in the respective reference indicated. The tamper method was adopted as a restoration work of road foundation after the 1983 Nihonkai Chubu Earthquake.

3.2 *Case histories during the 2011 Off the Pacific Coast of Tohoku Earthquake*

It was confirmed that there was no damage at any of the improved sites during the 2011 off the Pacific Coast of Tohoku Earthquake. Figures 4(a)–(b) indicate the conditions at the boundary of improved and unimproved areas and the layout/cross section of the sand piles. At each site, there was no manifestation of liquefaction, such as the occurrence of sand boil and settlement. Generally, settlement occurred mainly outside of the improved areas. Figure 4(c) shows the condition near a site improved by non-vibratory SCP method just after the earthquake. Water was ejected on the unimproved section.

4 LESSONS FROM PAST LARGE EARTHQUAKES

Next, the deformation behavior of compacted ground and the liquefaction resistance of compacted soil obtained from the SPT *N*-values are described to illustrate the lessons from past earthquakes.

4.1 *Behavior of ground improved by compaction*

4.1.1 *1995 Hyogoken-Nambu earthquake*

During the 1995 Hyogoken-Nambu Earthquake, less subsidence occurred on the improved areas as compared with those in unimproved areas at the two artificial islands called Port Island and Rokko Island. Matsuo et al. (1997) reported that significant subsidence did not occur on some improved areas even when the target SPT *N*-values were not reached. These SPT *N*-values ware obtained in between the piles. Figure 5 illustrates the relationship between the relative settlement for each improvement method at Port Island and Rokko Island and

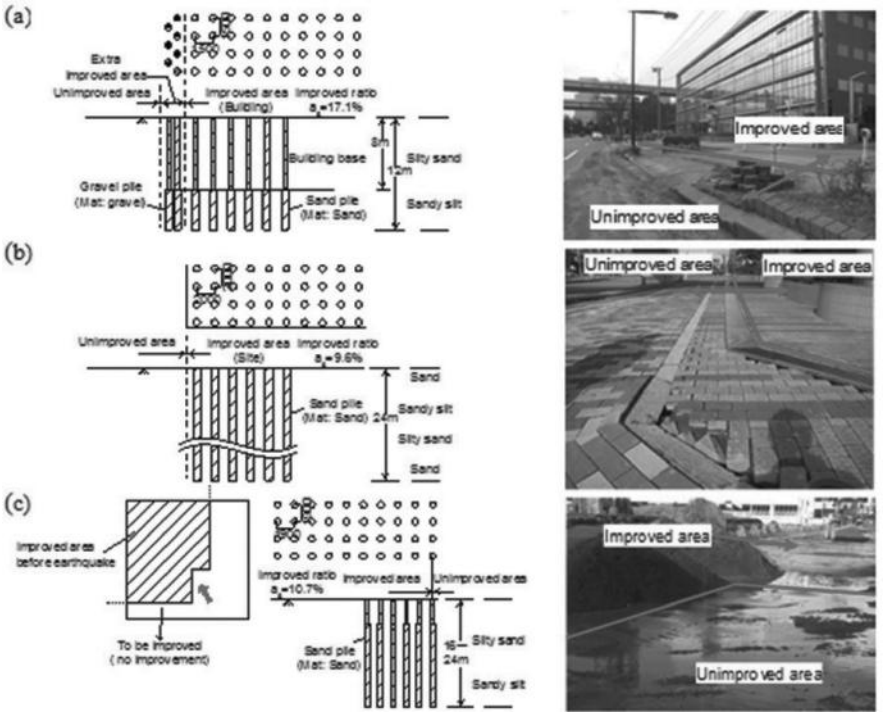

Figure 4. Conditions of improved areas following the earthquake (Nunokawa et al., 2012).

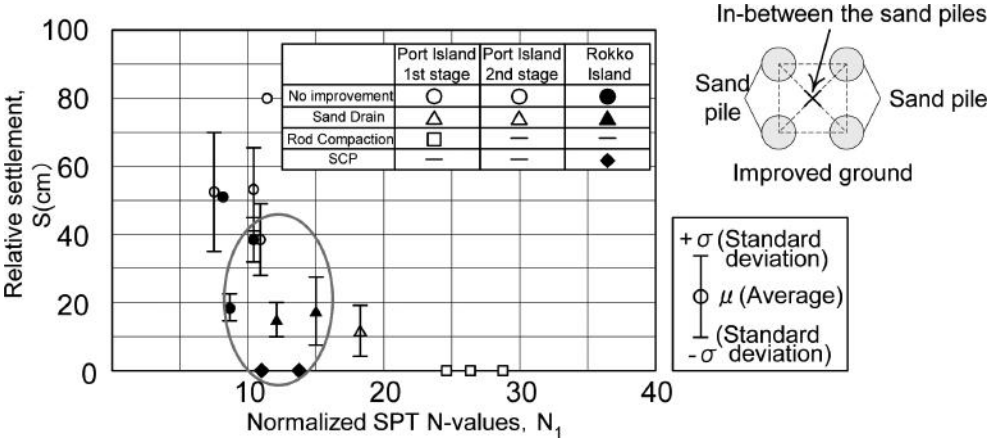

Figure 5. Relative settlement for each improvement method (Matsuo et al., 1997).

the normalized SPT N-values, N_1, derived from the following equation to take into account the effect of overburden pressure on N-values:

$$N_1 = \frac{1.7N}{\sigma'_v/98 + 0.7} \tag{1}$$

where σ'_v is the effective overburden pressure (kN/m^2). As shown by the data from Rokko Island which are within the indicated zone, almost no subsidence occurred on SCP-improved

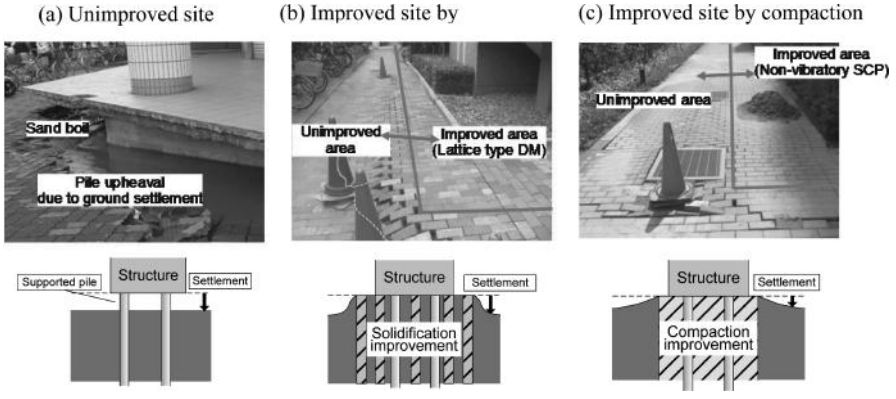

Figure 6. Behavior of ground adjacent to each structure with pile foundation (Harada. 2011).

ground (◆) while 20–40 cm settlements were observed in the unimproved ground (●) even though they have almost similar SPT *N*-values. Harada et al. (2011) pointed out that this is due to the increase in lateral stress ratio K_c ($= \sigma'_h / \sigma'_v$; σ'_h: effective horizontal stress, σ'_v: effective overburden stress) caused by the installation of sand piles and the effect of composite ground consisting of compacted sand piles and the ground around them.

4.1.2 *201 off the Pacific Coast of Tohoku Earthquake*

The conditions of the ground adjacent to buildings supported by pile foundation in Urayasu during the earthquake are shown in Figure 6. These three sites are located in almost the same district. Figure 6(a) shows the pile protruding out of the surface due to the subsidence of the liquefied ground around the piles. If the ground were treated by ground improvement methods, no such differential settlement would occur; instead, a little subsidence would occur at the boundary between the improved and unimproved areas. Figures 6(b) and 6(c) show the boundary between unimproved areas and improved sections by solidification method and compaction method, respectively. Comparing these figures, sections near compaction-improved grounds seem to deform more smoothly at the boundary than those near solidification-improved grounds.

4.2 *Liquefaction resistance of improved ground by compaction*

Figure 7 shows the relation between the SPT *N*-values obtained in-between piles and the shear stress ratio from the past earthquake to evaluate the performance of compacted ground. The data of improved sites suffered past earthquakes including improvement specification are indicated in Table 2.

The normalized SPT *N*-value, N_1, of the improved ground (given by Eq. 1) was corrected for the effect of fines content, as shown in Eq. 2. Liquefaction occurrence is related not only to the soil condition but also to the cyclic shear stress induced by the shaking. This was estimated using Eq. 3 as introduced by JRA (1990). The maximum surface acceleration was obtained from recorded motions near the site. Therefore we judge that the same level of ground surface shaking occurred as the recording station.

$$N_a = C_1 \cdot N_1 + C_2 \tag{2}$$

where

$$C_1 = \begin{cases} 1 & 0 \le F_c < 10 \\ (F_c + 40)/50 & 10 \le F_c < 60 \\ Fc/20 - 1 & 60 \le F_c \end{cases} \qquad C_2 = \begin{cases} 0 & 0 \le F_c < 10 \\ (F_c - 10)/18 & 10 \le F_c \end{cases}$$

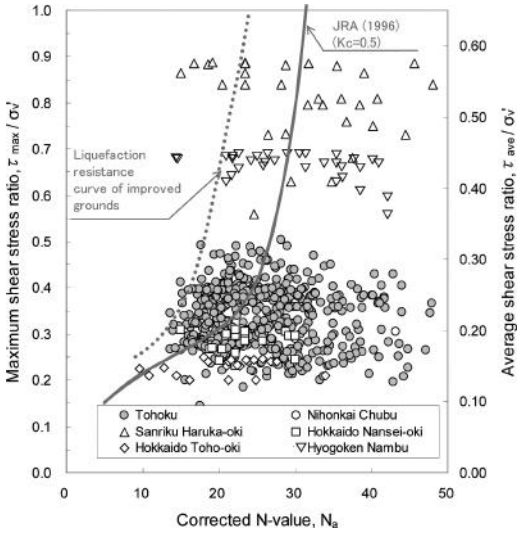

Figure 7. Relationships between shear stress ratio and corrected *N*-value (Iwata et al., 2013).

Table 2. Data of improved sites suffered earthquakes.

Earthquake	Occurrence year month	Max. acceleration at ground surface (gal)	Number of boring	Improvement spec. ( ) improvement ratio a_s (%)	Reference
Nihonkai Chubu	1983.5	200	1	Δ 2.0m (11)	Ohbayashi et al. (1998)
Hokkaido Nansei-oki	1993.7	220	3	□ 1.5m (17)	
Hokkaido Toho-oki	1994.10	200	4	□ 1.7m (13)	
Sanriku Haruka-oki	1994.12	440~600	12	□ 1.5m (17) Δ 1.9m (12)	
Hyogo-ken Nambu	1995.1	550	4	□ 1.8~2.0m (9~12)	Yasuda et al. (1997)
Off the Pacific Coast of Tohoku	2011.3	174~224	126	□ 1.5~2.1m (8~17)	Harada et al. (2012)

□ : square grid

$a_s = \frac{A_s}{x^2}$

△ : triangular grid

$a_s = \frac{2}{\sqrt{3}} \frac{A_s}{x^2}$

As: sectional area of sand pile

C_1, C_2: coefficient of corrected *N*-value; and F_c: fines content (%)

$$\frac{\tau_{\max}}{\sigma'_v} = (1 - 0.015z)\frac{\alpha_{\max}}{g} \cdot \frac{\sigma_v}{\sigma'_v} \tag{3}$$

where τ_{max}: maximum cyclic shear stress; α_{max}: maximum surface acceleration; g: acceleration due to gravity and σ'_v: effective overburden pressure (kN/m^2); σ_v: total overburden pressure (kN/m^2).

Figure 7 also shows the relationship between the maximum shear stress ratio and corrected SPT *N*-values in the improved grounds. The vertical axis on the right side shows the average shear stress ratio, which is 0.65 times τ_{max}/σ'_v. All data points represent non-liquefaction in the improved areas. It may be said that the liquefaction resistance curve of improved grounds

is best represented by the dashed curve, which is on the left side of the curve proposed by JRA (1996). Thus, the liquefaction resistance of the improved ground is higher than that of the natural ground even for the same *N*-values. This fact may be due to the same reason mentioned before.

5 TRENDS FOR LIQUEFACTION COUNTERMEASURES

Next, the lessons obtained from the facts described in the previous sections are compiled and analyzed, focusing on response towards performance-based design and towards existing structures as the future trend of ground improvement against large-scale earthquakes.

5.1 *Response toward Performance-Based Design (PBD)*

It is necessary to model the compaction-improved ground appropriately and to predict using simplified method the ground deformation precisely as well as effectiveness of restraining the deformation.

The procedure of the prediction method based on disturbed and undisturbed samples from element tests (Harada and Ishihara, 2013) are as follows (refer to Figure 8(a)):

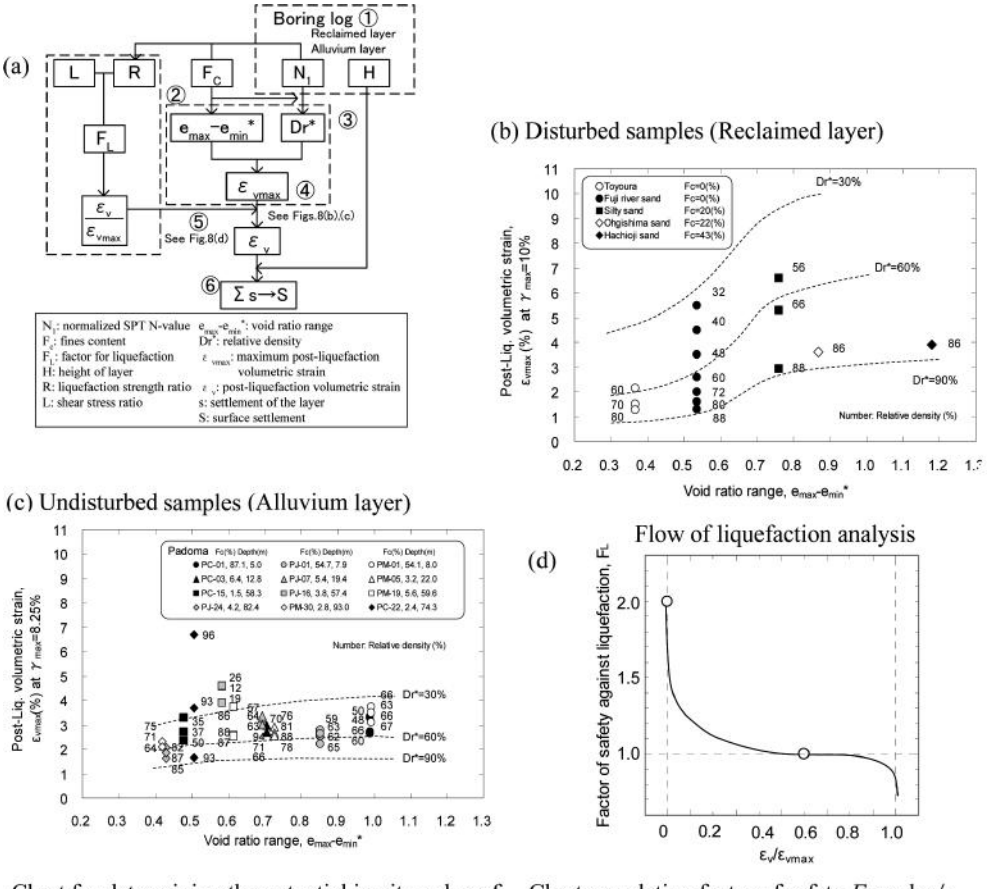

Chart for determining the potential in-situ value of volumetric change, ε_{vmax} (Ishihara et al., 2013)

Chart correlating factor of safety F_L and $\varepsilon_v/\varepsilon_{vmax}$ (Tsukamoto and Ishihara et al., 2004)

Figure 8. Charts used for liquefaction analysis.

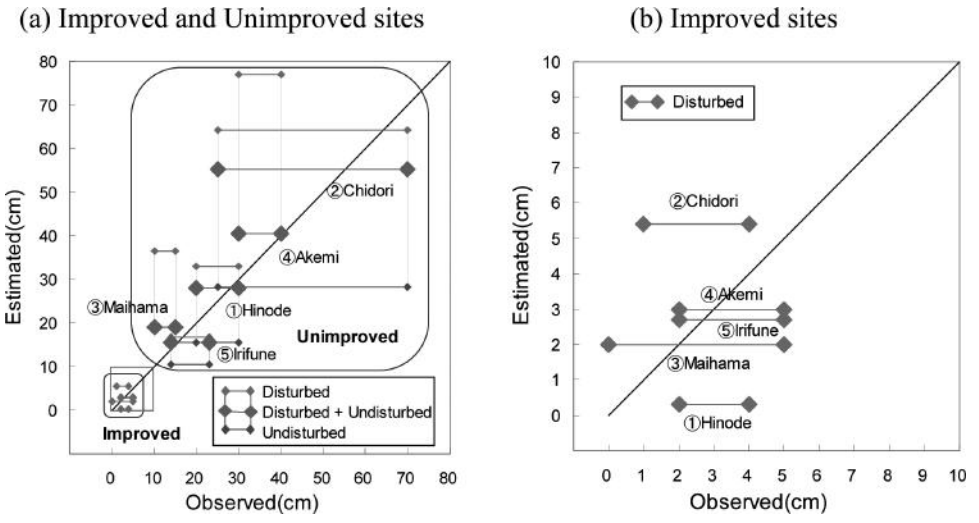

Figure 9. Comparison with observed and predicted settlement (Harada and Ishihara, 2013).

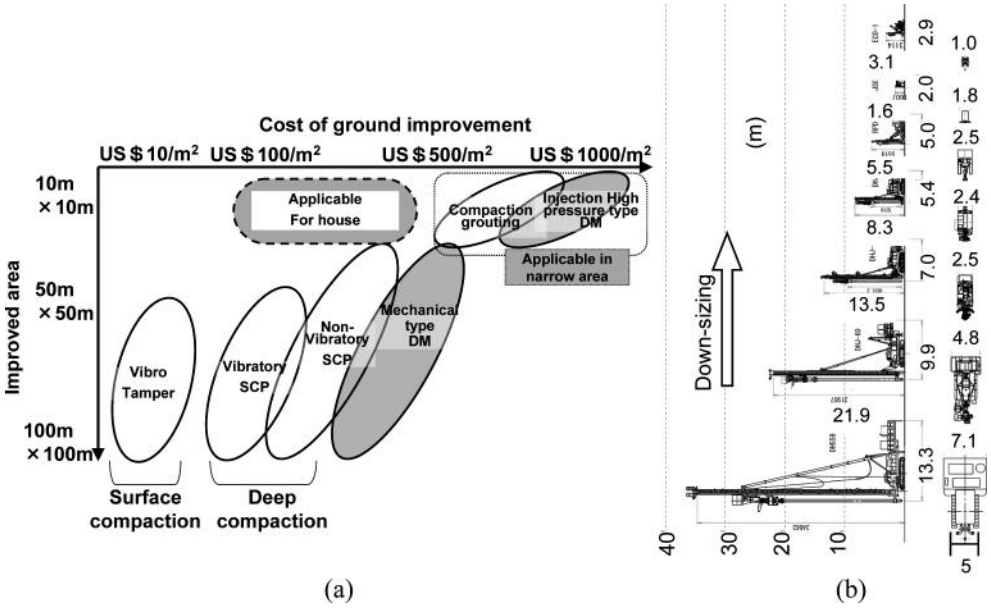

Figure 10. (a) Relationship between improved area and cost (modified from JGS, 2004); and (b) size of equipment used.

① Divide the reclaimed and alluvium layers from the boring log.
② Estimate the void ratio range, $e_{max} - e_{min}^{*}$ using fines content, F_c.
③ Estimate relative density D_r^{*} using fines content, F_c and normalized SPT N-value, N_1.
④ Obtain the maximum volumetric strain, $\varepsilon_{vmax,}$ from Figure 8(b) for the fill (reclaimed) layer and from Figure 8(c) for the alluvial layer.
⑤ Obtain volumetric strain/maximum volumetric strain, $\varepsilon_v/\varepsilon_{vmax}$ from Figure 8(d) using factor of safety against liquefaction, F_L, and volumetric strain, ε_v, from step (2).
⑥ Estimate the settlement from the layer thickness, H, and volumetric strain, ε_v.

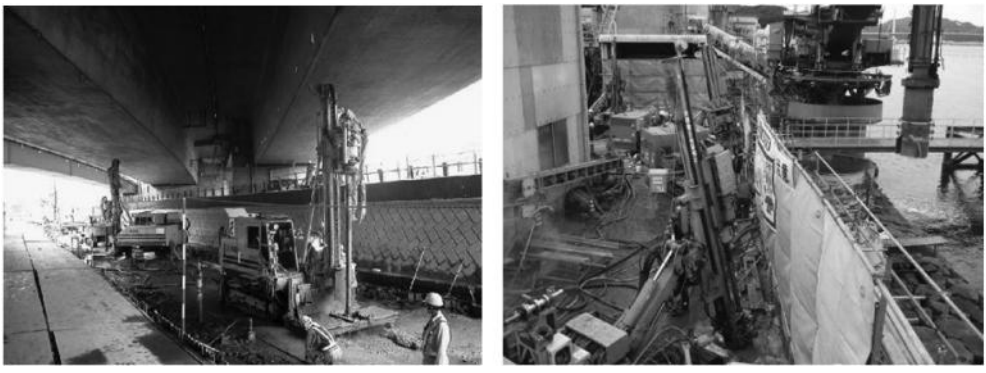

Figure 11. Examples of implementation under limited spaces.

Figure 9 shows the comparison between the observed and predicted settlements using this method. The observed settlement is obtained from the data in Urayasu City (CERC, 2011). Both values agree very well, clearly illustrating the effectiveness of the improvement.

5.2 *Response toward existing structures*

The relationship between improved area and cost of ground improvement is shown in Figure 10(a) (JGS, 2011). When the area to be improved is wide enough, large types of equipment, such as those used for SCP method and DM method, can be used without much expense. On the other hand, when the area to be improved is narrow or within limited space, only static compaction by injection method and high pressure injection type DM method, which make use of small-sized equipment, are applicable. The smaller the size of equipment, the higher is the cost because of the decrease in mobility and productivity. The tamper method, which densifies the surface area, is the most economical method among the liquefaction countermeasures when the area to be improved is wide.

Figure 10(b) shows the size of equipment used in liquefaction countermeasures (Harada et al., 2012). Recently, small-sized equipment has been developed to allow working on limited space, such as under the bridge girder and near existing structures, as shown in Figure 11.

6 SUMMARY

In this paper, the present state and case histories of liquefaction countermeasures were presented, and the lessons from past large-scale earthquakes were discussed. Among the ground improvement techniques, compaction method was observed to be very effective against earthquakes characterized by severe shaking, such as the 1995 Hyogo-ken Nambu Earthquake, and those with long duration, such as the 2011 off the Pacific Coast of Tohoku Earthquake.

In addition, responses toward Performance-Based Design (PBD) and toward existing structures were introduced as the current trends of liquefaction countermeasure for future earthquakes. Especially in PBD, it is important to set the performance of the target structure and the improvement level required based on prediction of damage to the structure. A simple technique was proposed to estimate the post-liquefaction settlement and its validity was evaluated based on the data from the 2011 off the Pacific Coast of Tohoku Earthquake. The lessons learned and the method developed will be used to further rationalize future ground improvement design.

REFERENCES

Chiba Environmental Research Center, CERC 2011. *Investigation Report on Liquefaction in Chiba - Lateral spreading phenomena and its damage (Part 3)*, (in Japanese)

Fudo Construction 1993. *Investigation Report on the 1993 Hokkaido Nansei-oki Earthquake* (in Japanese)

Fudo Construction 2000. *Investigation Report on the 2000 Tottori-ken Seibu Earthquake* (in Japanese)

Harada, K. 2011. Non-vibratory SCP method as countermeasures against liquefaction along coastal areas—Improvement effectiveness during the 2011 Off the Pacific Coast of Tohoku Earthquake. *Doboku Sekou*, No. 12, 54–57 (in Japanese)

Harada, K. and Ishihara, K. 2012. Study on soil containing fines of minimum void ratio and relative density. *Proc. Japanese Association of Earthquake Engineering*, 276–277 (in Japanese)

Harada, K. and Ishihara, K. 2013. Ground improvement effectiveness based on the simple prediction method for settlement due to liquefaction. *Proc. Japanese Assoc. Earthquake Engineering* (submitted, in Japanese)

Harada, K., Ando. S. and Imai, Y. 2012. Sand compaction pile method as a countermeasure against liquefaction—History of SCP method and its applications for restoration works during the 2011 Off the Pacific Coast of Tohoku Earthquake. *Doboku Sekou*, No. 5, 30–34 (in Japanese)

Harada, K., Ohbayashi, J., Taguchi, Y. and Yasuda, S. 2012. Verification on improvement effectiveness during the 2011 Off the Pacific Coast of Tohoku Earthquake. *Proc. 10th Symposium for Ground Improvement*, 83–90 (in Japanese)

Iai, S., Matsunaga, Y., Morita, T., Sakurai, H., Ohishi, H., Ogura, H., Ando, Y., Tanaka, Y. and Kato, M. 1993. Effects of remedial measures against liquefaction at 1993 Kushiro-oki Earthquake. *Proc. 5th US-Japan Workshop on Earthquake Resistant Design of Lifeline Facilities and Countermeasures against Soil Liquefaction*.

Ishihara, K., Harada, K. and Sakai, T. 2013. Prediction for settlement due to liquefaction based on disturbed and undisturbed samples. *Proc. Japanese Conf. on Geotechnical Engineering*, 1865–1866 (in Japanese)

Ishihara, K., Kawase, Y. and Nakajima, M. 1980. Liquefaction characteristics of sand deposits at an oil tank site during the 1978 Miyagiken-Oki Earthquake. *Soils and Foundation*s, 20(2), 97–112.

Iwata, Y., Ohbayashi, J., Harada, K. and Komatsu, H. 2013. Consideration on extra liquefaction resistance of improved ground by compaction (Part 3: site investigation). *Proc. Japanese Conference on Geotechnical Engineering in Kanto Region* (in Japanese, to be printed)

Japanese Geotechnical Society, JGS 1996. *Investigation Report on the 1996 Sanriku Haruka-oki Earthquake* (in Japanese)

Japanese Geotechnical Society, JGS 2004. Countermeasures against liquefaction. *Practical Affairs Series No. 18* (in Japanese).

Japanese Geotechnical Society, JGS Kanto Branch 2011. *Data of Earthquake Countermeasure for Residential Land Committee* (in Japanese).

Japan Road Association, JRA 1996. *Specifications for Highway Bridges* (in Japanese).

Japanese Society of Civil Engineers, JSCE 1986. *Investigation Report on the 1983 Nihonkai-chubu Earthquake* (in Japanese).

Matsuo, O., Yasuda, S., Yamamoto, M., Harada, K. and Hashimoto, T. 1997. Evaluation method of improved ground and damage sustained under level 2 Earthquake. *Proc. 24th Japan Conference on Earthquake Engineering*, 273–276 (in Japanese).

Nishikawa, J., Kamata, T. and Kaji, M. 1995. Damage to highways, railways and river embankments from the 1994 Hokkaido Toho-oki Earthquake. *Soils and Foundations*, 43(4), 7–10 (in Japanese)

Nunokawa, N., Harada, K., Imai, Y., Mishiro, T. and Taguchi, Y. 2012. Verification on liquefaction index for judgment and improvement effectiveness during the 2011 Off the Pacific Coast of Tohoku Earthquake. *Proc. Japanese Conference on Geotechnical Engineering in Kanto Region* (in Japanese)

Ohbayashi, J., Harada, K., Yamamoto, M. and Sasaki, T. 1998. Evaluation of liquefaction resistance in compacted ground. *Proc. 10th JAEE Symposium*, 1411–1416 (in Japanese).

Sasaki, Y., Tamura, T., Yamamoto, M. and Ohbayashi, J. 1995. Soil improvement work for river embankment damaged by the 1993 Kushiro-oki Earthquake. *Proc. 1st International Conference on Earthquake Geotechnical Engineering*, 43–48.

Suzuki, Y., Saitoh, S., Onimaru, S., Kimura, T, Uchida, A. and Okumura, R. 1996. Grid-shaped stabilized ground improvement by deep cemnt mixing method against liquefaction for a building foundation. *Journal of the Japanese Soc. Soil Mechanics and Foundation Engineering, Tsuchi to Kiso,* pp. 46–48. (in Japanese).

Tsukamoto, Y., Ishihara, K. and Sawada, S. 2004. Settlement of silty sand deposits following liquefaction during earthquake. *Soils and Foundations*, Vol. 44, No. 5, pp. 135–148.
Watanabe, T. 1966. Damage to oil refinery plants and a building on compacted ground by the Niigata Earthquake and their restoration. *Soils and Foundation*, 6(2), 86–99.
Yamamoto, S. and Suzuki, Y. 1984. Liquefaction and prevention for ground report: Southern Noshiro Road seismic damage and restoration works. *Foundation Engineering & Equipment*, 44–47 (in Japanese).
Yasuda, S., Harada, K. and Shinkawa, N. 1997. Soil conditions at liquefied and non-liquefied sites during the 1995 Hyogoken-Nambu earthquake. *Proc. 14th International Conference on Soil Mechanics and Foundation Engineering*, 1657–1660.
Yasuda, S. Harada, K. Ishikawa, K. and Kanemaru, Y. 2012. Characteristics of the Liquefaction in Tokyo Bay Area by the 2011 Great East Japan Earthquake. *Soils and Foundations*, 52(5), 793–810.
Yasuda, S., Ishihara, K., Harada, K. and Shinkawa, N. 1996. Effect of soil improvement on ground subsidence due to liquefaction. *Special Issue of Soils and Foundations*, 99–107.

Soil Liquefaction during Recent Large-Scale Earthquakes – Orense, Towhata & Chouw (Eds)

Effectiveness of inhibiting liquefaction triggering by shallow ground improvement methods: Initial field shaking trials with T-Rex at one site in Christchurch, New Zealand

K.H. Stokoe, II, J.N. Roberts, S. Hwang, B. Cox & F.Y. Menq
The University of Texas at Austin, USA

S. Van Ballegooy
Tonkin and Taylor Ltd., Auckland, New Zealand

ABSTRACT: Christchurch and the Canterbury region in New Zealand were devastated in 2010–2011 by a series of powerful earthquakes. The Christchurch area experienced widespread liquefaction that caused extensive damage. One critical problem facing the rebuilding effort is that the land remains at risk of liquefaction in future earthquakes. Therefore, effective engineering solutions must be developed to increase the resilience of homes and low-rise structures. To this end, a comprehensive series of full-scale field trials of multiple shallow ground improvement methods is underway. Initial field trials at one site involving five test panels of different ground improvements are presented. Each test panel and two unimproved natural soil test panels have been instrumented and characterized before shaking. A large mobile shaker, called T-Rex, has been used to perform an increasing sequence of dynamic horizontal loads to each test panel. The results are being analyzed but good and poor performance can already be differentiated.

1 INTRODUCTION

In 2010–2011, the city of Christchurch, New Zealand, was devastated by a series of powerful earthquakes, including six significant events. The most destructive of these events were the 4 September 2010 moment magnitude (M_W) 7.1 Darfield Earthquake and the 22 February 2011 M_W 6.2 Christchurch Earthquake. The proximity to the city, shallow depth, and fault mechanism of the Christchurch Earthquake generated the largest ground motions in the city, with horizontal Peak Ground Accelerations (PGAs) between 0.37 and 0.52 g recorded in the Central Business District (CBD). As discussed by Cubrinovski et al. (2012), the 2010–2011 earthquakes caused repeated liquefaction throughout the suburbs of Christchurch and the CBD. They noted that the liquefaction was very severe and widespread (covering nearly one third of the city area) and caused extensive damage to the built and natural environments. Interestingly, it was reported by some residents that liquefaction severity increased in subsequent events.

One critical problem facing Christchurch and the Canterbury region is rebuilding on land that remains at risk of liquefaction in future earthquakes. Bowden et al. (2012) have noted that "there is a need to develop simple, cost-effective engineering measures which increase the resilience of new houses to limit losses and disruption from future earthquakes." To this end, several field test trials of full-scale, shallow, ground improvement methods were performed in 2011 and 2012 to assess their effectiveness for use in improving residential foundation performance. The full-scale field trials used dynamic loading created by explosive charges (blasting) to induce liquefaction. As summarized in a report by Tonkin and Taylor (2013), the field trials generally "showed that undertaking shallow ground improvements increased site performance and decreased liquefaction vulnerability."

With information from the blast-loading field trials, Tonkin and Taylor decided in early 2013 to perform a comprehensive series of full-scale field trials of multiple types of shallow ground improvement methods. The field trials involved evaluating the ground improvements under two different loading conditions: (1) initially with a large mobile shaker, called T-Rex, on the ground surface and (2) then with explosive charges placed at depth. The purpose of the field trials was to determine if and which improvement methods achieve the objectives of inhibiting liquefaction triggering in the improved ground and are cost-effective measures. This knowledge is needed to develop foundation design solutions in areas outside the "Red Zone," the zone where structures will not be re-built, as well as for the repair of damaged land. This effort has been sanctioned by four New Zealand authorities (Earthquake Commission (EQC), Housing New Zealand (HNZ), Canterbury Earthquake Recovery Authority (CERA), and Ministry of Business Innovation and Employment (MBIE)) to be part of formulating the path forward in rebuilding the infrastructure in Christchurch and the Canterbury region.

In this paper, initial field trials using T-Rex at one of three test sites, Site 6, are presented. This work is a small part of a much larger testing program that began in early 2013 with a pre-liminary evaluation of seven potential test sites along the Avon River in the Christchurch area. From the seven sites, three sites were selected for the field trials based on their geotechnical characteristics, their similarity to future areas that will undergo ground improvements, and how readily and cost-effectively the candidate ground improvements could be installed and tested at each site. The information herein covers: (1) the four types of ground improvement methods that were investigated at Site 6, (2) installation of the sensor array at each test panel used to monitor ground motions and pore water pressure generation during shaking, (3) characterization of the unimproved and improved ground conditions at the test pads before shaking, (4) example records of pore water pressure generation and shear strain during shaking, and (5) preliminary observations of the effectiveness of each ground improvement method.

2 TESTING OF FULL-SCALE GROUND IMPROVEMENT METHODS AT SITE 6

2.1 *Selected ground improvement methods*

Four ground improvement methods were selected by Tonkin and Taylor for the full-scale field trials at Site 6. The improvement methods are shown in Figure 1. They are: (1) Rapid Impact Compaction (RIC), also known as dynamic compaction, Figure 1a, (2) Rammed Aggregate Piers (RAP), which consist of gravel columns, Figure 1b, (3) Low-Mobility Grouting (LMG) with a cement paste, also referred to as compaction grouting, Figure 1c, and (4) construction of a Single Row of horizontal Beams (SRB) or a Double Row of horizontal Beams (DRB) beneath existing residential structures via soil-cement mixing, Figure 1d. The RIC, RAP, and LMG methods were constructed as they would be used in the reconstruction effort; hence, the term "full-scale" field tests. Each improvement was designed to extend to a depth of about 4 m. All horizontal beams were: 0.5 m in diameter, made of moderate stiffness, fine-aggregate concrete, and positioned with a minimum of 0.5 m of soil cover over either the SRB or DRB. The beams were also constructed as expected in the reconstruction effort, so "full-scale" testing was performed. More information about the ground improvement methods can be found in van Ballegooy et al. (2014).

2.2 *Generalized site area and test panels*

Site 6 is located within 25 m of the Avon River in the suburb of Bexley. The plan dimensions of Site 6 are about 40 by 50 m. Seven test panels, each nominally 7 by 7 m, were distributed around the site. The seven test panels were the RIC, RAP, LMG, SRB, DRB, and two unimproved soil areas. Ample space existed between the test panels to allow construction and testing equipment to move around the site without disturbing the test panels.

The soil profile at each test panel was determined after completion of all in-situ penetration and small-strain seismic characterization tests and after completion of shaking with T-Rex.

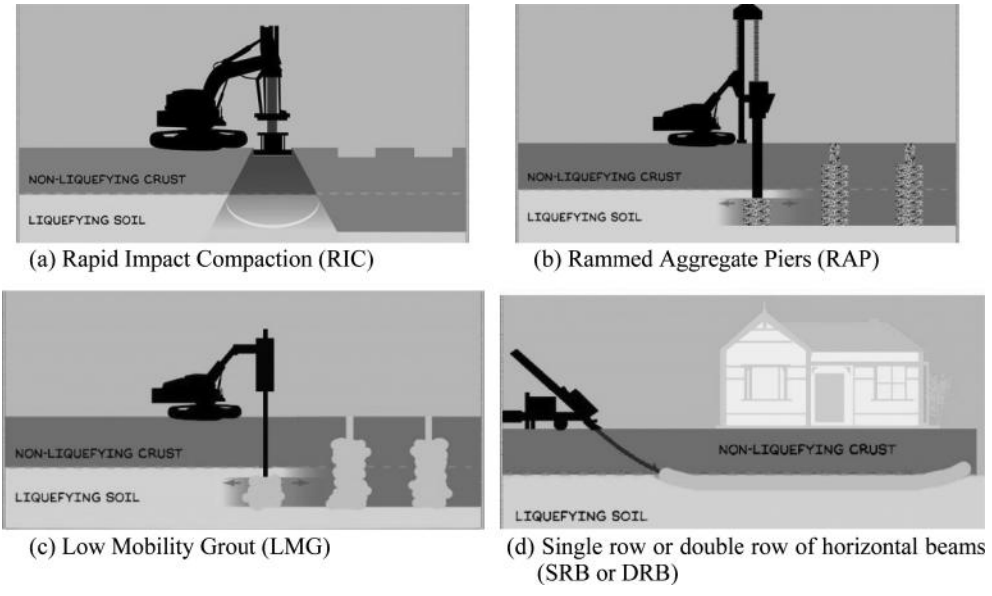

Figure 1. Illustration of the four ground improvement methods evaluated in the field trials at Site 6.

Each profile was determined by dewatering the test panel, trenching along the centerline to a depth that ranged between 2.5 to 3.5 m, logging and photographing the trench wall, and recovering disturbed samples for laboratory testing. The soil profile varied somewhat from panel to panel, with the number of layers ranging from 4 to 6. At this time, only a simplified, 5-layer profile with general soil descriptions is given. The simplified, 3-m deep profile is:

Layer 1—fine to medium, loose brown sand, trace of silt and some organics,
Layer 2—stiff, non-plastic sandy silt; brown and grey mottled,
Layer 3—stiff, non-plastic, grey silty sand; homogenous and dilatant,
Layer 4—grey silty fine sand; homogenous and loose; average depth to layer is 1 m, and
Layer 5—fine to medium loose grey sand, massive and organic odor.

2.3 *Instrumenting the test panels and shaking with T-Rex*

The relative effectiveness of the ground improvement methods to inhibit liquefaction triggering was evaluated by dynamically loading the ground and monitoring the movements and dynamic pore water pressures with embedded sensors. The sensor array was located in the soil between or around the ground improvements as discussed below. The preparation activities and field trials with T-Rex are discussed herein. T-Rex is operated by NEES@UTexas (http://nees.utexas.edu) and was used to: (1) install an array of embedded sensors at each test panel and (2) perform controlled shaking in a staged-loading sequence over a wide range of shaking levels. It is worth noting that the seven RAP columns shown in Figure 2c are located in the middle of a total of 22 columns in the overall test panel. Fewer sensors were installed in the SRB and DRB test panels and their locations were somewhat different due to obstructions created by the beams. The location of T-Rex during shaking at the RAP test panel is shown in a cross-sectional perspective in Figure 2d.

Before performing the shaking tests with T-Rex, the array of embedded instrumentation had to be constructed within each ground improvement and natural soil test panel. The plan dimension of the loading platen of T-Rex is 2.3 by 2.3 m so all embedded instrumentation was placed within the footprint area at each panel. Nearly all instrumentation was installed by the UTexas crew using the pushing mechanism at the rear of T-Rex (Figure 2a). The arrangement of the embedded instrumentation in the five test panels without horizontal

(a) Installing 2D velocity transducers (geophones) and pore pressure transducers (PPTs) with the hydraulic ram on the back of T-Rex.

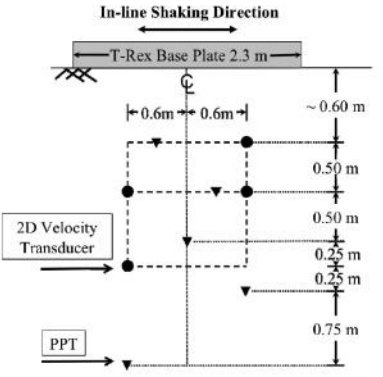

(b) Instrumentation array created in soil subsequently shaken by T-Rex; approximate locations projected on a vertical plane.

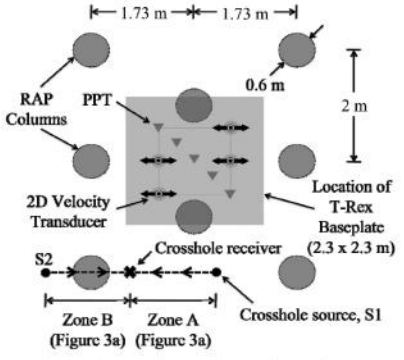

(c) Plan view of central portion of RAP test panel with locations of T-Rex baseplate and pre-shaking crosshole seismic tests.

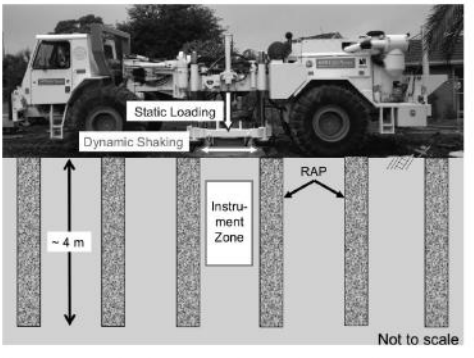

(d) Cross-sectional perspective of T-Rex in place to shake the RAP test panel. (Note: test panel is composed of a grid of 22 RAP columns.)

Figure 2. Example showing the installation of embedded sensors at the RAP test panel (a), the relative vertical and horizontal locations of the sensors beneath the T-Rex base plate ((b) and (c), respectively), and the location of T-Rex on the RAP test panel during shaking.

beams is shown in cross section in Figure 2b and in a plan in Figure 2c. The instrumentation is composed of four, 2D velocity transducers (also called 2D geophones) and five pore water pressure transducers (PPTs). As seen in Figure 2c, the instrumentation is located in the central portion of the test panel in the soil between the ground improvements.

3 INITIAL CHARACTERIZATION OF IMPROVED GROUND BEFORE SHAKING

3.1 *Motivation for small-strain crosshole seismic testing before shaking*

Crosshole seismic testing was used to determine profiles of constrained compression wave velocity, V_p, and shear wave velocity, V_s, to characterize the five test panels (RIC, RAP, LMG, SRB, and DRB) after construction and before shaking with T-Rex. The two natural soil panels were protected from the construction activities and were also characterized and used to represent unimproved ground at Site 6. The pre-shaking crosshole testing formed a critical part of the characterization of each test panel for three reasons. First, the V_s profiles of the unimproved (natural) ground were compared with the V_s profiles at each improvement

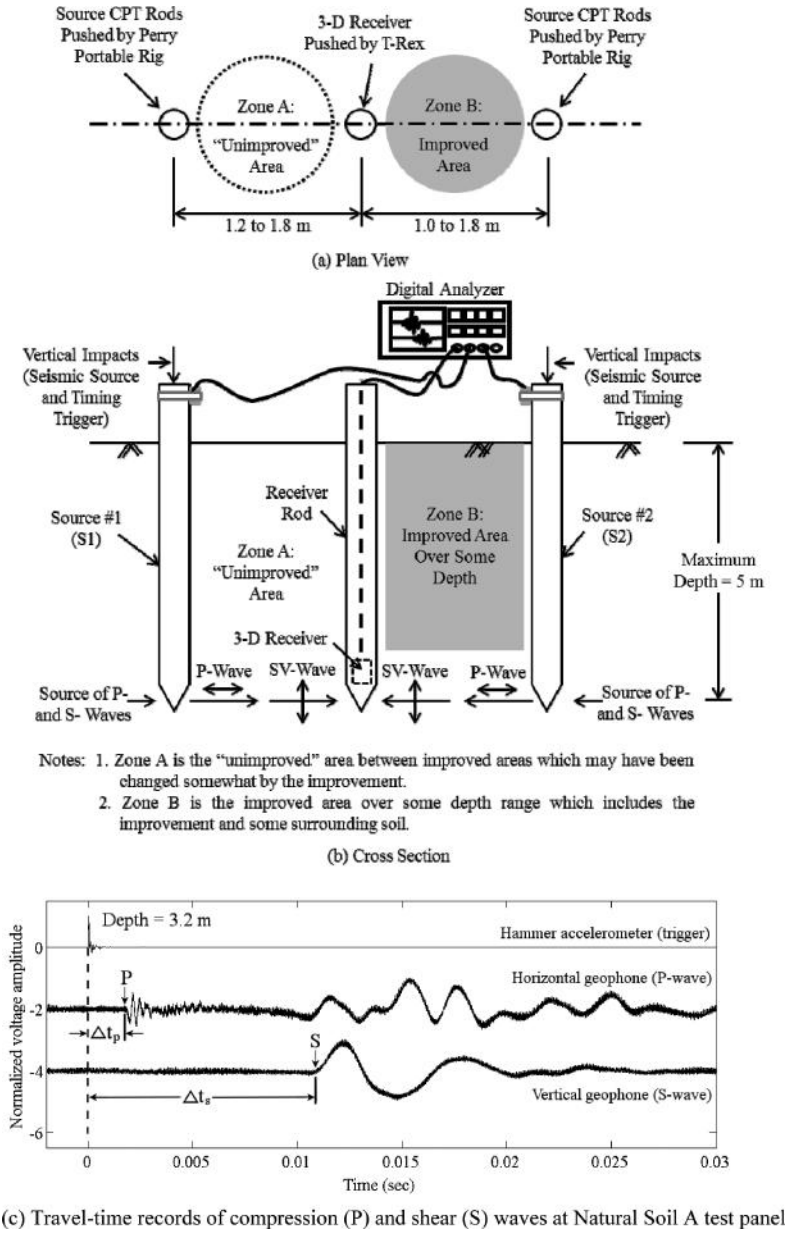

Figure 3. Schematic of generalized arrangement for small-strain crosshole seismic testing at Site 6 using two seismic sources and one, 3D receiver in the middle of the array (a) and (b); an example travel-time record showing P and S waveforms with wave arrivals and associated total travel times identified (c). (Note: Relative location of crosshole testing is shown in Figure 2c.)

panel to evaluate: (1) any changes in the soil in the "unimproved" zone between the improvements which occurred due to construction of the improvements (Zone A) and (2) the "average" stiffness of the improved zone which, in principle, included the improvement and some soil around the improvement (Zone B). (Note, the term "unimproved" in quotes is used to indicate the possibility that this zone has also been changed by construction of the adjacent improvements.) Both of these zones in the crosshole measurements are shown in Figures 2c (lower left area) and Figures 3a and 3b. Second, overburden-stress corrected V_s values were

used to estimate liquefaction triggering susceptibility using Andrus and Stokoe (2000). Third, the V_s values were also helpful in estimating the overall stiffness of each test panel. However, only changes due to construction of the ground improvement are discussed herein.

The V_p profiles were used for two purposes. First, and most importantly, the V_p values were used to determine at what depths the soil was either fully saturated or nearly saturated ($S_r \geq$ 98.5%) so that the dynamic pore pressure measurements would be correctly interpreted; that is, if $S_r < 98.5\%$, then little to no pore pressure generation would likely occur but it would not be misinterpreted as representing a denser, non-liquefiable soil. The use of S_r of 98.5% to separate behavior will be studied more in the future and is only used to begin the initial studies presented herein. Second, when the degree of saturation is low enough, Poisson's ratio of the soil skeleton will be calculated using the values of V_s and V_p.

3.2 *Crosshole seismic testing arrangement*

The generalized crosshole testing arrangement is illustrated in Figure 3. Crosshole testing involved pushing two dummy CPT cones, one on either end of a linear array (see Figures 3a and 3b). The cones and associated rods were used to transmit vertical impulses to the bottom of the rods where the cone tips acted as sources of both compression (P) and shear (S) waves in these small-strain tests. At the same time, a 3D velocity transducer was pushed in the center of the array using T-Rex. The 3D velocity transducer acted as the receiver for each seismic source. The spacing between each source and receiver ranged from about 1.0 to 1.8 m.

Crosshole testing began at a depth of 40 cm and continued in 20-cm increments, usually to a final depth of about 5 m. Both seismic source rods and the 3D receiver were pushed to the same depth for each measurement. The reason for the two measurement paths (source #1 (S1) to the receiver (R) and source #2 (S2) to the receiver (R)) is that one path was positioned within the "unimproved" soil zone between improvements while the second path was across the improved zone at the test panels with improvements. These two zones are shown in Figures 3a and 3b as Zones A and B for the "unimproved" and improved areas, respectively. At the two Natural Soil test panels, the same source-receiver arrangement was employed which resulted in each travel path occurring in unimproved, natural soil.

3.3 *Crosshole seismic testing results*

The P-wave velocities were measured to identify three different saturation conditions in the soil. The first condition is when the soil is saturated. This condition is represented by V_p in the range of about 1,450 to 1,700 m/s at Site 6. The second condition is when the soil is nearly saturated; that is, the degree of saturation is greater than about 98.5%. This condition is represented by V_p between 600 and 1,450 m/s. The third condition is when the soil is unsaturated and V_p is less than 600 m/s. In this case, the water in the soil skeleton can be assumed to have essentially no effect on V_p.

3.3.1 *P-wave velocities*

The V_p profiles at the test panels show that the depth at which 100% saturation occurs ranges from 1.3 to 2.8 m at all but the RIC and DRB panels (Figure 4a). At the RIC and DRB test panels, there is a perched, 100% saturation zone in the depth range of about 1.6 to 2.0 m. An unsaturated zone that is 0.5 to 1 m thick underlies this zone. Below 2.8 m, the soil at the RIC and DRB test panels is 100% saturated. As a note, identification of 100% saturation is based on a high–frequency signature in the P-wave record, as shown in Figure 3c. Such a record always gives $V_p \geq$ 1,450 m/s.

The average depth of the water table during seismic testing at each test panel was measured with a piezometer near the center of Site 6. The average water table depth during about 10 days of testing averaged about 0.48 m below the ground surface. The distance below the water table to the point at which 100% saturation was continuous (not perched) ranged from 0.82 to 2.32 m.

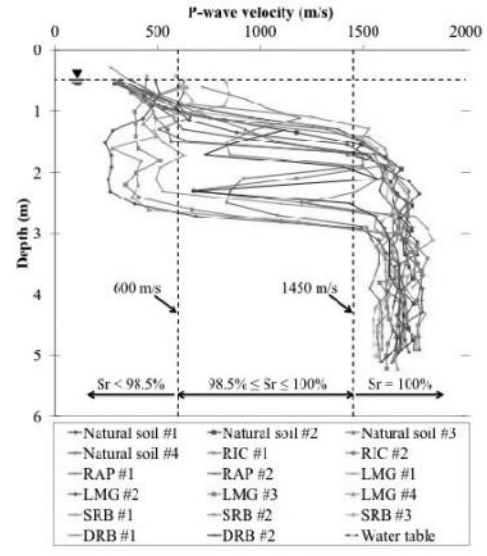

(a) P-wave velocity profiles of all test panels

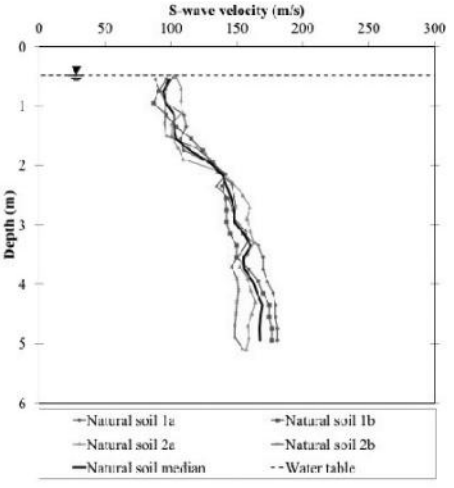

(b) S-wave velocity profiles of both unimproved natural soil test panels with median profile

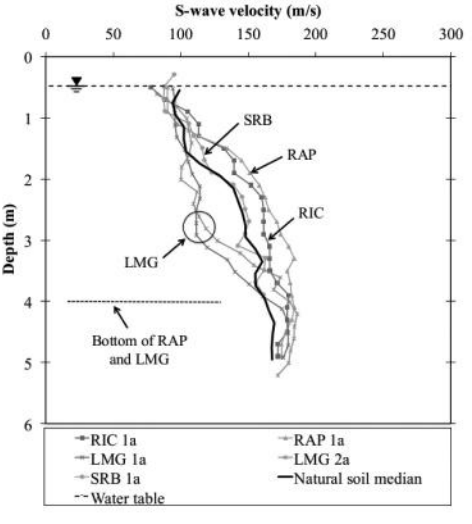

(c) S-wave velocity profiles of soil between improvements compared with median unimproved natural soil profile

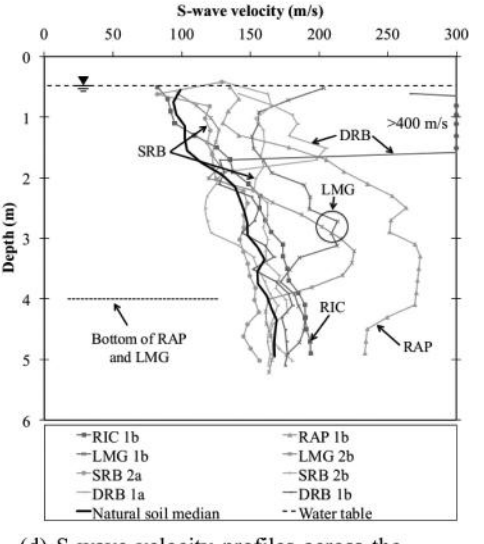

(d) S-wave velocity profiles across the improvements compared with median unimproved natural soil profile

Figure 4. Profiles of compression (P) and shear (S) wave velocities at the seven test panels at Site 6.

3.3.2 *S-wave velocities*

The V_s profiles at the two natural soil panels are shown in Figure 4b. A median profile is also shown and is used for comparison with V_s profiles at the five improvement test panels. The range in V_s values from the median average about ± 8%. This variation is quite reasonable considering the variability in material found during logging the trenches at the test panels.

The V_s profiles of the "unimproved" ground between the improvements are presented in Figure 4c and are compared with the median profile of the natural soil. No profile is shown for the DRB because measurements could not be performed between the beams. The profile shows the following. First, the soil between improvements at the RIC and RAP panels was stiffened over much of the profile, even extending below 4 m, the bottom of the RAP. Second, the "unimproved" zone between the single beams has the same V_s profile as the median profile of the Natural Soil test panels. Hence, installation of the SRB did not affect the surrounding soil. Finally, the low V_s values in the zone between the LMG columns show that zone was disturbed, mainly in the range of 2 to 3.5 m. This disturbance probably was caused by high injection pressures fracturing the shallow soil that was under low confining stress. Additional studies are warranted to understand more completely the reasons for the disturbance and possible modifications to improve this application of the method.

In Figure 4d, the V_s profiles of the improved zones at the RIC, RAP, LMG, SRB and DRB test panels are compared with the median V_s profile of the Natural Soil test panel. The RAP improved zone shows significant improvement over the total depth of 5 m and the most improvement of any method below 1.8 m. The LMG improved zone shows good improvement from 0.4 to 3.6 m. The RIC improved zone shows some improvement in the depth range of 1.4 to 4.8 m, an increase of almost 10% in V_s. This moderate increase in V_s at the RIC test panel did significantly change the liquefaction triggering performance as discussed below. The SRB test panel showed some increases in V_s at shallow depths as did the DRB test panel. The increases in V_s are likely due to averaging of velocities of soil and portions of the beams(s). Below the beams, the DRB test panel even showed a decrease which has not been found at the other two test sites under evaluation.

4 T-REX SHAKE TESTING RESULTS

At each test panel, the dynamic loading from T-Rex was: (1) horizontally oriented, (2) applied at 10 Hz for 100 cycles (10 seconds of shaking), and (3) performed in stages, going from the lowest level (± 13 kN) to the highest level (± 107 or ± 133 kN), normally in five stages. The PPT output is expressed as r_u, the excess pore water pressure (u) divided by the initial vertical effective stress which includes vertical loading from T-Rex. The shear strain at each PPT was

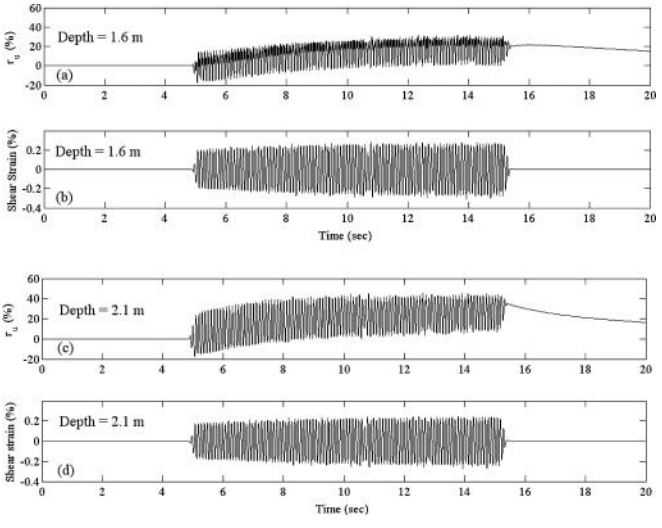

Figure 6. Variations of pore water pressure ratio and shear strain with time determined from data recorded at the Natural Soil test panel during T-Rex shaking at 10 Hz for 10 seconds; the final loading stage (± 107 kN) and PPT depths of 1.6 and 2.1 m.

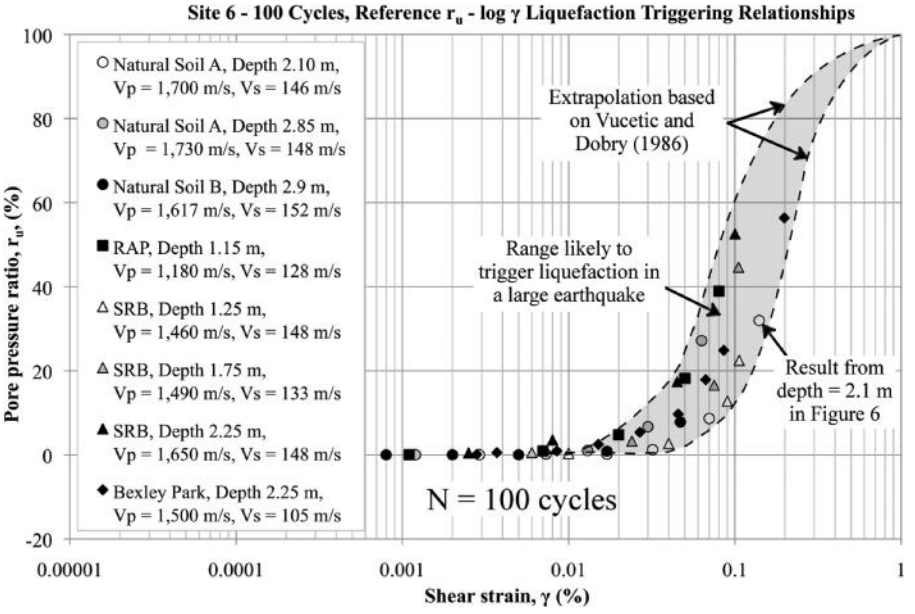

Figure 7. Compilation of results from the 7 test panels that indicated soil liquefaction would be triggered in a large earthquake.

estimated using the displacement-based shear strain calculation method as discussed by Cox (2009). In Figure 6, examples are shown of derived time histories for pore water pressure ratio and shear strain at two depths, 1.6 m and 2.1 m, in the Natural Soil A test panel for the highest shaking level, 107 kN. These results and other similar measurements were used to evaluate r_u–logγ relationships at all PPTs in the test panels.

4.1 *Pore water pressure ratio versus shear strain*

In this initial work, which is still ongoing, the thrust of the T-Rex shaking tests is directed towards evaluating the r_u–logγ relationships at selected numbers of loading cycles (N) for each test panel. All data have been reviewed and a generalized range in the r_u–logγ relationships was developed for natural soils and soils at the improvement test panels that are 100% saturated and are likely to have liquefaction triggered in a "large" earthquake. At this time, the liquefaction-triggering has only been developed for $N = 100$ cycles. The range in r_u–logγ relationships is shown by the shaded zone in Figure 7. Data from Site 6 as well as Bexley Park (another site tested by the UTexas team) that were used to develop the range are shown in the legend in Figure 7. All data exhibit a reasonable trend in the r_u–logγ relationships as follows. At low shear strains, strains below 0.01%, no excess pore water pressure is generated ($r_u = 0$). As shear strain increases above some threshold, in the strain range of 0.01 to 0.04%, r_u begins to increase with increasing strain. The varying strain threshold is likely related to differences in material types. Clearly, the trend in the r_u–logγ relationships indicated the potential for liquefaction triggering in a large earthquake.

5 CONCLUSIONS

Crosshole testing and T-Rex shaking were successfully completed at seven test panels at Site 6. This field work provided strong evidence regarding soil liquefaction susceptibility of the natural soil as well as soil with ground improvements. The average water table depth at the seven test panels was approximately 0.5 m. Measurements of V_p showed that the point

at which 100% saturation was continuous (not perched) ranged from depths of about 0.8 to 2.3 m below the water table. Relative changes in the value of V_s between different ground conditions (native soil, soil between "improved" zones and soil within improved zones) were used to identify zones of improvement, zones of disturbance, and zones of little to no change.

Shaking with T-Rex generated substantial pore water pressures at depth. The results from the shaking tests that are presented in this paper deal mainly with soils with S_r = 100%. The natural ground test panels exhibited significant variability in the pore pressure ratio versus log shear strain (r_u–logγ) relationships, with several layers predicted to have liquefaction triggered in a large earthquake and other layers predicted not to trigger. As evaluated these tests, the ground improvement methods that inhibited liquefaction triggering the most were RIC, RAP, and DRB; the ground improvement methods that exhibited poor performance to inhibit liquefaction triggering were LMG and SRB. However, additional analyses are still underway.

The V_p profiling revealed that the crust (depth ~0.65 m) was unsaturated. For the unsaturated crust with V_p less than about 600 m/s, T-Rex shaking tests showed that liquefaction triggering is unlikely, even in a large earthquake. T-Rex shaking trials showed a wide range in the r_u–logγ relationship in the top 3 m that is likely due to differences in soil type, density, fabric, and/or degree of saturation.

ACKNOWLEDGEMENTS

Financial support for this study was provided through the National Science Foundation under grants from the RAPID program (CMMI-0343524), NEES@UTexas (CMMI-0927178), and the Graduate Research Fellowship Program (DGE-1110007). Other significant financial support was received from the New Zealand Earthquake Commission (EQC). This support is gratefully acknowledged. A special thanks is extended to the engineers and staff at Tonkin and Taylor Ltd. and to Prof. Misko Cubrinovski at the Univ. of Canterbury for their support throughout the project. Thanks also goes to graduate students and staff at the Univ. of Texas at Austin including Andrew Keene, Andrew Stolte, Mr. Cecil Hoffpauir, Mr. Andy Valentine, and Mr. Robert Kent.

REFERENCES

Andrus, D.R. and Stokoe, K.H., II. 2000. Liquefaction Resistance of Soils from Shear-Wave Velocity. ASCE, *Journal of Geotechnical and Geoenvironmental Engineering*, Vol. 126, No. 11, pp. 1015–1025.

Bowen, H.J., Millar, P.J., Traylen, N.J. 2012. Full Scale Testing of Ground Remediation Options for Residential Property Repair Following the Canterbury Earthquakes. in *New Zealand Society for Earthquake Engineering Annual Conference*. April 2012 Christchuch, New Zealand. 7 pp.

Cox, B.R., Stokoe, K.H., II, Rathje, E.M. 2009. An In-Situ Test Method for Evaluating the Coupled Pore Pressure Generation and Nonlinear Shear Modulus Behavior of Liquefiable Soils. *ASTM Geotechnical Testing Journal*. Vol. 32, No. 1, 11–21 pp.

Cubrinovski, M., Henderson, D., Bradley, B.A. 2012. Liquefaction Impacts in Residential Areas in the 2010–2011 Christchurch Earthquakes. *One Year after 2011 Great East Japan Earthquake: International Symp on Engrg. Lessons Learned from the Giant Earthquake,* March, 2012. Japan. 14 pp.

Tonkin and Taylor Ltd. 2013. *Workstream—Ground Improvement Testing Trials*. Mr. John Leeves, T&T Ref: 52020.0200, April, 29 pgs.

Van Ballegooy, S. and others. 2014. Christchurch Ground Improvement Trials Report, in preparation.

Vucetic, M. and Dobry, R. 1986. Pore Pressure Build Up and Liquefaction at Level Sandy Sites During Earthquakes. *Research Rpt*., Depart. of Civil Engrg., Rensselaer Polytechnic Institute, Troy, New York.

Soil Liquefaction during Recent Large-Scale Earthquakes – Orense, Towhata & Chouw (Eds)

The design of open grid Deep Soil Mixing (DSM) foundation on earthquake related projects

A. O'Sullivan
Hiway Geotechnical, Auckland, New Zealand

S. Terzaghi
Arup, Sydney, Australia

R.P. Orense
Department of Civil and Environmental Engineering, University of Auckland, New Zealand

ABSTRACT: The demand for economic forms of ground improvement in seismically active, urban areas continues to increase as cities expand. This is especially so in areas where the underlying soils are prone to liquefaction. While current design methods for Deep Soil Mixing (DSM) and other forms of ground improvement such as stone columns and vibro-replacement take some account of the increase in overall shear stiffness of the improved ground, they do not adequately take the significant installation effects on the surrounding soil into account. As a result, more efficient ground improvement layouts cannot be justified during detailed design phase. This paper will describe the underlying theory and validation of an open grid DSM foundation arrangement designed to improve the performance of the ground under seismic loading. A layout using 1 m diameter DSM columns on an open triangular grid at 3 m spacing will be analysed. The results demonstrate that, when the confinement effects of the DSM installation are taken into account, the following changes in the in-situ stress regime are observed: (a) the value of K_0 at the mid-point between the individual DSM columns increases from 0.5 to around 0.8 in loose sand, (b) the material between the DSM columns becomes over-consolidated which leads to an increase in principal stresses at failure and (c) the in-situ shear stress is dramatically reduced. These result in an increase in Cyclic Resistance Ratio (*CRR*) for the surrounding soils of around 30%. The analysis ignores the additional benefits of increased shear stiffness of the DSM columns. The theory is validated through numerical simulation of the installation as well as field measurements taken both pre- and post- DSM installation.

1 INTRODUCTION

Deep Soil Mixing (DSM) has been used successfully for over 50 years in a number of key areas of geotechnical engineering, most notably for consolidation related problems. In more recent times, it has begun to gain wider acceptance in the area of liquefaction/lateral spreading mitigation. The general practice, in this application, is to install DSM columns as a series of overlapping columns in a cellular arrangement, with the dimensions of each cell typically being in the order of 5 to 8 times the column diameter. While this is proven to be effective, this arrangement can be costly and may not always represent the optimum design for a project.

When analysing cellular DSM configurations, a number of considerations need to be carefully assessed. One such issue is that at a spacing beyond 5–6 times the DSM column diameter, the influence of the DSM columns within the soil mass dramatically reduces to a point where the behaviour of the surrounding soil is no longer influenced by the presence of the DSM columns. As triggering of liquefaction may not be inhibited in the surrounding soils, the shear capacity of the individual cell walls needs to be analysed for a scenario where the soil no longer provides any lateral restraint to the DSM columns under seismic excitation. Another issue is that the

stress (and resultant strain) distribution is highly uneven within the cells; a scenario which may result in the development of differential settlements across the cells.

The theory will be applied to the widely used, simplified method for the evaluation of liquefaction triggering developed by the NCEER/NSF group (Youd TL, 2001). The installation of individual DSM columns in an open grid arrangement has two main functions. The first is that the DSM columns provide high lateral confinement to the surrounding soil. This is achieved through the installation process where a significant net volume of grout (typically 20–30% of the total column volume in the field) is injected into the soil mass, resulting in lateral volumetric strains to the surrounding soils. This is sufficient to improve lateral confinement but generally not sufficient to rotate principal stresses. The second is to provide significant increase in shear capacity through the introduction of closely spaced, high modulus elements. This paper will deal with the confinement issue only. The shear transfer section will not be addressed in this paper but would offer significant additional benefits to the *CRR* of the treated soil block. In the following sections, the underlying theory behind the confinement philosophy, as well as validation through numerical modeling and field testing will be described.

2 UNDERLYING THEORY

The introduction of a lateral volumetric strain element, through the installation process, increases the value of σ'_3 in the soil mass between the DSM columns.

This translates to a significant increase in the earth pressure coefficient (K_0) in the soil between the DSM columns from, typically, 0.5 to 0.8. This effect is illustrated in τ/σ' space in Figures 1a and 1b below, where the Mohr circle for in-situ stress is shown for the pre- and post-DSM installation phase in Figure 1a, where the in-situ stress circle decreases from σ'^{i}_3 and σ'^{i}_1 (the initial minimum and maximum principle stresses) prior to DSM installation to their new, post-installation stress positions: σ'^{DSM}_3 and σ'^{i}_1. The equivalent Mohr circles at failure stress are shown in Figure 1b. Here, the yield stress circle increases from σ'^{if}_3 and σ'^{if}_1 (the initial minimum and maximum principle stresses at yield) prior to DSM installation to their new, post-installation yield stress positions: σ'^{DSMf}_3 and σ'^{DSMf}_1.

The reduction in the size of the in-situ Mohr circle in Figure 1a signifies that the initial stress state (relative shear stress) of the soil is reduced as a direct result of the DSM column installation. In addition, in Figure 1b, we observe that the undrained shear strength of the soil increases from $(\sigma'^{if}_1 - \sigma'^{if}_3)/2$ to $(\sigma'^{DSMf}_1 - \sigma'^{DSMf}_3)/2$.

The implication, from a liquefaction triggering perspective, is that the Cyclic Resistance Ratio (*CRR*) of the soil increases from CRR_i (the initial value based on initial K_0 value [K_{oi}]) to CRR_{DSM} (the revised, higher value of K_0 [K_{0DSM}] following DSM installation). Using the guidance provided by Salgado et al. (1997) for estimating the revised CRR value, based on values of K_0 exceeding the normally consolidated value, $K_{0\,NC}$, we obtain the following estimate for the increase in *CRR* following DSM installation:

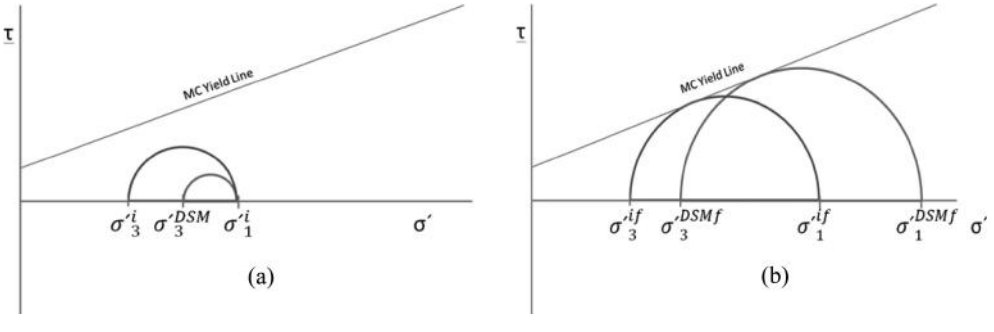

Figure 1. (a) Effect of additional confinement as a result of DSM installation on Mohr Circles at in-situ stress for pre- and post-DSM installation; and (b) equivalent Mohr Circles at failure.

$$CRR_{DSM} = CRR_i \, x \, \frac{(1+2K_{0DSM})}{(1+2K_{0i})} \quad (1)$$

3 VERIFICATION OF DESIGN PHILOSOPHY—INCREASE IN CONFINEMENT

In order to demonstrate that the proposed DSM layout will provide sufficient confinement to the group, a simple axi-symmetric model was entered into the finite element programme Plaxis to demonstrate the confinement effects. For the analysis, the Hardening Soil Small strain (HSsmall) model was used to capture the behaviour of the sand layer. The model in Figures 2 and 3 below show the typical arrangement of a group of DSM columns and their representation in an axisymmetric model.

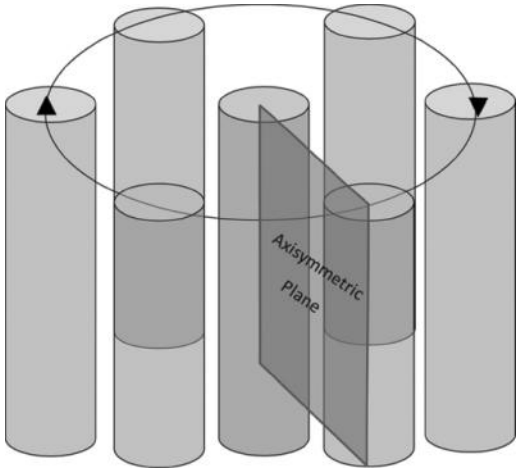

Figure 2. A 3-D Presentation of the DSM columns at 3 times the diameter spacing showing the axi-symmetric plane represented in Figure 3 below.

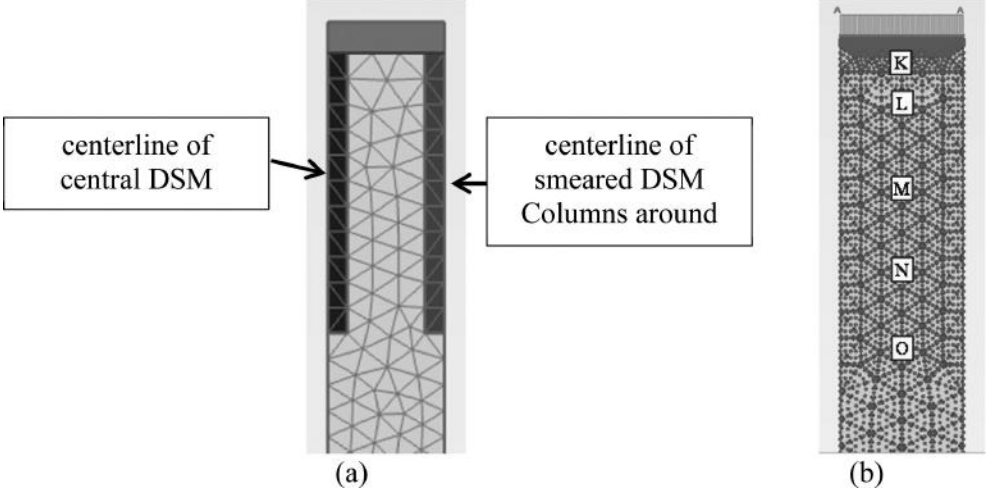

Figure 3. (a) Axi-symmetric model of unit cell analysis; and (b) Location of Stress points for the FE programme.

The model shows a typical unit cell of DSM columns in a triangular arrangement, with one of the DSM columns at the centre of the model and 4 smeared columns around the perimeter. The DSM columns were modelled to a depth of 8 m, with the total depth of liquefiable soils extending to 20 m. The soil between the DSM columns was modelled as a loose sand (shear modulus at 50% of peak strength, $E_{50} = 8$ MPa; apparent cohesion, $c' = 2$ kPa; angle of internal friction, $\theta' = 30°$; dilation angle, $\psi = -1°$). A monotonic undrained triaxial simulation of the material was carried out using the virtual lab facility in Plaxis. The results of this simulation are shown in Figure 4 and reflect the characteristic behaviour associated with liquefiable material.

The DSM columns are modelled as 1 m diameter at 3 m c/c in a triangular arrangement. This is equivalent to a replacement ratio of around 20%. The DSM columns were modelled as a highly cemented soil with the following soil parameters: $E_{50} = 450$ MPa; $c' = 250$ kPa; $\theta' = 30°$. As the DSM elements were modeled as soil, this minimized any potential issues regarding soil/structure interaction.

The following stages were modelled:

1. Initial gravity stage
2. Installation of Central DSM column ($\varepsilon_v = 8\%$)
3. Installation of perimeter DSM columns ($\varepsilon_v = 2\%$)
4. Curing of DSM columns
5. No DSM installed (CONTROL)

For the DSM column installation (stages (2) and (3) above), the soil parameters for the DSM column elements were reduced to those approximating a wet grout ($E_{50} = 250$ kPa; $c' = 1$ kPa; $\theta' = 12°$) and a volumetric strain applied to these elements. The isotropic volumetric strain was set to 8% for the central column and 2% for the smeared surrounding columns. The effect of the volumetric strains introduced in stage (2) and (3) above are shown in Figures 5a and 5b respectively. (Note that these are shown on exaggerated scales). The volumetric strain was used to model the net injection of grout into the soil. For the subsequent model stages (5 and 6), the full strength DSM column parameters were used in the modelling with no further application of volumetric strains.

A series of stress points were taken at the mid-point between the DSM columns at various depths (0.8 m, 2 m, 4, 6 m and 8 m) and the Cyclic Stress Ratio (CSR) examined pre- and post-installation of the DSM columns. These points are shown in Figure 3b above (points K, L, M, N & O). The results of the analysis are provided below. Figure 6 reflects the confinement theory described above, where the in-situ shear stress is reduced following installation of the DSM columns.

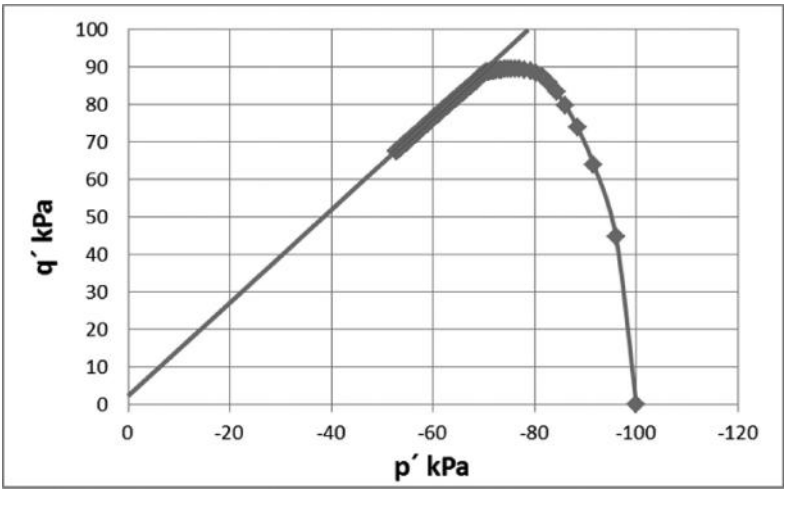

Figure 4. Simulation of monotonic undrained shearing of surrounding sand layer in model (*note that compression is negative in Plaxis).

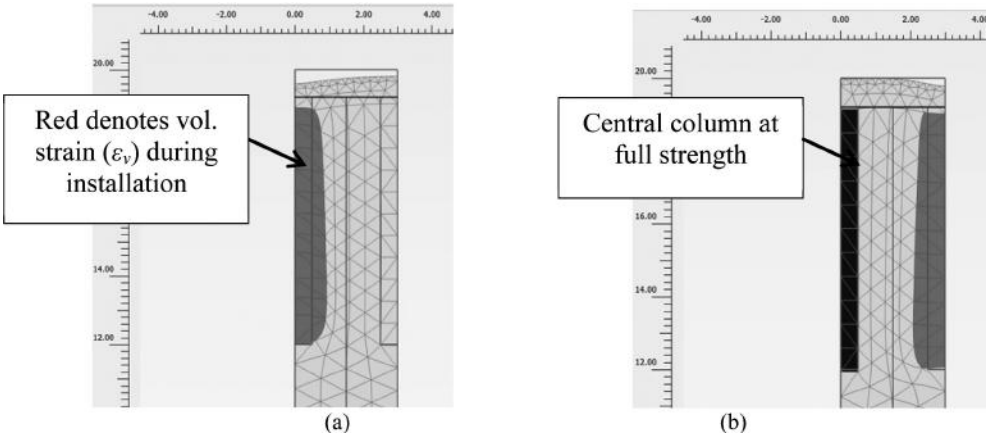

Figure 5. FE model showing effect of: (a) central DSM column. (FE Model Stage 2); and (b) smeared perimeter DSM columns (FE Model Stage 3).

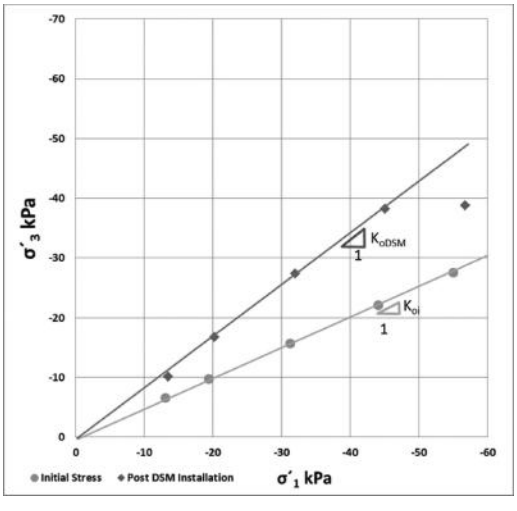

Figure 6. Confining maximum (σ'_1) and minimum (σ'_3) principal stresses at mid-point between DSM columns pre- and post-installation.

When the results shown in Figure 6 are plotted in σ'/τ space, the results clearly show the lower in-situ stress state of the soil post-installation. Figure 7 reflects the different and lower shear stress, but higher σ'_3 three and mean stress post-DSM installation.

4 APPLICATION TO LIQUEFACTION TRIGGERING ASSESSMENT

The analysis so far has demonstrated that the in-situ static shear stress (τ_{mob}) post-DSM installation is significantly reduced and that the in-situ static shear strength (τ_{max}) post-DSM installation of the material between the DSM columns has increased.

In order to assess the impact which the installation process has on the liquefaction triggering potential, the *CSR* demand ($CSR * \sigma'_v$) was calculated for the initial pre-DSM installation stress state of the soil and this was compared to the theoretical CSR demand post-DSM installation. Alarcon-Guzman et al. (1988) noted that "when a sand specimen is subjected to

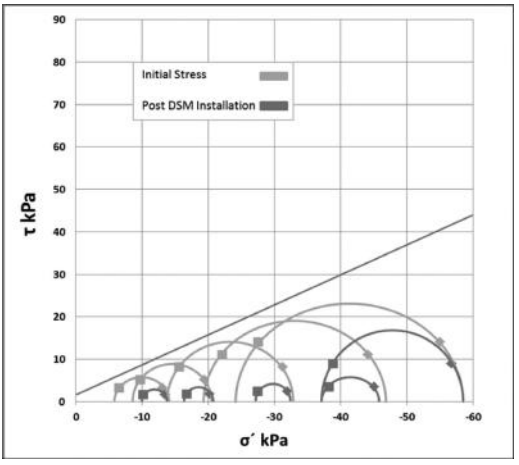

Figure 7. Comparison of shear stress (τ) versus effective stress (σ') prior to installation (initial stress) and post-DSM installation.

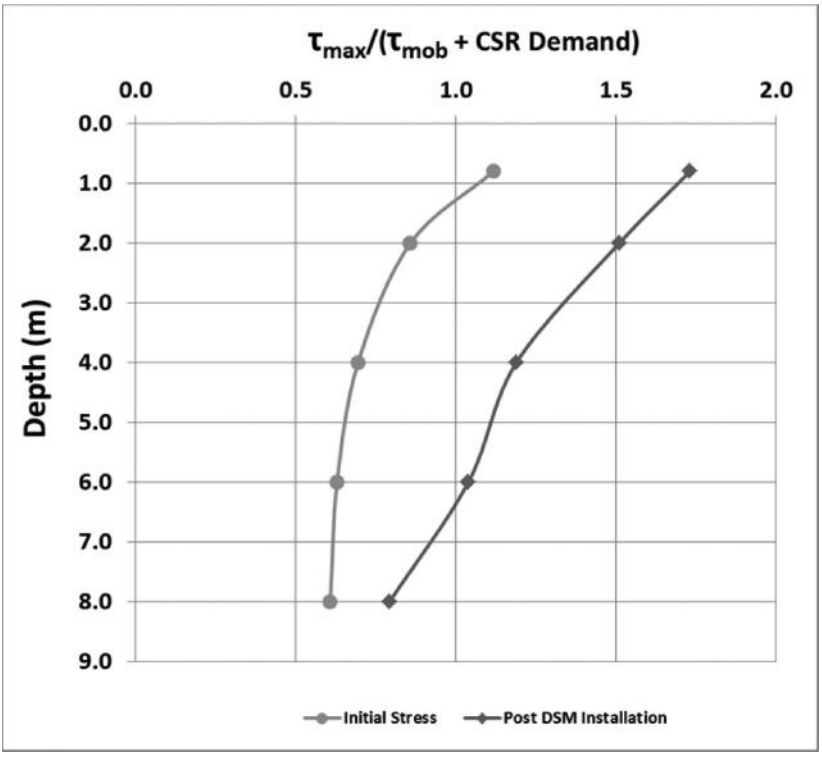

Figure 8. Comparison in τ_{max} / [τ_{mob}+(CSR*σ'_v)] against depth for initial stress and Post-DSM installation stress.

cyclic shear stress amplitudes smaller than the undrained steady-state strength, the stress path eventually moves from the contractive to the dilative region in the state diagram as a result of pore pressure buildup, but it cannot reach the CSR line for that particular void ratio." Therefore from the numerical model we obtain the following values for τ_{max} / [τ_{mob} + (CSR*σ'_v)] at various depths mid-point between the DSM columns. The results are shown in Figure 8 below. For these results a pga = 0.3 g was assumed.

5 FIELD VALIDATION

In order to verify the results, in-situ testing using a seismic dilatometer (sDMT) was carried out on a DSM project in Hamilton, New Zealand. The soil types ranged from SAND to sandy SILT. The layout of the DSM columns is shown in Figure 9 below along with the test locations. The DSM columns were 750 mm in diameter and were installed at 2.4 m c/c in a triangular grid pattern. This equates to a replacement ratio of approximately 20%. Three test locations were taken: 300, 600 and 900 mm from the edge of one of the DSM columns and sDMT tests performed prior to (initial stress) and approximately one month following installation of the DSM columns.

The results of the in-situ sDMT K_0 profile are shown in Figure 11 for the initial stress state (Before) and post-DSM installation (After). This is compared with the increase predicted by

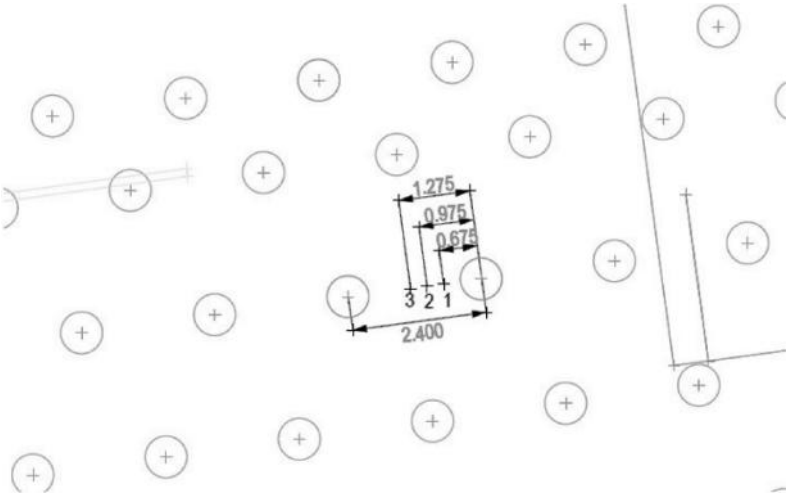

Figure 9. Layout plan of sDMT test locations relative to DSM columns at Wairere Drive.

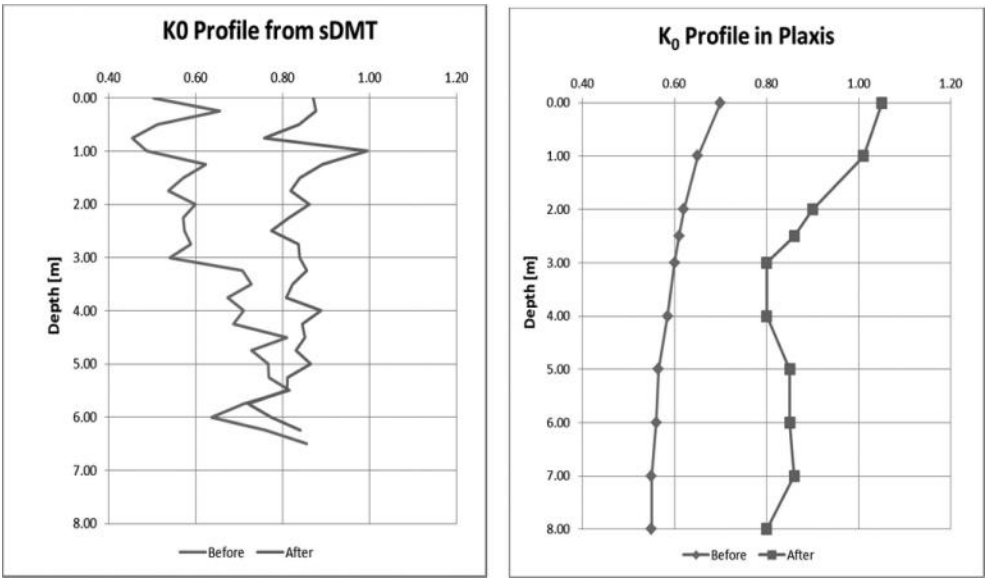

Figure 10. K_0 profile measured and predicted at mid-point between DSM columns.

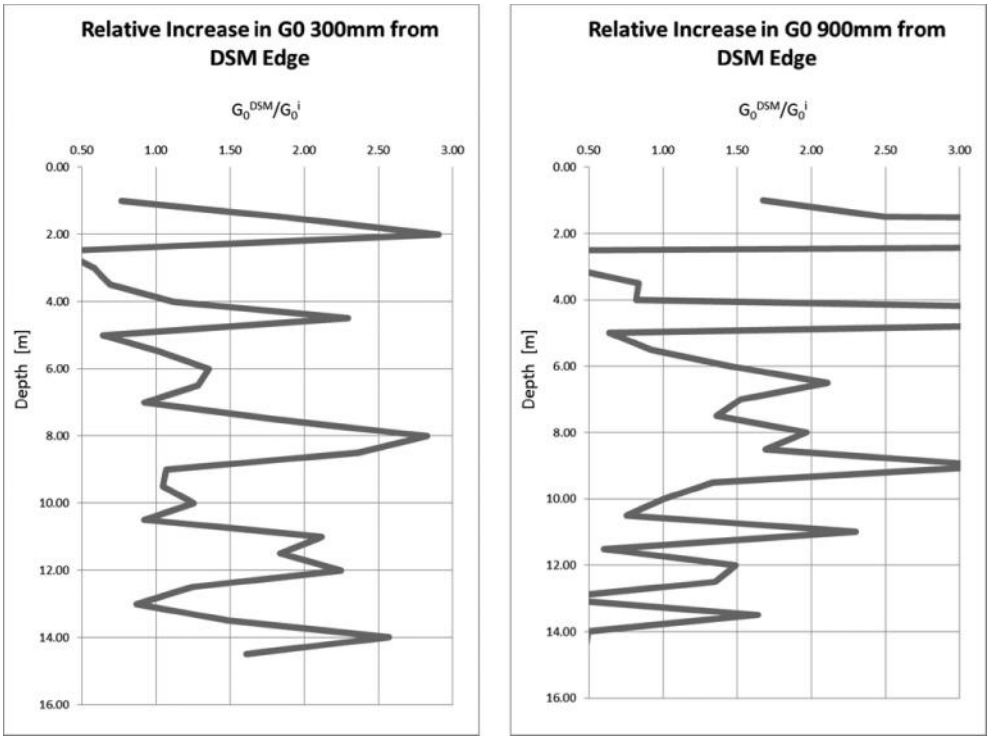

Figure 11. Relative increase in G_0 profile measured at 300 mm and 900 mm from edge of DSM column.

the Plaxis model for the same location. Note the wide scatter in G_0 values in Figure 11 is due to the highly layered nature of the soil profile at the site. In addition, shear wave velocity testing was carried out by Ground Investigations Ltd and the results verified by Prof. L. Marchetti in Italy. The results of the shear wave velocity testing are shown in Figure 12 below in terms of a ratio of G_0^i (the initial value of G_0) and G_0^{DSM} (the post-DSM installation value of G_0). As can be seen, the soil experienced a dramatic increase in G_0 (typically between 50–200% increase) at the mid-point between the DSM columns. In addition, the K_0 increased from typically 0.6 to 0.85 (40% increase), which is consistent with the prediction in the model.

6 DISCUSSION AND CONCLUSIONS

While a large number of papers exist in the literature, which address the issue of shear transfer between ground improvement elements, such as stone columns and DSM columns, and the surrounding soils, the research done on the installation effects of these elements in terms of confinement is much more limited.

The results of the analysis indicate that the effects of confinement induced by installation effects are highly important in understanding the response of the ground post-improvement to seismic excitation, particularly when simplified *CSR*/*CRR* comparisons are to be used as part of the liquefaction triggering potential. In addition, the field validation has demonstrated that the numerical modelling of the installation effects is valid and can be relied upon to provide a reliable indication of the post-installation behaviour of the soil surrounding the ground improvement elements. The main result of the analysis is that the installation of the ground improvement elements (in this case, the DSM columns) dramatically increases the lateral confining stress (σ'_3). As a result, the relative shear stress in the soil surrounding the DSM columns is dramatically reduced and, by extension, its distance

to the yield surface. This translates into an increase in the factor of safety against liquefaction triggering.

This effect cannot be captured in simplified elastic perfectly plastic (Mohr-Coulomb type) models as the installation effects will result in a purely elastic stress path. The analysis can demonstrate that the confinement effects alone may result in an increase in resistance against liquefaction triggering of up to 30%. While the results in this case indicate that liquefaction triggering was not inhibited over the full depth of the DSM columns, the anticipated near surface settlements are expected to reduce dramatically as a result of the installation effects. When the additional benefits of the increase in shear stiffness are taken into account any surface settlements would be expected to reduce even more.

REFERENCES

Alarcon-Guzman, A., Leonards, G., and Chameau, J. 1998. Undrained Monotonic and Cyclic Strength of Sands. *Geotech and Geoenv. Eng*, 1988 114: 1098–1109.

Salgado R., Boulanger, R., and Mitchell, J. 1997. Lateral Stress Effects on CPT liquefaction Resistance Correlations. *J. Geotech and Geoenv. Eng*, 726–735.

Seed H B and Idriss, I.M. 1971. Simplified Procedures for Evaluating Soil Liquefaction Potential. *J. Geotech. Engrg. Div ASCE 97(9)*, 1249–1273.

Youd, T., Idriss, I., Andrus, R., Arango, I., Castro, G., Christian, J., Dobry, R., Finn, W., Harder, L., Jr., Hynes, M., Ishihara, K., Koester, J., Liao, S., Marcuson, W., III, Martin, G., Mitchell, J., Moriwaki, Y., Power, M., Robertson, P., Seed, R., and Stokoe, K., II. 2001. Liquefaction Resistance of Soils: Summary Report From The 1996 NCEER and 1998 NCEER/NSF Workshops on Evaluation of Liquefaction Resistance of Soils . *J Geotech and Geoenv Eng*, 817–833.

This page intentionally left blank

Soil Liquefaction during Recent Large-Scale Earthquakes – Orense, Towhata & Chouw (Eds)
© 2014 Taylor & Francis Group, London, ISBN 978-1-138-02643-8

Liquefaction mitigation using secant piles wall under a large water tank

E. Sáez & C. Ledezma
Department of Structural and Geotechnical Engineering, Pontificia Universidad Católica de Chile, Santiago, Chile

ABSTRACT: Two-dimensional and three-dimensional numerical models were developed to evaluate the effectiveness of a foundation perimeter wall on the mitigation of the effects of liquefaction in a 64 m diameter, reinforced-concrete water tank. The response of the tank was evaluated in terms of differential settlements induced by an actual earthquake recording by comparing the situations with and without this mitigation strategy, consisting of 20 m-long, 1 m-diameter secant piles wall. Although the mitigation strategy did not significantly reduce the liquefaction-induced settlements, it enforced a relatively homogeneous distribution of these settlements leading to less structural damage.

1 INTRODUCTION

The effectiveness of the proposed solution to mitigate the effects of liquefaction was evaluated using both two-dimensional plane-strain as well as three-dimensional finite element models of the main cross-section of the tank. These models were used to assess how the installation of the rigid impermeable barriers (secant piles wall) might impact the effects of liquefaction on the tank response.

The analyses included the following general steps:

- Definition of the model geometry based on topographic and stratigraphic information provided by the owner, and construction of a finite element mesh adapted to the different stages of construction and analyses considered in this study.
- Calibration of available constitutive models of the various materials involved in the model, consistent with the provided geotechnical data.
- Static Analysis: This stage involved a nonlinear stress-strain simulation of the rigid screen's construction process to obtain the initial stress state of the model. This stress state defines the initial condition for the dynamic analysis that follows.
- Dynamic analysis: Non-linear time-history simulations were run to study the effect of the proposed solution on the dynamic forces and co-seismic settlements acting on the tank. The selected input ground motion was recorded during the M7.8 March 3, 1985, Chile earthquake at the UTFSM station, and it has a high damage potential as defined using Arias intensity. The selected ground motion was recorded on outcropping bedrock, and it was properly deconvoluted to the base of the numerical model.

Two analyses were conducted:

- Two-dimensional seismic analysis of the tank completely filled with water, considering a sloped stratification of the liquefiable layer.
- Three-dimensional analysis of the tank filled with 9 m of water, and a sloped stratification of the liquefiable layer.

Each of the above analyses were performed both for the original situation (without the screens or "inclusions") and for the situation with the screens installed.

The behavior of the liquefiable soil was modeled using a set of parameters from the authors' materials library, corresponding to a liquefiable loose sand (void ratio of ~1.2), with SPT N_1 values in the range of 10 to 20 blows/foot. A different set of properties was used to model the dense sand layer.

In summary, two 2D static analyses were performed: full tank, sloping liquefiable layer, with and without the rigid inclusions. In addition, two 3D static analyses were done: 9 m of water inside the tank, sloping liquefiable layer, with and without the rigid inclusions. Each static analysis was followed by its corresponding dynamic analysis using the N70E un-scaled component of the March 3, 1985 M7.8 Chile earthquake recorded at the UTFSM station. The 3D seismic analysis was performed applying the earthquake along two orthogonal directions, which were the most critical ones with respect to the stratigraphy.

2 GEOMETRY AND FINITE ELEMENT MESH DEFINITION

Based on the information provided by the owner, a 2D finite element model, representative of a unit strip through the center of the tank (Figure 1), was developed. A level ground condition was assumed, and the foundation depth was set at 2.3 m. The phreatic level was assumed at that same depth. Next, the soil profile was discretized into two homogenous horizontal soil layers: a layer of loose sand of approximately 17 m in thickness, and a layer of dense sand 20 m thick, underlain by competent bedrock with a shear wave velocity of 2000 m/s (Figure 2).

The soil profile was discretized into two homogenous sloping soils layers. Based on the results of four SPT tests it was established that the thickness of the liquefiable layer was not uniform, but it increased towards the zone where the secondary clarifier was located.

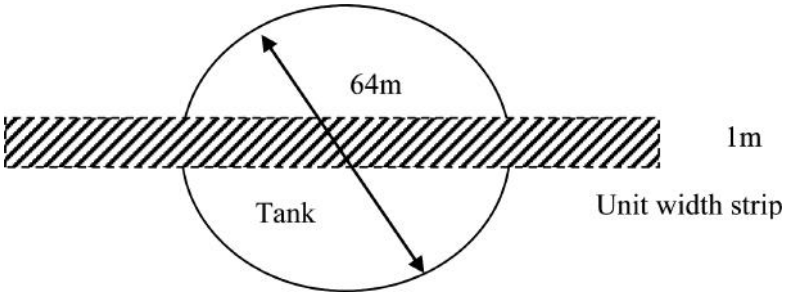

Figure 1. Schematic plan-view of the 2D model (not to scale).

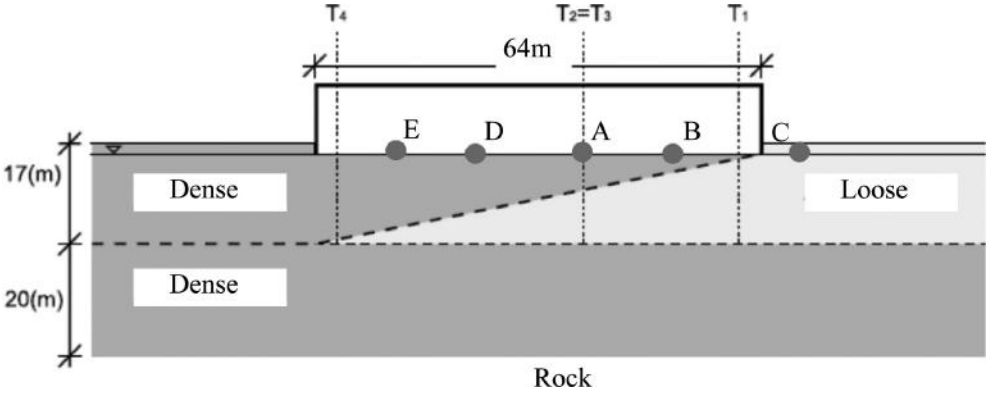

Figure 2. Idealization of the loose sand layer under the tank (not to scale).

It was assumed that this variation was linear from one end of the tank to the other (see Figure 2). The dense sand layer is underlain by competent bedrock with a shear wave velocity of 2000 m/s. Due to the adopted geometry for the liquefiable layer, the model loses its axial symmetry, which required additional 3D analyses to verify the proposed solution.

The construction of a finite element mesh requires limiting the extent of the problem, both horizontally and vertically. Vertically, the model was extended 5 m below the bedrock, and paraxial elements were used below this level (Modaressi and Benzenati, 1994). The function of these elements is twofold: on one hand they are used to introduce the earthquake loading to the model after de-convolution from the outcropping bedrock, and on the other, they absorb the waves originated inside the model by the vibration of the tank, as well as the waves reflected on the surface and those at the interfaces between layers of soil. The horizontal extension of the model was limited to 40 m at each side of the tank, i.e., total width of about 150 m. This distance was large enough to avoid the parasitic wave reflections on the side edges. Since the model is completely inelastic, traditional absorbent elements cannot be used on the edges. One way to solve this problem is to use periodic boundary conditions between the two vertical boundaries, to ensure "free-field" conditions far away from the tank.

The finite element meshes used to model the current situation and the situation with rigid inclusions are shown in Figure 3 (2D) and Figure 4 (3D), respectively, where each color corresponds to a group of items, internally defined in the program, that match the different material properties that were considered.

The 2D mesh is composed of about 8,500 nodes, 8,000 2D solid quadrilateral, triangular, and beam-type elements, for a total of 24,000 degrees of freedom (mechanical and hydraulic). The 3D model consists of about 40,000 linear tetrahedral elements of 4 nodes, for a total of around 8,000 nodes and 30,000 degrees of freedom (mechanical and hydraulic). This 3D finite element mesh is fine enough for the considered problem, since it satisfies the condition of having at least eight nodes by wave length up to 10 Hz. Lateral interaction between the water tank and the rigid inclusions is controlled by one-directional contact elements located at the tank's base mat. Water mass is lumped at base mat, and no explicit dynamic fluid-structure interaction is considered in the model. Elastic behavior was adopted for the piles, using a Young modulus of 500 MPa according to suggestions provided by a jet grouting contractor. The piles extended 5 m below the loose sand stratum.

All calculations were carried out with the program GEFDyn (Aubry & Modaressi, 1996), which is capable of modeling thermo-hydro-mechanical coupled problems on static, quasi-static, as well as dynamic regimes. The static part of the problem was modeled including

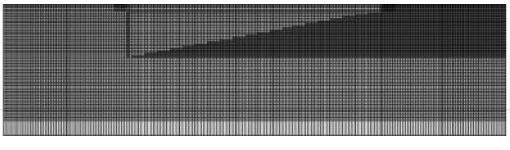

Figure 3. Finite element mesh used in the 2D model.

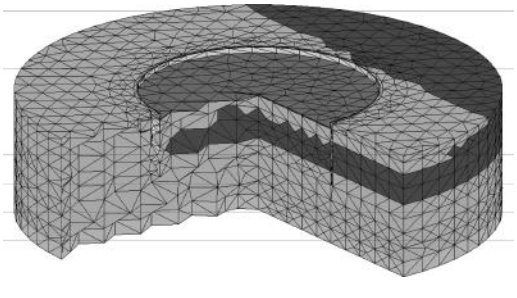

Figure 4. Finite element mesh used in the 3D model.

the phases of excavation, installation and construction of the tank, and earth filling of the lateral surroundings of the tank. In the model with rigid inclusions, the problem was modeled considering the digging phase, the excavation and installation of the piles, and the earth filling of the lateral surroundings of the tank. Between computation phases, the state of the material is continuously updated in terms of cumulative plastic deformations and hardening material parameters to include stiffness, strength and density evolutions. The main objective of the static phase is to achieve a representative stress and material state of the soil before the earthquake. To simulate the construction phases a continuous deformation approach was used (Aubry and Modaressi, 1989). Once the initial stress state is achieved, the seismic analysis is performed "around" the initial static situation, which corresponds to a dynamic disturbance analysis.

Regarding the content of the tank, only the situation of the tank filled with 9 m of water above the foundation level was considered. Since the final goal was to study the soil behavior, the fluid-structure interaction effects between the tank and its content were not included. The fluid was considered as a gravitational weight fort the static part, and as an added mass to the tank for the dynamic analyses.

3 SOIL CHARACTERISTICS

Two sand models, consistent with the SPT data from the site, were selected from a materials library. The Ecole Centrale Paris's (ECP) elasto-plastic multi-mechanism model (Hujeux, 1985) was used to represent the sand behavior. This model can reproduce the soil behavior in a large range of deformations. The model is written in terms of effective stress, and the representation of all irreversible phenomena is made by four coupled elementary plastic mechanisms: three plane-strain deviatoric plastic deformation mechanisms in three orthogonal planes, and an isotropic one. The model uses a Coulomb-type failure criterion and the critical-state concept. The evolution of hardening is based on the plastic strain (deviatoric and volumetric strains for the deviatoric mechanisms, and volumetric strain for the isotropic one). A kinematical hardening, based on the state variables at the last load reverse, is used to take into account the cyclic behavior. The soil behavior is decomposed into pseudo-elastic, hysteretic, and mobilized domains. Material parameters for the soils used in the model are displayed in Table 1.

Table 1. Parameters of ECP model for dense and loose sand.

Parameter name	Dense sand	Loose sand	Meaning
G_{ref} (MPa)	222	290	Reference shear modulus
K_{ref} (MPa)	444	628	Reference bulk modulus
n_e	0.4	0.5	Degree of nonlinearity for elastic modulus evolution with confinement
P'_{ref} (MPa)	1.0	1.0	Reference confinement for non-linear elasticity
n (–)	0.35	0.56	Initial porosity
ϕ'_{pp} (°)	31	30	Friction angle at critical state
ψ_c (°)	31	30	Characteristic angle (limit between contractive and dilative behavior)
β	43	33	Plastic compressibility (related to density's hardening)
d	3.5	2.0	Distance between virgin Isotropic Consolidation Line (ICL) and Line an Critical State Line (CSL)
b	0.2	0.2	Yield surface shape factor ($b = 0$ is Mohr-Coulomb type and $b = 1$ is Cam-Clay type)
p'_{co} (kPa)	50	1800	Projection of initial void ratio on CSL
k (m/s)	10^{-4}	10^{-3}	Saturated permeability
a_m	4×10^{-3}	5×10^{-3}	Hardening coefficients for isotropic mechanisms (monotonous and
a_{cyc}	1×10^{-4}	1×10^{-4}	cyclic)
c_m	6×10^{-2}	4×10^{-3}	Hardening coefficients for shear mechanisms (monotonous and
c_{cyc}	3×10^{-2}	2×10^{-3}	cyclic)

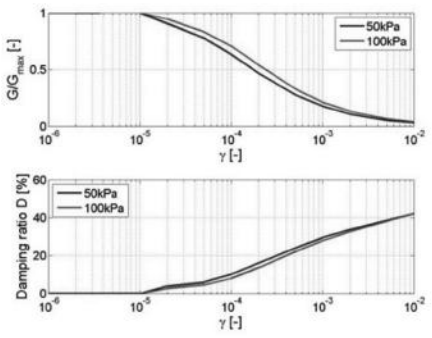

(a) Simulated G/G_{max} and damping versus shear strain curves

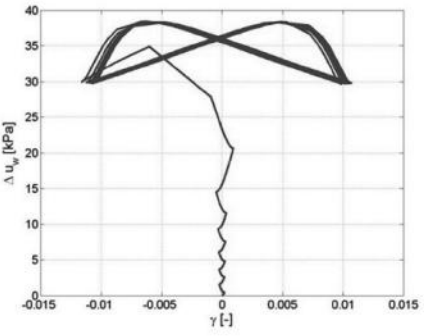

(b) Shear strain versus pore pressure increment

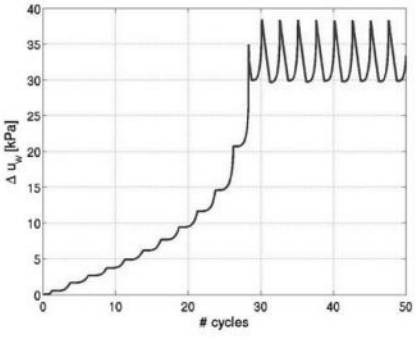

(c) Number of cycles versus pore pressure increment

Figure 5. Drained and undrained cyclic shear tests.

The model's capacity to reproduce the soil's cyclic behavior is illustrated in Figure 5a were the G/Gmax versus shear strain and the equivalent damping versus shear strain curves are shown for stress confinements of 50 kPa and 100 kPa using loose-sand parameters. These curves were obtained from simulations of drained cyclic shear tests.

The model's ability to reproduce liquefaction is illustrated in Figure 5b and 5c where the simulation results of undrained cyclic shear tests using the loose-sand parameters are shown, considering an initial confinement of 40 kPa and a stress deviator of 8 kPa.

4 RESULTS

4.1 *Full tank, 9 m of water, sloping layer, 2d model: post-earthquake settlements*

As indicated previously, only one filling condition of the tank was considered (9 m of water), and the sloping condition of the liquefiable layer was included. The analysis requested by the owner consisted in studying the evolution of the post-earthquake differential settlements, i.e., to obtain the settlements versus time history due to the dissipation of excess pore pressures induced by the contractive behavior of the material.

To simulate the expected behavior, the time of analysis was extended to approximately 200 seconds, i.e., approximately 2.5 minutes were added to the end of the recorded ground motion to capture the post-earthquake settlements. During this period of time there is no ground motion, and the problem is that of non-stationary flow which ends when the pore pressures reach the initial hydrostatic values; the duration of this process is primarily controlled by the permeability of the material and the drainage conditions.

To illustrate the dissipation of the excess pore pressures, Figure 6 presents filled 2D contour plots of the parameter R_u defined as:

$$R_u = \frac{\Delta u_w}{\sigma'_{zz}(t=0)} \tag{1}$$

where Δu_w is the increment of the pore water pressures and σ'_{zz} ($t = 0$) corresponds to the initial effective vertical stress (before the earthquake). When liquefaction occurs, the increase in the pore pressures is similar to the initial vertical stress and R_u is about one. It should be noted that in this case, due to the vibration of the tank, the total vertical loads varies during the earthquake, which means that it is possible to find values of R_u above 1. This effect does not occur in the free-field.

Figures 6a through 6c show the 2D contour plots of the parameter R_u for the situation without the rigid inclusions: (a) during the strong movement (at about 30 s); (b) immediately after the ground motion (at about 60 s); and (c) two and a half minutes after the end of the ground motion (after 200 s). The same scale of colors was used for the three figures, where the dark red color corresponds to a situation of complete liquefaction.

According to Figures 6a and 6b, liquefaction occurs in a great volume of soil under the tank and extends as the ground motion keeps shaking the model. In fact, almost the whole layer of loose sand liquefies. However, after 200 s of analysis, the excess pore pressure has markedly dissipated in the soil mass, especially in the portion below the tank; indeed, as the dense soil located immediately below and to the sides of the tank did not liquefy, there is a large hydraulic gradient that helps the rapid dissipation of the excess pore pressure.

The main purpose of the impermeable rigid inclusions (secant piles wall) is not to avoid the liquefaction but to control the amount of settlements. In effect, by preventing the water flow during the earthquake, the vertical load acting on the liquefied soil is supported mainly by its fluid phase during the shaking. As the fluid is virtually incompressible, uncontrolled settlements during the earthquake are minimized. After liquefaction, the loads are progressively transferred back to the solid skeleton reaching a stress state similar to the one before the earthquake.

To illustrate the post-seismic settlements evolution, five control points were considered (see Figure 2): one at the center of the tank (Point A), two points ~16 m off-center towards

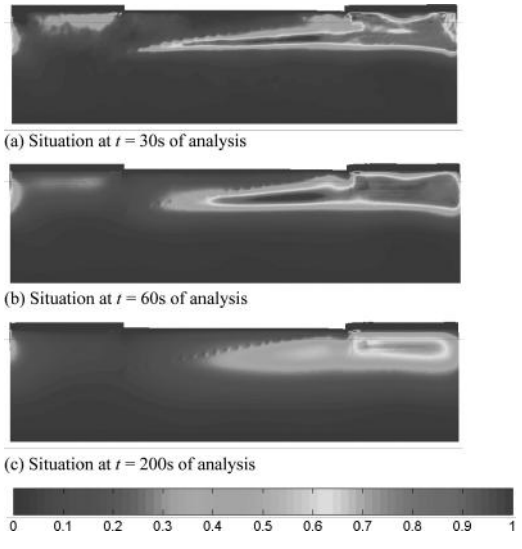

Figure 6. Distribution of R_u for the case of the full tank, sloping liquefiable layer, and without rigid inclusions.

to and away from the clarifier (point B and D, respectively), and two at the perimeter wall of the tank close to and away from the clarifier (points C and E, respectively). Figure 7 shows the calculated settlements in these five control points for the situation with and without rigid inclusions, considering a full tank (9 m of water), sloping liquefiable layer, and including the post-seismic analysis up to a total of ~200 s. Table 2 shows the settlements at the control points immediately after the earthquake (co-seismic), and once the excess pore pressure dissipation is almost over (post-seismic).

Figure 7 and Table 2 show that settlements at the center of the tank or in the intermediate zones are similar for the cases with and without rigid inclusions (points A, B and D). However, variations between both cases are pronounced below the tank edges (points C and E). In effect, the mitigation measure can slightly increase the settlements (10 to 20% in points A and D); however, the opposite is true close to the edges of the tank (points C and E). In Point C, settlements without the rigid inclusions are up to 6 times higher than that of the case with rigid inclusions. Therefore, the mitigation solution tends to uniform the settlements, reducing the internal efforts in the slab of the tank, and therefore decreasing the potential damage due to an earthquake capable of inducing ground liquefaction.

Regarding the settlements evolution, the results show that the values remain virtually constant after 60 s of analysis. In other words, the dissipation of excess pore pressures after the earthquake did not have much influence on the final settlements.

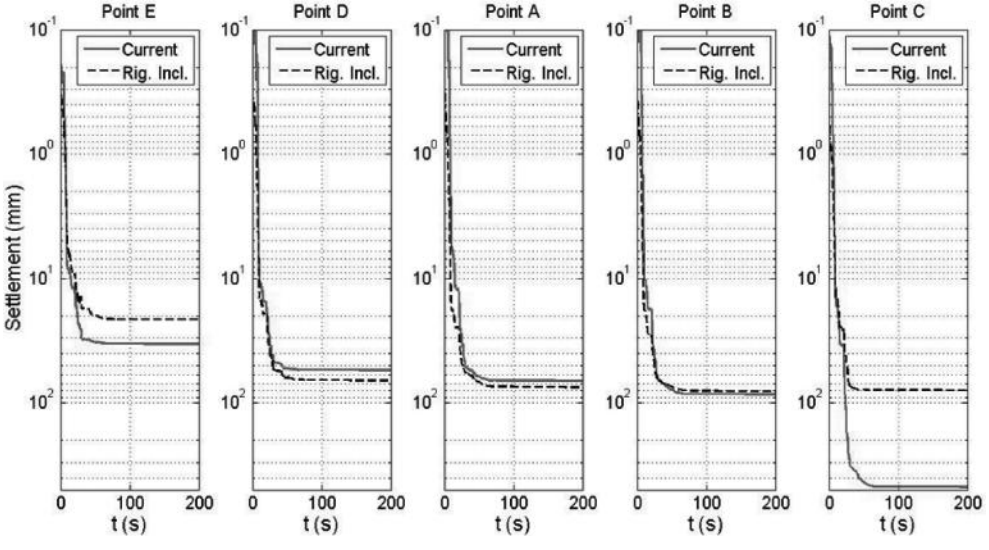

Figure 7. Settlements at the control points for the case of the full tank, sloping liquefiable layer, without rigid inclusions, and including post-earthquake settlement evolution.

Table 2. Settlements in control points considering full tank and sloping liquefiable layer.

	Without rigid inclusions		With rigid inclusions	
Settlement (mm)	80 s co-seismic	200 s post-seismic	80 s co-seismic	200 s post-seismic
A	66	67	74	75
B	84	85	80	81
C	472	473	79	79
D	54	54	65	66
E	33	34	21	21

4.2 *3D versus 2D Model (sloping liquefiable layer)*

The modeling assumptions of the 3D model are essentially the same as those used for the 2D, i.e.: inelastic behavior of the soil, but not of the tank, hydro-mechanical coupled model for the saturated soil, and fluid-structure interaction effects included approximately through the added mass to the tank. Periodic boundary conditions were used to impose pure shear deformation on the direction of shaking. Paraxial elements were used at the bottom of the model to impose the incident seismic field, as well as to absorb the waves reflected from the inside of the model.

Like the 2D case, the 3D model includes the static simulation of the construction and subsequent filling of the tank, and the seismic analysis is performed around the static equilibrium condition. Due to the dimensions of the problem, the implementation is much slower than the two-dimensional case (about 50 times slower) so that the three-dimensional model is used mainly to verify the results obtained from the two dimensional analysis.

The effect that the variable thickness of the liquefiable layer had on the tank's response was also studied using the 3D model. As Figure 3 shows, this variability was idealized as an inclined plane from one end of the tank to the other, starting from the point and depth where the geotechnical exploration determined the existence of a dense soil to the surface at Point C. The normal to the inclined plane lies on the *x*-*z* plane of the 2D modeling (Figure 5). Since the problem loses the axial symmetry, it is important to perform the seismic analyses in two orthogonal directions.

Figure 8 compares the results of the 2D and 3D models without rigid inclusions but including the sloping liquefiable layer and considering a longitudinal earthquake. The graphs show the calculated settlements for control points E, D, A, B and C for both models. These results show that the settlements using the 3D model are of the same order of magnitude of the results using the 2D model, although they tend to be around 20% higher at the center (Point A) and in the intermediate zone (Point B). The opposite is true close to the edge of the tank (Point C), where the 2D modeling gives conservative results when compared against the 3D model (3 times less settlement).

In the case with rigid inclusions (Figure 9) under longitudinal seismic loading, the 3D results confirm the beneficial effects of the piles, and the trend indicates that the settlement reduction is even more effective than that estimated using the two-dimensional analysis. The expected settlements are reduced to a quarter of the value when three-dimensional effects are incorporated.

When comparing the results with and without the rigid inclusions (Figures 8 and 9), a reduction on the expected settlements of at least 4 times was observed. Based on these analyses, the secant piles mitigation system not only reduces the settlements, but it also induces a

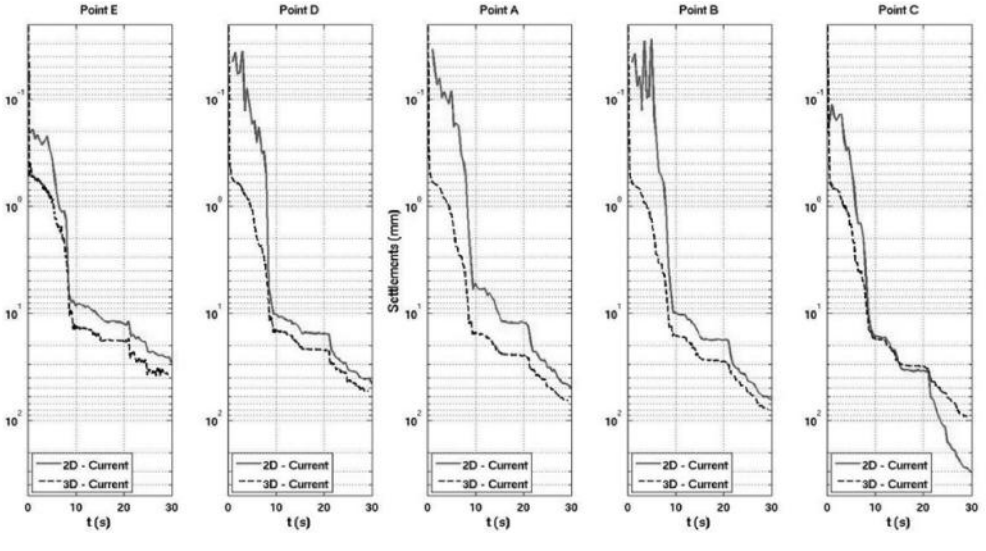

Figure 8. 2D versus 3D analysis. Settlement at the control points without rigid inclusions and a sloping liquefiable layer.

more homogeneous distribution of vertical displacements under the tank. The calculated values when the time of analysis equals 25 seconds are summarized in Table 3. In this table, the settlements corresponding to the case where the earthquake was imposed in the transverse direction (perpendicular to the 2D model) have been included. The calculated settlements are slightly smaller when the shaking is applied in the transverse direction, with the exception of the center point (A) where the values are practically identical.

Table 3 includes two additional control points (A2 and A3) located along the axis perpendicular to the plane of the 2D model that passes through the center of the tank, A3 is A2's diametric opposite. The proposed mitigation solution significantly reduces the settlements, for the earthquake acting in both longitudinal and transverse directions, and it achieves a relatively uniform soil settlement under the tank. Due to the stratification that was considered and the use of automatic mesh generators to develop the FE model, the results are virtually symmetrical in the transverse direction (i.e., settlements in A2 and A3 very similar) for both longitudinal and transverse earthquake. Along the longitudinal direction of the tank, the effects of sloping stratification are expressed in the different settlements obtained for points B and C. On the other hand, from a practical point of view, the direction of the earthquake did not have an impact on the results. In fact, for the case with rigid inclusions, the settlements are very similar (in the order of 10 mm) no matter what the incident direction of the earthquake is.

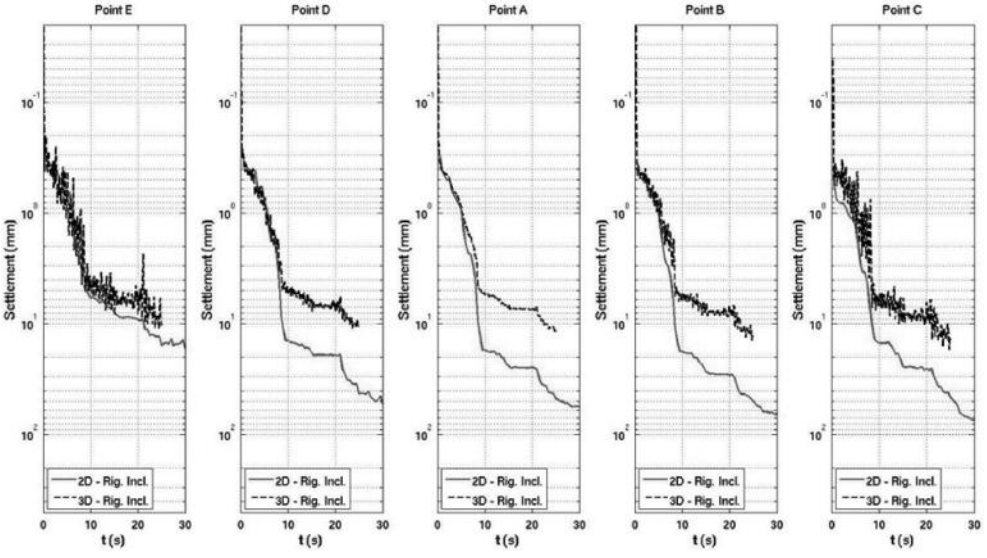

Figure 9. 2D versus 3D analysis. Settlement at the control points with rigid inclusions and a sloping liquefiable layer.

Table 3. Settlements in control points after 25 s of analysis using a 3D model, full tank, and sloping liquefiable layer.

Settlement (mm)	Without rigid inclusions	With rigid inclusions	
	Longitudinal	Longitudinal	Transverse
A	48	12	11
B	54	12	10
C	61	13	8
D	48	11	12
E	35	10	14
A2	48	11	12
A3	49	12	10

As expected, given the problem characteristics and since the 2D section that was modeled corresponds to the most critical one (longest distance from rigid inclusion to rigid inclusion), the two dimensional analysis was on the conservative side with respect to the actual 3D situation. In effect, in all the other cross-sections that do not pass through the center of the tank, the rigid piles are relatively closer to each other which favors its effectiveness. The axis symmetry was lost once the sloping liquefiable layer was incorporated, which required seismic analysis in two perpendicular directions. The results of the analyses show that the expected average settlements are in the order of 10 mm regardless the direction of the ground motion.

5 CONCLUSIONS AND RECOMMENDATIONS

From the results of the 2D and 3D analyses presented in this article we can conclude that:

- If the tank has a water level of 9 m, the proposed solution tends to homogenize the settlements under the tank which should have a favorable impact on reducing its expected damage.
- The results from the 3D analyses confirm the ones obtained with the 2D ones, although the latter tend to be more conservative. Also, the 3D models anticipate a better behavior of the proposed mitigation strategy than the 2D model does.
- The geometry for the proposed solution (piles' length and diameter) seems appropriate for characteristics of the soil, tank, and shaking.
- Due to the relative settlement that will take place between the tank and the secant piles wall, there should be no shear connector between the tank and the connecting top beam of the piles.

It must be emphasized that the present analysis was carried out under a number of assumptions, e.g.:

- The soil properties were obtained from a library of materials and they are only compatible with the Standard Penetration Tests (SPT) results. In effect, this kind of information only allows the evaluation of the liquefaction potential, but it does not provide enough information to carry out detailed analysis of the level presented in this article. Therefore, the results should be considered as qualitative, and they do not represent precise predictions of the expected behavior of the tank.
- The conclusions drawn in this report have been established on the basis of the analysis of a single earthquake. Given the characteristics of dynamic non-linear problems, this study should be repeated using a large collection of different earthquakes to properly capture the variability of the expected results.
- All the non-linear effects of the structural elements (piles and tank) have been neglected, as well as the fluid-structure interaction effects. These effects could have a significant impact on the actual structural response of the tank.

ACKNOWLEDGEMENTS

The authors would like to thank Macarena Ayarza, Technical Manager of Pilotes Terratest S.A., for all the valuable discussions and critical input. Any opinions, findings, conclusions and/or recommendations expressed in this material are those of the authors.

REFERENCES

Aubry, D. and Modaressi, A. 1989. A rational approach to the analysis of construction filling or excavation. *Proceedings of Numerical Models in Geomechanics*, NUMOG III, 455–462.

Aubry, D. and Modaressi, A. 1996. *GEFDyn: Manuel Scientifique*, Ecole Centrale Paris (in French).

Hujeux, J.-C. 1985. Une loi de comportement pour le chargement cyclique des sols. *Génie Parasismique*, Presse ENPC, 287–302 (in French).

Modaressi, H. and Benzenati, I. 1994. Paraxial approximation for poroelastic media. *Soil Dynamics and Earthquake Engineering*, 13, Issue 2, 117–129.

Soil-structure interaction in non-liquefied ground

This page intentionally left blank

Soil Liquefaction during Recent Large-Scale Earthquakes – Orense, Towhata & Chouw (Eds)
 ISBN 978-1-138-02643-8

Effect of SFSI on the response of soil

X. Qin & N. Chouw
Department of Civil and Environmental Engineering, University of Auckland, Auckland, New Zealand

ABSTRACT: In current design practice, the seismic response of a structure is estimated using the free-field ground motions. However, in reality the earthquake loading is characterized by the interacting forces at the footing-soil interface. These interacting forces depend on the dynamic properties of the structure, soil and the incoming seismic waves. Consequently, the actual earthquake loading of the structure and the free-field ground motions are not the same, and the structural response cannot be properly estimated using the free-field motions. This study aimed to investigate the behaviour of soil with Structure-Foundation-Soil Interaction (SFSI). Shake table tests on a laminar box that allows shear deformation of soil were conducted to obtain the dynamic response of the soil. The difference between the soil responses under two conditions, i.e. free-field and soil with structure, were considered. The result shows that because the presence of the structure, the vertical movement of the soil was impeded and the weight increased the settlement of the soil. This altered the shear behaviour of soil and therefore changed the acceleration of the soil. This finding indicates the likelihood that the seismic response of structures cannot be obtained using free-field ground motion.

1 INTRODUCTION

In most current seismic design of foundation, the effect of Soil-Foundation-Structure Interaction (SFSI) has not been incorporated. The structure is designed with an assumed fixed base condition. The design action is determined based on the earthquakes recorded from free-field soil sites. During an earthquake, the response of a building will impose forces to the soil foundation. The interaction between structure, foundation and soil will alter the behaviour of the supporting soil and the seismic wave propagation.

Most of the previous study on SFSI mainly focused on the performance of the super-structure. Larkin (2008) has concluded that the stiffness of the supporting soil can lengthen the period of the structure and could result in a variation of force development when compared to analyses performed without considering SFSI. A structure supported on soft soil has more degrees of freedom and therefore different dynamic characteristic than a fixed base structure (e.g. Veletsos and Meek 1974). As Veletsos and Meek mentioned a flexible ground can act as a damper. This can reduce the design action imposed on a structure. This effect is not evident in fixed base structures as most of the energy remains in the structure. Previous studies by Malhotra and Veletsos (1994) concluded that storage tanks supported on a flexible ground were less prone to buckling at the junction of the tank wall and base plate. The beneficial effect of SFSI was acknowledged to the energy dissipation due to the supporting soil plastic deformation. In addition, research has shown that SFSI can lead to favourable reduction in the plastic hinge development of structure (Qin et al. 2013). In studies on SFSI by Shirato and Kouno (2008), they examined the nonlinear foundation response of a large scale model with pier footings on sand. The experiment was carried out using a laminar box on a shake table. The results showed that the residual displacement of the footing depends on the duration and the intensity of the excitation; and the uplift of the model significantly affects the foundation behaviour. In fact, SFSI can also alter the response of soil. The excitation of the structure could be altered significantly depending on this interaction. Designing a structure using excitation obtained

from free-field ground motion would lead to incorrect estimation of the seismic action on the structure. However, this phenomenon was not much considered in previous studies.

To simulate the response of soil during earthquake, laminar box is commonly applied. Wu and Sun (2002) designed a laminar box which had dimensions of 2 m long by 1.5 m wide by 2 m high, consisting of 100 mm steel square hollow sections for each layer. Bearing tracks were fitted externally to create a sliding mechanism. Steel walls were used to confine the laminates such that movement was allowed only in the longitudinal direction. The internal walls were lined with 2 mm rubber membrane to contain the soil and for waterproofing. Free vibration tests were conducted on the empty laminar box and produced a frequency response of 1.4 Hz. When the laminar box with sand was tested the frequency obtained was approximately 10 Hz. The disparity between the natural frequencies suggested that the resonance of the laminar box had negligible effects on the response of the soil. In a research on centrifuge modelling of earthquake induced lateral spreading in sand, a laminar cylinder was constructed using 39 thin rings (Taboada-Urtuzuastegui and Dobry 1998). These rings were used to provide flexibility and to simulate a continuous shear strain field in the soil during shaking. Bearings were inserted between each ring to transfer the weight and reduce the friction of the laminar rings due to lateral displacements. From the experiment the authors concluded that as the input acceleration increases, the permanent shear strain and settlement of soil would either stay constant or increase. However, as the input frequency was increased, the pore water pressure, thickness of liquefied soil, soil acceleration, lateral permanent displacement, settlement and shear strain, all decreased.

The aim of this study is to investigate the effect of SFSI on the horizontal soil movement. A laminar box was constructed to simulate the shear behaviour of soil during earthquake. A SDOF structural model was used to represent the superstructure. Two different boundary conditions were considered on a laminar box, i.e. with and without structure, filled with dry sand. Shake table test was conducted and simulated ground motion based on the Japanese design spectrum was utilized. Laser transducer was used to measure the settlement at the surface of soil. To measure the acceleration developed at the surface of the soil during earthquake, accelerometer was used. The lateral displacements at different locations of the laminar box were measured to obtain the overall shear deformation of the soil. The response of soil with and without the effect of SFSI is discussed.

2 LAMINAR BOX AND SHAKE TABLE TEST

2.1 *Laminar box*

A laminar box has the advantage that the vertically propagating shear waves from the bedrock to the surface of the soil can be simulated. This laminar box is composed of discrete layers that can move relative to each layer by a sliding mechanism. The response of the specimen is driven by the soil and not the laminar box itself. In this research the laminar box comprised of twelve layers with an area of 800 mm × 800 mm (Figure 1(a)). To minimized inertia of the laminar layer induced to the soil, aluminium section was used.

Shake table was used to generate the ground excitation of the sand specimen in the laminar box. The depth of sand filled in the box was 500 mm depth. Laser transducer was pointed to the surface of soil to measure the soil settlement during the experiment (Figure 1(b)). The lateral displacements of the laminar layer which correspond to the bottom and surface of the soil were also measured. An accelerometer was placed on the sand surface, at 300 mm away from the centre of soil. When SFSI was considered, a model structure was placed at the centre of the soil surface.

2.2 *Structural prototype*

The prototype was a four-storey structure with an inter-storey floor height of 3 m. The dimension of each floor was 7 m × 7 m. The columns of the building were 250UC73. The beams of the structure were 310UB46. Double-T floor slab units with depth of 350 mm were used on each floor with an additional 125 mm concrete topping. According to the New Zealand

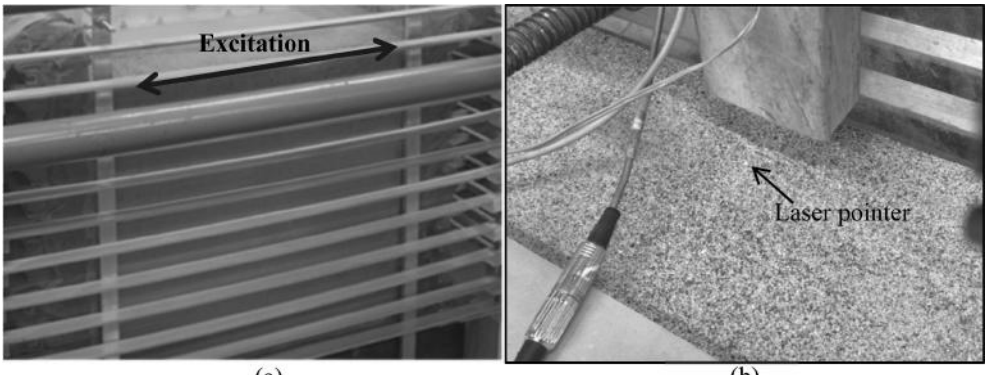

Figure 1. Experimental setup. (a) Laminar box and (b) surface measurement location.

Standard for Structural Design Actions (1170.5, 2004), the seismic mass of each floor was found to be 28.75 t. The collective lateral stiffness of each floor was 76000 kN/m. The fundamental period the structure with fixed base assumption was 0.61 s.

2.3 *SDOF representation*

Generally, the influence of higher modes on structural response was considered to be negligible compared to the fundamental mode (Qin and Chouw 2010). An equivalent Single Degree-Of-Freedom (SDOF) model was used to represent the fundamental mode of the prototype structure. It has also been confirmed that a SDOF model was suitable for characterizing the overall behaviour of a Multi-Degree-Of-Freedom (MDOF) building (e.g. Decanini, Mollaioli et al. 2001).

The effective mass and height for the fundamental mode of the prototype can be obtained using the equilibrium of activated inertia forces and bending moment at the base (e.g. Chopra 2007). For the case considered the SDOF structure has an effective mass of M^* of 91.97 t that was equal to 80% of the total prototype mass. The effective height h^* was calculated to be 8.85 m. The lateral stiffness of the SDOF system was obtained by matching its fundamental period with that of the prototype.

2.4 *Model scaling*

Large scale experiments would be expensive and impractical in laboratory. In this study, the limitation of using shake table is the hydraulic capacity to move the structure. To overcome this difficulty a scaled model is used to represent the prototype structure.

The physical property of the scale model should be selected so that its dynamic behaviour is the same as that of the full scaled building. Qin et al. (2013) has proposed a dimensionless variable to obtain the relationship between the dynamics of a prototype and its scaled down model. Based on Buckingham π theorem (Buckingham 1914) and Hooke's law, Qin et al. has demonstrated that the dynamic response of a structure during earthquake can be represented by a reformulated Cauchy number (Equation 1).

$$\frac{ma}{ku} \tag{1}$$

where m and k is the mass and stiffness of the structure, respectively; u and a is the elastic deformation and acceleration.

The properties of the model (mass, lateral stiffness and dimension) and the acceleration of the excitation in the shake table test can be obtained based on the Cauchy number using the

Table 1. Properties of the SDOF system and the model.

	Total mass (kg)	Lateral stiffness (kN/m)	Total height (m)	Natural period (s)	PGA (g)
SDOF system	91970	7953000	8.85	0.59	PGA
Experimental model	19.16	6630	0.59	0.28	PGA/3.75

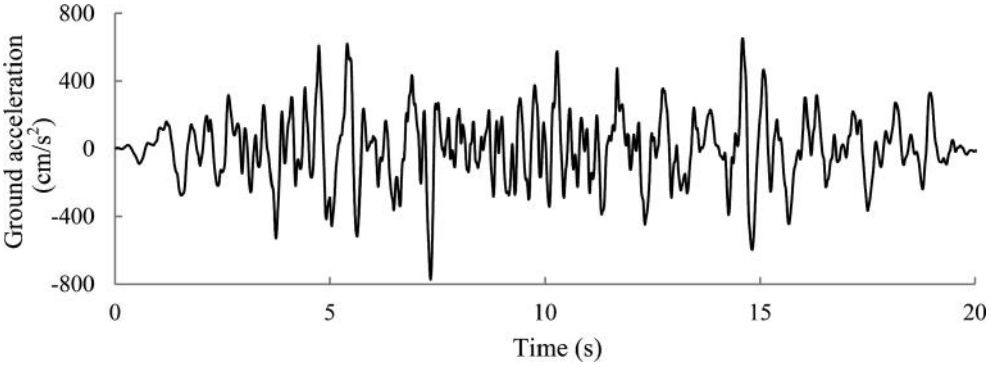

Figure 2. Ground excitation.

variable of prototype system. Table 1 summarizes the mass, lateral stiffness and dimension of the SDOF system and the model for the experiments.

2.5 *Earthquake excitation*

The ground motion (Figure 2) was simulated based on the Japanese design spectrum for hard soil condition (JSCE 2000). They were selected because of their clear defined frequency content (Chouw and Hao 2005).

3 EFFECT OF SFSI ON THE SOIL RESPONSE

3.1 *Settlement of soil with SFSI*

In this study, the settlement of the soil surface during the ground excitation was measured using laser displacement transducer (Figure 1). Figure 3 shows the comparison of the soil settlement between when free-field and SFSI was respectively considered. With SFSI, the development of the surface settlement increased. The weight of the structure confines the soil and causes a greater settlement of the soil. As shown in the figure, the vertical displacement of the soil surface without and with structure developed similarly. However, the soil displacement with the structure was always greater than that at the soil surface without structure. At the end of the excitation, a permanent settlement at the soil surface with SFSI was 12.36 mm. The settlement was 2.77 mm greater than that of the soil with free-field condition.

3.2 *Shear deformation*

The shear deformation (τ) of soil was assumed to be the same as the lateral displacement of the laminar layers that correspond to the bottom and the surface of the soil. The difference between the displacements at these two laminar frames represents the overall shear deformation of the specimen. Figure 4 shows the comparison of the shear deformation of the soil with different conditions. The maximum shear deformation of the soil with and without SFSI was 8.91 mm and 13.13 mm, respectively. The corresponding permanent shear deformation

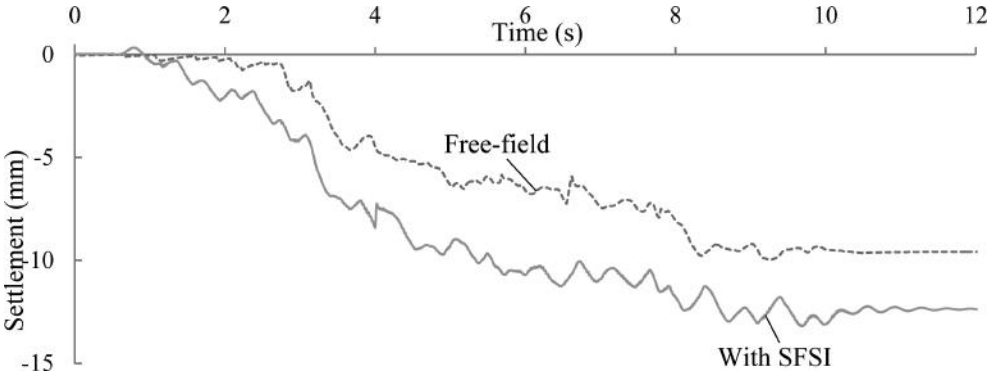

Figure 3. Settlement at the soil surface.

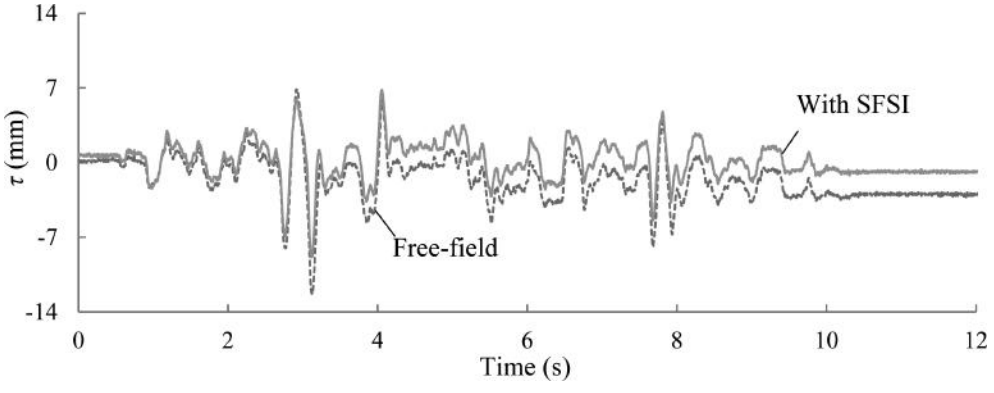

Figure 4. Relative horizontal displacement between the surface and the bottom of soil.

in the soil at the end of the excitation was 0.85 mm and 3.02 mm. As demonstrated, SFSI will increase the development of settlement in the soil during earthquake. The raising of density in the soil due to settlement enhances the shear module of the specimen. Therefore, the shear resistance of the soil increases and shear deformation of soil during earthquake reduces.

3.3 *Acceleration at the surface of soil with SFSI*

It is also found that the change of soil shear behavior due to SFSI will affect the acceleration development at the soil surface. Figure 5(a) shows the acceleration (a) recorded at the soil surface. The accelerometer was located in the transverses direction, at 300 mm away from the center. From the time history, the acceleration at the soil surface with and without SFSI appears similar. However, when comparing the response spectra of the accelerations, it is found that SFSI will lessen the spectrum acceleration. Figure 5(b) shows the response spectra (Spa) of the accelerations at the surface of soil with a 5% damping ratio.

It can be seen that in the region between the period of 0.225 s and 0.5 s (indicated by vertical lines in Figure 5(b)), the spectrum values with SFSI was significantly smaller than those at the free-field soil surface. At the fixed base fundamental period of structure ($T = 0.28$ s), the spectrum value for the case with and without SFSI was 1.51 g and 1.58 g, respectively. Apart from this range, the spectrum values were similar. It is shown that the effect of SFSI on the acceleration at the surface of soil depends on the property of the structure.

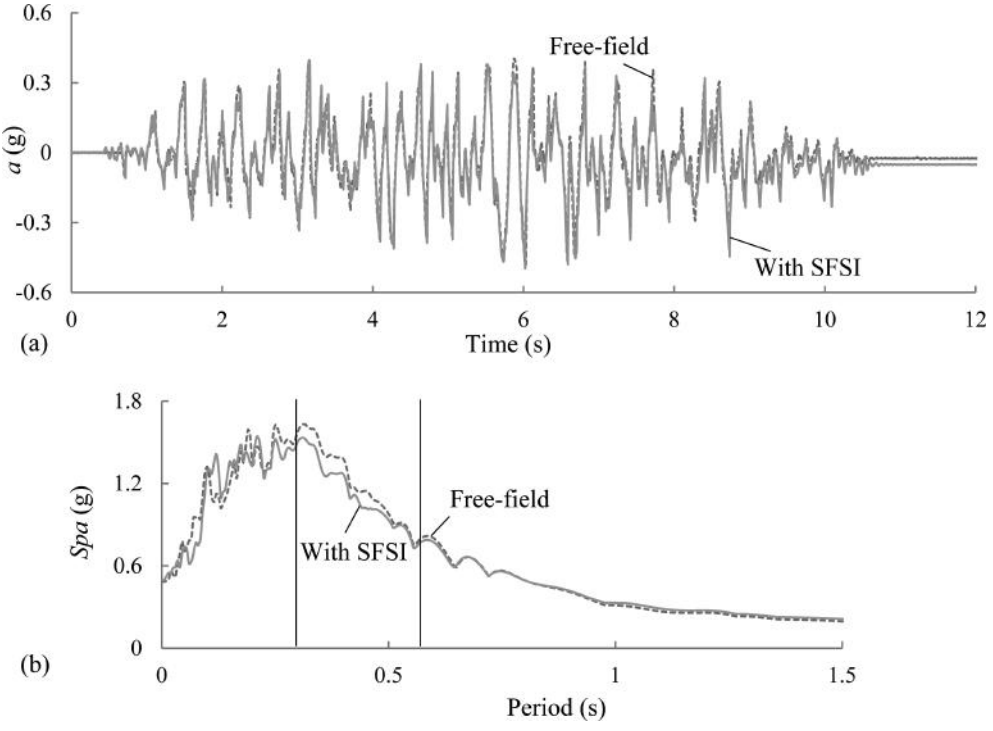

Figure 5. Acceleration at the soil surface. (a) Time history and (b) response spectrum.

4 CONCLUSIONS

This study aimed to investigate the response of soil with SFSI. Shake table test on a laminar box with dry sand fill was utilized to simulate the seismic shear deformation of soil. A SDOF model was used to simulate the overall behaviour of a four-storey structure with a surface footing. Two different boundary conditions, i.e. with and without structure were considered. Accelerometer was placed at surface of the sand to measure the response of the specimen during earthquake. The settlement and shear deformation of the soil were also considered.

This preliminary experimental study reveals that:

- The vertical confinement of the soil due to the structural weight increases the soil settlement during earthquake.
- With a greater development of soil settlement due to SFSI, the shear module of soil was increased. The shear deformation in the soil with SFSI is therefore smaller than that in the soil with free-field condition.
- The spectrum acceleration at the soil surface with SFSI is smaller than that at the free-field soil surface.

ACKNOWLEDGEMENTS

The authors would like to thank the University of Auckland for the support under the FRDF Award 3700551 and the Ministry of Business, Innovation and Employment through the Natural Hazards Research Platform under the grant 3303249.

REFERENCES

1170.5, S. N. Z. 2004. *Structural Design Actions. Part 5: Earthquake Action*. Standard New Zealand.

Buckingham, E. 1914. On physically similar systems; illustrations of the use of dimensional equations. *Physical Review*, *4*(4), 345–376.

Chopra, A. K. 2007. *Dynamics of Structures. Theory and Applications to Earthquake Engineering*, Third Edition.

Chouw, N. and Hao H. 2005. Study of SSI and non-uniform ground motion effect on pounding between bridge girders. *Soil Dynamics and Earthquake Engineering*, Vol. 25: 717–728.

Decanini, L. and Mollaioli F. 2001. Equivalent SDOF systems for the estimation of seismic response of multistory frame structures. *Advances in Earthquake Engineering* 9: 101–110.

Japan Society of Civil Engineers (JSCE) 2000. *Earthquake Resistant Design Codes in Japan*, Tokyo, Maruzen.

Larkin, T. 2008. Seismic response of liquid storage tanks incorporating soil structure interaction. *ASCE Journal of Geotechnical and Geoenvironmental Engineering* 134(12): 1804–1814.

Malhotra, P. K. and Veletsos. A. S. 1994. Uplifting response of unanchored liquid-storage tanks." *Journal of Structural Engineering* 120(12):3471–3488.

Qin, X. and Chouw, N. 2010. Experimental investigation of uplift effect on structures in earthquakes. *Proceeding of the Annual NZSEE Conference*, Paper Number 14.

Qin, X., Chen, Y., & Chouw, N. 2013. Effect of uplift and soil nonlinearity on plastic hinge development and induced vibrations in structures. *Advances in Structural Engineering*, *16*(1), 135–148.

Shirato, M. and Kouno. T. 2008. Large-scale experiments on nonlinear behaviour of shallow foundations subjected to strong earthquakes. *The Japanese Geotechnical Society* 48(5): 673–692.

Taboada-Urtuzuastegui, V. M. and Dobry, R. 1998. Centrifuge modelling of earthquake-induced lateral spreading in sand. *Journal of Geotechnical and Geoenvironmental Engineering* 124(12): 1195–1206.

Veletsos, A. S. and Meek. J. W. 1974. Dynamic behaviour of building-foundation systems. *Earthquake Engineering and Structural Dynamics* 3: 121–138.

Wu, X. P. and Sun L. M. 2002. Development of laminar shear box used in shaking table test. *Journal of Tongji University* 30(7).

This page intentionally left blank

Soil Liquefaction during Recent Large-Scale Earthquakes – Orense, Towhata & Chouw (Eds)
© 2014 Taylor & Francis Group, London, ISBN 978-1-138-02643-8

Effects of subsoil on seismic wall stresses in liquid storage tanks: Experimental findings

M. Ormeño-Godoy, T. Larkin & N. Chouw
Department of Civil and Environmental Engineering, University of Auckland, Auckland, New Zealand

ABSTRACT: Previous studies have demonstrated that strong earthquakes may cause severe damage to liquid storage tanks. Tanks as part of the lifeline system are often built near the coast on soft soils. Because the stiffness of the tank (very stiff) and the soil (flexible) is so different, the interaction between soil foundation and structure (SFSI) plays a significant role in the seismic response, often due to an elongation in the period of the impulsive mode. There is a very little experimental work about the effect of the subsoil on tank response. This paper reports a series of experiments on this topic using a shake table. A physical model is used to evaluate the effects of SFSI. Sand in a box is used to simulate the foundation soil. The experiments were performed using actual records scaled to the New Zealand design spectrum and two different tank aspect ratios (height/radius). The development of the horizontal displacement of the top of the tank and the shell stresses are discussed.

1 INTRODUCTION

After an earthquake, the continuation of basic supplies as oil, water and food are essential. For this reason, liquid storage tanks should remain operational during the post-earthquake period and be designed to prevent leakage in an earthquake. Even for less important tanks the economic and social loss due to damage to a tank can be significant. However, evidence in the literature (Haroun, 1983, Manos and Clough, 1985, Cooper, 1997) has shown that large earthquakes have caused damage, even collapse of storage tanks. Design guides and standards (NZSEE (2009), API 650, Eurocode 8) have been developed due to the importance of these structures.

Figure 1 shows the usual model for liquid storage tanks given by Housner (1957) which is used by the current design specifications. It uses an equivalent springs-mass system to take into account the interaction between fluid and structure. The mass of the contents is divided into parts which move with different frequencies.

The first mode, where the mass is considered to move together with the tank wall, is called the impulsive mode (M_i), while the other mode, which involves mainly the upper body of the contents, is known as the convective or sloshing mode (M_c). In most practical cases, storage tanks can be considered as a single degree-of-freedom (SDOF) system, taking into account only the impulsive mode (Larkin 2008). The impulsive mode has a very short period (a few tenths of a second). When storage tanks are placed on soft soils, SFSI will be a significant feature that

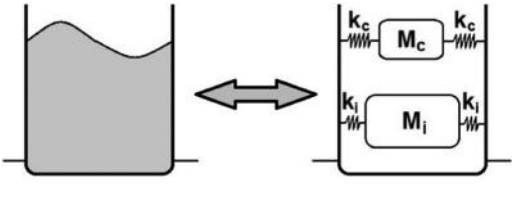

Figure 1. Spring mounted masses after Housner (1957).

determines the seismic behaviour of the structure. Veletsos and Meek (1974) reported that there are two main factors that explain the difference in the seismic behaviour between the same structure placed on firm soil and on soft soil: a) structures on a flexible base have more degrees of freedom and, thus, different dynamic characteristics than structures fixed on rigid base; and b) a part of the vibration energy of a structure placed on a flexible base will be dissipated by propagation of waves into the surrounding soil and by damping in the soil.

Veletsos and Tang (1990) solved the problem of SFSI in the frequency domain and included the foundation of the tank while considering the impulsive and convective modes of vibration. They concluded that: a) the system has a smaller natural frequency when SFSI is present; b) an increase in damping of the system reduces the peaks in the seismic response; c) in comparison to a fixed base system slender tanks have a larger reduction of the natural frequency than squat tanks because the rocking component of the foundation motion is more dominant for slender tanks; d) a reduction in peak response is more significant for squat tanks than for tall, slender tanks because these squat tanks dissipate more energy by radiation damping; and e) the effects of SFSI on convective modes are negligible. The authors also mentioned that SFSI is mainly governed by the relative stiffness of the supporting medium, i.e., by the ratio of structural to soil stiffness. When storage tanks are placed on soft soils, SFSI may have a strong influence on the seismic response.

Larkin (2008) investigated the seismic response of storage tanks including SFSI for layered sites. In his work Larkin confirmed the results given by Veletsos and Tang (1990) with respect to the predominant mechanism of energy dissipation as a function of aspect ratio (liquid height to radius ratio). Larkin found that the seismic response may increase or decrease depending on the characteristics of the tank, the type and depth of soil and the frequency content of the earthquake motion.

Most SFSI investigations have been performed numerically and focused mainly on the overall structural behaviour (e.g. Orense et al. 2009 and Ormeño et al. 2012). Very little experimental data has been reported about the effect of SFSI on the tank shell stress although it is the principal parameter that controls the design of this type of structure. The objectives of this work are to quantify the effects of SFSI on storage tanks in terms of the axial and hoop stresses in the tank wall. The study entails the use of an earthquake motion applied to a shake table that supports a sand box used to simulate the subsoil, with a PVC model tank on the surface of the soil.

2 METHODOLOGY

2.1 *Tank model*

A PVC tank is used to model a prototype steel tank. Two different aspect ratios (H/R: liquid height to radius ratio) were studied, $H/R = 2$ and 3. The properties of the model and prototype are shown in Table 1. Two different boundary conditions were utilised, rigid base (tank placed on the shake table) and flexible base (tank placed on the sand box). Figure 2 shows both cases. The dynamic properties were computed using NZSEE (2009). The scale factors used to meet the similitude requirements are shown in Table 2.

2.2 *Set up*

Strain gauges were installed on the tank wall to measure the distribution of axial stresses. A ring of horizontal strain gauges located at a height of 150 mm were used to measure the hoop stresses. Figure 3 shows the setup use.

2.3 *Ground motions*

A set of two different earthquake records were used in testing the tank model. The earthquakes selected are shown in Table 3. The earthquakes were scaled using the procedure given

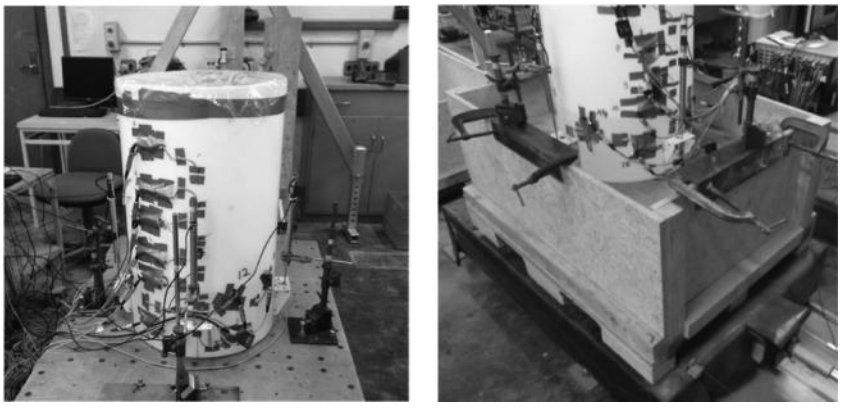

Figure 2. Rigid base case (left) and flexible base case using the sand box (right).

Table 1. Dimensions and properties of tank model and prototype.

	Model	Prototype
Material	PVC	Steel
Young's modulus (MPa)	$1.6*10^3$	$2.068*10^5$
Diameter (m)	0.50	10.00
Height (m)	0.75	15.00
Wall and base thickness (mm)	4	10
Mass of the contents (kg)	147	1178097

Table 2. Scale factors.

Dimension	Scale factor
Length	20
Mass (liquid content only)	8000
Time	4.64
Stiffness	369.5
Acceleration	0.93
Force	7440

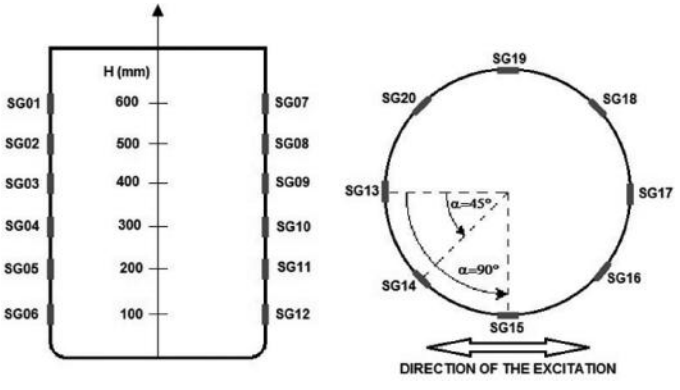

Figure 3. Arrangement of the strain gauges at the outer tank shell. Elevation (left) and plan view (right).

Table 3. Earthquake records selected.

Record Name	El Centro, USA	Matahina, Dam D, NZ
Date	19 May 40	02 Mar 87
Magnitude (Mw)	7	6.6
Distance (km)	6	16
Depth (km)	10	10
Fault Mechanism	Strike-Slip	Normal

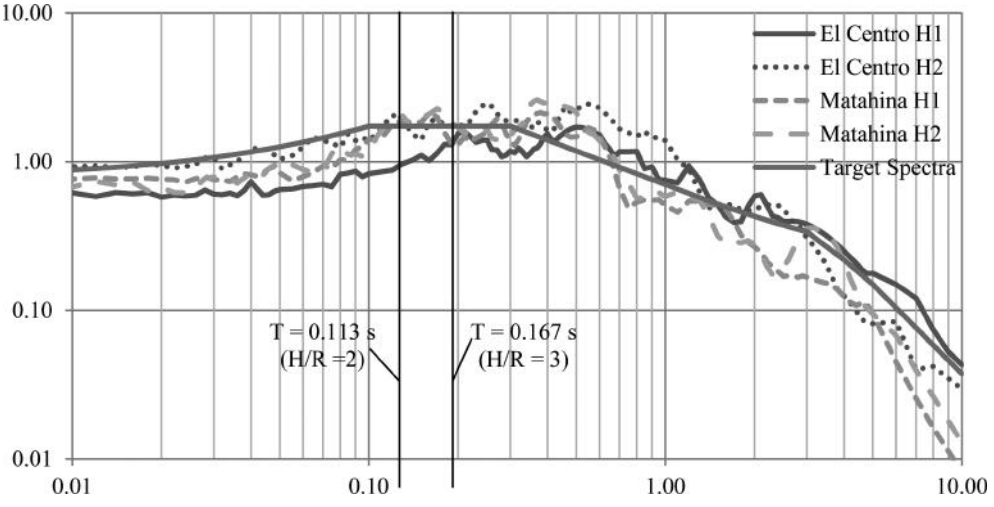

Figure 4. Scaled earthquake spectra and target NZ design spectrum.

by NZS 1170.5 (2004). Both horizontal components (H1 and H2) were utilised. The parameters necessary to compute the spectrum given by the NZSEE recommendations (2009) were selected for Wellington and a site classification of C. The scaled response spectra of the earthquakes and the target spectrum are shown in Figure 4. A shake table was used to simulate the ground motions. The similitude requirement was met by applying the time scale factor shown in Table 2.

2.4 *Subsoil*

To model the subsoil, a sand box was used (Figure 2). The internal dimensions of the sand box are 1100 × 800 × 500 mm. The box was filled to a height of 400 mm. The quartz sand utilised to fill the box has a relative density of 88%.

3 RESULTS

The parameter that largely controls the design of liquid storage tanks is the stress in the tank shell. Figures 5 and 6 show the maximum outer axial compressive stress obtained in the case of both components of El Centro and for the two aspect ratios considered.

In Figures 5 and 6 it is noticeable that the axial compressive stress decreases when the tank was placed on the sand box. To provide an overview of the effect of SFSI on the axial compressive stresses, the reduction in stress at the base of the tank wall, the position of highest stress, is shown in Table 4. The stress in the tank wall when supported on the shake table was used as the reference value.

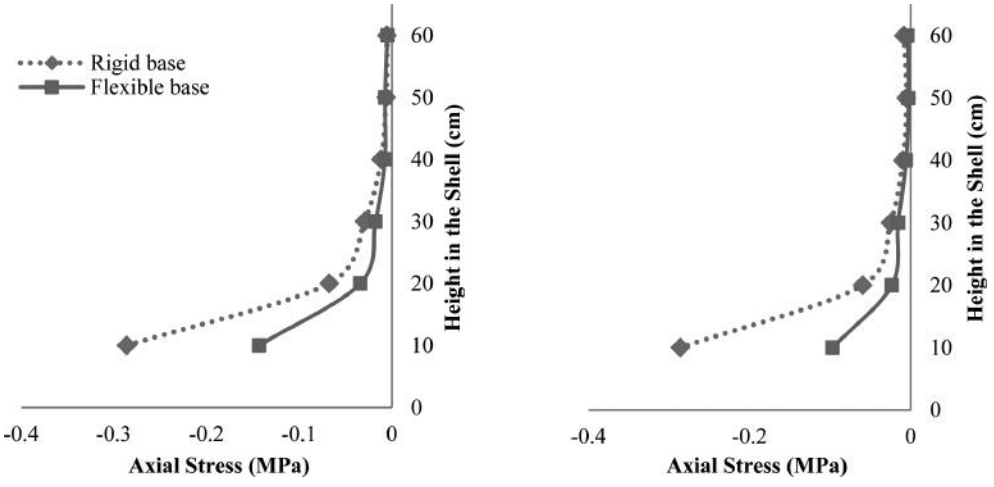

Figure 5. Maximum axial compressive stress for $H/R = 2$. El Centro H1 (left) and El Centro H2 (right).

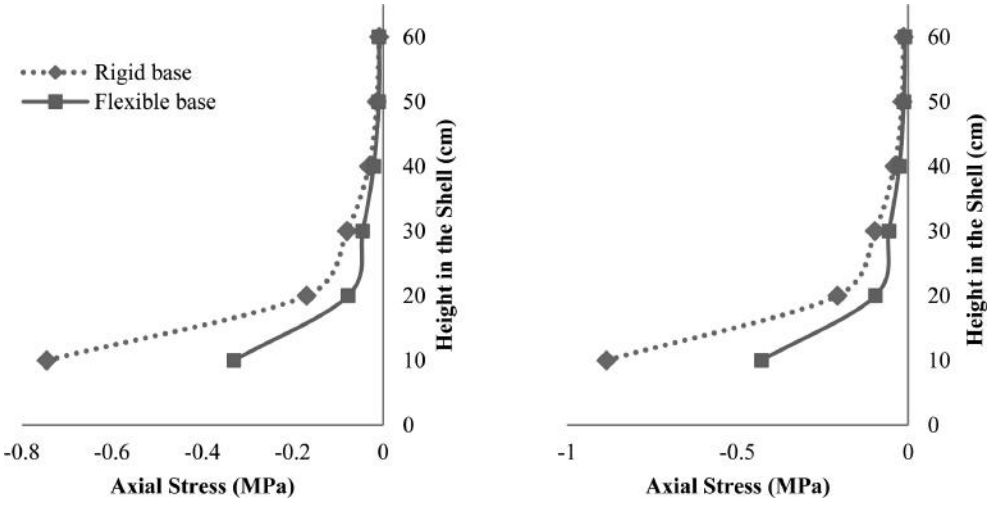

Figure 6. Maximum axial compressive stress for $H/R = 3$. El Centro H1 (left) and El Centro H2 (right).

Table 4. Decrease of the maximum axial compressive stress due to SFSI.

Ground motion	H/R = 2	H/R = 3
El Centro 1	49.92%	55.65%
El Centro 2	66.11%	51.45%
Matahina 1	17.12%	76.39%
Matahina 2	60.09%	79.82%

Table 4 shows that for all cases analysed the maximum axial compressive stress of the tank shell decreased when the tank was placed on a flexible base. In the cases considered (4 time-histories and 2 aspect ratios) SFSI always had a beneficial effect in terms of the axial compressive stresses.

The maximum shell hoop stresses obtained from Matahina (both components) and for both aspect ratios and two support conditions are shown in Figures 7 and 8. Because of

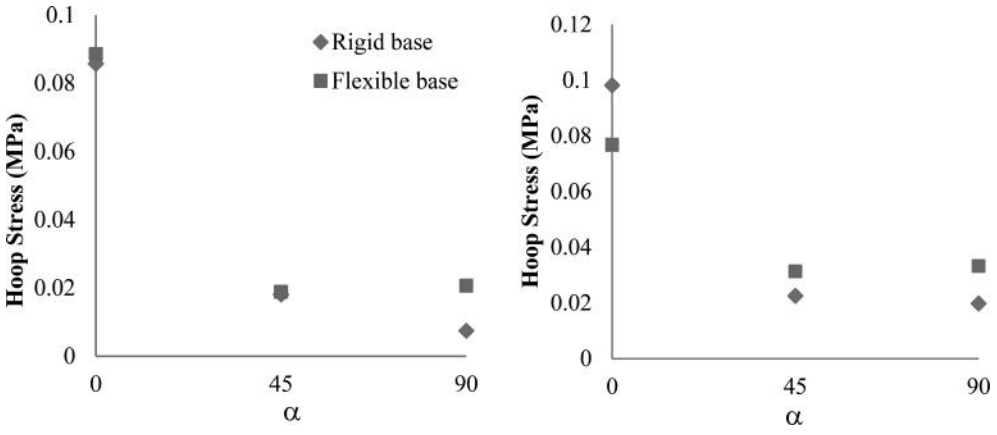

Figure 7. Maximum hoop stresses at the outer tank shell 150 mm above the base, $H/R = 2$ for Matahina H1 (left) and Matahina H2 (right).

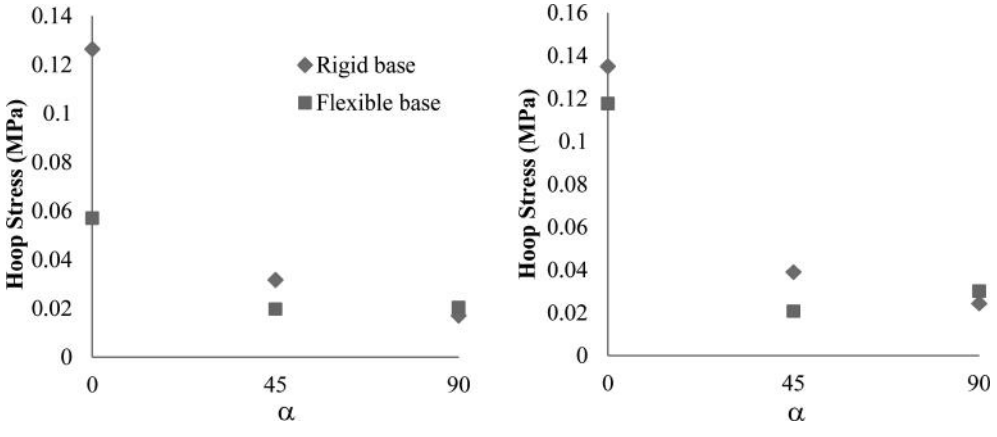

Figure 8. Maximum hoop stresses at the outer tank shell 150 mm above the base, $H/R = 3$ for Matahina H1 (left) and Matahina H2 (right).

the symmetrical radial arrangement of the strain gauges (Figure 3), the results are shown in the locations that form an angle of 0°, 45° and 90° (SG13, SG14 and SG15) with the load direction.

In all the cases the maximum hoop stress was measured in SG13 ($\alpha = 0°$). At this location, this stress varied more significantly than the other points when the support condition was changed. On the other hand, the lowest hoop stress was measured for $\alpha = 90°$ (SG15) in most cases. From Figures 7 and 8 it is not possible to identify a pattern that explains how SFSI affects the hoop stresses of the tank shell outer fiber. However, all these values were obtained at the same height (150 mm). The important value for design of the shell course is the maximum hoop stress. MHSR, at a distance of 150 mm above the base, may be defined as the ratio of the maximum hoop stress with the tank placed on the sand box to that placed on a rigid base, as given in Equation (1). Table 5 shows the MHSR for both ground motions and both aspect ratios.

$$MHSR = \frac{Maximum\ hoop\ stress\ measured\ \ for\ the\ \ flexible\ base}{Maximum\ hoop\ stress\ measured\ \ for\ the\ rigid\ base} \tag{1}$$

Table 5. Maximum hoop stress ratio.

Ground motion	$H/R = 2$	$H/R = 3$
El Centro H1	0.623	0.584
El Centro H2	0.820	0.768
Matahina H1	1.033	0.452
Matahina H2	0.781	0.871

Table 5 shows that SFSI is beneficial in nearly all of the cases (7 of 8) in terms of hoop stresses. The beneficial effect seems to increase when the aspect ratio increases, i.e., the reduction of the maximum hoop stresses due to SFSI is higher when the aspect ratio is higher. This finding confirms what Larkin (2008) found regarding the effect of the aspect ratio on the energy dissipation. Larkin (2008) concluded that in the case of tall slender tanks, most energy is dissipated by foundation rotation, which seems to be in agreement with the results shown in Table 5. Most energy is dissipated by rotation in the case of the aspect ratio equal to 3 and thus, the decrease in the stresses is more pronounced than in the case of aspect ratio equal to 2.

4 CONCLUSIONS

The main aim of this work is to investigate the effect of SFSI on storage tanks under seismic loading using a shake table, while specifically focussing on tank shell axial and hoop stresses. A series of experiments on a model PVC liquid storage tank, with 2 aspect ratios and two base conditions, a rigid base and a sand base, have been described. These experiments were carried out to determine the effect of SFSI on the outer shell stress of liquid storage tanks using 2 earthquake records scaled to the New Zealand design spectrum for a specified site. Previous theoretical studies carried out by other researchers have reported the effect of SFSI on the seismic forces acting on storage tanks. The authors found very few publications on experimental studies that investigated directly the effect of SFSI on tank shell stresses. The shell stresses are the critical design parameters for liquid storage tanks, particularly under seismic loading.

The experimental results showed that SFSI lowers the maximum axial compressive stresses of the tank shell. In all cases using 4 earthquake acceleration time-histories and 2 aspect ratios, i.e. 8 cases, the recorded maximum compressive stress decreased by between 17% and 80% when SFSI is considered.

In 88% of the experiments the maximum hoop stress measured was higher when the tank was placed on the rigid base. The beneficial effect of SFSI in terms of maximum tensile hoop stresses is more significant for high values of aspect ratio.

ACKNOWLEDGEMENTS

The authors wish to thank the Chilean Government for awarding the first author the scholarship "Becas Chile" for his doctoral study at the University of Auckland and the Ministry of Business, Innovation and Employment through the Natural Hazards Research Platform under Award No. 3703249 for the support of this research.

REFERENCES

American Petroleum Institute (API) 2007. Welded steel tanks for oil storage, *API Standard 650*, 11th Edition.

Cooper, T.W. 1997. A study of the performance of petroleum storage tanks during earthquakes, 1933–1995. NIST No. GCR 97–720, *U.S. Dept. of Commerce, National Institute of Standards and Technology*, Gaithersburgh, MD.

Eurocode 8 2004. Design of structures for earthquake resistance - Part 4: Silos, tanks and pipelines. *European Committee Standardization*.

Haroun, M.A. 1983. Behavior of Unanchored Oil Storage Tanks: Imperial Valley Earthquake. *Journal of Technical Topics in Civil Engineering (ASCE)*; 109 (1): 23–40.

Housner, G.W. 1957. Dynamic pressures on accelerated fluid containers. *Bulletin of the Seismological Society of America,* 47: 15–35.

Larkin, T. 2008. Seismic Response of Liquid Storage Tanks Incorporating Soil Structure Interaction. *Journal of Geotechnical and Geoenvironmental Engineering, ASCE*, 134(12): 1804–1814.

Manos, G.C. and Clough, R.W. 1985. Tank damage during the May 1983 Coalinga earthquake. *Journal of Earthquake Engineering and Structural Dynamics*, 13 (4): 449–466.

New Zealand Standard NZS1170.5 2004. Structural Design Actions, Part 5: Earthquake Actions—New Zealand Standard. *NZS*.

NZSEE 2009. Seismic Design of Storage Tanks - Recommendations of a Study Group of the New Zealand National Society for Earthquake Engineering. *NZSEE Recommendations*.

Orense, R.P., Chouw, N., Pender, M.J. 2010. Soil-foundation-structure interaction. *CRC Press*, 241pages. ISBN: 978–0-415–60040–8

Ormeño, M., Larkin, T., and Chouw, N. 2012. Influence of uplift on liquid storage tanks during earthquakes. *International Journal of Coupled Systems Mechanics,* 1(4): 311–324.

Veletsos, A.S. and Meek, J. 1974. Dynamic Behaviour of Building-Foundation Systems. *Earthquake Engineering and Structural Dynamics,* 3: 121–138.

Veletsos, A.S. and Tang, Y. 1990. Soil-Structure Interaction Effects for Laterally Excited Liquid Storage Tanks. *Earthquake Engineering and Structural Dynamics,* 19: 473–496.

Soil Liquefaction during Recent Large-Scale Earthquakes – Orense, Towhata & Chouw (Eds)
 ISBN 978-1-138-02643-8

Summary of discussion session 1

ABSTRACT: At the end of each day of the workshop, a discussion session was conducted with the aim of eliciting important comments about issues and new trends related to the current state of understanding of soil liquefaction and related processes. The first discussion session dealt with soil/site characterisation and liquefaction triggering issues.

SPECIAL NOTE

The two discussion sessions were conducted under intense yet enjoyable exchange of opinions among the workshop participants. Because of the inherent difficulty in capturing everything what was said and perhaps losing the context when transforming them into a written form, readers are cautioned that what follows represents the best efforts of the editors to capture the flow and cut-and-thrust of the discussions.

1 SITE CHARACTERISATION

1.1 *Geological variability and control*

An accurate characterization of a target site that has a large amount of variability in terms of the geological aspects is very important. For example, when analysing alluvial deposits, a slight change in location could result in very different soil properties. If the soil behaviour type index (I_c) is used to estimate the fines content of these types of soil, it will result in a very large amount of scatter. Some of the scatter could be due to the way the data are collected and compared to geological variability, or even possibly due to fundamental limitations, i.e. I_c may not be the right index for estimating fines content alone. For example, results from Christchurch investigations confirmed the large scatter in the results indicating that I_c is not a good predictor of fines content. Such uncertainty may eventually lead to one making decision as to whether soil samples should be obtained for further tests to develop soil-specific correlations.

An example of uncertainty issues is the CBGS data (as presented in the paper by Wotherspoon et al.) where comparisons of point-to-point measurement produced scatters that are not particularly meaningful. Due to the highly interlayered materials at the site, the resistance varied substantially with the different layers present in the site; very high for sandy layers, and very low for silty ones. In these cases, comparison of Standard Penetration Tests (SPT) and Cone Penetration Tests (CPT) may not be indicative of the inherent correlation between the two because of the uncertainty by which the types of soil are plotted together, independent as to whether the sites are homogenous or heterogeneous.

Another example is the CHHC site (also in Christchurch) with fairly thick sand layer. Considering the depth between 5 m–10 m from the ground surface with similar geological units, the variability of SPT/CPT data can be random. In these cases, it would be best to compare the average (mean) or median values within the same geological unit, rather than point-to-point measurement. This is mainly because the data samples are usually not enough for point-to-point measurements.

Additionally, the scale of the natural geologic heterogeneity relative to the failure mechanism is important to be considered, especially for individual pipeline, utility line or small residential homes located on top of a loose pocket of soil.

1.2 *Investigation of geologic conditions and incorporation in regional practice*

It was suggested that geotechnical engineers should work with geologists in performing non-invasive tests to obtain some indications on how the subsurface ground varies and to analyse the underground properties carefully before deciding which type of tests, i.e. CPT or SPT, to be performed, is the most cost-effective way to get the most of the geotechnical investigation. This collaboration between engineers and geologists is exemplified in general geotechnical engineering practice in New Zealand, where a third of the staff usually consists of engineering geologists whose work includes performing desktop studies, scoping investigations and advising geotechnical engineers at the site in addition to performing explorations in the field.

In Japan, on the other hand, the practice is slightly different; if during an investigation, the results found are close to the triggering point of liquefaction (borderline), more detailed investigations are conducted, as opposed to simply relying on SPT/CPT correlation (e.g. perform detailed cyclic tests on frozen undisturbed samples). Similar to New Zealand practice, the geologists' contribution in planning and conducting field explorations is common in Japan. It was also pointed out that joint research work between geologists and geotechnical engineers should address two important issues: (1) ageing effect on soil; and (2) formulating micro-zoning maps.

Different from New Zealand and Japan practice, it was noted that in the United States, the collaboration between geotechnical engineers and geologists are not sufficient, especially in planning and conducting explorations. From a research interest standpoint, one of the difficulties is that geologists mainly focus on rock rather than on soil. The reasons could vary from the education background of pure geologists to the support of research funds in certain research areas. Certainly, there are firms that integrate geological information upfront and perform very well in practice. However, there were also geotechnical failures in practice that could be attributed to missing geologic details and lack of geological information and therefore, the collaboration between geologists and geotechnical engineers should be improved. Nevertheless, the role of geologists in design practice may vary depending on the firm and the scale of the project; companies at different locations for the same parent firm may have different proportion of geologists. For larger, more important projects, there is usually greater involvement of the geologists than for smaller projects.

2 MAGNITUDE SCALING FACTOR (MSF)

Fatigue problems are always a combination of loading and soil properties. However, historically, the focus in liquefaction studies is more on the properties of the earthquake motion rather than on the liquefaction resistance of the soils. For example, previous data from high-quality frozen sand samples showed that the slope of the liquefaction resistance curve (plotted in log-log space) indicated a value of $b = 0.34$, which was subsequently used by Idriss (1999) when he derived his Magnitude Scaling Factor (MSF). However, data show that for sands, the slope systematically varies; dense sands may give values close to $b = 0.5$, while loose sands may have flatter slopes, with $b = 0.08$–0.15. This means that the relative density of the sand significantly affects the b-value, even if the samples considered are clean sands. This observation is also supported by other research that showed the effects of different fines content and density of silt and clays on the range of the b-value. The work by Carter et al. (this volume) examines the maximum possible value of MSF (i.e. $b = 0.35$) for very short earthquake duration; MSF equals the ratio of the expected number of cycles for reference earthquake with magnitude 7.5 to the number of cycles of the small magnitude earthquake, raised to the power of b. It was also shown that the relationship between MSF and parameter b depends on the material characteristics and how they respond to the cyclic loading.

It is therefore expected that the magnitude-duration effects, as exemplified by the MSF, be accounted for by the following: (1) role of soil type/density; and (2) role of ground motion characteristics. Different density and soil composition will have different liquefaction resistance curves. At low number of cycles, the curve tends to have the steepest slope. Referring to the liquefaction resistance curves with different b values and replacing the number of cycles by earthquake magnitude, it can be noted that dense soil needs many cycles to liquefy. When the fines content is increased in clean sand, the curve becomes flatter, i.e. non-plastic fines content lowers the b value.

For magnitude 9 earthquake events where there is a very long duration of shaking (e.g. 3 minutes), such as that observed in the 2011 earthquake in Japan, excess pore water pressures can generate over a long period of time. This can cause drainage issues, such as redistribution of excess pore water pressure which is usually ignored during conventional analyses. A totally new approach is required to capture this phenomenon.

During the Christchurch earthquake sequence, small earthquake magnitudes induced liquefaction (even those with magnitude 5). However, for these low magnitude earthquake events, the conventional MSF-based approaches did not give a good correlation between the expected damage and actual damage observed. For Christchurch sites consisting of different layers (alternating sequences of low and high density sand and silts), different magnitude scaling factor for each layer may be necessary.

Thus, it was suggested that the parameter b used for determining the magnitude scaling factor can pose more uncertainty than characterising the ground motion. Low magnitude events have the largest MSF, so this is where the b parameter matters the most. As the magnitude moves further away from M7.5, the magnitude scaling factor matters more and more. The use of current MSF derived using $b = 0.34$ which is appropriate for dense sand is unconservative to evaluate the liquefaction potential of loose sand.

It was countered that the b value can be determined from shear modulus and damping degradation curves developed for use in equivalent linear site response analyses, where the curves are a function of effective confining stress, density, and plasticity index. Based on a quick parametric study, b values only ranged from about 0.3 to just over 0.35. This is in contrast to the large range of b values stated by the other workshop participant.

In New Zealand practice, magnitude-related peak ground accelerations (PGA) provided by the code are still being widely used, notwithstanding the huge variability in seismicity. However, it should be emphasized that the MSF value indicated in the NZ standard is actually based on the loading standard restricted to structure only and should not be applied to geotechnical engineering analysis. There were also suggestions to include source-to-site distance in determining MSF, which is not only dependent on the number of cycles but also on the PGA and ground motion excitation, which in turn are related to duration and frequency content. It may be important to understand that differences in source-to-site distance have huge effect on the PGA and vibration frequency; thus, ignoring this factor may result in underestimating the liquefaction potential for near-fault earthquakes.

Therefore, the determination of MSF cannot be approached by simply addressing it as a function of one particular parameter. As an example, consider a soil sample under a confining pressure of 100 kPa. If the fines content is changed, the density will also change and the G-γ curve will be shifted according to the change in the stiffness. Suppose the material is changed into gravel, then the result would be a very stiff sample that no strain will be detected in the material, although it might have similar non-linear pattern compared to sand (but significantly higher).

3 LIQUEFACTION SUSCEPTIBILITY CRITERIA

3.1 *Fines content issues*

In conventional liquefaction analysis, it has been customary to take a definitive value of the soil behavior type index, I_c, to determine liquefaction susceptibility, i.e., when $I_c < 2.60$ the

soil is most likely granular in nature and would liquefy; however, this does not mean that when $I_c = 2.59$ the soil would indeed liquefy (and for that matter, $I_c = 2.61$ would not liquefy). Care needs to be taken, especially when using spreadsheets in liquefaction calculation to make sure that values close to the cut-off criteria are identified. An observation was made on a site in Christchurch where non-plastic silty material with high fines content still liquefied.

There is a need to distinguish between "liquefaction" and "cyclic softening". It was agreed that both failures cause deformation of the soil, although they are actually fundamentally different in terms of what actually happens to the soil. Liquefaction is often used to describe ground failure in both sands and low-plasticity silt/clay. Common engineering guidelines suggest that if silt or clay is "liquefiable", SPT/CPT liquefaction correlation should be used. Recommendations to sample and test potentially liquefiable silt/clay are often not followed. On the other hand, if silt or clay is deemed "non-liquefiable", it is immediately assumed that there would not be any problems, while it actually means that a different approach need to be implemented to evaluate strength loss and deformation of the soil.

Guidance provided by Bray & Sancio (2006) and Boulanger & Idriss (2006) recommends that laboratory testing of field samples is the preferred approach for silts/clays (with sufficient plasticity to sample). Laboratory tests are necessary because current SPT/CPT liquefaction correlations usually underestimate the strengths of these soils. It is also important to note that any soil can deform if the seismic stresses exceed its dynamic strength, independent as to whether it is liquefiable or not.

The precision of the judgment made based on plasticity index (*PI*) values was questioned. One of the most commonly used guidelines that $PI < 7$ indicates liquefiable soil should not be used as a sole indicator. For most cases, it is more important to consider geological aspects, e.g. perform sensitivity analysis and evaluate the fines content in the soil before deciding which criteria actually matter. It was agreed that while *PI* values are not representative, dealing with the scale of the material and the spatial distribution should not be overlooked. It was strongly emphasised that no one should use the Chinese liquefaction susceptibility criteria anymore as they are no longer acceptable.

3.2 *Field tests vs laboratory tests*

In current engineering practice in NZ, in-situ vane shear tests are usually favoured over laboratory or CPT tests to avoid complications, e.g. disturbance of soil sample. To determine soil properties in individual residential areas, laboratory tests are often left out due to limited time and budget. Even for larger projects where tests are acknowledged to be important, more detailed sampling are still often not carried out, especially at largely free-field sites. Sometimes, it is immediately assumed that soil liquefaction may occur and preventive designs are adopted instead.

However, it was suggested that performing laboratory tests could potentially reduce the conservatism from assuming that the soil would liquefy as well as the total construction cost. Compared to the consequences, e.g. casualties and tremendous economic loss due to possible failures, it is the duty of the engineers to convince their clients about the invaluable insights one may get from representative samples and laboratory tests to understand soil response under cyclic loading.

For soil with clay-like behaviour, vane shear tests are indeed crucial. Moreover, when dealing with residual deformations caused by initial static shear stress, the importance of performing undrained cyclic triaxial tests on anisotropically consolidated samples was also put forward. Although it may seem to result in spending more time and money at first, eventually it will reduce the total construction cost for the client. It is also important to make sure which type of soil one is dealing with before doing tests, e.g. heterogeneity and consolidation condition. Especially for volcanic soils, where the material properties are not known, assumption of existing correlation may not be valid. Thus, good quality sample and laboratory tests are compulsory. Geotechnical engineers must sell the benefits of spending money on laboratory testing to the client.

4 DIFFICULT SOILS: GRAVELS, OLD AND/OR LIGHTLY CEMENTED SOIL

A discussion was made on the complexity of gravel, which represents a number of different soil types, ranging from continuous layer to mixed with sand. A case history was presented about a project which dealt with highly interlayered material and where an Instrumented Becker Penetration Test (IBPT) was used to measure the blow-by-blow energy at the tip. The problem when using this instrument was the high friction which developed along the shaft, especially when analysing dense hard layer or when deep drilling was needed. Pulling back to measure the friction would not help because when the instrument was moved back forward, it introduced different mechanism which consequently gave inaccurate reading. Additionally, finding appropriate measuring device to be located at the tip of the instrument that can withstand the pounding force also proved to be challenging.

In NZ, a typical approach to characterize gravel is by shear wave velocity tests. This is done by creating a hole, backfilling with sand, and then doing a shear wave velocity test in the hole. In Japan, the practice still tend to favour SPT. Based on experience, it appeared that large penetration device that can reasonably accommodate shear-wave velocity measurements worked best. Moreover, compared to other tests such as SPT, sonic core drilling proved to be the most useful as it showed steady reading when dealing with all-gravel sites.

MAJOR CONTRIBUTORS

R. Boulanger (Session Chairman), P. Brabharan, B. Bradley, J. Bray, P. Clayton, M. Cubrinovski, R. Green, S. Iai, I.M. Idriss, K. Stokoe, I. Towhata, S. van Ballegooy, S. Yasuda.

This page intentionally left blank

Soil Liquefaction during Recent Large-Scale Earthquakes – Orense, Towhata & Chouw (Eds)
© 2014 Taylor & Francis Group, London, ISBN 978-1-138-02643-8

Summary of discussion session 2

ABSTRACT: The second discussion session was patterned on the earlier discussion session but the focus was on issues related to liquefaction effects on structures and countermeasures.

SPECIAL NOTE

The two discussion sessions were conducted under intense yet enjoyable exchange of opinions among the workshop participants. Because of the inherent difficulty in capturing everything what was said and perhaps losing the context when transforming them into a written form, readers are cautioned that what follows represents the best efforts of the editors to capture the flow and cut-and-thrust of the discussions.

1 ESTIMATING THE CONSEQUENCES OF LIQUEFACTION TO STRUCTURES

1.1 *Use of liquefaction indices to estimate deformation*

Various liquefaction indices are commonly used to estimate the consequences (deformations and damage) of soil liquefaction. These indices include: thickness of non-liquefiable soil layer (H_1) and underlying liquefiable soil layer (H_2); liquefaction potential index (LPI); liquefaction induced ground settlement (Sv_{1D}); liquefaction severity number (LSN); liquefaction severity index (LSI); or combinations of these. It is generally accepted that relying solely on these indices may not be sufficient to estimate the damage to structures. The discussion focused on assessing how well these indices can correlate with liquefaction-induced deformation and damage.

It is generally accepted that liquefaction indices are not very accurate; however they do have a role in design against the effects of liquefaction. It was suggested that liquefaction indices need to be suitable for the structure under consideration and different structures at the same site will have different deformation behaviour due to the soil-structure interaction effect. For example, the use of liquefaction indices for the design of small residential houses may be acceptable; however, larger projects will require more detailed analysis. Moreover, different indices will have different levels of importance depending on the structure being considered. For example, deeper layers of liquefiable soil would be of greater significance for deep bridge foundation than for small residential houses at the same site.

Care must be taken when employing these indices. Noting that factor of safety (F_s) is incorporated in all these indices, an example comparing liquefaction of two soil layers was discussed. Both layers have safety factor less than 1, i.e. 0.8 for one layer and 0.4 for the other. When a range of earthquake events occurs, the layer with $F_s = 0.4$ will liquefy several cycles before the other layer. It is possible that the other layer (with $F_s = 0.8$) may not liquefy at all because of the change in ground response due to the liquefaction in the first layer. Current indices cannot explain this phenomenon, and may be conservative. From this perspective, design procedure should integrate the damage of individual layers by considering the interaction between layers.

A detailed analysis is needed to gain better insight into liquefaction effects and countermeasures. For larger projects, a requirement for more detailed analysis needs to be "sold" to

the client, particularly on projects where, for example, building tilts at a higher level and large non-uniform loads beneath the structure.

It was pointed out that previous research in New Zealand and Japan have provided a number of high quality cases to better understand the effect of ground motion and soil profile to determine safety factors. However, it is still doubted whether using liquefaction indices alone could generate good design decisions due to the uncertainties in ground motions and soil profiles. Consequently, when liquefiable material in the foundation is discovered, the best way may be to do more detailed analysis before deciding whether to make improvements on the soil or accepting the condition as it is. Generalizing different types of structures should be avoided because different types of structures have different categories of problems and uncertainties that need to be assessed individually.

Moreover, it is very important to assess the type and weight of the structure as well as the foundation types. For residential houses and most lightweight structures, e.g. one or two-storey buildings with light cladding or relatively light structural elements, using liquefaction indices may be sufficient. However, for larger and heavier structures, the foundation details, e.g. spread footing, deep foundations, etc., need to be considered for further analysis. Engineers should be encouraged to differentiate the types of building and to understand the influencing factors and the likelihood of underperformance of the structures and to inform the clients if more detailed analysis is required.

1.2 *Timing of ground deformation occurrence*

In past earthquake events in Japan, settlement of short buildings (up to 3-storey high) occurred several days after shaking, although different behaviour was observed for taller buildings. In the two earthquake events in June 2011 in Christchurch which were 80-minutes apart, it was observed that two minutes after shaking, the ground around the bank of Avon River started to crack. Observation revealed that most of the lateral spreading movement happened after the strong shaking. The timing of settlement of foundation is very important, especially when attributed to the occurrence of lateral spreading. Commonly, the timing is categorized into three instants: i.e. during, immediately after, or well pass the shaking. Knowing the timing could give valuable insights in anticipating different scenarios of settlement and failure mechanisms. It was suggested that the delay was due to the time needed for the pore pressure to migrate and cause lateral spreading movement.

In terms of whether there is a standard for a "good timing", settlements usually occur at different times following different earthquake events. During the 1964 Niigata earthquake in Japan, lateral spreading occurred a minute after shaking and caused a bridge to collapse. Considering the case in Christchurch, two minutes may be considered as a good timing.

It is important to distinguish between high-magnitude and long-duration shaking with low-intensity and near-fault shaking where liquefaction occurs very quickly. For example, rapid rates of cyclic loading are likely to cause settlement during the earthquake shaking, while longer duration, lower intensity events may cause settlement later. In addition, light structure goes along with the liquefaction process and settles after shaking while heavy structure may experience significant settlement during the strong shaking phase due to inertial effect. Thus, settlement does not always occur after strong shaking as it may also occur during the shaking. There appears to be a tendency to over-generalise when settlement actually takes place vis-avis earthquake shaking, i.e. settlement is likely to occur at different times for different earthquake events.

1.3 *Liquefaction consequences*

The overturning moment of a building is an important factor controlling the tilt angle of the structure. Tilt angle increases as the overturning moment increases, and consequently leads to a decrease in safety factor. A general trend observed from actual structures is that if the contact pressure increases, e.g. in tall buildings, larger settlement and overturning moments may occur and result in the tilting of the building. It is generally agreed that no shallow

foundations shall be constructed on potentially liquefiable soil. Even in medium dense or dense sand, infrastructures founded on such condition can develop pore water pressure within the soil at very intense level of shaking.

One of the issues that cause problems in understanding is the generalization of different types of liquefaction and their consequences. One phenomenon with severe consequence is the cyclic flow, i.e. liquefaction with large unlimited strain potential. This type of liquefaction could cause buildings or large infrastructures to be carried away, and leads to large lateral spreads. Slightly less severe is the cyclic mobility with limited strain potential. In extreme loading, accumulation of displacements could occur in many cycles. This type of liquefaction could also generate pore water pressure even in dense soil under extreme loading, albeit having less severe consequences. Thus, it is important to distinguish liquefaction based on the severity of the consequences.

1.4 *Numerical procedures*

One of the limitations of current settlement calculations is that they only consider 1D volumetric settlement. In reality, the effects of initial shear stress, soil-structure-interaction (SSI) ratcheting and the ejection of liquefied soil will also contribute to the overall vertical permanent settlement of the structure. A common numerical procedure to analyse ground deformation involves application of initial static shear stress, followed by cyclic shear stress. Settlement or movement of the foundation will then be determined. It was proposed that two-dimensional deformation shall be considered instead of the typical one-dimensional volumetric settlement. From a practical point of view, the two-dimensional approach would be more accurate because it includes the effect of soil-structure interaction and shear deformation to estimate the overall vertical settlement. However, in reality, it is still difficult to perform; moreover, SSI ratcheting can be dominant but it is difficult to measure and quantify. It was added that current numerical models have limitations, e.g. difficulty in simulating accurately the effect of static shear stress. In many cases, the numerical models may look convincing, but may not represent the actual behaviour in the field.

Even with today's knowledge, numerical models are still unable to capture the formation of liquefied soil ejecta on ground surface and this phenomenon may cause significant settlement not accounted for in the conventional approaches. Low bearing capacity in addition to liquefaction triggering generally results in ejecta. In practice, this is being addressed by the application of *LSN*-based methodology by considering the role of the upper crust.

1.5 *Effects of long duration and aftershocks on deformation and damage to structures*

A footage showing the effects of long duration and subsequent events following the main shock on liquefaction was presented. The crust on the site where the footage was taken is one metre thick. Strain softening of the lower liquefied layer occurred not only due to the long duration of the M9.0 main shock, but also due to the M7.9 aftershock, which occurred before the excess pore water pressure was fully dissipated. Secondary liquefaction, i.e. softening of the non-liquefied upper layer due to the combined effects of upward migration of excess pore water from the underlying liquefied layer and cyclic loading caused by the aftershock, was also observed.

Regarding aftershock effects on liquefaction, a brief discussion about an earthquake aftershock study in Urayasu City, Japan was presented. From the dynamic effective stress analysis, it was found that the maximum value of pore water pressure could occur after the aftershock, and thus suggested that the aftershock can be more significant than the main shock when dealing with liquefaction due to large magnitude events.

1.6 *Shallow and deep liquefaction*

Shallow liquefaction matters most for short buildings such as residential houses. Residential houses usually have shallow foundations, and thus, liquefaction occurring within the

foundation ground will have greater influence to the foundation, and consequently, to the structures. In many cases, shallow liquefaction that occurs right beneath the structure will have more significant effect compared to deep liquefaction that occurs well below the structure. In terms of building settlement, deep liquefaction may have significant effect to bridge structure, which can be categorized as short structure, but significantly stiffer. Additionally, differential settlement may also be introduced; soil-structure interaction at one end of the bridge may be different from the other end.

2 DESIGN PROCEDURES FOR PILE FOUNDATIONS IN LIQUEFIABLE SOILS

The discussion focused on the assessment of damage to piles in laterally spreading area and how small acceleration in liquefiable soils can have significant effect on the deformation. During the 1995 Kobe earthquake, significant effects of ground displacements on pile foundations were observed. There were indications of extensive lateral spreading of the liquefied soil layer along the coastline. There were variations in horizontal displacements from the shore line that caused different types of failures. Most of the design codes use effective ground displacements and simplified pseudo-static analysis to consider the lateral force from superstructure and ground displacement to estimate lateral spreading failures.

In designing piles in liquefiable soils, small movements, such as mere 30–40 mm, can cause kinematic loading. From shaking table test results of previous research, it was suggested that simplifications of the numerical analysis can help make good decisions. Inertia forces can cause significant damage to quay walls. Moreover, there is a need to consider the relative displacement of soil over the length of the pile.

It is important to address group pile performance within the upper crust soil layer, since the movement of crust in-between the piles may have certain governing factors on the overall pile deformations that could lead to more complications. Overall, pile groups normally will not be severely impacted by lateral displacement, but each individual pile might. The overall resistance of the pile group may also change significantly due to the additional governing factors. Finally, there is a need to recognise that liquefaction of deeper layers is generally not good for piles, and the effects of the deeper liquefiable layers will depend on the structure under consideration.

3 REMEDIAL MEASURES AGAINST LIQUEFACTION-INDUCED DAMAGE

The discussion on remedial measures against soil liquefaction to preserve structures started off with the introduction of a structure that survived liquefaction without significant damage while the surrounding soils underwent lateral spread. One of the more popular solutions is to install soil-cement piles to mitigate uneven settlement of structures under static loading. In Japan, 80–90 percent of residential houses are built on ground without any soil treatment. However, the superstructures are usually quite strong that even when they are tilted, the buildings only suffer minor damages.

It was pointed out that for soil restoration, it is better to do large-scale repair. However, one major problem in Japan is that it is very difficult to get all the residents and land owners to unanimously agree on the repair, most commonly because such works are very expensive. Thus, restoration of one residential site at a time may be a feasible option. However, instead of just residential sites, the entire area including roads and parks could be damaged, and affect the residential sites, even after those areas have been restored. Therefore, overall repair may be the best solution. Due to the high cost of residential houses in Japan, soil improvement could be a better solution to avoid demolition.

After the 2011 Japan earthquake, several methods to level up tilted wooden house were introduced: using jacks, compaction grounding, chemical injection, and underpinning with concrete plates or steel pipe piles. Similar methods were also used in Christchurch where currently, certain trials were performed in the red-zone sites to improve the soil condition.

These were implemented not to prevent liquefaction but rather to provide preventive solutions to achieve acceptable level of performance of structures. It is believed that this is the most cost-effective solution considering current limitations, e.g. varying ground conditions, shallow water tables, and high costs. From commercial development viewpoint, more interests are focused on building new structures rather than improving the soil. The complexity of land ownership issues in Christchurch when determining the extent of ground improvement and construction is also an issue. A large construction project close to the boundary of an adjacent site can place additional load onto the soil at the neighbouring site.

It was suggested that designing structure to resist liquefaction may cost less compared to performing ground improvements. However in Japan, due to the high cost of land, ground improvements are possibly more worthwhile than in other locations where the land is less valuable.

Ground improvements for residential houses in New Zealand can be complicated, especially for newly proposed solutions with no precedence. Engineering decisions tend to follow restrictions coming from existing guidance and insurance covers, although more suitable design may be available. For example, the guidelines suggested that stabilized shallow raft may not be used for all structures with a liquefiable layer greater than 10 m; however, this approach can provide satisfactory performance for small lightweight residential structures. One solution to this issue is to find a balance between guidelines and engineering judgment, focusing on using the same solution with alteration to comply with the guidelines, e.g. reducing the thickness to acceptable region.

4 ASSESSMENT OF CARBON EMISSION DUE TO GROUND MODIFICATION

Although presented during the first Discussion Session, this topic is incorporated here for consistency. It was pointed out in that there is an increasing interest in the study of carbon emission due to ground modification and liquefaction-induced settlement repairs. Thus, the purpose of the presentation was to introduce carbon emission assessment for residential houses related to structural performance, i.e. settlement and tilting and their correlation to earthquake and geotechnical engineering. It was noted that it is important to convince clients to be more aware of carbon emission and such consideration shall be incorporated during the decision making process, although it might increase the initial construction cost. In this case, optimisation between cost and carbon emission needs to be made. In terms of the amount of cost needed, doing preventive works (ground modifications) upfront may be more beneficial than doing repairs after earthquake events. There are three possibilities when carbon-reducing works could be done and their consequences: (1) no preventive works will need extensive post-earthquake repairs, and lead to high carbon emission; (2) moderate preventive works combined with mild post-earthquake repairs will require moderate carbon emission; and (3) substantial preventive works will need no post-earthquake repairs, and lead to low carbon emission. It is also important to note that carbon-reducing works are usually proportional to the increase in safety of the structure itself.

MAJOR CONTRIBUTORS

K. Tokimatsu (Session chairman), R. Boulanger, P. Brabharan, B. Bradley, J. Bray, N. Chouw, M. Cubrinovski, A. Elgamal, S. Iai; A. O'Sullivan, M. Stapleton, Y. Tamari, I. Towhata, S. Yasuda.

This page intentionally left blank

Soil Liquefaction during Recent Large-Scale Earthquakes – Orense, Towhata & Chouw (Eds)
© 2014 Taylor & Francis Group, London, ISBN 978-1-138-02643-8

Photos

K. Inadome (Consul General, Japanese Consulate at Auckland) delivering his welcome remarks.

S. Gomibuchi (Ministry of Business, Innovation and Employment) delivering his welcome remarks.

View of the workshop.

View of the workshop.

I. Towhata (University of Tokyo) delivering his invited presentation.

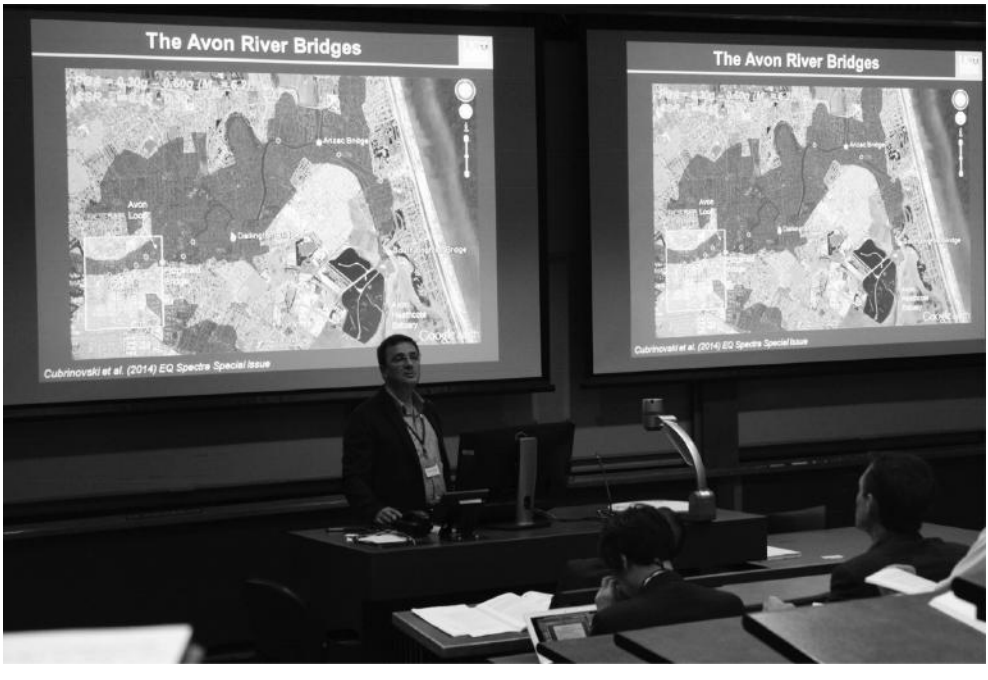

M. Cubrinovski (University of Canterbury) delivering his invited presentation.

K. Stokoe (University of Texas at Austin) delivering his invited presentation.

E. Sáez (Pontificia Universidad Católica de Chile) delivering his invited presentation.

R. Boulanger (UC Davis) leading the first of the discussion sessions.

K. Tokimatsu (Tokyo Institute of Technology) leading the second of the discussion sessions.

S. Iai (Kyoto University) making a comment during the discussion session.

J. Bray (UC Berkeley) making a comment during the discussion session.

S. van Ballegooy (Tonkin & Taylor) making a comment during the discussion session.

Networking during the socials.

Exchanging pleasantries during the tea break.

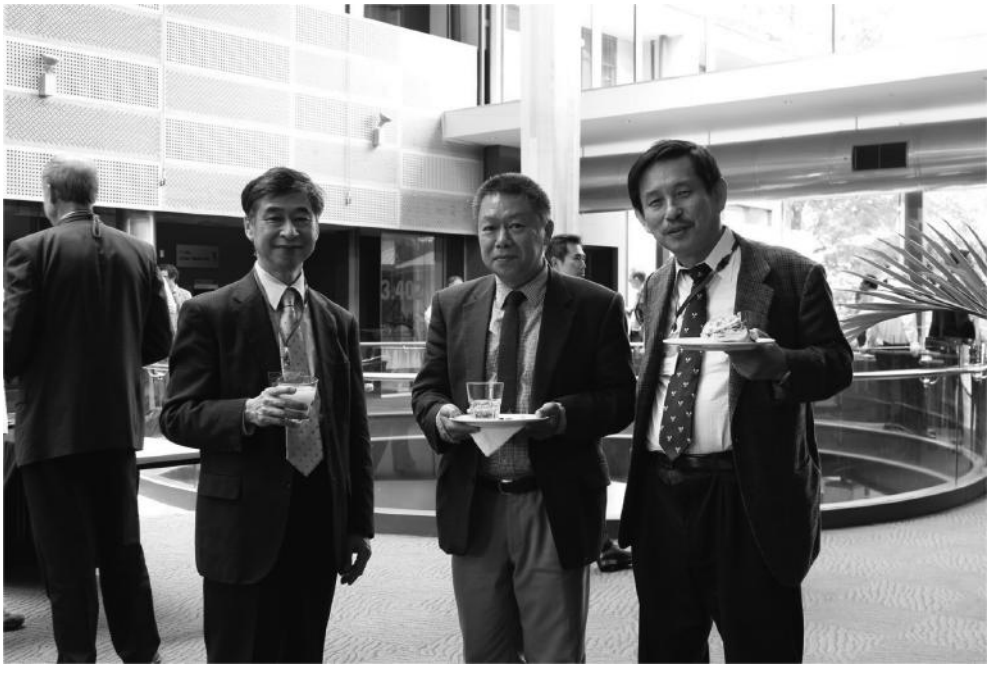

Exchanging pleasantries during the tea break.

Exchanging pleasantries during the tea break.

Exchanging pleasantries during the tea break.

M. Pender (University of Auckland) delivering his welcome remarks at the workshop dinner.

I. Idriss (UC Davis) giving a speech during the workshop dinner.

This page intentionally left blank

Soil Liquefaction during Recent Large-Scale Earthquakes contains selected papers presented at the New Zealand - Japan Workshop on Soil Liquefaction during Recent Large-Scale Earthquakes (Auckland, New Zealand, 2-3 December 2013).

The 2010-2011 Canterbury earthquakes in New Zealand and the 2011 off the Pacific Coast of Tohoku Earthquake in Japan have caused significant damage to many residential houses due to varying degrees of soil liquefaction over a very wide extent of urban areas unseen in past destructive earthquakes. While soil liquefaction occurred in naturally-sedimented soil formations in Christchurch, most of the areas which liquefied in Tokyo Bay area were reclaimed soil and artificial fill deposits, thus providing researchers with a wide range of soil deposits to characterize soil and site response to large-scale earthquake shaking.

Although these earthquakes in New Zealand and Japan caused extensive damage to life and property, they also serve as an opportunity to understand better the response of soil and building foundations to such large-scale earthquake shaking. With the wealth of information obtained in the aftermath of both earthquakes, information-sharing and knowledge-exchange are vital in arriving at liquefaction-proof urban areas in both countries. Data regarding the observed damage to residential houses as well as the lessons learnt are essential for the rebuilding efforts in the coming years and in mitigating the potential danger to buildings located in regions with high liquefaction potential.

As part of the MBIE-JSPS collaborative research programme, the Geomechanics Group of the University of Auckland and the Geotechnical Engineering Laboratory of the University of Tokyo co-hosted the workshop to bring together researchers to review the findings and observations from recent large-scale earthquakes related to soil liquefaction and discuss possible measures to mitigate future damage.

Soil Liquefaction during Recent Large-Scale Earthquakes will be of great interest to researchers, academics, industry practitioners and other professionals involved in Earthquake Geotechnical Engineering, Foundation Engineering, Earthquake Engineering and Structural Dynamics.

ISBN 978-1-138-02643-8

9 781138 026438

CRC Press
Taylor & Francis Group
an **informa** business
www.crcpress.com

6000 Broken Sound Parkway, NW
Suite 300, Boca Raton, FL 33487
Schipholweg 107C
2316 XC Leiden, NL
2 Park Square, Milton Park
Abingdon, Oxon OX14 4RN, UK

an **informa** business